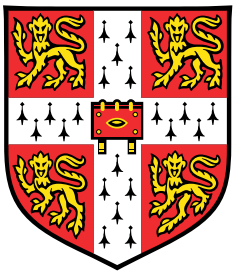

Quantum oscillation studies in the unconventional superconductor YFe_2Ge_2 and in the Dirac semimetal candidates NbXSb (X = Ge/Si)

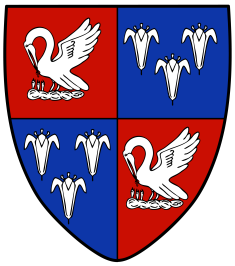

Keiron James Murphy

Department of Physics
University of Cambridge

This thesis is submitted for the degree of
Doctor of Philosophy

Corpus Christi College

January 2020

DECLARATION

This thesis is the result of my own work and includes nothing which is the outcome of work done in collaboration except as declared in the Preface and specified in the text. It is not substantially the same as any that I have submitted, or, is being concurrently submitted for a degree or diploma or other qualification at the University of Cambridge or any other University or similar institution except as declared in the Preface and specified in the text. I further state that no substantial part of my thesis has already been submitted, or, is being concurrently submitted for any such degree, diploma or other qualification at the University of Cambridge or any other University or similar institution except as declared in the Preface and specified in the text. This thesis contains fewer than 60,000 words including appendices, bibliography, footnotes, tables and equations and has fewer than 150 figures.

Keiron James Murphy
January 2020

ABSTRACT

Quantum oscillation studies in the unconventional superconductor YFe_2Ge_2 and in the Dirac semimetal candidates NbXSb (X = Ge/Si)

We have performed experiments to probe the ground state dynamics of YFe_2Ge_2, NbGeSb and NbSiSb. An unusually large Sommerfeld coefficient ($\gamma \sim 100$ mJmol^{-1}K^{-2}) has been observed in the d-electron system YFe_2Ge_2. It also shows an anomalous power law temperature dependence of the electrical resistivity ($\rho = \rho_0 + AT^{3/2}$) which indicates Fermi liquid breakdown, possibly connected to its vicinity to a quantum critical point. The materials NbXSb (X = Ge,Si) have been theoretically predicted via initial density functional theory (DFT) calculations to harbour Dirac/Weyl-like features in their electronic band structure.

YFe_2Ge_2: Quantum oscillations were measured in the range 5-18 T using the de Haas-van Alphen effect. The observed quantum oscillation frequencies have been compared to DFT calculations of the electronic structure. Several Fermi surface sheets predicted by DFT have been observed and their quasiparticle masses have been measured. The context of these measurements with regards to the electronic structure in YFe_2Ge_2 has been discussed. It was found that the quasiparticle effective mass enhancement of the detected Fermi surface sheets can account for only $\sim$40% of the mass enhancement previously observed from specific heat measurements.

NbXSb (X = Ge/Si): Quantum oscillations were measured over the range 3-18 T using the Shubnikov-de Haas effect in NbXSb. Many frequencies have been observed in NbSiSb which also shows an extremely large magnetoresistance. We have considered the origin of parts of the quantum oscillation spectrum at high fields and briefly discussed this in relation to magnetic interactions and magnetic breakdown. One clear frequency has been seen in NbGeSb, which also shows an unusual negative magnetoresistance at low fields. Quantum oscillation frequencies in both materials have been compared to DFT calculations. The Berry phase has been estimated for the observed Fermi surface sheets in both materials, suggesting a topological nature in these materials.

Keiron James Murphy

I would like to dedicate this thesis to my friend Thomas Ventress and to my wife Meg, you always believed in me and I wouldn't be here without you.

ACKNOWLEDGEMENTS

During my time as a PhD student I have been introduced to many fantastic people who have encouraged me to become a better researcher. My fellow members of the Quantum Matter group have made my PhD experience most enjoyable and it has been a pleasure to spend the past three years working with them. I would like to thank my supervisors: Michael Sutherland and Malte Grosche both of whom have been invaluable mentors. With seemingly never ending patience they have provided direction, encouragement and have helped me to achieve my goals. Because of their enthusiasm I have been inspired to pursue a career in research. I must give special thanks to Jordan Baglo with whom I worked closely in the 'big fridge' room. He has been very patient with me when sharing his vast experimental experience of low temperature techniques (as well as many others), I have learnt so much from him for which I am incredibly grateful.

Without the tireless efforts of fellow PhD student Jiasheng Chen a large proportion of this thesis would not have been possible. His work in the systematic improvement in sample quality of YFe_2Ge_2 has resulted in the measurements which form a large part of this work. We have also had many useful discussions throughout my PhD for which I am very grateful. I am indebted to Jonathan Alaria who I worked with at the University of Liverpool on NbXSb and with whom I continue to collaborate. Monika Gamza performed single crystal XRD analysis on NbXSb crystals and DFT calculations on these systems were performed by Bartomeu Monserrat and his PhD student Bo Peng. I would also like to express a special gratitude to Patricia Alireza and Siân Dutton who have always looked out for me and encouraged me while I have been at the Cavendish.

I have made great friends in David Jarvis, Matt Coak and Phil Brown who have made my experiences in the lab as well as outside of work most enjoyable. I am also grateful to the many past and present members of the Quantum Matter group who have helped me during my time as a graduate student. I would particularly like to thank Alex Davies, Indy Liu, Alex Eaton, Thomas Gruner, Cheng Liu, Konstantin Semenuik, Sofia Taylor-Coronel, Puthipong Worasaran and Paromita Mukherjee and the rest of the quantum matter group for their friendliness and helpfulness.

Finally, I would like to thank my wife Meg, who has encouraged me and pushed me further than I thought I could reach, thank you for all of your support.

TABLE OF CONTENTS

LIST OF FIGURES

LIST OF TABLES

CHAPTER 1

INTRODUCTION

The study of emergent quantum phenomena has developed into a central theme in condensed matter at low temperatures. A physical description of any material has its origins in quantum mechanics, which relates how atoms bond and electrons interact at a fundamental level. In many cases the quantum effects can be approximately captured using a classical picture at the macroscopic level, recently however, material systems in which the effects of quantum mechanics persist over a much wider range of energy and length scales have seen a huge surge in interest. These so-called quantum materials are defined as solids with exotic physical properties, arising from the quantum mechanical properties of their constituent electrons, with no classical analogue. They include graphene, topological insulators, Dirac/Weyl semimetals, quantum spin liquids and spin ices, and unconventional superconductors. The quantum properties of many of these materials originate from a confinement of electrons to two-dimensional sheets. Additionally, many quantum materials share a common feature in that their electrons can no longer be treated as independent particles but have strong interactions which give rise to collective excitations known as quasiparticles. The ability to experimentally realise quantum phases of matter and to be able to control their physical properties is a key goal in quantum materials research. To achieve this goal requires the synthesis of high quality bulk crystals, thin films and nanostructures of materials which demonstrate the complex interplay between the emergent quantum behaviour and additional factors such as topology, Coulomb interactions, dimensionality and symmetry.

Emergent quantum phenomena are likely to be crucial in the development of the next-generation of quantum technologies needed to meet the urgent technological demands of a safe and sustainable society. Figure 1.1**a** shows a history of the development of quantum materials research, from quantum Hall physics and high-T_c cuprate superconductivity in the 1980's, to current research interests such as topological insulators and the anomalous Hall effect (AHE) and spin Hall effect (SHE), to future prospects including topological electronic devices. The major technological fields likely to benefit from this vast area of research are electronics using topological currents and quantum spins (spintronics), photovoltaics and thermoelectrics, and secure quantum computing and communication. A substantial amount of research is still needed, however, to bridge the gap between the present day

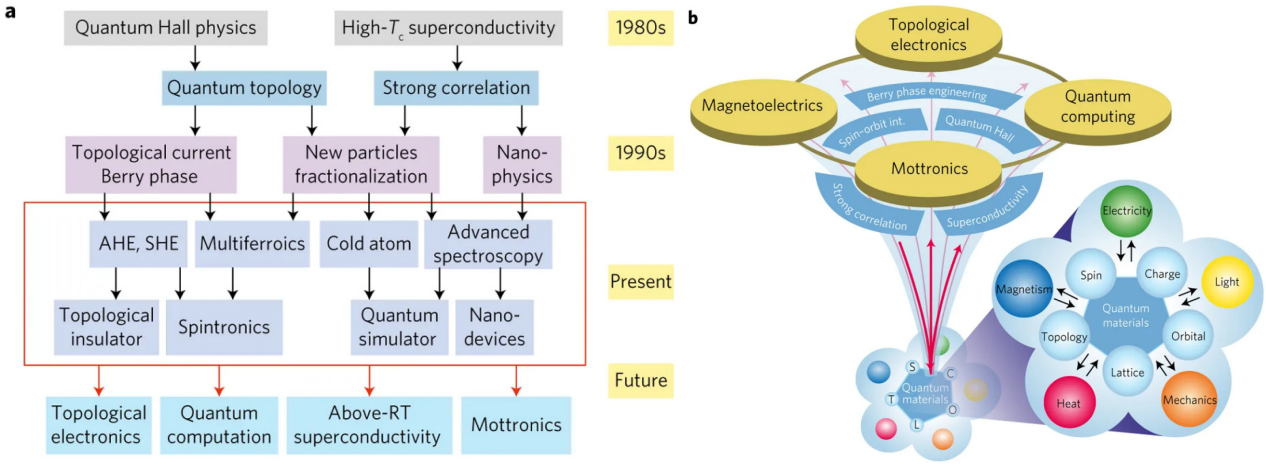

Fig. 1.1 **(a)** Timeline showing a history of quantum materials and the possible future direction of research. **(b)** The various degrees of freedom demonstrated in strongly correlated electron systems, in response to external stimuli. Strong interactions lead to emergent functions with the cross correlations among different physical observables and to developments towards the applications of emergent functions such as Mottronics, magnetoelectrics, topological electronics, and quantum computing. Reprinted by permission from Springer Nature [1]).

and future prospects as outlined in the figure. An indication of the size of the quantum matter research field is indicated in Figure 1.1**b**, where the interplay of the various degrees of freedom demonstrated in strongly correlated electron systems, in response to external stimuli, is highlighted.

This thesis focuses on fermionic systems which host several aspects of emergent quantum phenomena, namely the unconventional superconductor YFe_2Ge_2, which appears to be located close to a quantum critical point (QCP), and the topological semimetal candidates NbGeSb and NbSiSb. A phase transition at zero temperature occurs at a QCP, which gets its name from the fact that the fluctuation in the order parameter are quantum in nature. In 1956 Lev Landau introduced the groundbreaking theoretical simplification to describe fermionic systems when he showed that strongly interacting fermions can be described in terms of new non-interacting particles known as quasiparticles in his Fermi liquid theory [2]. This theory is the cornerstone of most materials in modern condensed matter physics, however, Fermi liquid theory can breakdown in a number of interesting situations such as in the vicinity of a QCP where strong correlations can destroy the Landau quasiparticle [3]. It has been suggested that topological quantum critical phenomena can also be displayed in topological semimetal materials, specifically in Dirac/Weyl semimetals [4, 5], leading to non-Fermi liquid behaviour. How we can adapt the Fermi liquid picture to account for new states that cannot be described in the simple non-interacting picture is a question of fundamental importance in these systems.

A generic phase diagram of a quantum phase transition is depicted in Figure 1.2. The phase transition occurs as the zero temperature limit of a finite temperature phase transition between an ordered state and a quantum disordered state. A quantum critical point is typically achieved by a continuous

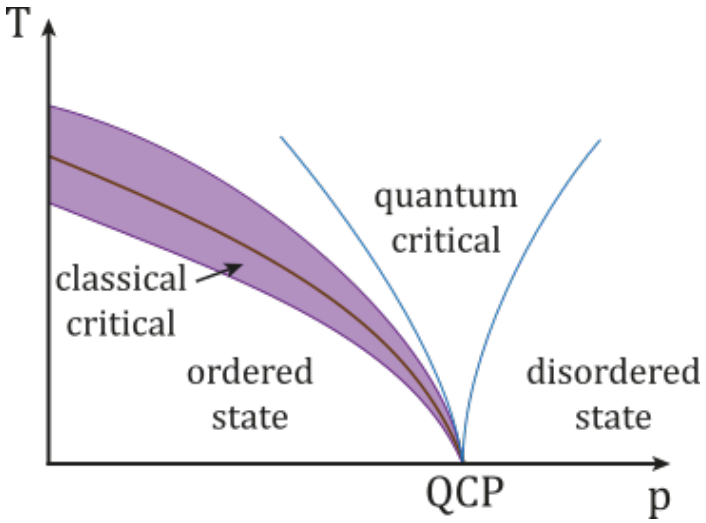

Fig. 1.2 A generic phase diagram at a continuous quantum phase transition, temperature (T) and tuning parameter (p) showing the quantum critical point (QCP) and quantum phase transitions.

suppression of a non-zero temperature phase transition to zero temperature by the application of an external stimulus such as pressure, magnetic field, or via chemical doping. Thermal fluctuations destroy coherence of the order parameter at high temperatures resulting in a macroscopic state with no order parameter. At zero temperature, in the absence of any thermal fluctuations which lead to conventional phase transitions, quantum phase transitions are triggered by the zero point quantum fluctuations associated with Heisenberg's uncertainty principle. Long wavelength quantum fluctuations can give rise to non-universal material properties in the intermediate quantum critical region. The region of the phase diagram in which exotic phases of quantum matter are expected to form is the quantum critical region.

In fermionic systems Landau's Fermi liquid theory gives a solid base from which to relate the unusual quantum phases of matter to regions of parameter space where the weakly interacting quasiparticle picture hold, away from phase transitions. The challenge of understanding the macroscopic behaviour of quantum matter is to apply quasiparticle dynamics and evaluate if the quasiparticle picture remains valid. This idea provides motivation for our experiments.

This question has received interest not only from the theoretical community but there have already been many reports of materials which challenge the notion of the Landau quasiparticle. A number of material classes demonstrate remarkable changes to quasiparticle behaviour, or some that show a complete breakdown of the quasiparticle picture. Fermi liquid breakdown has been suggested as the cause of the anomalous behaviour seen in the heavy fermion materials such as $CeCu_{6-x}Au_x$ [6], $YbRh_2Si_2$ [7], and $CeRhIn_5$ under pressure [8]. It has been suggested that the Landau quasiparticle is destroyed in these materials and the Fermi temperature goes to zero. There are also situations in which a number of materials demonstrate a marginal Fermi liquid state, in which the Fermi liquid state does

not completely breakdown, but is subject to long range fluctuations which result in unusual properties. This marginal Fermi liquid behaviour has been used to explain the properties of $ZrZn_2$ [9, 10], and has also been suggested to explain the normal state behaviour of the high-T_c cuprate superconductors [11]. Fermi liquid breakdown has also been suggested to appear in topological materials such as topological double- and triple-Weyl semimetals [12], and in Dirac semimetals [5].

The emergence of an unusual phase has been suggested in the first of the materials investigated in this thesis. The unconventional iron-based superconductor YFe_2Ge_2 shows a breakdown in Fermi liquid theory and lies close to a quantum critical point in parameter space [13]. Chemical doping of Y in $Lu_{1-x}Y_xFe_2Ge_2$ suppresses an antiferromagnetic phase and reduces the Néel temperature to zero at an optimal doping of x = 0.2 where a quantum critical point has been predicted to reside beneath a possible superconducting dome [14]. The two remaining materials that have been investigated, NbGeSb and NbSiSb have been suggested as candidate topological semimetal materials from band structure calculations, we have set out to attempt to uncover any signatures of this behaviour in this work.

We have performed measurements of the electronic structure in YFe_2Ge_2, NbGeSb and NbSiSb using the de Haas - van Alphen and Shubnikov - de Haas effects as a function of magnetic field and temperature. These measurements have allowed us to determine some aspects of the Fermi surface in these materials which are to the best of our knowledge the first bulk electronic structure measurements in these materials.

1.1 Thesis layout

In Chapter 2, a brief overview of the key theoretical concepts underpinning the experimental results discussed in the later chapters is presented. These include theory of Fermi liquids, the theory of magnetic oscillations in metals: specifically the theory of the de Haas-van Alphen effect, and magnetic breakdown. Chapter 3 describes the low temperature experimental techniques required to measure the physical properties of samples presented in later chapters, the main focus are quantum oscillation measurement techniques performed using a multi-sample rotation probe on the Cambridge dilution refrigerator.

In Chapter 4, the results of a quantum oscillation rotation study, using the de Haas - van Alphen effect, in high purity single crystal samples of YFe_2Ge_2 are presented. A comparison of theoretical calculations to the quantum oscillation measurements is used to discuss the implications for the electronic structure of YFe_2Ge_2.

In Chapter 5, the results of a growth procedure for synthesising high-quality, single crystal samples of NbXSb (X = Ge,Si) samples are presented. Preliminary thermodynamic and transport measurements of these samples are introduced before the results of a detailed quantum oscillation rotation study are

presented. The measurements were performed using the Shubnikov - de Haas effect, in high purity single crystal samples of Nb*X*Sb. A comparison of theoretical calculations to the quantum oscillation measurements is used to discuss possibilities of the electronic structure of both materials. An analysis of the quantum oscillation data is used to ascertain any topological nature in each of the materials via a calculation of the Berry phase.

Finally, in Chapter 6, a short summary is given where I discuss the broader relevance of the study on YFe_2Ge_2, as well as a discussion of the topological nature of NbGeSb and NbSiSb. The potential for future work based on the results obtained is also discussed.

CHAPTER 2

THEORETICAL BACKGROUND

This chapter covers the necessary background theory needed to analyse and interpret the results of measurements included in chapters four and five. First, Landau's Fermi liquid theory is introduced which is key in our understanding of strongly correlated electron systems. An overview of the theory of magnetic oscillations in metals (quantum oscillations) is then given, highlighting the use of this measurement technique as a powerful probe of quasiparticle dynamics.

2.1 Fermi liquid theory

The requirement for a theory governing the normal state behaviour of metals dates back to the first applications of quantum mechanics to the metallic state, there were several puzzling experimental observations that could not be explained theoretically such as the classical specific heat contribution of $^3/_2 k_B T$ per electron, far greater than was observed experimentally, and the departure from the expected $^1/_T$ Curie temperature behaviour of a free magnetic moment. These problems were solved by Pauli when he adapted Fermi statistics, in addition to the exclusion principle, to describe the electron [15]. The ground state that results from this approach is made up of a filled Fermi sea of occupied states in momentum space with a sharp separation from the the higher energy unoccupied states at the Fermi level ε_F (this defines the Fermi surface). Low energy excited states are achieved via the promotion of electrons from just below the Fermi surface to available states just above it, the empty state left just below the Fermi surface is labelled as a hole. It is clear in this picture that only a small number of electrons in a metal are available to contribute to the specific heat and magnetic susceptibility, resolving the puzzles proposed earlier as such a large proportion of electrons are so far below the Fermi surface that it is energetically unfavourable for them to move to the unoccupied quantum states required to carry excess heat or be magnetised. Only electrons that are within $k_B T$ of the Fermi surface can contribute k_B the specific heat and so it is small and linear with temperature. Similarly, only electrons within $\mu_B B$ of the Fermi surface can be magnetised with a corresponding moment

of $\sim \mu_B$ resulting in a temperature-independent magnetic susceptibility. While these developments described the experimental observations of metals very well, they posed an additional problem: in a system in which interactions are clearly important, how can a theory which was developed from a non-interacting perspective work so remarkably well? The solution was provided by Lev Landau and utilises the concept of 'adiabatic continuity' [2].

2.1.1 The electron quasiparticle

Landau's approach was to describe the the interacting gas of electrons via adiabatically turning on the interactions between electrons slowly in the non-interacting Fermi gas. He postulated that the low energy eigenstates of the interacting system would directly map onto the eigenstates of the non-interacting Fermi gas. The idea of Fermi particle and hole excitations which carry the same quantum number labels as the electrons in the non-interacting Fermi gas picture is retained. The excitations are called quasiparticles as the quantum number labels are no-longer associated with the electrons of the free Fermi gas. The Fermi sphere is described as a vacuum from which quasiparticles are created, the term quasiparticle will be used to describe the weakly interacting excitations of a strongly interacting system in this thesis. The concept of the fermion quasiparticle is the key idea in Fermi-liquid theory [3].

2.1.2 Properties of Fermi liquids

The resulting measurable physical properties that are relevant to this thesis are a linear electronic heat capacity (C_{el}) at low temperatures, which is modified by a mass enhancement due to the effective mass (m^*) of the quasiparticles, and T^2 power law dependence of the electrical resistivity (ρ). Using the total energy of the isotropic interacting system calculated by Landau [2], expressions for the specific heat and resistivity are obtained:

$$C_{el}^* = \frac{m^*}{m_e} C_{el} \ , \tag{2.1}$$

where m^*/m_e is the mass enhancement factor. The electronic part of the heat capacity dominates at low temperatures, at higher temperatures the full form of the heat capacity is:

$$C_v = \gamma T + \beta T^3 = C_{el} + C_{phonon} \ , \tag{2.2}$$

where C_{el} and C_{phonon} are the electronic and phononic contributions to the specific heat respectively. The expression for the resistivity comes from the fact that close to the Fermi level, the scattering time scales as $\tau^{-1} \propto \varepsilon_k^2$, where ε_k is the energy relative to the Fermi energy:

$$\rho(T) = \rho_0 + AT^\gamma \ , \tag{2.3}$$

where A is referred to as the A-coefficient, which quantifies the quasiparticle-quasiparticle scattering lifetime, and γ is the exponent of the temperature dependence of the resistivity (where $\gamma = 2$ for Fermi liquids). These properties are found in a large variety of materials, an impressive example being the heavy Fermi liquids such as UBe_{13} which have shown mass enhancements of up to a factor of 1000 [16]. Metallic materials which deviate from the properties outlined above are referred to as displaying non-Fermi liquid behaviour.

2.1.3 Beyond Fermi liquid theory

There are examples where the usual properties of a Fermi liquid, as described above, are not observed, but the concepts of Fermi liquid theory can still be applied. An example of this is in the disordered electronic systems such as thick metallic films, further details of which can be found in [17]. A breakdown of Fermi liquid theory has also been demonstrated in the vicinity of a quantum critical point, however, Fermi liquid concepts have been used to describe a magnetic quantum phase transition [18, 19]. It is necessary to differentiate between situations in which it is still possible to explain material properties using the picture of quasiparticles which are no longer considered independent, to that of a picture in which the concept of the quasiparticle is no longer valid.

2.1.4 Luttinger's theorem

A volume enclosed by a material's Fermi surface is equal to the density of particles, this is Luttinger's Theorem [20]. In general, it has been shown that this theorem holds whenever the system can be described as a Fermi liquid [21] making it a powerful tool in the study of strongly correlated electron systems. When Luttinger's theorem is applied to quantum oscillation data, a number of complications can arise, the most significant of which is that the identification of whether a given Fermi surface is electron-like or hole-like is not usually possible using quantum oscillation data alone. For 3D Fermi surfaces which have multiple connections, an exact determination of the Fermi surface volume can be unreliable, however, electronic structure calculations can aid in the interpretation of the data.

2.2 Quantum oscillations

In 1930, the work of Lev Landau predicted that the magnetisation of metals would show a strong non-linear and periodic magnetic field dependence at sufficiently low temperatures and in strong magnetic fields [22]. Landau also stated that it would be unlikely that this effect could be observed in any experiment due to practical technological limitations in achieving a strong enough homogeneous magnetic field. Shubnikov and de Haas actually observed similar behaviour to the periodic dependence predicted by Landau before his work was published, when they measured the magnetoresistance

of single crystals of bismuth [23]. Later in that same year and, unaware of the predictions of Landau, de Haas and van Alphen observed periodic oscillations (in inverse magnetic field), in the magnetisation (or magnetic susceptibility) again in single crystals of bismuth [24]. The two effects of periodic oscillations in electrical resistivity and in magnetic susceptibility came to be known as the Shubnikov-de Haas (SdH) effect and the de Haas-van Alphen (dHvA) effect respectively. These periodic oscillations are also observable in many other physical properties (such as, for example, magnetothermal oscillations) and are collectively known as quantum oscillations. Great advances in the theory governing the phenomena, as well as in methods of an experimental detection have simultaneously been made, and quantum oscillations are now a powerful experimental technique widely used today to probe the electronic structure of metals. A comprehensive overview of the theory of quantum oscillations as well as many aspects of the development of experimental techniques is given by Shoenberg [25].

2.2.1 Landau levels

For independent fermions with a parabolic dispersion, the formation of Landau levels in an externally applied magnetic field can be demonstrated [22]. The following derivation is adapted from [25]. In the semi-classical approximation, a free electron moving in a homogeneous magnetic field will experience a force (known as the Lorentz force) and will undergo helical motion along the direction of the applied field. This circular motion of a particle (in momentum space) is described by the Bohr-Sommerfeld quantisation rule for periodic motion:

$$\oint \mathbf{p} \cdot dr = 2\pi\hbar\,(n + {}^1\!/_2) \ , \tag{2.4}$$

where p and r are the momentum and position variables and n is an integer. An electron in a magnetic field has as its momentum variable $\mathbf{p}$:

$$\mathbf{p} = m\mathbf{v} - e\mathbf{A} \ , \tag{2.5}$$

where $\mathbf{A} = {}^1\!/_2(\mathbf{r} \times \mathbf{B})$ is the magnetic vector potential of the magnetic field $\mathbf{B}$, $\mathbf{v}$ is the velocity, e is the electron charge and m is the electron mass. The Lorentz force is defined as

$$\mathbf{F} = -e\,(\mathbf{v} \times \mathbf{B}) = m\dot{v} = \hbar\dot{k} \ , \tag{2.6}$$

where $\hbar$ is the reduced Planck's constant and k is the momentum space wavevector. This can be used in conjunction with Stokes' theorem to obtain

$$\begin{aligned}\oint \mathbf{p}\cdot dr &= -e\oint (\mathbf{r}\times\mathbf{B})\cdot d\mathbf{r} - e\oint \mathbf{A}\cdot d\mathbf{r} \\ &= e\oint \mathbf{B}\cdot(\mathbf{r}\times d\mathbf{r}) - e\int_{area}(\nabla\times\mathbf{A})\cdot d\mathbf{s} \\ &= eBA_{\mathrm{r}} = 2\pi\hbar\,(n+1/2)\ ,\end{aligned} \tag{2.7}$$

in which A_{r} is the real space orbital area of the cyclotron motion of the electron. Using the definition of the Lorentz force in equation 2.6, the orbital area in momentum space, A_{k}, is related to the real space orbital area, A_{r}, via

$$A_{\mathrm{k}} \equiv \pi k_n^2 = \left(\frac{eB}{\hbar}\right)^2 A_{\mathrm{r}} = \frac{2\pi\,(n+1/2)\,eB}{\hbar}\ , \tag{2.8}$$

where k_n is the momentum space orbital radius, this is the famous Onsager relation [26]. The relation severely limits the allowed values of k in a magnetic field which can be visualised via the geometric construction shown in Figure 2.1 in which the orbits form the so-called Landau tubes. For the simple case of a free electron gas, the Landau tubes are straight coaxial cylinders around the axis of the applied magnetic field, the cross-sectional areas of which are given by equation 2.8. In a real material, assuming the independent electron approximation, the eigenstates of the system in an applied magnetic field shift from the usual lattice of states within the Fermi surface to concentric rings around the Landau tubes, as depicted in Figure 2.1. This simple picture is also valid if electron-electron interactions are slowly turned on (Fermi liquid theory) allowing the simple picture of states confined to Landau tubes to be applied to real materials. Increasing the magnetic field strength results in an expansion of the Landau tubes, the radii of the orbital states in momentum space will grow as $\sqrt{B}$ and the energy of the states increases with B. As the magnetic field strength is increased, the radius of the outermost Landau tube expands and approaches the radius of the extremal cross-section of the Fermi surface perpendicular to B. At this point the density of states (DOS) at the Fermi level diverges and, with a further increase in the field strength the Landau tube height shrinks to zero and the DOS drops sharply. The DOS is maximised when one of the many Landau tubes matches up with the Fermi surface such that:

$$A_{\mathrm{k}} = A_{\mathrm{Fs}}\ , \tag{2.9}$$

where A_{Fs} is the area of an extremal orbit of the Fermi surface perpendicular to the magnetic field B. Therefore, each time a Landau tube (containing the k-states) crosses the Fermi surface, there will be a peak in the DOS at the Fermi level, which leads to oscillatory behaviour. As the physical properties of a real material at low-temperatures are determined by DOS at the Fermi level, all thermodynamic and transport properties derived from the DOS should oscillate as a function of a changing magnetic field.

The oscillations are periodic in $^1/_B$ and the period between oscillations which satisfies equation 2.9 is:

$$\Delta\left(\frac{1}{B}\right) = \frac{2\pi eB}{\hbar A_{\mathrm{Fs}}} \,. \tag{2.10}$$

The oscillation frequency, which has units of magnetic field strength (T), is

$$f \equiv \frac{1}{\Delta\left(^1/_B\right)} = \frac{\hbar}{2\pi e} A_{\mathrm{Fs}} \,. \tag{2.11}$$

For Fermi surfaces which have a more complicated structure, the quantum oscillation frequency is a measure of only the extremal cross-sectional area of the Fermi surface perpendicular to the applied field. This is a result of the DOS remaining approximately constant as the Landau tubes move across all parts of the Fermi surface except at the extremal cross-sectional areas perpendicular to the magnetic field. Measurements presented in this thesis are primarily concerned with the field dependence and oscillatory behaviour of: magnetic susceptibility, known as the dHvA effect (Chapter 4), and of resistivity, known as the SdH effect (Chapter 5).

2.2.2 The thermodynamic potential and physical observables

It can be shown, as outlined by Shoenberg [25], that in a metal in an externally applied magnetic field, the grand thermodynamic potential of electrons has an oscillatory component $\widetilde{\Omega}$ which has a field dependence as:

$$\widetilde{\Omega} \propto B^{5/2} \sum_{p=1}^{\infty} \frac{1}{p^{5/2}} \cos\left(2\pi p\left(\frac{f}{B} - \frac{1}{2}\right) \pm \frac{\pi}{4}\right). \tag{2.12}$$

This result is valid at zero temperature for a perfect crystal and does not account for the interaction of spins with the magnetic field. The sum is due to the Fourier series decomposition and the integer p accounts for harmonics. The phase shift of $\pm\,\pi/4$ accounts for whether the extremal area of the Fermi surface is a minimum (a neck with a positive phase shift) or a maximum (a belly with a negative phase shift). Differentiating the grand thermodynamic potential $\widetilde{\Omega}$ with respect to B allows the magnetisation along the field direction to be calculated and a second differentiation results in the corresponding component of the magnetic susceptibility $\widetilde{\chi}$. To account for any imperfections or crystal lattice defects the theory needs to take into account the effects of finite temperature and electron spins. The influence of both of these effects can be added to the model via a superposition of several oscillations each carrying a phase shift with a varying distribution. This is equivalent to a reduction in the amplitude of the oscillations by a certain factor, a process known as phase-smearing. The reducing factor is related to the Fourier transform of the phase shift distribution.

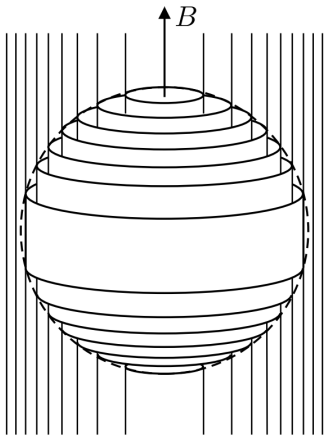

Fig. 2.1 Schematic of a Fermi sphere rearranged into Landau tubes. Electronic k-states within a spherical Fermi surface (dashed line) for electrons in an applied magnetic field B. Figure adapted from [25, p. 23].

2.2.3 Effect of impurities and temperature

The effect of finite temperature can be introduced to the model via the Fermi-Dirac distribution:

$$f(\varepsilon) = \frac{1}{e^{(\varepsilon-\mu)/k_{\mathrm{B}}T}+1} \,, \tag{2.13}$$

where ε is the energy, T is the temperature, $\mu(T)$ is the chemical potential and k_{B} is the Boltzmann constant. The reduction in the quantum oscillation amplitude is due to the smearing of the Fermi surface which in turn is due to a broadening of the Fermi-Dirac distribution step function at finite temperature. The effect of this is to broaden the frequency f, which is equivalent to phase smearing. The reduction factor, R_T, expressed for the p^{th} harmonic is:

$$R_T = \frac{X}{\sinh(X)} \quad \text{and} \quad X = \frac{2\pi^2 p k_{\mathrm{B}} T m^*}{e\hbar B} \,, \tag{2.14}$$

where the theory has been extended to include systems with interacting electrons by introducing the effective quasiparticle mass, m^*. Crystalline defects and impurities will also alter the oscillations, the effects from this can be accounted for via the mean scattering time τ. The mean scattering time can be related to the average distance travelled by electrons between the scattering events. This distance l, is known as the mean free path and is often used to quantify the quality of crystals, it is given by:

$$l = v_F \tau = \frac{\hbar k_{\mathrm{F}} \tau}{m} \,, \tag{2.15}$$

where $v_{\mathrm{F}} = {}^{\hbar k_{\mathrm{F}}}/_{m}$ is the Fermi velocity. Any finite scattering time will result in an uncertainty in the associated energy levels (due to the uncertainty principle) which is equivalent to a broadening of the Fermi energy. R. Dingle characterised this broadening using a Lorentzian distribution which results in a reduction factor to the quantum oscillations of:

$$R_D = \exp\left(\frac{-\pi p m^*}{eB\tau}\right) = \exp\left(-X\frac{T_{\mathrm{D}}}{T}\right) , \tag{2.16}$$

where R_{D} is known as the Dingle factor and the Dingle temperature $T_{\mathrm{D}} = {}^{\hbar}/_{2\pi k_{\mathrm{B}}\tau}$ has been introduced to make the expression in a similar form to that of equation 2.14 [27]. The Dingle temperature, in addition to equations 2.10 and 2.15, can be used to estimate a measure of the mean free path:

$$l_{mfp} = \frac{\sqrt{2e\hbar^3 f}}{2\pi m^* k_{\mathrm{B}} T_{\mathrm{D}}} . \tag{2.17}$$

2.2.4 Spin splitting

In a magnetic field the up and down spin degeneracy of electrons is lifted due to Zeeman splitting, and each energy level is split into two levels which are separated by an energy

$$\Delta\varepsilon = \frac{g\hbar eB}{2m_e} , \tag{2.18}$$

where g is the spin g-factor (assumed to be = 2). Electrons with different spins will become separated in energy by $\Delta\varepsilon$, resulting in two components to the quantum oscillations separated by a phase of:

$$\Delta\phi = 2\pi\frac{\Delta\varepsilon}{{}^{e\hbar B}/_{m^*}} , \tag{2.19}$$

where ${}^{e\hbar B}/_{m*}$ is equal to the energy difference between neighbouring Landau levels. The superposition of the two oscillations is equivalent to an additional multiplication factor to the amplitude of (utilising equations 2.18 and 2.19) :

$$R_s = \cos\left(\frac{1}{2}p\Delta\phi\right) = \cos\left(\frac{1}{2}p\pi g\frac{m^*}{m_e}\right) , \tag{2.20}$$

again for the p^{th} harmonic.

2.2.5 The Lifshitz-Kosevich formula

Combining the corrections relating to finite temperature, impurities and defects, and spin splitting, a full formula describing quantum oscillations, known as the Lifshitz-Kosevich formula (or just LK formula) is obtained [28]. The significant contribution to oscillations in the magnetic susceptibility (the dHvA effect) along the direction of the magnetic field is given by:

$$\widetilde{\chi} = \left(\frac{8\pi e^3}{\hbar^3}\right)^{1/2} \frac{k_{\mathrm{B}} T f^2}{|A_{\mathrm{k}}''|^{1/2} B^{5/2}} \sum_{p=1}^{\infty} \frac{\exp\left(-X\frac{T_{\mathrm{D}}}{T}\right)\cos\left(\frac{1}{2}p\pi g\frac{m^*}{m_e}\right)}{p^{-1/2}\sinh(X)} \cos\left(2\pi p\left(\frac{f}{B}-\frac{1}{2}\right)\pm\frac{\pi}{4}\right) , \quad (2.21)$$

where X is defined in equation 2.14 and $A_{\mathrm{k}}^{''}$ is the curvature of the Fermi surface along the magnetic field direction at the extremal orbit. Utilising the reduction factors R_{T}, R_{D} and R_{s} detailed above the dependence of the oscillatory component for a 3D system is given by the proportionality:

$$\chi \propto -\sqrt{B} R_{\mathrm{T}} R_{\mathrm{D}} R_{\mathrm{s}} \sin\left[2\pi\left(\frac{f}{B}+\lambda-\Delta\right)\right] , \quad (2.22)$$

where a Berry phase has been taken into account for a topological system. The oscillations of χ are described by the sine term with a phase factor (λ - Δ), in which λ = ($^1/_2$ - $^{\Phi_B}/_{2\pi}$) and Φ_B is the Berry phase. The dimensionality of the Fermi surface determines the phase shift Δ which has a value of $\pm$ 1/8 for 3D cases, with the sign depending on whether the probed extremal cross-sectional area of the Fermi surface is a maxima (-) or minima (+), and 0 for 2D cases [28].

Quantum oscillation measurements are a powerful tool for mapping out the Fermi surface of a sample material using the frequencies of the oscillations. By varying the orientation of a sample with respect to the applied magnetic field direction, a picture of the 3D structure of the Fermi surface can be built up. Often the frequencies obtained from quantum oscillation measurements are not sufficient on their own to determine the shape of a Fermi surface, this is particularly true for non-trivial complicated Fermi surface structures. Practically, the nature of the Fermi surface of a sample can be established via a combination of experimental quantum oscillation measurements with a comparison to predictions of the band structure using theoretical numerical calculations. Further insight into the electronic nature of a material can be gained by exploiting equation 2.14. A measurement of quantum oscillations as a function of increasing temperature can be used to extract estimates of the effective quasiparticle mass of a given oscillation frequency by fitting the form of the finite temperature damping factor to the oscillation amplitudes. Once an estimate for the effective mass has been made the Dingle temperature can also be calculated via the field dependence of the amplitude, this can then be used in conjunction with equation 2.17 to estimate the mean free path.

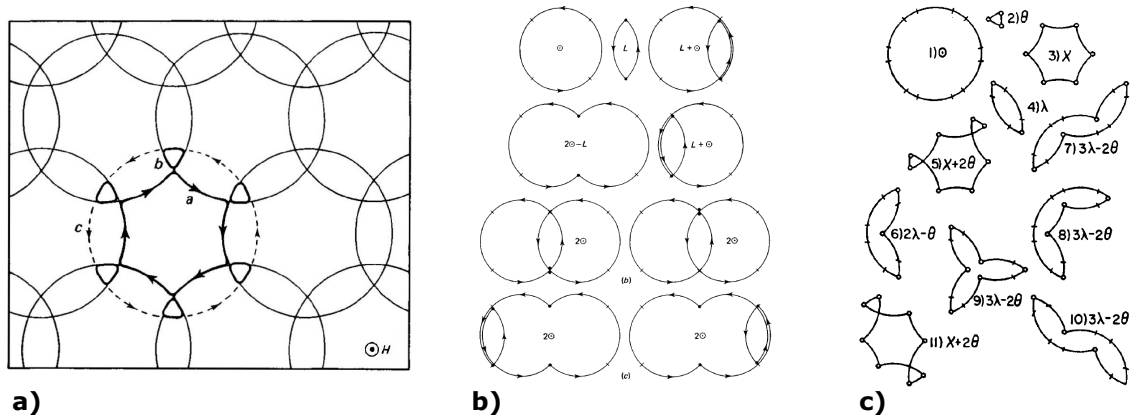

Fig. 2.2 **(a)** Extremal orbits (*a,b*) for the free electron-like Fermi surface of a hexagonal metal, at high fields MB causes the large circular orbit *c*. **(b)** and **(c)** Some typical orbits due to MB from the Fermi surface of **(a)**. Figure adapted from [25]

2.2.6 Magnetic breakdown and magnetic interaction

The idea of magnetic breakdown (MB) first came to light after the discovery of a so-called giant orbit frequency in the dHvA spectrum of elemental magnesium [29]. The observation of an orbit area larger than that of the hexagonal cross-section of the Brillouin zone was puzzling, this giant orbit was later explained to be a MB orbit. For a Fermi surface made up of multiple sheets/pockets of the same or different carrier type that are separated by a small energy gap $\Delta\varepsilon$ in k-space, a phenomenon, known as MB can occur when the applied magnetic field reaches a specific breakdown value. Above this field value there is a non-zero field dependent probability that a charge carrier can tunnel through a forbidden region in k-space to reach an adjacent Fermi sheet/pocket. The frequency spectrum of the FFT of dHvA or SdH measurements can become quite complex as a result of extremal MB orbits adding to the fundamental extremal orbits originating from each individual Fermi surface sheet/pocket. Additional frequencies can appear at combinations and differences of the characteristic low field individual orbits. The criterion for MB is [30]:

$$\hbar\omega_c \gtrsim {}^{\Delta\varepsilon}/_{\varepsilon_F} \,, \tag{2.23}$$

where ω_c is the cyclotron frequency, $\Delta\varepsilon$ is the energy gap between adjacent Fermi surface sheets and ε_F is the Fermi energy. Typically ${}^{\Delta\varepsilon}/_{\varepsilon_F}$ can be less than 0.01 which can, given the right conditions, give an appreciable MB contribution in fields of as low as even a few Tesla.

For free electrons, the probability P of MB to occur is given by:

$$P = \exp\left(\frac{-H}{H_0}\right) \tag{2.24}$$

with the breakdown field, H_0 given by:

$$H_0 \sim \frac{H\Delta\varepsilon^2}{\hbar\omega_c\varepsilon_F}\,, \tag{2.25}$$

and so the criterion for appreciable MB of $H \gtrsim H_0$ is equivalent to equation 2.23. As an example consider the free electron-like Fermi surface of a hexagonal metal perpendicular to the hexagonal axis, as seen in Figure 2.2. At fields below the MB field the only allowed orbits are those of the large hole-like and smaller electron-like orbits (labelled a and b respectively in Figure 2.2). As the magnetic field is increased and the MB field is reached a larger circular orbit (labelled c) become increasingly more likely. Assuming two spherical Fermi surfaces there are two basic MB orbits made from combinations of the orbits labelled a and b, these two orbits are denoted $\odot$ (the circular orbit c of Figure 2.2a) and L shown in Figure 2.2b. The various combinations of these two orbits are shown but it is important to note that some combinations are forbidden as only one direction of circulation (per electron- or hole-like orbit) is allowed, so a combination of $\odot$ - L cannot occur. The idealised orbits shown in Figure 2.2b are modified in real crystals due to the crystal lattice potential which will round out sharp corners. Figure 2.2c shows some further possible orbits in the hexagonal network: electron orbits are donated by $\odot$, θ and λ, while the hole-like orbit is denoted by χ. The effective masses of these orbits are outlined in Table 2.1.

Table 2.1 Effective masses of the orbits from Figure 2.2 normalised to the mass of the orbit $\odot$. The parameter α is the ratio of the arc length of each side of the triangular orbit θ to the circumference of the full circle.

Orbit	Mass (m_e)
1 $\odot$	1
2 θ	3α
3 χ	1 - 6α
4 λ	$1/3 + 2\alpha$
5 $\chi + 2\theta$	1
6 2λ - θ	$2/3 + \alpha$
7 3λ - θ	1
8 3λ - 2θ	1
9 3λ - 2θ	1
10 3λ - 2θ	1
11 $\chi + 2\theta$	1

Each MB orbit has an associated weight factor, an indication of how likely a particular orbit is likely to occur at a given magnetic field, this is discussed in great depth in [25, p. 337-352].

So far in the discussion of the dHvA effect it has been taken for granted that the total magnetic field experienced by the electrons is equal to that of the externally applied magnetic field. The oscillating magnetisation of the metal has been ignored as it is assumed to be very small compared to

the external magnetic field. In certain conditions of low temperature and high fields, however, even though the amplitude $|4\pi M|$ is tiny compared to H, it can approach the period H^2/f. This can lead to a modification of the form of the oscillations given by the LK formula. The magnetic interaction (MI) effect can result in harmonics ($2f_1$, $2f_2$ etc.) and combinations ($f_1 \pm f_2$ etc.) of the fundamental frequencies observed in quantum oscillation data [25, p. 254]. These frequencies are the same as those that can also be observed due to MB orbits. Distinguishing between the two effects is important and is made possible because the FFT peak amplitudes of the MI vary with magnetic field and temperature differently to those produced by MB. The fundamental cause of the MI effect is due to the origin of the Landau level quantisation. This occurs as a result of the oscillations in the free energy, which are caused by the flux enclosed by the quasiparticle orbits, not being a function of the applied magnetic field H but instead are a function of the magnetic flux density B. The effect can be described using the magnetisation from the Lifshitz-Kosevich formula (equation 2.21 above):

$$\chi_{\mathrm{MI}} = \sum_{f_i} A_i \sqrt{B} R_{\mathrm{D}}^i R_{\mathrm{T}}^i R_{\mathrm{s}}^i \sin\left[2\pi\left(\frac{f_i}{B} + \lambda - \Delta\right)\right], \tag{2.26}$$

with $B = \mu_0 H$ and the f_i being the observed fundamental frequencies. The MI effect can then be generated via a second iteration, with $B = \mu_0 (H + \chi_{\mathrm{MI}})$. To translate this into oscillations in the magnetoresistance it is assumed that the SdH effect is proportional to the susceptibility. Experimentally determined values of $\mathrm{R_T}$, $\mathrm{R_D}$ and $\mathrm{R_s}$ can be fed into the calculation, and the amplitude A_i can be determined from a measurement of the oscillatory magnetisation (dHvA effect).

CHAPTER 3

EXPERIMENTAL TECHNIQUES

Presented here are the experimental and analytical techniques used in later chapters, with a specific focus on the Cambridge dilution refrigerator. All of the measurements presented in this thesis required low temperatures (many below 100 mK). The methods used to reach these temperatures are well documented elsewhere, but we briefly review them here, highlighting any refinements and custom measurements relevant to this work. A good knowledge of the temperature is extremely important for analysis of quantum oscillation amplitudes and so thermometry calibration and a consideration of possible sources of error are discussed.

3.1 Low temperature techniques

3.1.1 The ^{3}He - ^{4}He dilution refrigerator

The idea of the ^{3}He - ^{4}He dilution refrigerator was first published in 1962 [32] in which the latent heat of mixing of two helium isotopes is used for cooling. Three years later a group at Leiden University built the first refrigerator and the design was gradually improved by groups working in Manchester and in Dubna (see [33, p. 149] and references therein). The basic design has not really changed much since then and the ^{3}He - ^{4}He dilution refrigerator is the only continuous cooling method to reach temperatures below 300 mK, making it a powerful research tool for experiments at low temperatures. The principle of operation is based upon the phase separation of a ^{3}He - ^{4}He mixture, which occurs when cooled below $T \lesssim 870$ mK, forming a ^{3}He-rich phase (known as the concentrated phase) and a ^{4}He-rich phase (known as the dilute phase). Figure 3.1 shows a phase diagram of a ^{3}He/^{4}He mixture. Below $T \sim 180$ mK the concentrated phase is essentially 100% pure ^{3}He, while the dilute phase contains approximately 6.6% ^{3}He diluted in 93.4% ^{4}He. The phase separation between the two isotopes is due to the influence of quantum mechanics, specifically the zero-point motion. As the electronic structures of the two isotopes are identical, the van der Waals forces between them are

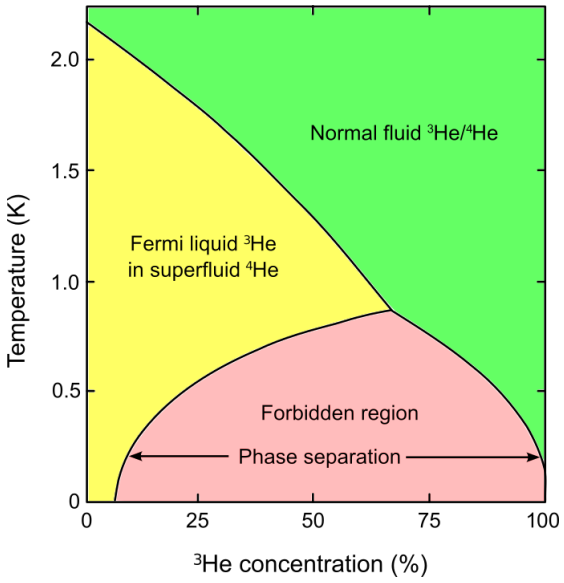

Fig. 3.1 Phase diagram of a liquid ^{3}He/^{4}He mixture showing the phase separation region, the x-axis shows the percentage of ^{3}He in ^{4}He. Even at zero temperature the phase separation occurs leaving approximately 6.4% ^{3}He in ^{4}He (in the dilute phase), as well as a pure (almost 100%) ^{3}He rich phase. Image obtained under a creative commons license from [31].

identical, however, the ^{3}He atoms have a larger zero-point motion than the ^{4}He atoms due to their smaller mass. When in the liquid phase, the ^{4}He atoms occupy a smaller volume than the ^{3}He atoms and so the ^{3}He atoms can be closer to the ^{4}He atoms than other ^{3}He atoms. This results in a stronger interatomic interaction between ^{3}He-^{4}He atoms than between ^{3}He-^{3}He atoms. There is a preference for the ^{3}He to stay in the dilute phase relative to the concentrated ^{3}He-rich phase. This preference leads to 6.6% ^{3}He remaining in the ^{4}He-rich phase. As the ^{3}He phase is less dense (due to its smaller mass) it floats on top of the ^{4}He-rich phase (the dilute phase).

The working fluid of the dilution refrigerator is ^{3}He, which is circulated in a closed cycle by sealed vacuum pumps at room temperature. Figure 3.2a shows a schematic of the system, the dilution unit (everything below the helium bath line in the schematic) sits at high vacuum inside the inner vacuum can (IVC) which itself sits in the helium bath at 4.2 K. In this system the helium bath is separated from room temperature via a series of three vacuum chambers with no need for a liquid nitrogen jacket. Starting at the ^{3}He pump at the top of the schematic, a concentrated gas of ^{3}He is sent down the condenser line (via a trap at 4.2 K to freeze out any non-helium impurities) where it liquefies at the 1K pot via heat exchangers (the 1 K pot is cooled via pumping on a small bath of ^{4}He, as a continuously operating ^{4}He evaporation cryostat). The pure ^{3}He then flows through a high impedance line to a second set of heat exchangers at the still, where it is further cooled to around 600 mK. After a second high impedance line and more heat exchangers (with the return line from the mixing chamber at $T \approx 80$ mK) the pure ^{3}He reaches the mixing chamber where it adds to the concentrated ^{3}He-rich phase. By applying a small amount of heat at the still, which is carefully set so that only ^{3}He

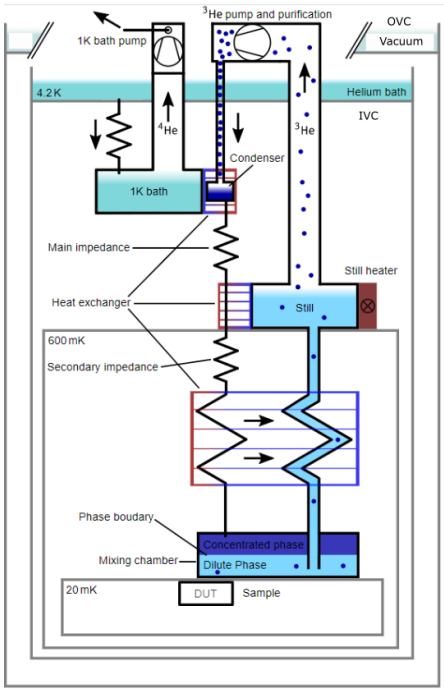

(a) Schematic of a dilution refrigerator.

(b) The custom dilution refrigerator.

Fig. 3.2 **(a)** Schematic showing the operating principle of a dilution refrigerator. Image obtained under a creative commons license from [34]. **(b)** The Cambridge dilution refrigerator used in this study.

evaporates from the surface of the ^{3}He/^{4}He mixture (due to the different vapour pressures of ^{3}He and ^{4}He), an osmotic pressure is built up at the phase boundary between the concentrated phase and the dilute phase. This is because, as ^{3}He leaves the dilute phase at the still (and goes round for another cycle, via the ^{3}He pump), the concentration of ^{3}He in the dilute phase should drop, but as discussed above, this is forbidden, and so ^{3}He is drawn into the dilute phase from the concentrated phase at the mixing chamber. Continuous cooling is achieved at the mixing chamber by the enthalpy difference (ΔH) between ^{3}He in diluted ^{4}He, and pure ^{3}He multiplied by the ^{3}He flow rate:

$$\dot{Q} = \dot{n}_{^3\mathrm{He}} \Delta H \ , \tag{3.1}$$

where Q is the heat removed from the concentrated phase and dumped into the dilute phase and $\dot{n}_{^3\mathrm{He}}$ is the flow rate of ^{3}He. The Cambridge dilution fridge unit (manufactured by Oxford Instruments) used here is shown in Figure 3.2b, the mixing chamber is at the bottom and above this several heat exchangers can be seen. The system has been equipped with three CMR LTT-m low temperature transformers (LTT) which make it possible to match the impedance's of the wiring coming from the samples in the low temperature region with an impedance of order 1Ω to that of the external preamplifiers at room temperature, which have an impedance of order 1MΩ. The use of the LTT allow a much better signal to noise ratio with a typical value for the noise floor being of order 30 pV$/\sqrt{\mathrm{Hz}}$.

Fig. 3.3 The experimental setup for the measurement of the nine samples that are summarised in Table 3.1. **(a)** The seven SR830 lock-in amplifiers and Lakeshore resistance bridges. **(b)** The electromagnetically shielded box for sample voltage leads, **(c)** the dilution fridge insert, **(d)** the helium dewar containing the 20.4 T superconducting magnet and **(e)** the magnet power supply.

3.1.2 Measurement system and thermal considerations

The custom dilution refrigerator in Cambridge has a base temperature in the region of $\sim$15 mK (with no load attached) and is equipped with a 18.4/20.4 T superconducting magnet (with the highest fields attainable using a lambda-point refrigerator to cool the magnet to $\sim$2 K, otherwise it is limited to 18.4 T). It features 12 pairs of superconducting measurement wires allowing the simultaneous measurement of resistivity in up to six samples, additionally there are three coaxial wires for sample measurements allowing measurements using the tunnel diode oscillator method or capacitive measurements. All of the measurement wires have been well heat sunk at various stages along the insert to reduce the thermal load on the mixing chamber. To increase the output from the dilution refrigerator in Cambridge, much effort was put into maximising the number of samples that could be measured in a single experiment cool down. With this in mind the measurements that are presented in the following chapters were all taken during a single cool down of the fridge in which nine samples were simultaneously mounted and measured. A detailed description of the samples and how they were set up on a rotation tail is presented in Section 3.2, here we focus on the methods employed to reduce noise in the measurements to achieve the highest sensitivity possible.

There are a number of general problems which arise when attempting highly sensitive measurements at low temperatures:

1. Vibrations: mechanical heating can introduce unwanted noise into the measurement signal, additionally eddy current heating (if a magnetic field is used) can also add to the noise. These can also limit the lowest achievable base temperature of the dilution fridge.

2. Radio Frequency (RF) noise: there are now sources of RF noise everywhere around the laboratory thanks to wireless networks and mobiles phones among other sources. Generally, any non-shielded wire can act as an aerial for RF signals.

To overcome these first of these issues, the Cambridge fridge is mounted on a concrete platform which acts to damp vibrations from the room, the platform is decoupled from the rest of the lab and from the vacuum pumps. The rotation probe tail is constructed from a quartz tube around which the measurement wires are wrapped and secured with GE varnish and Teflon tape. While the thermal conductivity of quartz is very poor at low temperatures, there will be no eddy current heating as a result of sweeping the magnetic field. To provide a good heat link to the samples from the mixing chamber, three high purity silver wires run down the probe tail (along the quartz tube) and connect to the samples (further details provided in Section 4.2.1). To tackle the second problem, all of the measurement wires have metallic screening which were carefully grounded in such a way so that no ground loops developed. Figure 3.3 shows the experimental setup used when collecting the data presented in the following chapters. A shielded box (b) contains the breakout box from the measurement (voltage) lines from the samples, high frequency noise is directed to ground by placing low-pass RC or Butterworth filters onto the voltage measurement leads. Any preamplifiers and room temperatures transformers were also placed in the shielded box to keep RF interference from the room to a minimum. Phase sensitive lock-in detection techniques were employed using a series of Stanford Research SR830 lock-in amplifiers (a). The magnet power supply (e) supplied a current to the superconducting magnet within the ^{4}He dewar (d) into which the dilution fridge insert (c) is lowered.

3.1.3 Quantum Design Physical Properties Measurement System

The Quantum Design (QD) Physical Property Measurement System (PPMS) is a versatile, commercially available, and user friendly cryostat system which offers heat capacity, resistivity as well as other measurement capabilities to low temperature and in high magnetic fields. The PPMS used in this work is equipped with a superconducting magnet, capable of producing magnetic fields at the sample between (-9 $\leq B \leq$ +9) T, and uses evaporative cooling (using a heater and by pumping on the vapour above the ^{4}He bath) to obtain sample temperatures below 2 K. An additional ^{3}He refrigerator option can be added which allows temperatures below 400 mK to be reached using a closed-cycle ^{3}He probe (as ^{3}He has lower boiling point than ^{4}He). The PPMS was used extensively in the initial

characterisation and screening of samples of NbGeSb and NbSiSb from Chapter 5, made possible by the quick measurement turn around times of the PPMS, before a select few samples were mounted onto the dilution fridge.

3.1.4 Low temperature thermometry

In order to perform measurements at the temperatures accessible by a dilution refrigerator, a well calibrated set of thermometers are required so that the temperature can be measured with confidence. A useful thermometer should fulfil the following requirements [33, p.277]:

- should have a wide operating temperature range and should be insensitive to environmental changes such as magnetic fields.
- the property (x) to be measured must be easily, quickly, reproducibly and exactly accessible to an experiment.
- the temperature dependence of the measured property x(T) should be expressible by a reasonably simple law.
- the sensitivity $\left(\frac{\Delta x}{x}\right) / \left(\frac{\Delta T}{T}\right)$ should be high.
- the thermometer should reach equilibrium in a 'short' time, both within itself and with its surroundings whose temperature it is supposed to be measuring. Therefore it should have a small heat capacity, good thermal conductivity and a good thermal contact to its surroundings (the thermal contact problem is ever present at $T \leq 1$ K).
- the relevant measurement should introduce a minimum of heat to avoid heating of the surroundings of the thermometer and, essentially, heating of itself - this becomes more important the lower the temperature.

The thermometry used on the custom dilution refrigerator comprises several resistive RuO_2 and Cernox thermometers each of which has been optimised for a different temperature range. These resistive thermometers are secondary thermometers, meaning that they need to be calibrated against an already calibrated thermometer before they can be used. The majority of the thermometers on the dilution fridge have been previously factory calibrated, but for this work several RuO_2 thermometers were specially calibrated against a Cerium Magnesium Nitrate (CMN) magnetic susceptibility thermometer, which is a primary thermometer. The basis of CMN as a useful thermometer is in its reliable Curie law T^{-1} temperature dependence of the magnetisation or magnetic susceptibility down to its ordering temperature at $T_C \sim 2$ mK. This temperature is below the lowest operating temperature of the dilution fridge at which the measurements presented in later chapters were performed, and so was a good benchmark to calibrate our thermometers against. There are a number of known issues when using RuO_2 thick film chip resistors as thermometers at very low temperatures such as: the very small

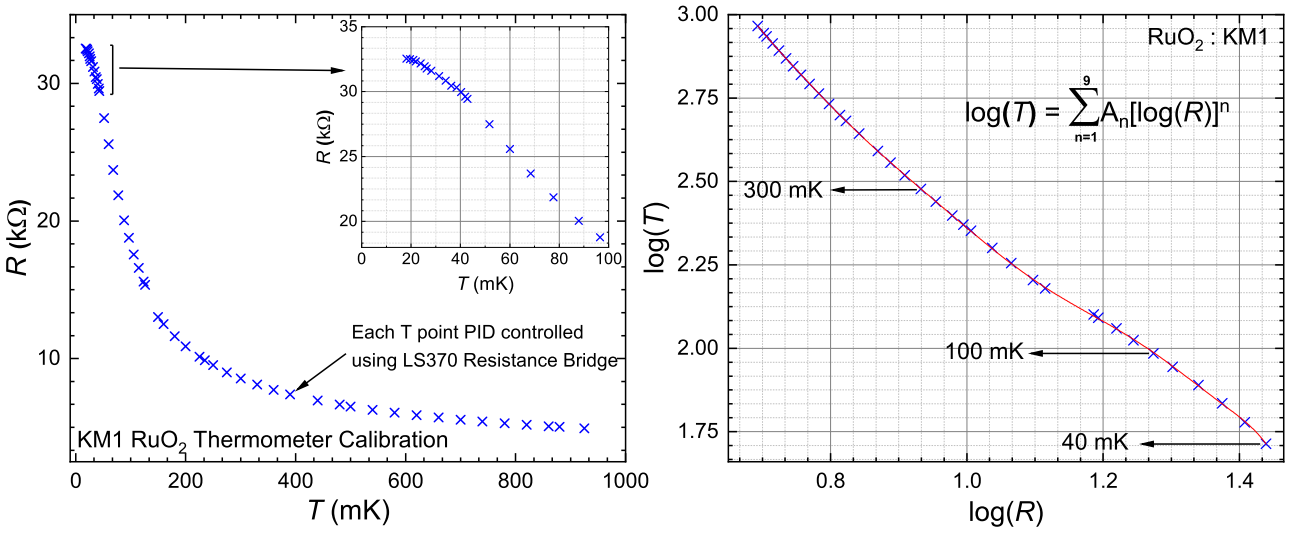

(a) Calibration of KM1 RuO_2 thermometer.

(b) Fitting of log(R) vs log(T).

Fig. 3.4 Calibration of the RuO_2 thermometer labelled KM1. **(a)** R vs T plot, inset shows in the low temperature region where the curve starts to plateau indicating self heating of the thermometer. **(b)** log(T) vs log(R) and a 9^{th} order polynomial fit. Data below 40 mK have been excluded from the fit.

thermal conductivity, thermal contact issues, and the self heating of the device due to the measuring current. Each of these issues was addressed when mounting and calibrating the thermometers.

The resistivity of RuO_2 usually has no simple, a priori known temperature dependence and so calibration is essential [33, p.287]. It has been demonstrated that before calibration of the resistors, at least 60 temperature cycles are needed in order to obtain consistency of data from a RuO_2 chip (after this they become very stable) [35]. Before calibrating any of the thermometers, they were put through at least 60 thermal cycles from room temperature to 2 K. Figure 3.4a shows the calibration curve for a RuO_2 thermometer labelled KM1 which was calibrated against a CMN magnetic susceptibility thermometer using an AC resistance bridge (Lakeshore LS370) in the range ($17 \leq T \leq 925$) mK while it was thermally anchored to the mixing chamber of the dilution fridge using GE varnish. The measurement leads were well heat sunk to the mixing chamber using an oxygen free high conductivity (OFHC) Cu post onto which the leads were tightly wound. Great care was taken to avoid ground loops to ensure unwanted currents in the thermometer were kept to a minimum. All of the leads were shielded from RF, as the thermometer has a high resistance and, together with its leads, may be well matched to absorb large amounts of RF energy in the lab. The measurement leads in the low temperature region are superconducting to keep the heat flow into the thermometer as low as possible, and are thermally anchored. Each data point was taken by PID (proportional integral derivative)

controlling the temperature to a desired set point (as measured using the mixing chamber thermometer, with reference to CMN thermometer), then allowing time for the RuO_2 thermometer to thermalise with the mixing chamber. In the temperature region below 40 mK the curve deviates from the expected trend, this has been attributed to self heating of the thermometer (even at the lowest excitation setting of the resistance bridge). This doesn't effect our later measurements as our working base temperature was greater than 50 mK and so the data below 40 mK in the calibration were not used.

Figure 3.4b shows a log-log plot of temperature vs resistance with a 9^{th} order polynomial fit from which a temperature can be extracted from a measured resistance (data below 40 mK have been excluded from the fit). The thermometer KM1 was mounted on the middle bobbin of the rotation tail (see Figure 3.5) and was used as a reference thermometer to compare temperatures of the sample stage (within the bore of the magnet) to the temperature of the mixing chamber thermometer. The dilution system is equipped with a set of magnetic field compensation coils which produce an effective zero field region at the mixing chamber, all of the thermometry, with the exception of KM1, are located in this region. It should be noted that the thermometer was not calibrated in field in the same detail as the zero field calibration (due to time constraints). RuO_2 thermometers do display a small magnetoresistance, however, the main purpose of the thermometer was in the initial optimisation of the eight samples at zero applied magnetic field. Due to the thermometers close proximity to the other samples, any self heating of a sample while optimising its excitation current would be seen in KM1 with a very short time constant, allowing appropriate excitation currents to be set for each sample. A rule of thumb in which the excitation current was reduced by a factor of two (thus a four-fold reduction in power) until no self heating can be detected was employed during sample signal optimisation. The thermometer also allowed any temperature increases due to field modulation (see Section 3.3) to be identified quickly, allowing an appropriate modulation amplitude to be set.

3.2 The rotation tail and sample preparation

A custom rotation tail was adapted to perform measurements on a large number of different samples, which are summarised in Table 3.1. The rotation tail comprises a quartz tube (as described in Section 3.1.2) which attaches to the mixing chamber of the dilution fridge at one end, via a gold-plated OFHC copper coupler, with a rotation mechanism at the other end which is machined from G10 (a high-pressure fibreglass laminate with excellent thermal properties at low temperatures). The rotation mechanism comprises three rotating bobbins with space for sample mounting on two faces giving a total of six sample platforms. Figure 3.5 shows a schematic diagram of the bottom of the rotation probe, where three high purity (4N) Ag rods (a) were used to heatsink the samples and the tunnel diode oscillator (TDO) boards (c) to the mixing chamber. Two 0.5 mm diameter rods (Goodfellow: AG005150 Ag rod, purity: 99.99%, temper: annealed - one of which is not visible in Figure 3.5) were used for the samples. A larger 1.0 mm diameter rod (Goodfellow: AG005160 Ag rod, purity: 99.99%,

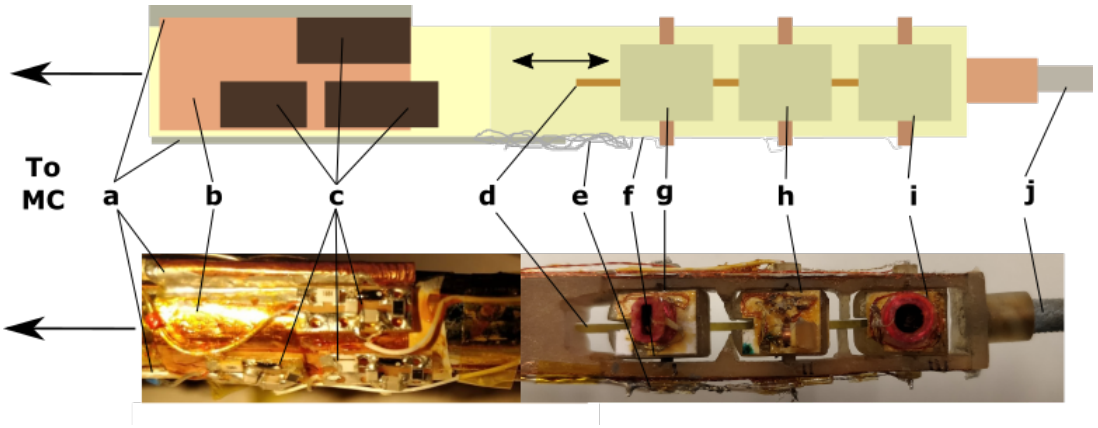

Fig. 3.5 Schematic of the rotation mechanism used in this study: **(a)** Ag wires for heat sinking to the mixing chamber (MC), **(b)** OFHC Cu sheet to heatsink the three TDO boards [**(c)**]. **(d)** vertical translation post that converts up-down movement into rotation of the platform via a hinge. **(e)** Ag wire bundle allowing some flexibility for rotation mechanism **(f)** 50 μm Ag wire to heatsink dHvA/TDO samples. **(g-i)** Sample platforms 1-3 (from left to right) and (reverse side) 4-6. **(j)** Mount for centering mechanism.

temper: annealed), which was soldered to an oxygen-free high conductivity (OFHC) Cu sheet (b), was used for three TDO boards which were mounted using GE varnish. A wire mesh of 50 μm high purity Ag wire (Goodfellow: AG005110 Ag Wire, purity: 99.99%, temper: annealed) was carefully wound (e) and was used to thermally connect the Ag rods to the non-SdH samples (f). The mesh acted as a spring-like link which allowed the small amount of movement necessary during the rotation of the sample platforms, whilst keeping vibrational noise to a minimum. The three bobbins (g - i) rotate about a central axle through an angle of 90° via a vertical translation (= horizontal translation in Figure 3.5) of a central post (d) attached to each of the platforms via a hinge (seen more clearly in Figure 4.7). This vertical motion is produced from a rotation at the top of the fridge insert which is coupled to a screw and thread mechanism located at the mixing chamber. At the bottom of the tail a centering mechanism is attached (j) which is made from G10 and is thermally isolated from the probe using Kevlar thread, this ensures the probe sits vertically in the bore of the magnet without it touching the inside of the IVC which would create a thermal short.

In order to fit all nine samples (eight measurement samples and one RuO_2 thermometer labelled KM1), careful thought had to be put into the thermal load put on the dilution fridge, especially when the TDO technique was employed as powering the tunnel diodes introduces a large heat load into the fridge. To account for this the three TDO boards were attached to a OFHC copper sheet which in turn was soldered to a Ag rod as discussed above. This design allowed the heat produced by the TDO when they were powered to be dumped directly into the mixing chamber. Ag was chosen for this as it has a smaller nuclear Schottky anomaly at mK temperatures. Careful management of measurement and diagnostic wiring also had to be considered, for the TDO technique for example, shielded coaxial wire is required and a new type of very small diameter coaxial cable (Picocoax: PCX42K10AB from

Table 3.1 Summary of the samples measured on the rotation probe on the Cambridge dilution fridge. The orientation is relative to $\phi = 0°$ (defined in Section 4.2.2). LTT = low temperature transformer, ID = inner diameter.

Sample	Name	Platform	Orientation	Measurement	Additional Info.
YFe_2Ge_2	JT1902-06 RRR ∼350	1	H‖a	dHvA	Ag wire heatsink, LTT 1:30. Flux growth, 18.7 mg, Dimensions (260 × 190 × 85) μm
NbGeSb	KM1908-122 RRR ∼13	2	H‖c	SdH	LTT 1:1000
YFe_2Ge_2	JC1904-02 RRR ∼500	2	H‖a	TDO	Ag wire heatsink, 9.2 mg. Coil: 23 turns 40 μm Cu wire, 2.0 mm ID
YFe_2Ge_2	JC1904-08 RRR ∼500	3	H‖c	dHvA	Ag wire heatsink. Horizontal liquid transport growth, 31.3 mg, dimensions (270 × 250 × 115) μm
NbGeSb	KM1908-130 RRR ∼11	4	H‖c	TDO	Coil: 9 turns 40 μm Cu wire, 0.9 mm ID
YFe_2Ge_2	JC1904-04 RRR ∼500	4	H‖c	SdH	Lost contact on cooling down
YFe_2Ge_2	JC1904-03 RRR ∼500	5	H‖c	TDO	10.5 mg Coil: 23 turns 40 μm Cu wire, 1.9 mm ID
RuO_2	KM1	5	H‖c	4-wire resistance	Calibrated thermometer
NbSiSb	KM1908-201 RRR ∼220	6	H‖c	SdH	LTT 1:1000

Axon Ltd) was employed that was small enough to fit through a feed-through hole located at the centre of the rotation axle. Space was limited in the six feedthroughs (two per bobbin: left (right) side of the axle going to the top (bottom) platform). The feedthroughs also needed threaded through them two twisted pairs of 80 μm Cu wire for transport measurements and a 50 μm Ag wire for sample heat sinking.

3.2.1 Electrical resistivity measurements

One of the most common techniques used in experimental condensed matter physics is the measurement of electrical resistivity with a wide range of applications such as detection of quantum oscillations in the magnetoresistance (the SdH effect), detection of phase transitions, and in the screening of new samples to get an indication of their purity. The standard method for measuring the electrical resistivity is the four-point probe method, where four wires are connected to a sample, two

to supply a current and two to measure the resultant voltage drop across the sample. Devices used to measure this voltage have very a high input impedance and so any current that flows through the voltages leads will be so small that it can be ignored, and so the the resistance of the voltage leads will not add anything to measured voltage across the sample. The resistance can be calculated via Ohm's law as $R = V/I$, where the supplied current is well known. The resistance can then be converted into a resistivity (ρ) using the sample geometry and the locations of the contacts via:

$$\rho = \frac{RA}{l} \, , \tag{3.2}$$

where A is the cross-sectional area of the sample and l is the distance between the voltage contacts. There are a number of ways in which the overall signal to noise ratio during a measurement can be improved. To minimise additional noise sources from electrical interference and allow the use of transformers for signal amplification, resistivity measurements can be conducted using an AC technique with an AC current and lock-in amplifiers. Placing the positive and negative contacts on a sample as far apart from each other as possible will increase the measured resistance, this can also be increased by selecting a long thin sample (maximising A/l in equation 3.2) both of which can improve the signal-to-noise ratio. Good electrical contacts with low resistances are essential for low temperature resistivity measurements and so a lot of time should be spent to ensure the contacts are Ohmic with a low resistance and a small contact area. Contact wires are typically high purity gold or silver wires of 25 μm or 12.5 μm diameter and the lowest contact resistances can be achieved using a spot welding technique (for metallic samples). This technique works by pressing the sharpened point of a tungsten wire against a gold contact wire in position on the sample, a pulse of current is then passed through this point contact which locally heats up the interface between the gold wire and the sample melting the two metals causing them to fuse. Care must be taken when selecting the voltage to apply across the point contact as it is easy to damage the sample, a robust mechanical and electrical contact is desired with minimal damage to the sample. A good spot welded contact will have a resistance of order 100 mΩ, with a small contact area of several square microns. A small amount of 4929 silver loaded epoxy by DuPont provides additional mechanical support when placed over the spot welded contact.

A commonly used measure to quantify sample quality in materials where nonmagnetic impurities determine the purity is the residual resistivity ratio (RRR). This is less useful when there are impurities related to off-stoichiometric phases of the desired material, but it is convenient to measure. RRR is defined as the ratio between the resistance measured at room temperature and that measured at low temperature (say 2 K) or extrapolated to zero temperature from higher temperature. For consistency, throughout this thesis I will use a RRR defined as:

$$RRR = \frac{R_{300K}}{R_{2K}} \, . \tag{3.3}$$

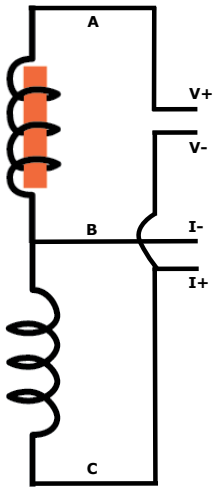

Fig. 3.6 Basic setup of a balanced pair of dHvA coils. Two coils are wound with the same diameter and an equal number of turns, so that the signal is effectively nulled when measured across A and C (as AB = -BC). When a sample is placed in the coil between A and B , the signal measured across A and C is due to the magnetic susceptibility of the sample with very little background contribution.

3.3 Quantum oscillation measurements

In Section 2.2.1 the formation of Landau levels was discussed. These Landau levels were shown to develop in the density of states of non-interacting charged fermions and, as discussed in Section 2.1, this extends to the quasiparticles from the Fermi liquid state of real materials. Quantum oscillations originate from oscillations in the density of states and so should be observable in many measurements that can be performed. Described here are the techniques that were employed to detect quantum oscillations in this thesis, as well as their relative sensitivities.

3.3.1 de Haas-van Alphen effect: field modulation technique

It has been shown in Section 2.2.1 that the formation of landau levels in a (changing) magnetic field can lead to oscillations in the magnetisation of a sample, known as the dHvA effect. This effect can be seen in measurements of the magnetic susceptibility, the basic experimental setup of which is shown in Figure 3.6. A pair of balanced pick up coils are wound in opposite directions so that when the coils are empty the measured signal across A - C is effectively nulled out. Introducing a sample into one half of the coil set between A and B , the signal measured across A and C is due to the magnetic susceptibility of the sample with very little background contribution. The full compensated signal across the coil set is connected to the voltage lines (V), while the signal across just the compensation (empty) coil is connected to the current lines (I).

The field modulation technique was fist developed after technological advances in superconducting magnets allowed steady and homogeneous magnetic fields to be achieved at fields up to ten Tesla, and today hybrid magnets (using both resistive and superconducting magnets) can produce fields as strong as 45 T. This allowed the possibility of more sensitive inductive techniques to be developed to measure the dHvA effect. As mentioned earlier the sample is still placed in a balanced pair of pickup coils but an induced electromotive force, caused by varying the main magnetic field, is no longer measured. Instead the magnetisation can be made to vary periodically with time (with some small amplitude A, and frequency ω) and the induced electromotive force at frequency ω or a higher harmonic is measured. This method allows phase sensitive detection using a lock-in amplifier to be employed which greatly improves the signal to noise ratio. The techniques of field modulation for dHvA measurements are well described by Shoenberg and a summary will be given here [25, p. 102].

A periodic variation of the magnetisation can be achieved by adding a small periodic field on top of the main field:

$$H_{\text{mod}} = H_0 + h_0 \cos(\omega t), \tag{3.4}$$

where H_{mod} is the modulated field and H_0 is the unmodulated field, and h_0 is the amplitude of the component of the modulation. The electromotive force induced in a balanced pickup coil can be found by expanding the magnetisation in terms of the oscillatory field $h_0 \cos(\omega t)$:

$$v = -c\frac{dM}{dH}\frac{dH}{dt} = -ch_0\omega \sin(\omega t)\left[\frac{dM}{dH} + \frac{d^2M}{dH^2}h_o\cos(\omega t) + \frac{d^kM}{dH^k}\frac{h_o^{k-1}}{(k-1)!}(\cos(\omega t))^{k-1}\right] + ... \tag{3.5}$$

where c is a coupling constant that depends on the experimental details, and we have subbed in the expression for H given in 3.4. The magnetisation is assumed to be given by:

$$M(t) = A\sin\left(\frac{2\pi f}{H_0 + h_0\sin(\omega t)} + \phi\right). \tag{3.6}$$

subbing this into equation 3.5 and rearranging in terms of the harmonics k:

$$v = -2c\omega A\sum_{k=1}^{\infty} kJ_k(\lambda)\sin\left(\frac{2\pi f}{H} + \phi - \frac{k\pi}{2}\right)\sin(k\omega t)\ , \tag{3.7}$$

where J_k are Bessel functions and

$$\lambda = \frac{2\pi f h_o}{H_0^2}\ . \tag{3.8}$$

Via a suitable choice of modulation amplitude (corresponding to λ) the amplitude of a particular harmonic of v can be enhanced. The quantum oscillation amplitude that is observed when using the field modulation technique is given by:

$$A_{\text{mod}} = c_{\text{mod}} \left(\frac{f^2}{m^* H^{3/2}} \right) R_D R_S R_T \times \omega k J_k(\lambda) \ , \tag{3.9}$$

where c_{mod} is a field modulation specific constant of proportionality (containing details of the particular orbit being measured and and the experimental setup).

3.3.2 Shubnikov-de Haas effect

Oscillations appearing in the magnetoresistance, known as the Shubnikov-de Haas effect, are generally much weaker than the dHvA effect, however, they are most pronounced in materials with low carrier densities, such as semiconductors and semimetals. A full theory governing the effect was described by Adamns and Holstein [36] but conceptually it can be described as a change in resistivity as the density of states available for scattering changes due to successive Landau levels passing through the Fermi level. For a free electron metal, the ratio of the amplitudes of the oscillatory components of the resistivity to the magnetisation at zero temperature is $\sim (2n)^{-1/2}$, where n is the Landau level index. As an example, a frequency of f = 10 kT measured at 10 T results in an oscillatory component of the resistivity with an amplitude of only 2% that of the oscillation amplitude of magnetisation. The expression for the amplitude of oscillations in the resistivity is given by:

$$\frac{\Delta\rho}{\rho_0} = c_{\text{SdH}} \left(\frac{H}{f} \right)^{1/2} R_D R_S R_T \ , \tag{3.10}$$

where c_{SdH} is a proportionality constant (with information from the Fermi surface being measured).

3.3.3 Calibration of the magnetic field

Before the main data in this study was taken, a field calibration was performed on the 18.4/20.4 T superconducting magnet in the dilution refrigerator, this was done by utilising the TDO coils to observe the ^{1}H, ^{63}Cu and ^{65}Cu nuclear magnetic resonance lines. Figure 3.7 shows the calibration curve of the magnetic field strength, B_z, (as a percentage of the nominal field as measured by a 1 Ω shunt resistor at the current source) as a function of distance (in mm) away from the field centre (maximum) for three data sets. Two of the data sets are from a previous measurement in 2018 (performed by Dr. J. Baglo), the third is from this work. The purple data show the calibration from this study, the locations of two YFe_2Ge_2 samples presented in Chapter 4, as well as two samples, NbGeSb and NbSiSb, presented in Chapter 5, are indicated when the rotation mechanism is set at

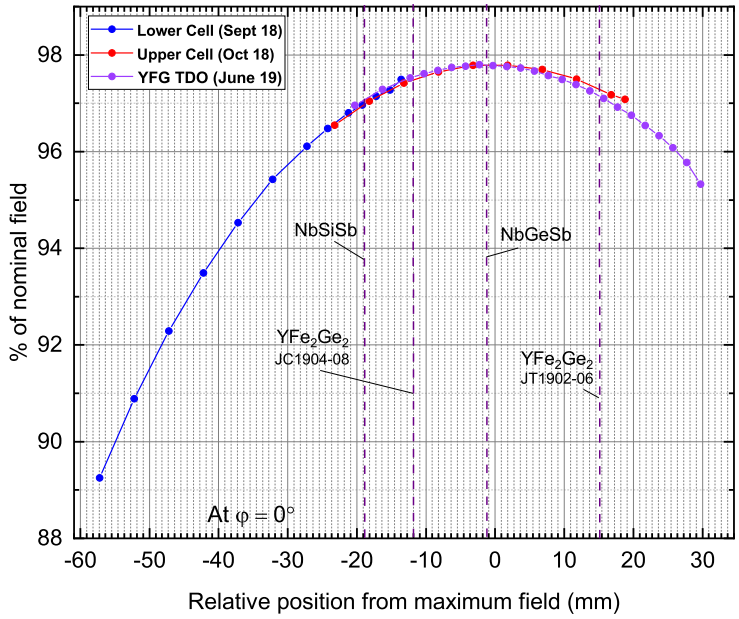

Fig. 3.7 Calibration of the external magnetic field used in this study, data from two TDO coils (2018 - measurements performed by Dr. J. Baglo), and a calibration from this work (purple).

$\phi = 0°$. Throughout the rest of this thesis, the angle ϕ represents the angle between the magnetic field direction (B_z) and the c-axis of YFe_2Ge_2 sample JC1904-08, which is aligned perpendicular to the platform on rotation bobbin three, as seen in Figure 3.5**i**. All angles of rotation of samples relative to the applied magnetic field are referenced to the angle ϕ.

3.4 Powder X-ray diffraction techniques

In a solid the crystal lattice is formed of an ordered array of atoms which can be described by its crystal structure, a useful technique for determining structural characteristics of such a material is powder X-ray diffraction (pXRD). The technique can also be useful in identifying any impurity phases that may be present in a crystalline solid after a new growth has been attempted. All XRD techniques are based upon exploiting the Bragg condition:

$$n\lambda = 2d\sin(\theta)\,, \tag{3.11}$$

where λ is the wavelength of the incident X-ray, n is an integer, d is the interplanar spacing and θ is the angle between the incident beam and the crystallographic plane.

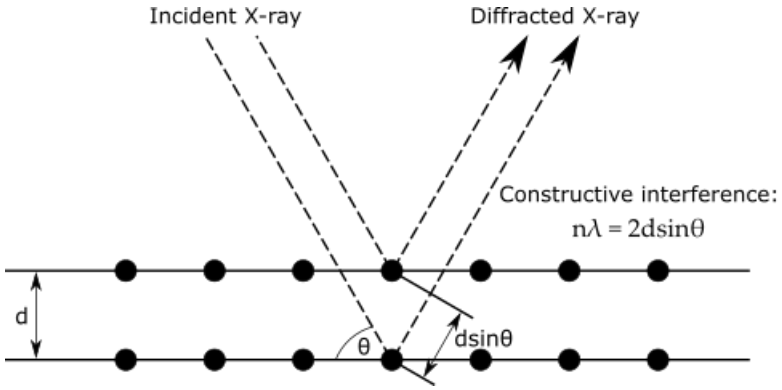

Fig. 3.8 Schematic of the derivation of Bragg's law, two X-ray beams with matching phase and wavelength are incident on a crystalline solid and are scattered off two different atoms within it. The lower X-ray traverses an extra length of $2d\sin\theta$. The condition for constructive interference occurs when this length is equal to an integer multiple of the X-ray wavelength.

Figure 3.8 shows that when the interplanar spacing, d, between the atomic layers satisfies the Bragg condition of equation 3.11, constructive interference occurs resulting in a high intensity of the outgoing X-ray beams at a diffraction angle of θ. Families of parallel planes within the lattice are identified by the Miller indices: h, k and l, corresponding to the reciprocal of the planes which intercept the a, b and c axis respectively. To perform a pXRD measurement, a sample is first crushed into a fine powder of small crystallites, of O(μm), and distributed evenly across a glass slide. To prevent any preferential alignment of flat facets with the glass slide, a thin layer of vacuum grease is used in order to secure the powder in place, without adding much to the background diffraction signal. Upon illumination from a collimated X-ray beam the random orientations of the small crystallites in the powder will allow the Bragg condition to be met by a representation of the different d spacings present in the lattice structure of the sample. For an X-ray beam of constant wavelength and phase, the Bragg condition ensures that diffraction spots will only be observed at certain discrete angles which are related to the lattice structure and lattice parameters. During a typical pXRD measurement, the X-ray detector is moved through different values of the scattering angle 2θ along a constant azimuthal angle ϕ, where it collects scattered radiation at each angle. A comparison of the measured pXRD to the calculated theoretical spectra allows structural information to be extracted for a given sample. The pXRD data presented in this thesis have been performed on a Bruker D8 X-ray diffractometer using Cu Kα radiation (selected due to the closeness of the atomic spacings d_{hkl} to the wavelengths). The diffraction pattern from a pXRD measurement allows details about the lattice parameters and space group symmetry to be inferred from the positions of the peaks at $2\theta_{hkl}$. A insight into the structural properties of the crystal such as the different atoms and their positions, and the lattice site occupancies can be obtained via the intensity and the shape of the peaks. Analysis is performed using native software from the Bruker diffraction suite called DIFFRAC.EVA.

CHAPTER 4

FERMIOLOGY OF YFe_2Ge_2

4.1 Introduction

4.1.1 Iron-based superconductors

Since the discovery of iron-based superconductivity in 2006 by Kamihara and coworkers' in the material LaOFeP, which has a superconducting transition of T_c = 5 K [37], there has been a huge effort by researchers to understand and explain the nature of the superconductivity in this new class of materials. Outperformed only by the copper oxide (cuprate) superconductors (and more recently the high pressure phases of H_2S [38] and LaH_{10} [39]) in terms of the highest superconducting transition temperatures, the iron-based superconducting materials are of particular interest due to the unconventional nature of superconductivity they exhibit. LaOFeP wasn't in fact the first discovery of superconductivity exhibited in compounds containing iron, which due to its strong local magnetic moment, had been considered detrimental to the development of superconductivity in a material (based on the BCS theory [40]). There are many well known iron-containing materials, in which the iron is non-magnetic, that exhibit superconductivity including Th_7Fe_3 (T_c = 1.8 K) [41], U_6Fe (T_c = 3.9 K) [42], $Lu_2Fe_3Si_5$ (T_c = 6.1 K) [43]. In fact, (non-magnetic) iron under pressure is itself a superconductor, with a T_c = 1.8 K at 20 GPa [44]. A large number of iron-based superconducting compounds have been found that combine iron with either a group-V pnictogen or group-VI chalcogen element. The iron pnictide or chalcogenide superconductors possess an unusual Fermiology showing a large variation with doping resulting in properties of both the normal and superconducting states which are very different to those of the standard 'conventional' electron-phonon coupled superconductors. In the iron pnictide/chalcogenide superconductors, there is a strong link between superconductivity and magnetism (or magnetic fluctuations) and these two states can even coexist in some compounds. There are several different structural families of the iron-based (unconventional) superconductors each of which is linked by a common iron pnictogen/chalcogen trilayer (Fe-M) in which a square planar

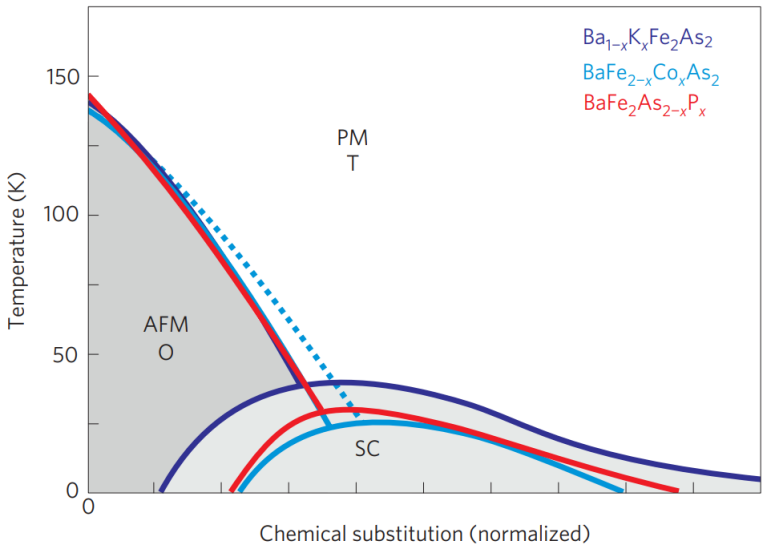

Fig. 4.1 Chemical-substitution phase diagram of the $BaFe_2As_2$ system, which is representative of most iron based superconductors. Reprinted by permission from Springer Nature [53]).

lattice is formed with iron atoms at the centre of a distorted tetrahedron formed by the M atoms. The several families can be divided into groups as: 11-type (FeSe [45]), 111-type (LiFeAs [46]), 1111-type (LaFeAsO [47]), 122-type ($BaFe_2As_2$ [48]) and the 21311-type (Sr_2ScO_3FeP [49]). All structures share a common feature of proximity to an antiferromagnetic ordered phase, and superconductivity can be induced in the (usually) antiferromagnetic parent compound by suppressing magnetic order in a number of ways. These include application of hydrostatic pressure [50], application of 'chemical' pressure (via isovalent substitution) [51], and by electron or hole doping [52]. There are many unresolved issues with this new class of materials (such as the superconducting nodal structure in many compounds) and improvement in sample quality is key to their solution. Here we will give a brief overview of the 122 structure Fe-based superconductors before focusing on the unconventional iron based germanide superconductor YFe_2Ge_2.

The 122 iron-containing superconductor structure includes members of the MFe_2As_2 family in which a superconducting transition of 38 K was discovered in 2008 in K-doped $BaFe_2As_2$ ($Ba_{0.6}K_{0.4}Fe_2As_2$) [48]. $BaFe_2As_2$ contains most of the interesting features of iron-based superconductors and will be the parent compound in the following discussion (referred to as Ba-122) [53], it has a tetragonal structure containing 2-dimensional (2D) FeAs planes (I4 mmm, space group number 139). The phase diagram of Ba-122 is shown in Figure 4.1 where it is tuned by chemical substitution, it is metallic with an antiferromagnetic (AFM) phase at low temperatures. This AFM transition arises at the same time as a structural transition from tetragonal to orthorhombic, and both transitions can be suppressed with chemical substitution inducing a superconducting transition as shown in Figure 4.1 [48]. The Ba-122 structure is well known and has been well investigated in materials superconductivity. The first heavy fermion superconductor, $CeCu_2Si_2$, also has this structure [54]. The crystal structures

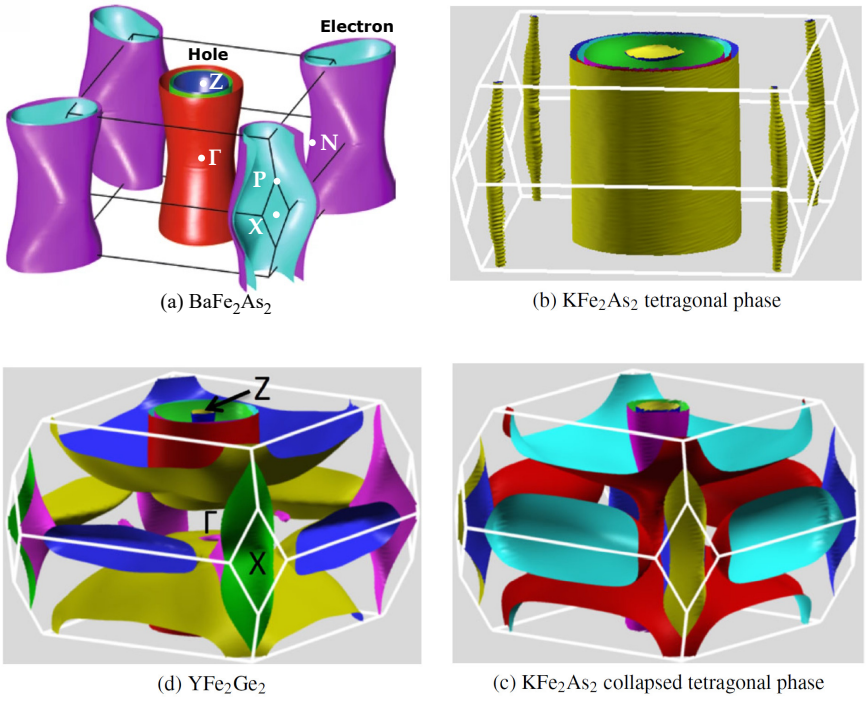

(a) $BaFe_2As_2$ (b) KFe_2As_2 tetragonal phase

(d) YFe_2Ge_2 (c) KFe_2As_2 collapsed tetragonal phase

Fig. 4.2 Fermi surfaces of several iron-based superconductors: **(a)** Calculated non-magnetic Fermi surface of $BaFe_2As_2$ in the tetragonal phase (adapted under a creative commons licence from [58]). **(b)** KFe_2As_2 in the uncollapsed tetragonal phase. **(c)** KFe_2As_2 in the pressured-induced collapsed tetragonal (CT) phase. **(d)** YFe_2Ge_2. **(b)** - **(d)** Reprinted with permission from [59]. Copyright 2019 by the American Physical Society.

in all of the iron-based unconventional superconductors are very similar, however, their electronic properties can vary extensively [55]. In general, the electronic structure is composed of a number of iron d-bands near to the Fermi energy, resulting in relatively small electron/hole-like pockets which are strongly influenced by external perturbations such as hydrostatic or chemical pressure. A typical Fermi surface of the iron chalcogenides contains only electron-like Fermi surfaces and a single hole pocket, whereas in most iron pnictides, there are hole pockets in the middle of the Brillouin zone, with electron pockets at the zone boundaries. The electron Fermi surface at the zone-boundary can be replaced by very small hole pockets in the extremely hole-doped iron pnictides, such as KFe_2As_2 [56]. The electronic structure of the Ba-122 family is highly 2D and is formed of two electron-like cylindrical Fermi surface sheets centered on the X-point and three hole-like cylinders centred at the Γ-point (Brillouin zone centre, in the folded Brillouin zone with two Fe-atoms per cell) [57]. The calculated Fermi surface of (for example) $BaFe_2As_2$ is shown in Figure 4.2a.

Quantum oscillation measurements can give a useful insight into the electronic structure of the iron-based superconductors, such as the Ba-122 family. Analysis of the oscillations can highlight the transformation of the Fermi surface in the parent AFM members of the iron-pnictide family with smaller 3D Fermi surface sections to the paramagnetic overdoped members with quasi-2D electron and

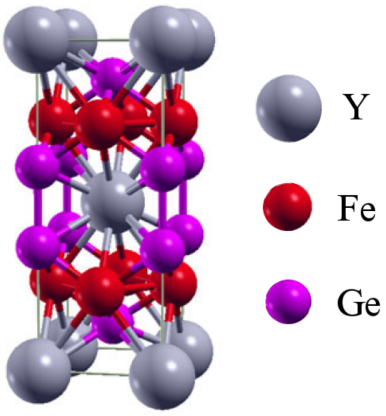

Fig. 4.3 The crystal structure of YFe_2Ge_2, the experimentally determined lattice constants are $a = 3.9617(5)$ Å and $c = 10.421(1)$ Å with the z coordinate of atomic position of Ge atom being 0.3789(3) [64].

hole cylinders. This transformation occurs via a possible quantum critical point (QCP) where a large effective quasiparticle mass enhancement can be seen [60]. The effective quasiparticle mass would be expected to diverge in the vicinity of a QCP and so quantum oscillations are an excellent experimental probe of this behaviour. Terishima *et al.* [61] performed Shubnikov-de Haas oscillation measurements on detwinned $BaFe_2As_2$ and de Haas-van Alphen oscillation measurements on KFe_2As_2 which have allowed their respective Fermi surfaces and quasiparticle effective masses to be determined and compared to theoretical calculations . The antiferromagnetic phase of $BaFe_2As_2$ has a Fermi surface consisting of two electron 3D pockets and a 3D hole pocket, which matches up well with density functional theory (DFT) calculations. An average mass enhancement from the bare band effective mass of m^* = 2-3 m_e was also found for the hole and electron pockets. For KFe_2As_2 four quasi-2D Fermi surface cylinders were found which agreed with earlier ARPES data [62], however the authors' DFT calculations failed to reproduce this Fermi surface. Later, Backes *et al.* successfully applied an extended DFT model which included additional correlation effects to obtain good agreement with both ARPES and quantum oscillation data [56]. Large effective masses ($m^* \geq 20$ m_e) have been reported in KFe_2As_2 (around 8–9 times larger than the band value, suggesting strong electronic correlations), which is consistent with the measured Sommerfeld coefficient from heat capacity measurements at low temperatures [63].

4.1.2 Motivation: YFe_2Ge_2

Closely related to the Ba-122 family of iron-based superconductors and possessing the same tetragonal $ThCr_2Si_2$ structure (space group I4/mmm, crystal structure shown in Figure 4.3), is the unconventional superconductor YFe_2Ge_2. The main difference between YFe_2Ge_2 (which, by electron counting, is similar to KFe_2As_2) and the Ba-122 iron-based superconductors is absence of a pnictogen or

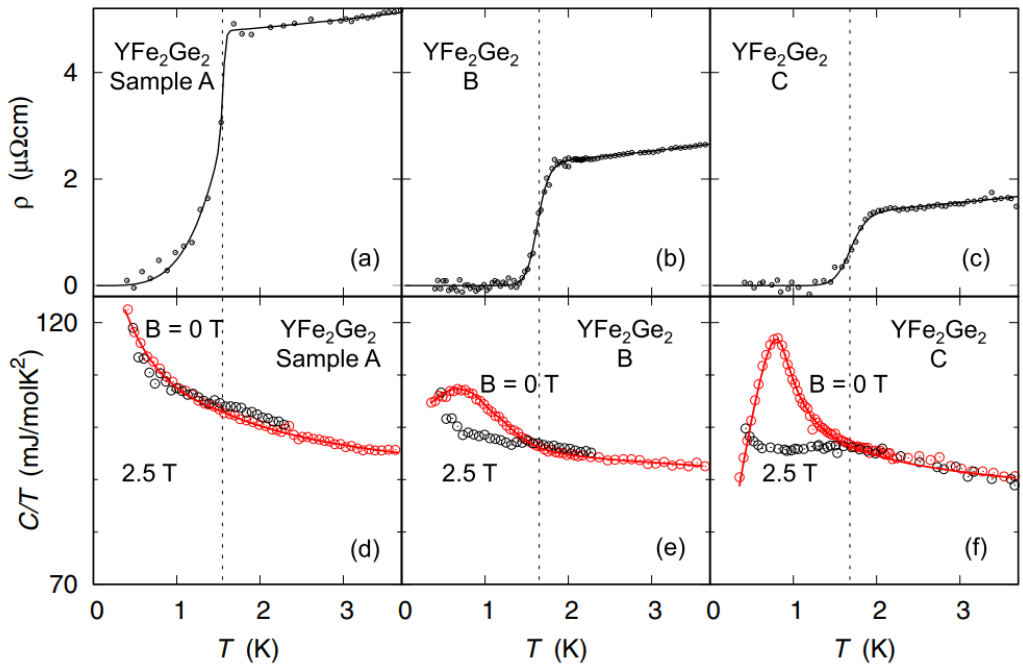

Fig. 4.4 Electrical resistivity ρ [upper panels (a)–(c)] and Sommerfeld coefficient of the heat capacity C/T [lower panels (d)–(f)] for three typical polycrystalline samples of YFe_2Ge_2 with different residual resistivity ρ_0. Sample A is as-grown but derives from the same ingot as a bulk superconducting annealed sample, for which data is presented in [59]. All three samples show resistive superconducting transitions, but a heat capacity anomaly indicating bulk superconductivity only appears in the purer, annealed samples B and C. When a superconducting heat capacity anomaly is absent (sample A), C/T displays a slow increase on cooling even in magnetic fields sufficient to suppress T_c fully, suggesting an underlying magnetic contribution. Reprinted with permission from [67]. Copyright 2019 by the American Physical Society.

chalcogen, which is replaced by the group-IV element Ge. Superficially, KFe_2As_2 would appear to be isoelectronic to YFe_2Ge_2, however, the presence of covalent Ge-Ge bonds between neighbouring Ge atoms in YFe_2Ge_2 changes the oxidation state of the Fe to +1.5 (compared with +2.5 in KFe_2As_2, which lacks As-As covalent bonds). This absence of As-As covalent bonds in KFe_2As_2 leads to a discrepancy in the aspect ratio of the unit cells between the two compounds. The ratio of c to a lattice parameters for YFe_2Ge_2 is 2.64, giving a much stronger three-dimensional character than in KFe_2As_2, with c/a = 3.608 [65]. The application of around 13–15 GPa hydrostatic pressure to KFe_2As_2 results in a structural transition to the collapsed tetragonal phase which reduces the c/a ratio of the unit cell down to a value close to that of the YFe_2Ge_2 unit cell (see Figure 4.2 b - d) [66].

Figure 4.2 shows the calculated Fermi surface using DFT for KFe_2As_2 in the uncollapsed (b) and collapsed (c) tetragonal structures, and the Fermi surface of YFe_2Ge_2 (d) [59]. Fundamentally, the Fermi surfaces of uncollapsed-tetragonal KFe_2As_2 and YFe_2Ge_2 are very different, as already discussed. The Fermi surface structure in uncollapsed tetragonal KFe_2As_2 is dominated by cylindrical

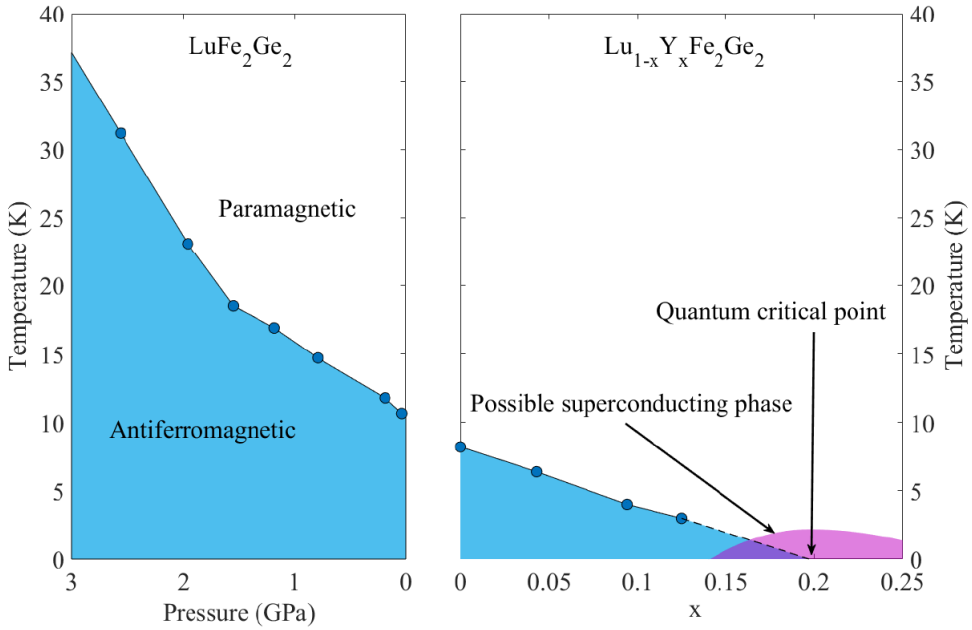

Fig. 4.5 Phase diagram showing the the effect of hydrostatic pressure on $LuFe_2Ge_2$ and of doping in $Lu_{1-x}Y_xFe_2Ge_2$ on the Néel temperature (Figure credit: [68], data obtained from [69, 14]).

hole sheets with small electron Fermi surface structures at the Brillouin zone corners. The Fermi surface of YFe_2Ge_2 harbours an electron pocket at X in the corner of the zone and nested 3D hole pockets at Z on the face of the Brillouin zone. The collapsed tetragonal Fermi surface of KFe_2As_2, however, has a very similar structure to that of YFe_2Ge_2 with the exception of a bulge of the largest hole pocket in collapsed-tetragonal KFe_2As_2 which encloses the Γ point and is not present in the corresponding hole pocket in YFe_2Ge_2.

Low temperature properties of YFe_2Ge_2 were first measured in 2004 by Avila *et al.* who measured resistivity, magnetisation and heat capacity of several rare earth iron germanide single crystals (RFe_2Ge_2, R = Y, Pr, Nd, Sm, Gd–Tm and Lu) [70]. The authors found that magnetic susceptibility data in YFe_2Ge_2 suggested it is paramagnetic and heat capacity measurements demonstrated a large Sommerfeld coefficient of about 100 $mJmol^{-1}K^{-2}$ (about 8 to 10 times that of the predicted band structure value [71]), indicating strong electronic correlations. In $LuFe_2Ge_2$ a clear anomaly was seen at 9 K, which also manifests itself in the heat capacity. This was later ascribed to the onset of AFM order in a study by Fujiwara *et al.* [14]. The effect of hydrostatic pressure on the ordering temperature was also investigated in this study and it was shown that an increase of pressure (up to 3 GPa) will enhance the AFM and increase the ordering temperature, while substituting Y for Lu was found to reduce the ordering temperature in another study [69].

Extrapolating to the point of complete suppression of the AFM phase suggested that replacing roughly 20% of Lu atoms with Y in $Lu_{1-x}Y_xFe_2Ge_2$ should reduce the Néel transition to zero temperature. This hinted that a QCP could exist in this material surrounded by a superconduct-

ing dome (as shown in Figure 4.5). A study by Zou *et al.* in 2014 [13] found the first evidence of a superconducting transition in YFe_2Ge_2 with a transition temperature of $\sim$ 1.8 K, however, the T_c was heavily dependent on sample quality. An unusual power law dependence of the normal state resistivity at low temperatures (below 10 K) was also seen, indicating non-Fermi liquid behaviour with a temperature exponent of $3/2$, which provided further evidence that YFe_2Ge_2 is in the quantum critical regime close to a QCP. A similar $T^{3/2}$ power law in resistivity was observed in the collapsed tetragonal phase of KFe_2As_2 from 20 K down to T_c in zero field, and down to 50 mK in a field of 5 T. This was attributed to the scattering of electrons off spin fluctuations with 3D character [72], however, later measurements reported a more familiar Fermi liquid $\rho \sim T^2$ [73]. At this time, heat capacity measurements in YFe_2Ge_2 did not show a clear superconducting transition anomaly in the bulk and it was not until much higher quality samples were grown (by a fellow PhD student, Jiasheng Chen) that a bulk superconducting transition was seen [59]. This and a subsequent study on composition dependence confirmed that superconductivity was in fact intrinsic to YFe_2Ge_2 and not due to some alien phase or was not filamentary in nature, see Figure 4.4 [67]. The presence of large fluctuating Fe moments has been demonstrated in YFe_2Ge_2 via an X-ray absorption and photoemission spectroscopy study [74], which suggests that YFe_2Ge_2 lies close to the border of magnetism. Additionally, the presence of both ferromagnetic and antiferromagnetic in-plane fluctuations in YFe_2Ge_2 has been shown in a recent inelastic neutron scattering experiment [75].

Following the initial discovery of superconductivity in YFe_2Ge_2, Subedi performed a first principles calculation of its electronic structure and magnetic interactions [76]. DFT calculations using the local density approximation (LDA) predicted a Fermi surface structure containing five sheets: a very 2D electron cylinder centered at the X point of the Brillouin zone, a large three dimensional disk shaped hole pocket at the Z point which encloses a cylindrical hole sheet and two almost spherical hole sheets. The 3*d*-electron states of iron were found to strongly influence the band structure in the vicinity of the Fermi level and the presence of a band either side of the Fermi level with Ge-4p_z character suggested a covalent Ge-Ge bond along the *c* axis. The Sommerfeld coefficient was calculated to be 10.63 $mJmol^{-1}K^{-2}$, which is almost an order of magnitude smaller than the experimentally obtained value. AFM spin fluctuations were proposed to give rise to a singlet $s^{\pm}$ superconducting state which has been seen in other iron-based superconductors [57, 77]. A competition between several magnetic configurations located relatively close to each other in energy were deemed to be responsible for the relatively low superconducting transition temperature of T_c = 1.8 K as well as the non-Fermi liquid behaviour seen in the normal state resistivity. A second DFT study put forward by Singh employed a different exchange and correlation functional (Perdew, Burke, and Ernzerhof generalised gradient approximation [PBE GGA]) [71]. Apart from some slight differences in the magnetic structure, the two calculations generally agree with the Singh's giving a similar Fermi surface structure with a clear 3D character. Singh's calculations also significantly underestimated the Sommerfeld coefficient as compared with the experimental value by a similar factor to Subedi's calculation.

One of the fundamental questions yet to be answered experimentally in YFe_2Ge_2 is the origin of the large normal-state Sommerfeld coefficient which has been observed in heat capacity measurements $C/T \simeq 100$ mJmol^{-1}K^{-2}, which is around 8-10 times larger than what is expected from the calculated band-structure value. In order to address this, quantum oscillation (de Haas - van Alphen) studies on some of the latest high quality single crystal samples with RRR's above 450 have been performed and will be presented below.

4.2 Measurement setup, procedure and results

Several generations of YFe_2Ge_2 single crystal growth methods have been developed since the first reported single crystal growth in 2004 [70]. With each generation came improvements in sample quality, as quantified by the residual resistivity ratio (RRR) and with single crystal XRD analyses [78]. Superconductivity in the bulk has been shown to be present only in samples with a RRR > 100 and all attempts to detect quantum oscillations had failed in samples with a RRR's as high as ~ 200 (as the Dingle factor likely dominates and suppresses the oscillation amplitude - see Section 3.3). In early 2019 a major breakthrough was made when extremely high purity samples of YFe_2Ge_2, with RRR's above 450, were prepared by fellow PhD student Jiasheng Chen (with Masters student James Tarrant) using a combination of Sn flux growth and horizontal liquid transport growth, the techniques of which are well described elsewhere [78]. Five samples from the latest growth batches of YFe_2Ge_2 were provided with the hope that the significantly improved quasiparticle mean free paths in these crystals would allow the detection of quantum oscillations for the first time. The methods used to measure these oscillations and the results obtained are presented below.

4.2.1 Sample preparation

In order to detect quantum oscillations in YFe_2Ge_2, dHvA and tunnel-diode oscillator (TDO) methods were employed, the former as described in Section 3.3 and the latter is well described in [79]. A preliminary measurement of samples from a flux growth batch of YFe_2Ge_2 (labelled JT1902) using both the dHvA effect in AC susceptibility and TDO measurement techniques were performed on a the Cambridge dilution refrigerator at fixed magnetic field angles of H$\|$c for the dHvA measurement and H$\|$a for the TDO. The preliminary results are presented in Appendix A.

The two dHvA coils used for measuring samples JT1902-06 and JC1904-08 (coils wound by J. Chen) can be seen in Figure 4.6a and 4.6c respectively. The coils for sample JT1902-06, which was mounted with H$\|$a at $\phi = 0°$, consist of a pair of pickup coils wound around a rectangular cuboid, each coil has approximately 1500 turns and a room temperature resistance of $\approx 400\ \Omega$. The two coils are connected with opposite polarity (as discussed in section 3.3) and the two coils were carefully wound such that they are well compensated when no sample was present. The coils for sample JC1904-08, which was

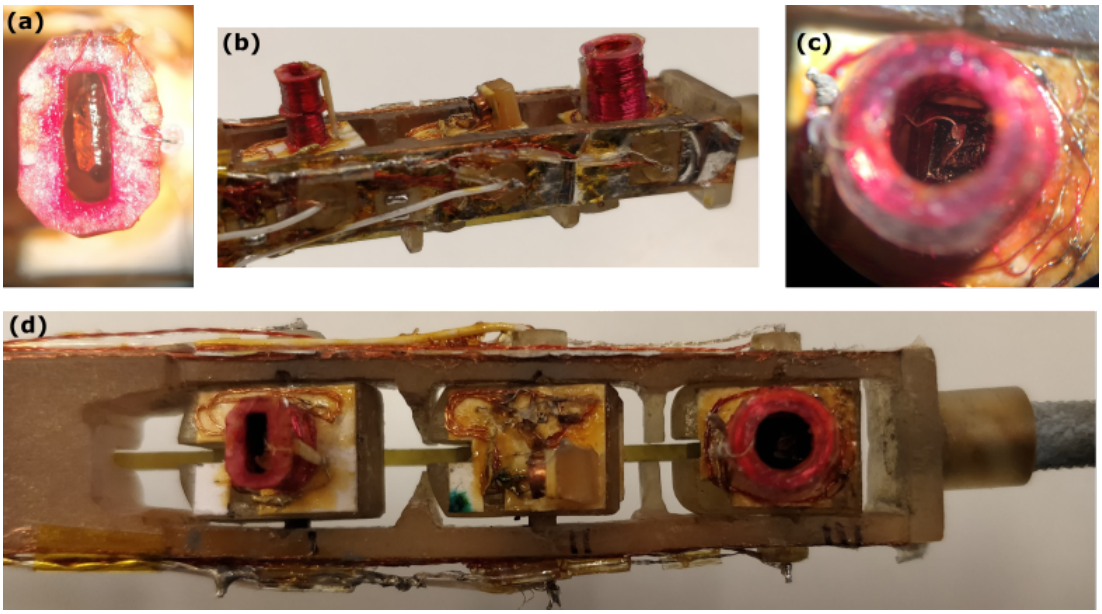

Fig. 4.6 **(a)** dHvA coil set up with YFe_2Ge_2 sample set up so that at $\phi = 0°$ H||a. **(b)** Side view of the rotation mechanism showing platforms 1-3. **(c)** dHvA coil set up with YFe_2Ge_2 sample set up so that at $\phi = 0°$ H||c. **(d)** Top down view of the rotation mechanism showing platforms 1-3.

mounted with H||c at $\phi = 0°$, have been wound in a similar fashion with the exception that the pair of pickup coils are wound around a cylinder to accommodate that sample in a different orientation. The coils are connected following the procedure in Figure 3.6. The *a*- and *b*-axes of sample JC1904-08 were carefully aligned to the rectangular edges of platform 3 as the coil-set was mounted (using GE varnish) which can be seen from Figure 4.6c. This ensured that, as the sample is rotated during the measurement, the applied magnetic field rotated in the ac-plane from H||c to H||a. A 50μm Ag wire was spot welded to the sample prior to mounting and secured with a small amount of H20E Ag epoxy cured at 80°C (shown in Figure 4.6c) to ensure good thermal contact to the mixing chamber. A similar procedure was followed for sample JT1902-06 with the only differences being that it was mounted with the *b*- and *c*-axes aligned to the platform edges resulting in the applied magnetic field being rotated again in the ac-plane but now from H||a to H||c. Mounting the two samples in this way allowed the effective full 90° rotation to be mapped out after only a 45° rotation of ϕ, and after a full 90° rotation the two data sets could be compared allowing a higher confidence in the measurement. Once all of the samples had been mounted and all wiring secured using GE varnish, a small amount of powdered molybdenum disulfide was applied to all parts of the rotation mechanism that moved. This reduces the risk of sticking during the measurement hence reducing the noise introduced by large jumps in the measurement signal as the platform(s) 'un-stick'. Figure 4.6b and 4.6d show the prepared samples mounted on the rotation tail to fit in the bore of an 18.4/20.4 T magnet (with an inner diameter of 24 mm) on the custom dilution refrigerator.

A field modulation technique was employed to measure the susceptibility signals (for details see Section 3.3.1), the field was modulated at a frequency of f = 28.64Hz with an amplitude of A $\approx$ 3.5 Gauss$_{p-p}$ provided by a 100 mV signal from a SR830 lock-in amplifier into a Yamaha P2700 audio amplifier. The drive signal was provided by the lock-in amplifier measuring the susceptibility coil from sample JC1904-08 which was used to reference the lock-in amplifiers measuring sample JT1902-06. A 1.349 Ω shunt resistor was used to monitor the the modulation amplitude (positive edge from transistor-transistor logic (TTL) out). The field modulation can be calculated as:

$$\begin{aligned} B_m(\mathrm{T_{p\text{-}p}}) &= \left(\frac{T}{A}\right)\cdot\sqrt{2}\frac{V_{\mathrm{shunt}}}{R_{\mathrm{shunt}}} = \frac{0.0035}{0.093}\cdot\sqrt{2}\frac{V_{\mathrm{shunt}}}{1.349} \\ &= 3.945\times10^{-5}\left(\frac{\mathrm{T_{p\text{-}p}}}{\mathrm{mV_{rms}}}\right) = 0.3945\left(\frac{\mathrm{G_{p\text{-}p}}}{\mathrm{mV_{rms}}}\right), \end{aligned} \tag{4.1}$$

where B_m is the modulation field measured in units of peak to peak Tesla (T$_{p-p}$) and the value of Tesla per Amp, *T/A*, is an intrinsic property of the experimental apparatus. V_{shunt} is the voltage measured on the shunt resistor of resistance R_{shunt} and V$_{\mathrm{rms}}$ is the root mean square voltage. The final modulation amplitude is quoted in units of peak to peak Gauss (G$_{\mathrm{p\text{-}p}}$). A low temperature transformer with a winding ratio of 1:30 as well as a SR552 bipolar preamplifier (set at a gain of $\times$100) were used for sample JT1902-06, while sample JC1904-08 had only a SR554 transformer/preamplifier (set at a gain of $\times$500) using A-B differential output ports, but only the single-ended input "A". Two YFe_2Ge_2 TDO measurements were also mounted onto the rotation tail, again one oriented with H$\|$a (JC1904-02) and one H$\|$c (JC1904-03). The setup of these TDO measurements were performed in the most part by Dr. Jordan Baglo, the preliminary results from which are presented in Appendix A.

During the signal optimisation, the signal-to-noise ratio of the detection circuits for both dHvA coil sets were checked using both the fundamental signal and the n$^{\mathrm{th}}$ harmonic (up to n = 7). There are several reasons why the dHvA effect is usually measured by looking at higher order harmonics rather than the fundamental signal [25, p. 107] which are briefly reviewed below:

1. As the pickup coils can never be perfectly balanced, a significant sin(ωt) component that is not associated with the magnetic properties of the sample is detected, this is suppressed when detecting at harmonics of ω, where ω is the field modulation frequency.

2. Due to eddy currents induced in the sample by the oscillating field, the balance of the pick up coils can be upset and the dHvA signals can appear on a sloping baseline, again detection at higher harmonics almost completely eliminates this effect.

3. A large noise contribution in the output signal comes from electromotive forces induced by vibrations in the pick up coils from sweeping the externally applied magnetic field, this will show up primarily in the fundamental signal.

When higher order harmonics were tested for the dHvA samples, there was significant noise on the harmonic signals resulting in a heavily distorted sine wave, particularly on the H||c (JC1904-08) sample. The noise signal did not show up on the compensation coil lock-ins, implying that it comes from either real non-linearity of the sample magnetisation signals or, more likely, from overloading the transformers or preamplifiers. For this reason detection was done on the fundamental signals in both YFe_2Ge_2 dHvA samples, as this gave the best signal-to-noise ratio. This is presumably due to the significant effort that was put into eliminating vibrations in the Cambridge dilution refrigerator when the system was designed and installed.

A previously calibrated RuO_2 resistive thermometer (KM1, see Section 3.1.4) was mounted on platform 5 (the centre platform) as a secondary check when optimising the samples detailed in Table 3.1. Turning on the field modulation results in a significant amount of heating. The base temperature of the fridge with the modulation field turned off reached a minimum of ∼51 mK. However with the modulation turned on to its maximum tested amplitude (at significant fields) of 36.5 G_{p-p}, the temperature rapidly rises to ∼130 mK. A compromise of heating to noise performance was made and the heating at the mixing chamber with a field modulation of 3.6 $G_{p\text{-}p}$ was measured to be of the order of 5 mK relative to the temperature with the modulation field turned off, and at the rotation tail (at zero applied field) this was closer to 6 mK which was deemed acceptable.

4.2.2 Quantum oscillation measurement

Before the quantum oscillation data can be analysed, corrections to the magnetic field strength, as experienced by each sample, are required. The compensation coil of sample JC1904-08 was used to define the zero of the rotation angle: $\phi = 0°$, the signal from the compensation coil should be a maximum when the coil set is aligned with the magnetic field along the length of the probe. The mechanism was carefully rotated back and forth around this maximum (the mechanism can rotate to a small negative angle of around -5°) until the maximum was located.

In addition to corrections for sample positions relative to the field maximum, the two dHvA YFe_2Ge_2 samples require corrections to the field strength due to their projection as a function of ϕ as they are rotated. This will change their vertical position relative to the maximal field by a small amount which is dependent on the rotation angle. These corrections were applied before any of the data was analysed.

After the samples and dHvA coil sets had been mounted onto the rotation mechanism, although great care was taken to mount the dHvA coils perfectly perpendicular to the rotation platform, there is a slight angular offset between bobbins one and three, as shown in Figure 4.7. The difference between the two angles $\Delta\theta = (\alpha - \beta) \approx 7°$ at $\phi \approx 60°$. This relative angle $\Delta\theta$ also varies as a function of ϕ, which needs to be accounted for when correcting for the projection of the samples and when comparing the two data sets. Before the measurements began, in order to estimate the magnitude of

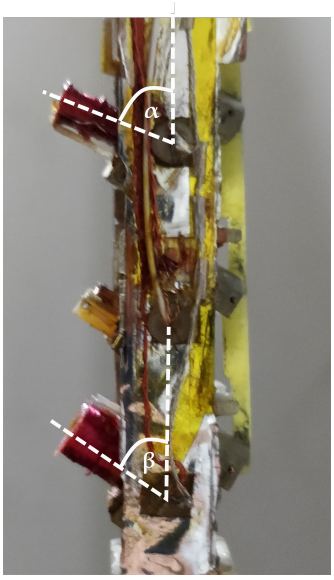

Fig. 4.7 Relative position offset, $\Delta\theta = (\alpha - \beta) \approx 7°$, of the two dHvA coil sets.

the offset angle $\Delta\theta$, a camera was set up to photograph the rotation mechanism at 10 angles between $0° \leq \phi \leq 90°$. The signal from the compensation coil for sample JT-1902-06 was used to determine the angle of the dHvA coil set at base temperature.

Figure 4.8a shows the normalised compensation signal from the coil sets of both samples, if both rotation platforms were aligned so that they rotated with the same angle and at the same rate the two curves should lie on top of each other. A relative angular shift of the two platforms, which increases with angle ϕ, is observed. Figure 4.8b shows the relative angular shift between the two platforms as a function of rotation angle ϕ, the trend is positive and linear. Platform one (JT1902-06) is ahead in rotation angle of platform three (JC1904-08). For each measurement taken at angle ϕ, the angle of sample JT-1902-06 has been adjusted accordingly by an amount $\Delta\theta$. It should be noted that, because YFe_2Ge_2 sample JT1902-06 is mounted with H$\|$a at $\phi = 0°$, the positive $\Delta\theta$ which is added to the rotation angle ϕ during the rotation study equates to a negative rotation angle shift when comparing the data to that of sample JC1904-08 which is mounted with H$\|$c at $\phi = 0°$. This is because sample JT1902-06 rotates from H$\|$a to H$\|$c while sample JC1904-08 does the opposite.

The rotation tails' vertical position relative to the magnetic field maximum is adjustable. Before starting the full rotation study, data sets have been taken with each sample centered at the field maximum. At $\phi = 0°$, magnetic field sweeps were performed over the range 0 - 18 T at T = 72 mK. Representative data sets from both YFe_2Ge_2 dHvA samples are shown in Figure 4.9. Sample JC1904-08 shows large oscillations, after a 4^{th} order polynomial background subtraction, down to below 6 T (Figure 4.9b) with several frequencies present. To decide the appropriate polynomial order, we have subtracted higher as well as lower order polynomial background, however, no visible change has been noticed above 4^{th} order, which replicate the background most appropriately.

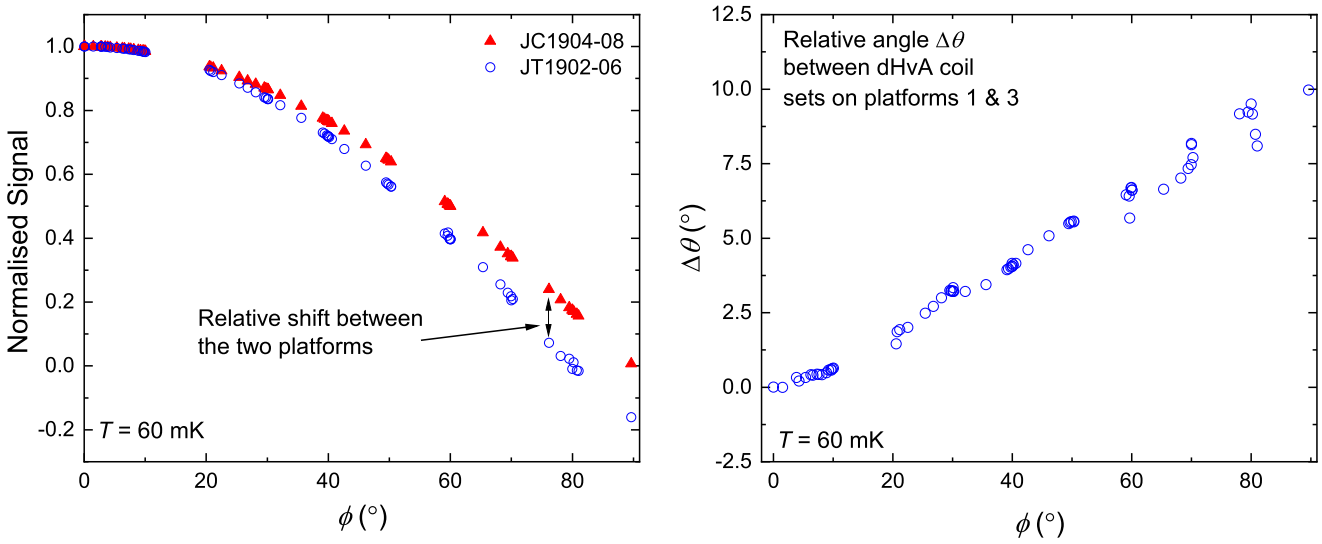

(a) Normalised compensation coil signal.

(b) Relative angle $\Delta\theta$

Fig. 4.8 **(a)** Difference in normalised signal from the two compensation coils containing samples JC1904-08 (red solid triangles) and JT1902-06 (blue open circles) at 60 mK. Both signals have been plotted against the rotation angle ϕ defined by sample JC1904-08. **(b)** Relative angular shift between platforms one and three as a function of rotation angle ϕ.

Table 4.1 Summary of the observed dHvA frequencies and mean free paths in YFe_2Ge_2 samples JT1902-06 and JC1904-08.

Sample	**Frequency (kT)**	**Mean Free Path (nm)**
JT1902-06	0.47	150 ± 10
	6.21	128 ± 3
	11.87	166 ± 4
JC1904-08	0.36	340 ± 10
	0.50	339 ± 8
	1.22	325 ± 3
	2.44	323 ± 6
	6.61	316 ± 4

Figure 4.10a shows the FFT of the oscillation data in the field range 6 - 18 T revealing five frequencies below 8 kT which are summarised in Table 4.1, the mean free paths have been calculated using equation 2.17. Sample JT1902-06 also shows large oscillations (after a 4^{th} order polynomial background subtraction) down to below 6 T (Figure 4.9a), although the signal is not as clean as is shown in sample JC1904-08. Figure 4.10b shows the FFT of the oscillation data in the field range 12 - 18 T displaying three frequencies below 20 kT, the noise floor is significantly higher than in sample JC1904-08.

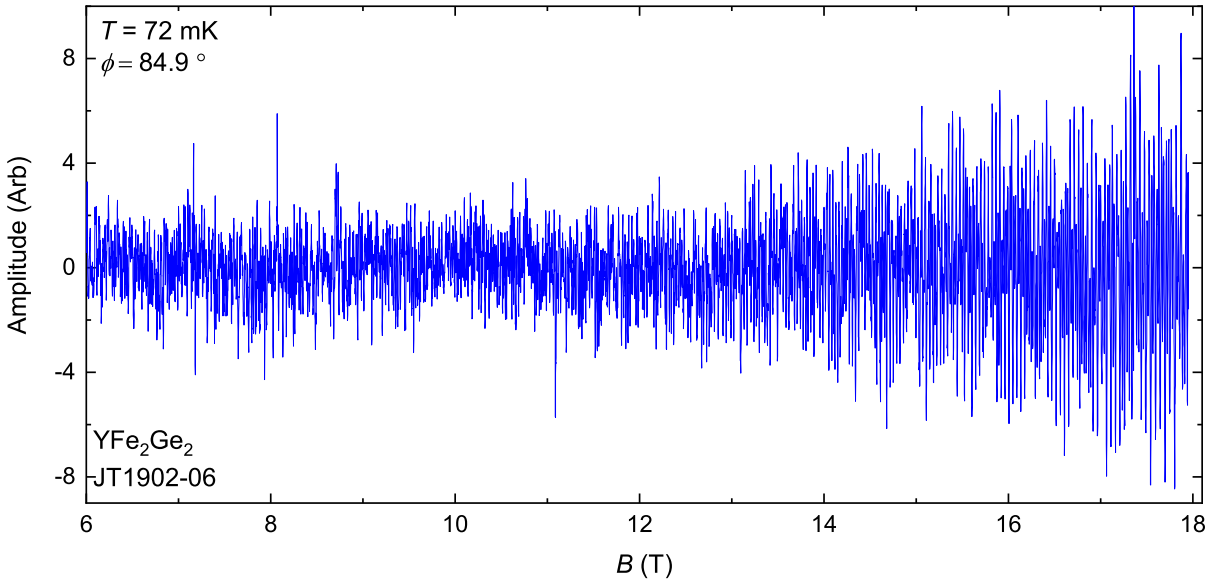

(a) YFe_2Ge_2 - JT1902-06.

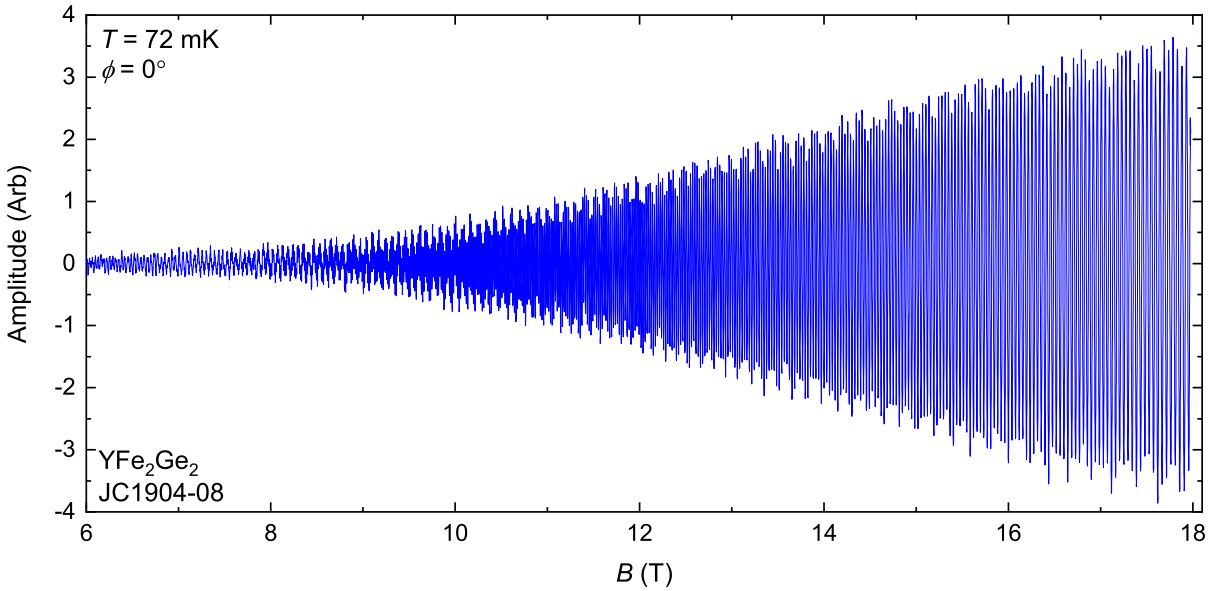

(b) YFe_2Ge_2 - JC1904-08.

Fig. 4.9 Quantum oscillation (dHvA) signals seen in samples **(a)** JT1902-06 and **(b)** JC1904-08 after a 4^{th} order polynomial background subtraction. The oscillations persist below 6 T in sample JC1904-08.

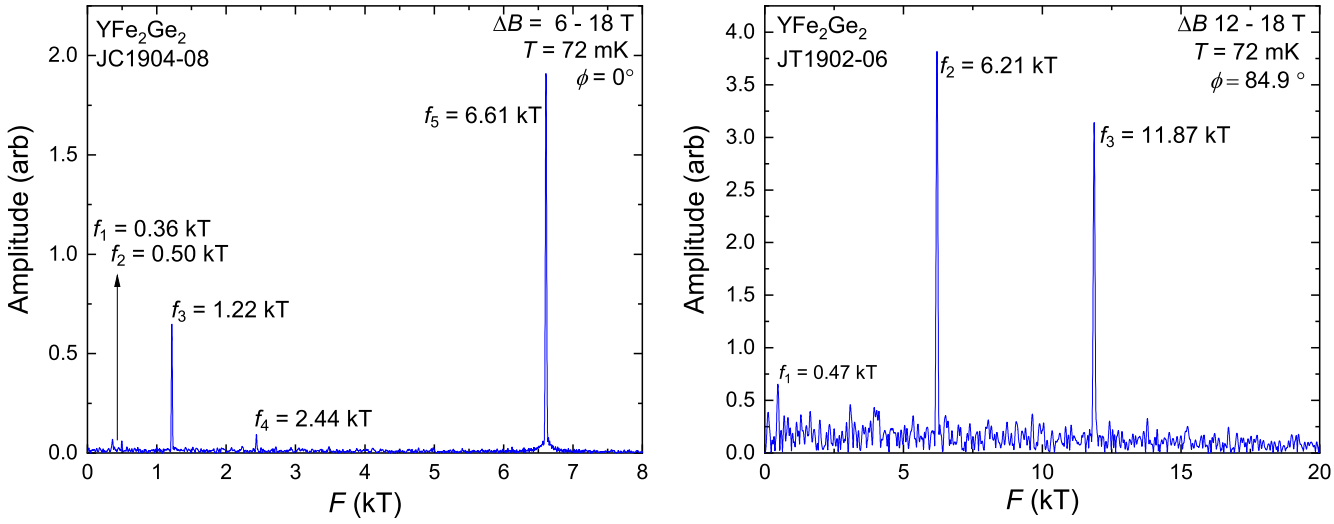

(a) JC1904-08 (b) JT1902-06

Fig. 4.10 FFT of the quantum oscillation (dHvA) signals seen in YFe_2Ge_2 samples **(a)** JC1904-08 and **(b)** JT1902-06.

Rotation study

Table 4.2 shows a summary of the magnetic field sweeps performed during this study, the Nb*X*Sb samples are detailed in Section 5.2.5, here we focus on the YFe_2Ge_2 samples. A compromise in terms of field sweep rates and ranges was made to best accommodate all of the samples. This was based on the frequencies observed during optimisation of all samples. As an example, fast sweeps over a wide field range worked well for NbSiSb where many low frequency oscillations were observed. In YFe_2Ge_2, however, slower sweeps were performed at higher fields to maximise resolution of the much higher quantum oscillation frequencies.

Table 4.2 Summary of magnetic field sweeps performed during this study.

Name	Range (T)	Rate (T/min)	Optimised for
Low Up	0 - 2	0.3	-
Fast Up	2 - 18	0.23	NbSiSb
Slow Down	18 - 12	0.06	NbGeSb and YFe_2Ge_2
Slow Up	12 - 18	0.06	NbGeSb and YFe_2Ge_2
Fast Down	18 - 2	0.23	NbSiSb
Low Down	2 - 0	0.3	-
Slow Low Up	0 - 1.2	0.023	NbGeSb
Slow Low Down	1.2 - 0	0.023	NbGeSb

Once the signals from both samples had been optimised a full rotation study was performed and data were taken at angles in the range $0° \leq \phi \leq 90°$ at intervals of $\Delta\phi = 2.5°$ for the fast sweep rates and some of the slow sweep rates (highlighted in Table 4.2). The slow sweep rate data between $20° \leq \phi \leq 80°$ was taken at intervals of $\Delta\phi = 5°$.

The angular dependence of the dHvA oscillation (in 1/B) FFT frequency spectra at base temperature (T = 55 mK) are shown in the waterfall plot of Figure 4.11: **(a)** JC1904-08 and **(b)** JT1902-06. Frequency peaks in the FFT spectra were systematically identified by looking at the frequency dependent background noise level in the vicinity of the peak. A peak was assigned when the height is (at least) 2.5 $\times$ the average local background noise level. After the initial set of peaks had been identified, the temperature dependence of the FFT peak amplitude (= the area under the curve after fitting to a Gaussian function) was used to further discriminate between real (originating from the Fermi surface) and spurious peaks: peaks which showed no resemblance to the LK temperature dampening of oscillation amplitude dependence were omitted (a plot of all peaks is shown in Appendix A).

Figure 4.12a shows the result of this peak identification in which the data from both samples JT1902-06 (open circles) and JC1904-08 (triangles) have been combined. A fast sweep rate (0.23 T/min) over a wide magnetic field range from $6 \leq B \leq 17.57$ T was used to identify peaks for sample JC1904-08. The same sweep rate but a different field range of $10.5 \leq B \leq 17.56$ T was used for sample JT1902-06. This was to maximise signal-to-noise in the FFT spectra, as the oscillations are less clear at lower fields in this sample. Five frequencies have been identified and have been labelled in accordance with the predicted frequencies from DFT calculations (see Section 4.3 below). There are a number of low lying frequencies ($f \leq 550$ T) which have been collectively labelled δ (purple). The frequency labelled α (red) at $f \sim 1.2$ kT, along with its first harmonic at $f \sim 2.4$ kT can be identified, both of which can be detected over most of the angular range in sample JC1904-08. Above 6 kT a new frequency emerges labelled β (blue) which is detectable over the full angular range. At angles above ϕ = 17.5° the highest observed frequency, labelled γ (green), is observed in both samples. The faster magnetic field sweep rate at lower fields enables a higher resolution of the lower frequency peaks in the FFT spectra which will prove useful when attempting to extract estimates for the effective quasiparticle masses of the frequencies labelled α and δ.

The angle ϕ has been shifted in sample JT1902-06 relative to that of sample JC1904-08 by $\Delta\theta$ based on the calculations outlined in Section 4.2.2 above. An additional shift of $\Delta\phi$ = -5.1° had to be added to JT1902-06 to match well with the frequencies of JC1904-08. Shifting only sample JT1902-06 is justified as the ϕ = 0° position of JC1904-08 was well calibrated using the methods outlined above. The source of this shift in angle could be due to one of a number of factors, or more likely, a combination of many:

1. The angle of sample JT1902-06 in the dHvA coil set, which although carefully positioned during the setup of the experiment (Figure 4.6(a)), could be shifted relative to JC1904-08. A

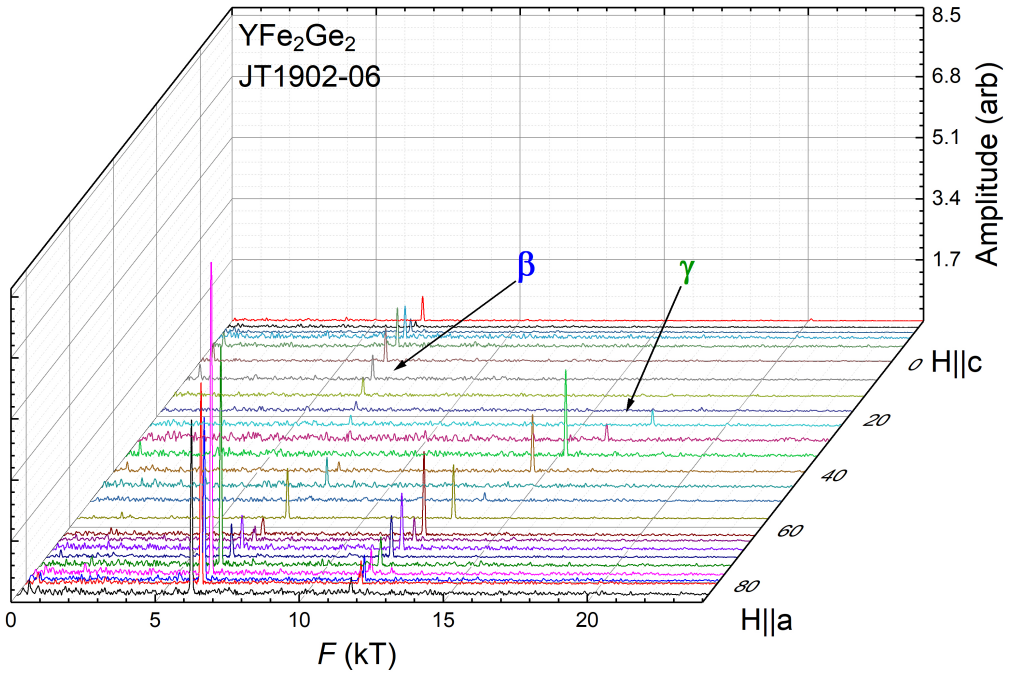

(a) YFe_2Ge_2 - JT1902-06.

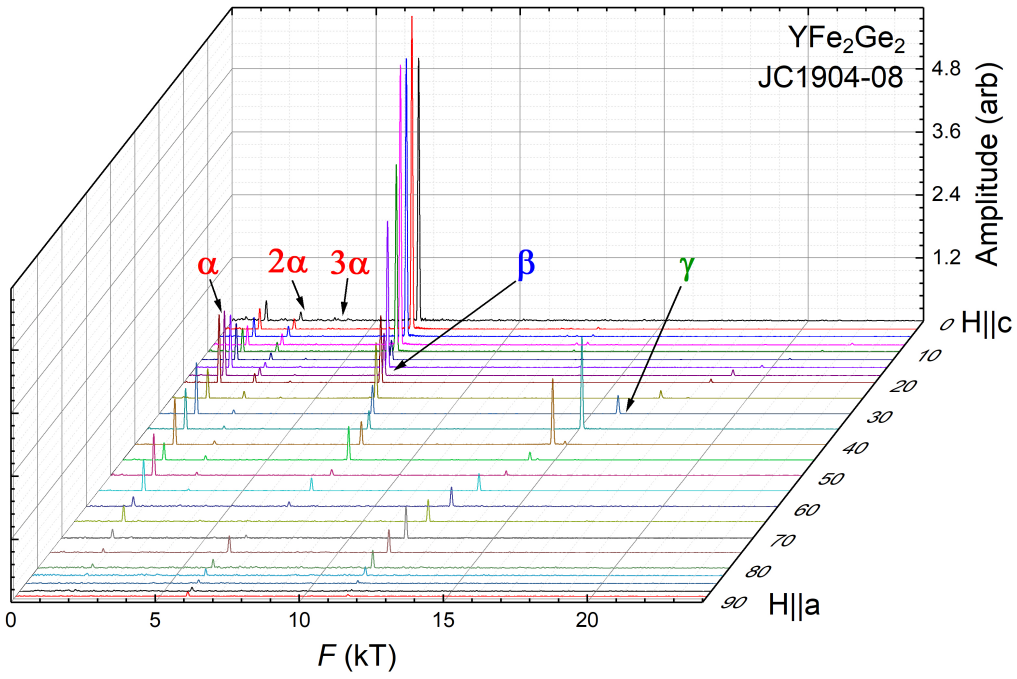

(b) YFe_2Ge_2 - JC1904-08.

Fig. 4.11 Waterfall plots showing the angular dependence of the dHvA frequencies from YFe_2Ge_2 samples **(a)** JT1902-06 and **(b)** JC1904-08. The z-axis runs from ϕ = -15 ° to 90 ° in (a) and ϕ = 0 ° to 90 ° in (b). Corrections of $\Delta\theta$ discussed earlier have been made to the angle of sample JT1902-06.

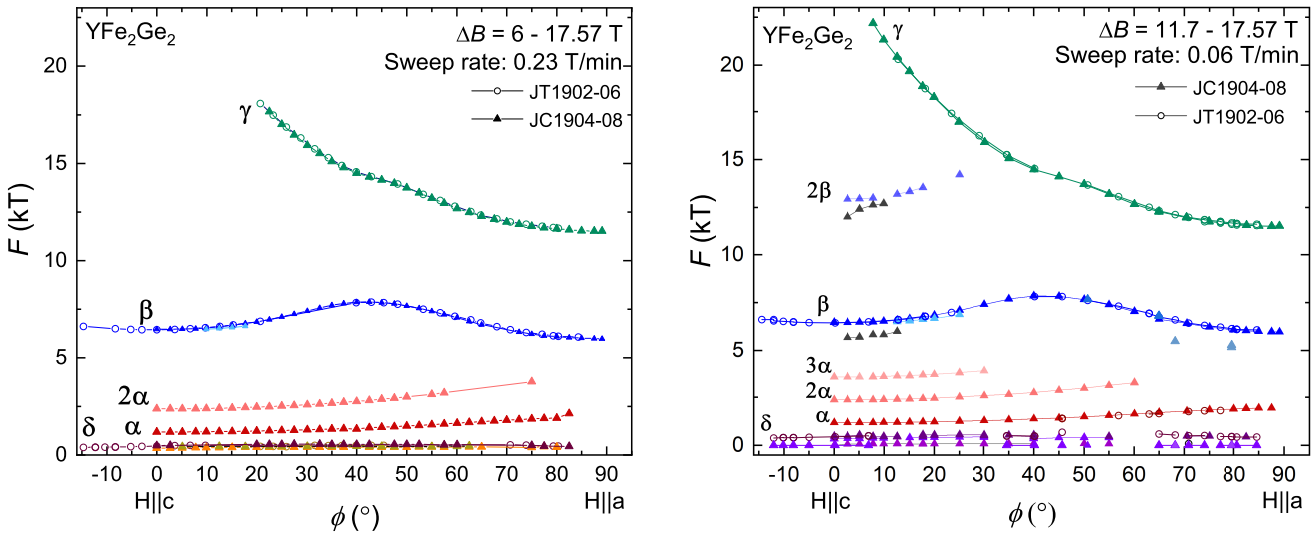

(a) YFe_2Ge_2 - Fast magnetic field sweeps.

(b) YFe_2Ge_2 - Slow magnetic field sweeps.

Fig. 4.12 Combined angular dependence of the dHvA frequencies from samples JT1902-06 (open circles) and JC1904-08 (solid triangles) with: **(a)** fast sweeps at 0.26 T/min and **(b)** slow sweeps at 0.06 T/min.

small angle of 1-2° may be difficult to spot, even with the aid of a microscope. There is also the possibility that the sample shifted slightly during to cooling of the fridge, either when the IVC was evacuated or upon cooling. a small amount of vacuum grease was used to secure the sample, this may have shifted the sample upon freezing during the cool down.

2. Similar to the first point, the angle of sample JC1904-08 could have shifted at some point after mounting, again great care was used when aligning the sample (Figure 4.6(c)) but a small angle of 1-2° may be difficult to spot.

3. Either sample could have been slightly shifted due to thermal contraction of the Ag wires spot welded to them for heat sinking purposes, although this is less likely to introduce a large shift in relative angle.

4. Magnetic field gradients across the samples could introduce shifts in the dHvA frequencies, although this would be a very small effect and is unlikely to introduce a coherent shift in (apparent) relative angle of the two samples. The amplitude of the oscillation frequencies can be more influenced than the frequency itself as a result of a gradient across the sample [80].

It is likely that the major contribution to the shift in angle between the two samples comes from a combination of the above factors, if the two samples were initially positioned offset from H||c and H||a by the estimated 1-2° for each sample, but in opposite directions, then a total shift of 5.1° required

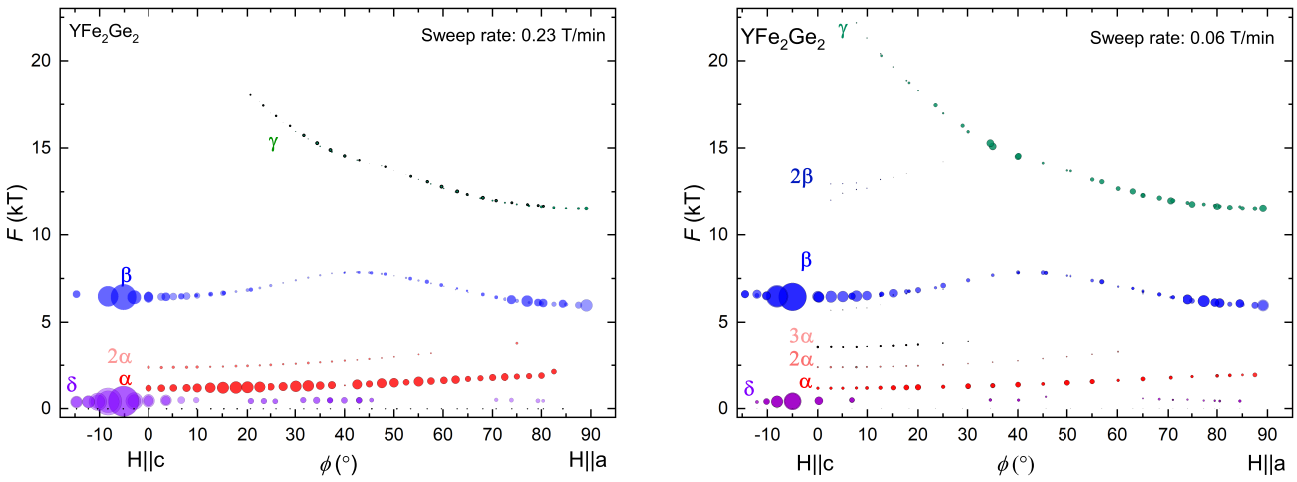

(a) YFe_2Ge_2 - Fast magnetic field sweeps.

(b) YFe_2Ge_2 - Slow magnetic field sweeps.

Fig. 4.13 Angular dependence of the dHvA frequencies from samples JT1902-06 and JC1904-08 with: **(a)** fast sweeps at 0.26 T/min and **(b)** slow sweeps at 0.06 T/min. The area of each data point represents the normalised amplitude of each FFT peak.

to line up the two data sets can be justified with the remaining $\sim$1.1° being introduced as a result of the cool down process. The major justification for introducing this shift comes from the fact that the two data sets line up, and they do so in two of the observed frequencies, γ and β (the frequency of which begins to increase in at negative angles, mirroring the angular dependence about $\phi = 0°$ (see Figure 4.12a,b). The data from the slow sweep rate, shown in Figure 4.12b also agrees with the same global angular shift in sample JT1902-06. The increased resolution of the higher frequencies now allows the α peak to be identified in sample JT1902-06, and, along with the γ and β frequencies, the angular dependence matches well with that of JC1904-08 after a shift of $\Delta\phi$ = -5.1°. Figure 4.12b shows the combined peaks identified for a series of slower field sweeps, at 0.06 T/min, in the field range $11.7 \leq B \leq 17.57$ T for both samples. In addition to the peaks identified from the fast field sweeps, there are two new harmonics, 3α and 2β, that can be identified. The γ frequency can now be tracked to a smaller angle of $\phi = 7.8°$, below which the amplitude is too small to reliably identify. Some further peaks appear at low angles (black triangles), both appearing just below β and its first harmonic, the origin of which is unknown. A splitting in the β frequency at $12.5° \leq \phi \leq 25°$ could be an additional part of the Fermi surface, or more likely due to some texturing of the part of the Fermi surface responsible for β, this frequency splitting can also be identified in Figure 4.12a.

The angular dependence of the combined dHvA data sets for both samples is shown in Figure 4.13. The size of each data point now represent the normalised amplitude of the FFT peaks which have been divided by $\cos(\phi)$. The frequencies seen near β and its first harmonic at low angles in Figure

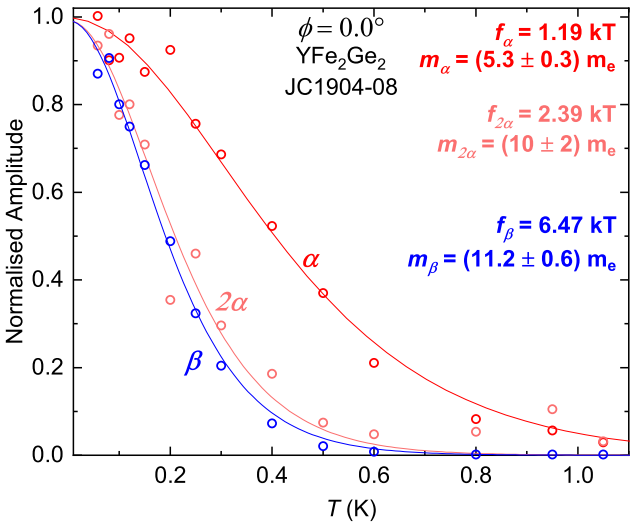

(a) $\phi = 0.0°$

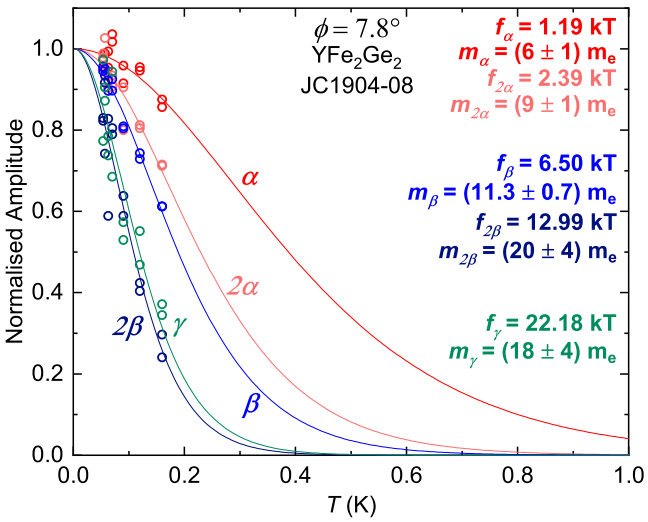

(b) $\phi = 7.8°$

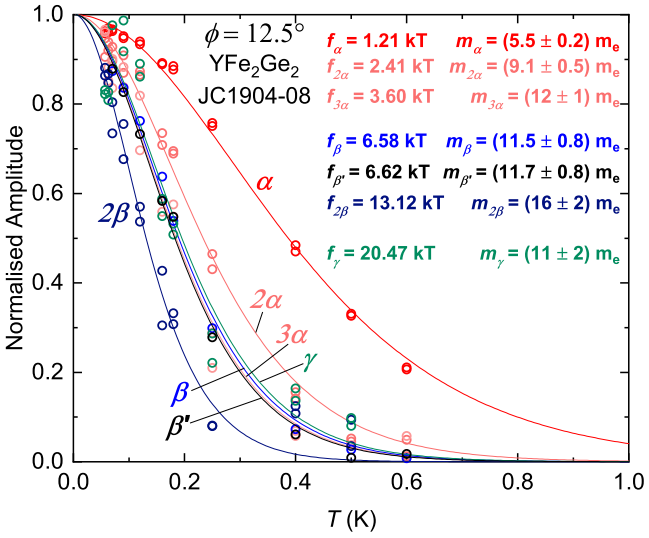

(c) $\phi = 12.5°$

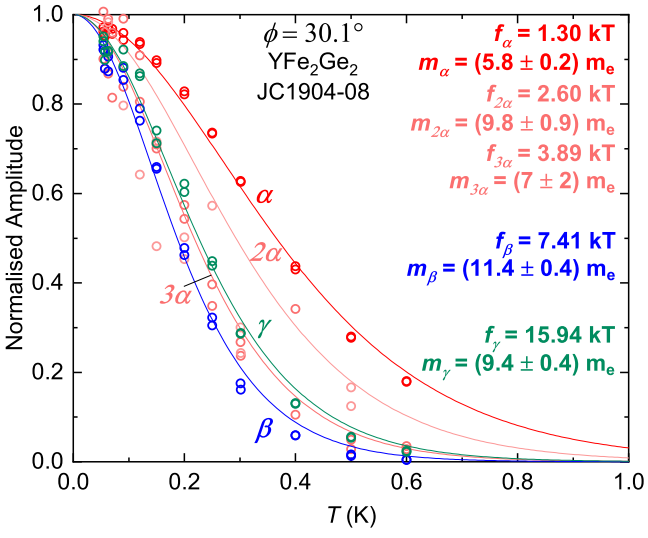

(d) $\phi = 30.1°$

Fig. 4.14 Fitting of the Lifshitz-Kosevich form of the temperature smearing factor (solid lines) to the amplitudes of the frequencies (open circles) present in samples JC1904-08. Mass studies were performed at angles of ϕ = **(a)** 0.0°, **(b)** 7.8°, **(c)** 12.5°, **(d)** 30.1°.

4.12b appear very small relative to the amplitude of the fundamental. The splitting in β at angles $12.5° \leq \phi \leq 25°$ appears to show a significant amplitude in both frequencies, an estimate of the effective quasiparticle masses from both frequencies will help to establish if there are two independent parts of the Fermi surface.

The temperature dependence of the dHvA peak amplitudes can be used to estimate the quasiparticle masses of the different parts of the Fermi surface. The effective quasiparticle mass m^* can be obtained through the fit of the temperature dependence of the oscillation amplitude to the thermal damping factor R_T (equation 2.14). In the case of multi-frequency oscillations, the oscillation amplitude for each frequency can be represented by the amplitude of FFT peak, and the parameter B^{-1} in R_T should be the average inverse field B^{-1}, defined as $B^{-1} = (B^{-1}_{\max} + B^{-1}_{\min})/2$, where B_{max} and B_{min} define the magnetic field range used for the FFT. Figures 4.14 and 4.15 show the temperature dependence of the FFT peak amplitudes (in $1/B$) of the background-subtracted dHvA data at various temperatures from both samples. The temperature dependence was measured at rotation angles of ϕ = (0°, 7.8°, 12.5°, 30.1°, 34.5°, 45°, 70.9°, 77.3° and 84.5°) at temperatures in the range ($55 \leq T \leq 1050$) mK.

The data from the slow sweep rate have been used to estimate quasiparticle masses of the frequency peaks which correspond to the three hole-like Fermi surface sheets. Data from the fast sweep rate has been used to estimate the effective quasiparticle mass of the possible low frequency candidate for the electron-like Fermi surface sheet. Figure 4.16 shows the temperature dependence of the FFT δ peak amplitudes (in $1/B$) of the background-subtracted dHvA data at temperatures in the range ($55 \leq T \leq 500$) mK. The data from both samples are quite noisy due to the very small amplitude of these peaks and useful data could only be extracted over the chosen magnetic field window at angles of ϕ = (0°, 30.1°, 34.5° and 84.5°). The errors associated with the estimated effective masses are large (relative to the magnitude of the mass estimates) and can only be used as a guide to the effective mass estimate of the δ peak.

4.3 Discussion

Comparison to Density Functional Theory calculations

Initial DFT calculations performed independently by D. Singh [71] and A. Subedi [76] suggested that the Fermi surface of YFe_2Ge_2 would consist of five Fermi surface sheets, as shown in Figure 4.17a. A more recent calculation has been performed by Prof. Malte Grosche using an experimentally measured input Z-parameter for the Ge- atoms ($Z = 0.3783$). The Z-parameter was extracted from the refinement of single crystal X-ray diffraction data on a sample of YFe_2Ge_2 with a RRR of around 170 (analysis by Dr. Monika Gamza, University of Central Lancashire). The updated calculation now predicts that only four bands will cross the Fermi level, resulting in four Fermi surface sheets which are shown in Figure 4.17b, the small hole pocket predicted by Subedi and Singh no

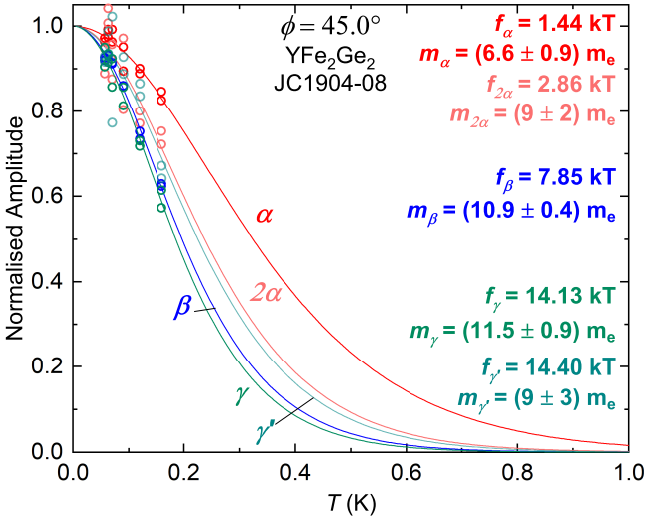

(a) $\phi = 45.0°$

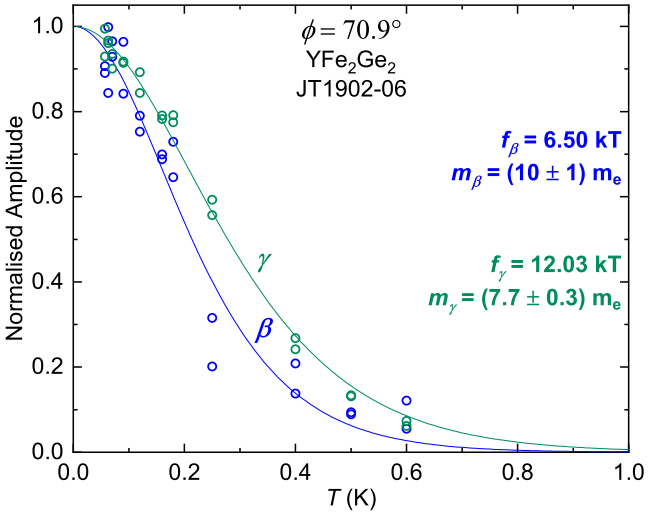

(b) $\phi = 70.9°$

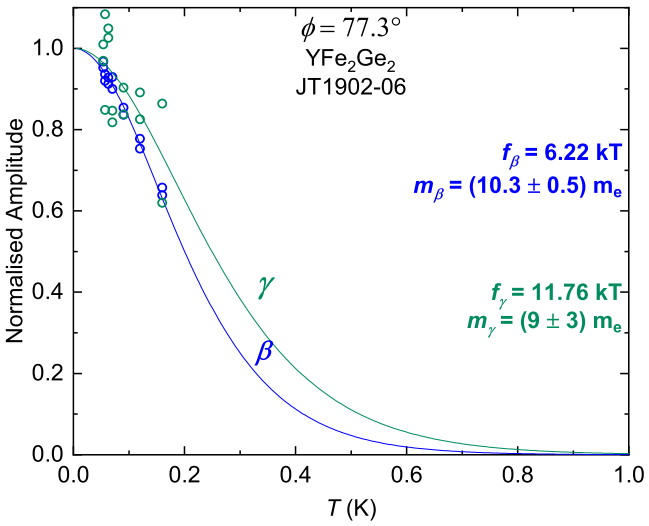

(c) $\phi = 77.3°$

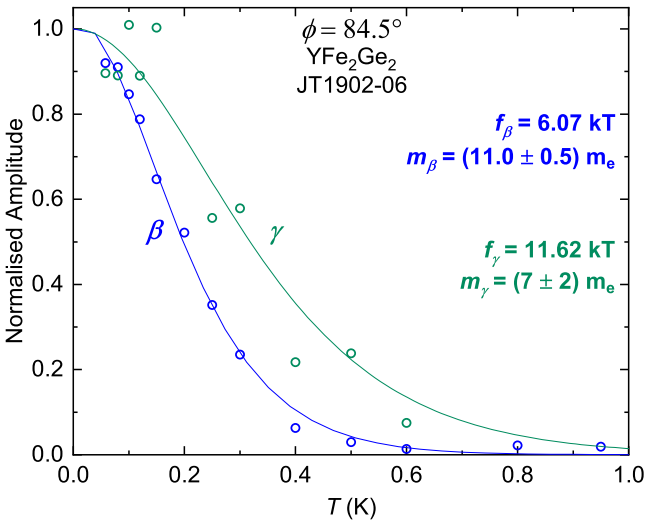

(d) $\phi = 84.5°$

Fig. 4.15 Fitting of the Lifshitz-Kosevich form of the temperature smearing factor (solid lines) to the amplitudes of the frequencies (open circles) present in samples JC1904-08 (**a**) and JT1902-06 (**b - d**). Mass studies were performed at angles of ϕ = **(a)** 45.0°, **(b)** 70.9°, **(c)** 77.3° and **(d)** 84.5°.

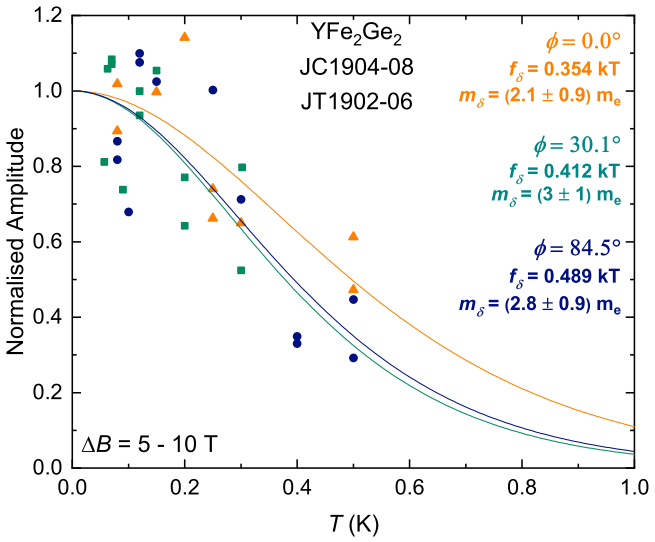

Fig. 4.16 Preliminary fitting of the Lifshitz-Kosevich form of the temperature smearing factor to the δ frequency present in samples JC1904-08 (ϕ = 0.0°, 30.1°) and JT1902-06 (ϕ = 84.5°). The data are quite noisy due to the very small amplitude of these peaks and as such the errors are large relative to the mass estimates. The magnetic field range was set at 5 - 10 T with a sweep rate of 0.23 T/min to maximise the resolution of the low frequency peak.

longer appears (sheet 1 of Figure 4.17a). With the exception of the missing hole pocket, the updated calculation remains qualitatively similar to previous calculations, with a relatively 3D Fermi surface.

With the aid of the Supercell K-space Extremal Area Finder (SKEAF) program [81], the latest calculation can be used to generate quantum oscillation (dHvA) frequencies for the extremal orbits as well as band masses as a function of applied magnetic field angle for the four predicted Fermi surface bands. These calculations have been compared to the measured dHvA frequencies and are shown in Figure 4.18a. There are several additional extremal orbits calculated for the electron pocket (purple dashed lines), this is mainly a result of the extrusion of the pocket towards the Γ point. A comparison of the calculated frequencies as a function of angle to the experimentally obtained frequencies allows the four predicted Fermi surface sheets to be assigned. Hole-like band 33 (green dashed line) matches up well with the peaks labelled γ (green triangles/open circles), showing a similar angular dependence (decreasing frequency which begins to plateau as ϕ approaches 90°) and magnitude of the frequency. The peak labelled β (blue triangles/open circles) matches qualitatively with hole-like band 34 (blue dashed line). There is a large deviation in frequency at angles $\phi \leq 60°$, however, the general shape of the angular dependence, including a hump around ϕ = 40°, and the magnitude of the frequencies are similar.

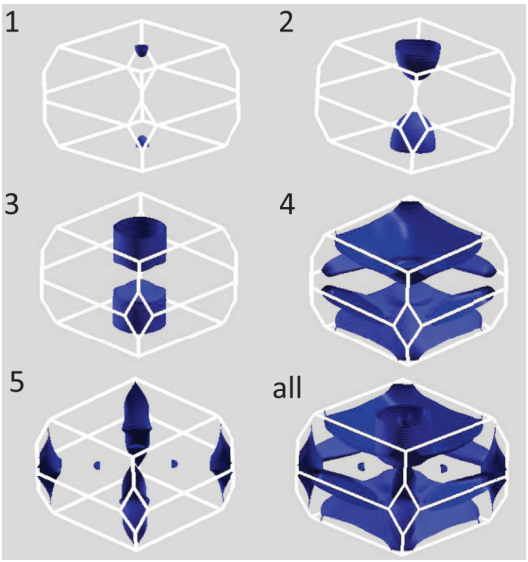

(a) YFe_2Ge_2 Fermi surface calculated by D. Singh.

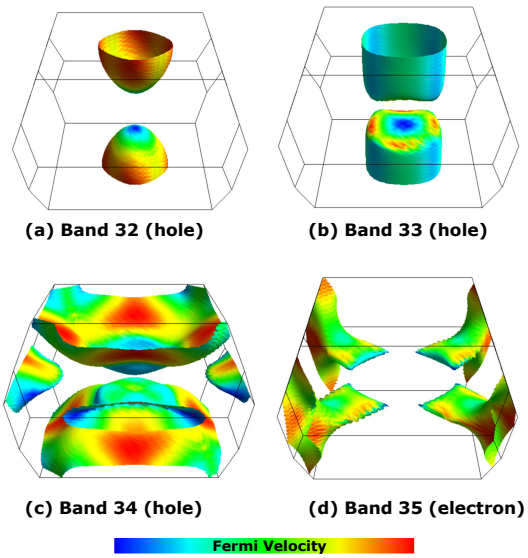

(b) YFe_2Ge_2 Fermi surface as calculated by Prof. F. M. Grosche (this work).

Fig. 4.17 **(a)** Calculated Fermi surfaces of YFe_2Ge_2 performed by D. Singh, five bands contribute to the Fermi surface (Reprinted with permission from [71]. Copyright 2019 by the American Physical Society). **(b)** Calculated Fermi surfaces of YFe_2Ge_2, in our calculation, only four bands contribute to the Fermi surface. Colour bar indicates the Fermi velocity (blue = low, red = high).

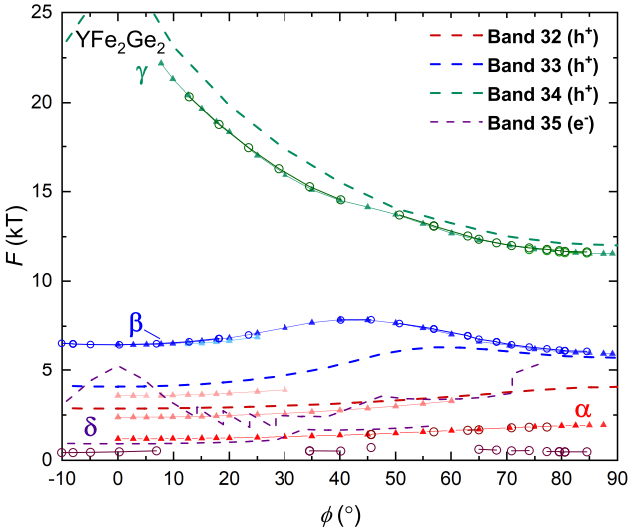

(a) dHvA Oscillation frequencies.

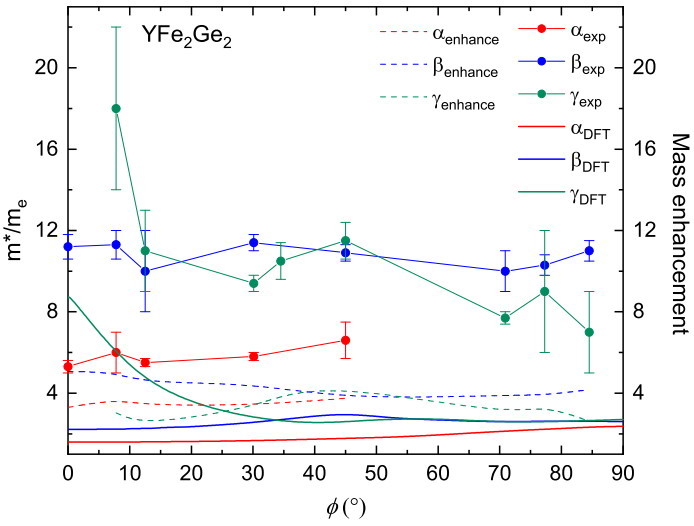

(b) Estimated effective masses.

Fig. 4.18 **(a)** Comparison of calculated frequencies (dashed lines) to the measured dHvA frequencies (solid triangles [JC1904-08] and open circles [JT1902-06]) in YFe_2Ge_2. **(b)** Comparison of numerical band masses extracted from DFT calculations (solid lines) to the measured effective quasiparticle masses in YFe_2Ge_2 (solid circles). The mass enhancement is shown by the dashed lines.

The SKEAF calculation predicts that hole-like band 32 (red dashed line) should result in a frequency at around f = 2.8 kT. This has been assigned to the peak labelled α (red triangles/open circles), which, although around half of the expected magnitude in frequency, has the same angular dependence as band 32, and does not follow the same angular dependence as the electron pocket of band 35. It is difficult to assign the electron-like band 35 to the collection of low frequency peaks labelled δ, as the peaks are only weakly visible, however, there is some evidence that the angular dependence of the experimentally measured peaks follow the calculation over the low angle range of $\phi \leq 30°$. A comparison of the effective mass of these peaks will help to distinguish these peaks as originating from band 35, however as stated earlier, the data from the mass estimates are somewhat unreliable for this peak. Nevertheless, the calculated masses of this peak from band 35 are at $\phi = 0°$: m* = 1.6 m_e and at $\phi = 30.1°$: m* = 2.5 m_e, which give mass enhancements of a factor of 1.3 ± 0.4 for $\phi = 0°$ and 1.2 ± 0.4 for $\phi = 30.1°$. There is no predicted low frequency contribution from band 35 at $\phi = 84.5°$. Further dHvA and possibly SdH measurements on higher quality single crystals will help to establish whether the low frequency peaks labelled δ are due to a contribution from the calculated band 35.

The latest DFT calculations, based on the experimentally determined z-parameter, give an increased value for the bare Sommerfeld electronic specific heat coefficient of $\gamma \approx 16$ mJmol^{-1}K^{-2}, compared to that predicted by D. Singh [71]. The experimentally determined normal state Sommerfeld coefficient of $\gamma \approx 97.5$ mJmol^{-1}K^{-2} (see Figure 4.19) is larger than the band-structure predicted value by a factor of six. This mismatch between the experimental normal-state γ and the calculated γ suggest that the quasiparticle effective masses should be enhanced by the same factor of six. The angular dependence of the estimated quasiparticle effective masses is shown in Figure 4.18b, the calculated band masses for bands 32, 33 and 34 which have been assigned to α, β and γ respectively are also displayed. The overall angular dependence of the three frequencies shows a qualitative resemblance to the band masses, however, as expected there is a significant underestimate of the magnitude of the effective mass, but only by around a factor of 3-5.

Table 4.3 shows a summary of the experimentally determined dHvA frequencies and estimated quasiparticle masses, with a comparison to the calculated dHvA frequencies and band masses from the latest DFT calculations. The mass enhancement has been calculated for bands 32, 33 and 34 and the enhancement factor lies in the range 2.5 to 5, the average mass enhancements are for band 32: (3.6 ± 0.2), band 33: (4.3 ± 0.3) and band 34 (3.3 ± 0.3). The discrepancy between the expected mass enhancement and what has been observed experimentally suggests that the specific heat enhancement of the Sommerfeld coefficient γ may not be accounted for by the hole sheets alone and there may be additional Fermi surface sheets that have not been observed with much heavier masses. The δ electron sheet may account for this, although preliminary estimates of the mass enhancement above suggest otherwise and additional measurements are needed to confirm this. It is also possible that the electron sheet is so heavy that we could not detect it (and the δ frequency above has been incorrectly assigned). The lowest temperatures we reached on the dilution fridge were not cold enough

Table 4.3 Summary of the measured dHvA frequencies and estimated quasiparticle effective masses and the calculated dHvA frequencies and band masses. The estimated mass enhancement is also shown.

Angle (ϕ)	Measurement			DFT			
	Orbit	F (kT)	Mass (m_e)	Band	F (kT)	Mass (m_e)	Mass Enhancement
0.0°	α	1.186	5.3 ± 0.3	32	2.79	1.58	3.3 ± 0.2
	2α	2.387	10 ± 2		-	-	
	β	6.467	11.2 ± 0.6	33	4.10	2.24	5.0 ± 0.3
	γ	not detected	-	34	27.61	8.85	
7.8°	α	1.191	6 ± 1	32	2.9	1.59	3.8 ± 0.6
	2α	2.394	9 ± 1		-	-	
	β	6.495	11.3 ± 0.7	33	4.15	2.25	5.0 ± 0.3
	2β	12.989	20 ± 4		-	-	
	γ	22.175	18 ± 4	34	24.13	5.54	3.3 ± 0.7
12.5°	α	1.208	5.5 ± 0.2		2.91	1.60	
	2α	2.413	9.1 ± 0.5	32	-	-	
	3α	3.604	12 ± 1		-	-	
	β	6.599	10 ± 2	33	4.21	2.28	4.4 ± 0.9
	2β	13.118	16 ± 2		-	-	
	γ	20.465	11 ± 2	34	22.21	4.44	2.5 ± 0.5
30.1°	α	1.301	5.8 ± 0.2		3.04	1.66	3.5 ± 0.1
	2α	2.602	9.8 ± 0.9	32	-	-	
	3α	3.892	7 ± 2		-	-	
	β	7.406	11.4 ± 0.4	33	4.76	2.56	4.5 ± 0.2
	γ	15.936	9.4 ± 0.4	34	17.39	2.74	3.4 ± 0.1
45.0°	α	1.438	6.6 ± 0.9	32	3.25	1.76	3.8 ± 0.5
	2α	2.863	9 ± 2		-	-	
	β	7.854	10.9 ± 0.4	33	5.75	3.01	3.6 ± 0.1
	γ	14.132	11.5 ± 0.9	34	14.71	2.45	4.7 ± 0.4
	γ'	14.399	9 ± 3		-	-	
70.9°	β	6.497	10 ± 1	33	6.04	2.60	3.8 ± 0.4
	γ	12.034	7.7 ± 0.3	34	12.55	2.58	3.0 ± 0.1
77.3°	β	6.222	10.3 ± 0.5	33	5.89	2.61	3.9 ± 0.2
	γ	11.756	9 ± 3	34	12.18	2.59	4 ± 1
84.5°	β	6.066	11.0 ± 0.5	33	5.75	2.61	4.2 ± 0.2
	γ	11.617	7 ± 2	34	12.05	2.65	2.6 ± 0.8

to see the associated high mass orbit. Comparing the measured mass enhancements to the mass obtained from heat capacity measurements, we can attempt to account for the 'missing' mass. Table 4.4 summarises the mass enhancements from the dHvA measurements, heat capacity and the DFT calculations.

About 40% of the heat capacity mass can be accounted for by the α, β and γ Fermi surface pockets we have measured, leaving around 60% missing. The latest DFT calculations predict that the nearly cylindrical electron pocket (δ) should contribute around 40% of the total mass (the largest

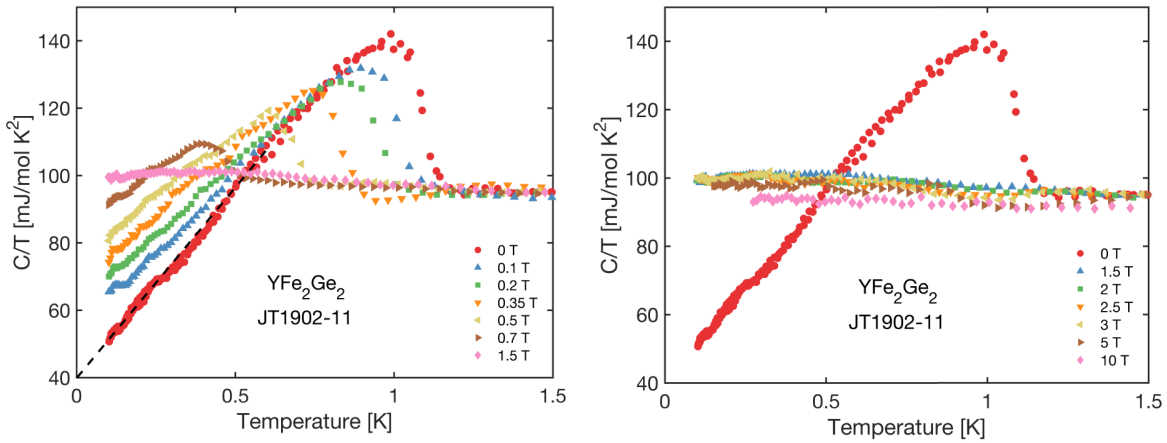

(a) Low magnetic field range.

(b) High magnetic field range.

Fig. 4.19 *C/T* vs *T* of YFe_2Ge_2 single crystal sample JT1902-11 at zero field and in **(a)** low fields with the black dashed line showing a linear extrapolation of the zero-field low-temperature *C/T* to zero temperature, and **(b)** at high fields. Analysis performed by J. Chen and figure reproduced with permission from [78].

Table 4.4 Comparison of the measured mass enhancement from dHvA measurements and to that of the DFT calculation to account for the mass measured via the heat capacity γ_C coefficient (indexed with a C here to avoid confusion with the γ Fermi surface sheet) γ_C ~100 mJmol^{-1}K^{-2}.

Band	m^*/m_e **(exp)**	m^*/m_e **(DFT)**	**Mass Enhancement**	γ_C **(DFT)** (mJmol^{-1}K^{-2})	γ_C **(Est.)** (mJmol^{-1}K^{-2})
α / 32	6 ± 1	1.59	~ 3.8	1.679	6.38
β / 33	11.3 ± 0.7	2.25	~ 5.0	2.953	14.77
γ / 34	18 ± 4	5.54	~ 3.3	5.300	17.49
δ / 35	2 - 3	0.92	~ 2 - 3	6.806	13.6 - 20.4
Total				**16.738**	**52.2 - 59.0**

contribution). If the mass enhancement from this sheet were in the region of 8.5, this would account for the missing contribution seen in the heat capacity. As the electron pocket is quite light to begin with (~1.6 m_e) this would indicate a measured mass of around 14 m_e. That the electron pocket was not observed is quite surprising given its cylindrical shape and our observation of heavier masses from other Fermi surface pockets.

Further heat capacity measurements (performed by J. Banda and Dr. M. Brando at CPfS (Dresden), data analysed by J. Chen) have shown that *C/T* in samples from YFe_2Ge_2 batch JT1902 shows signs of a small reduction at magnetic fields of 10 T when compared to C/T measured at lower fields, as shown in Figure 4.19. This may be an indication that, in strong applied magnetic fields, the electronic correlations could be reduced, and further measurements of the heat capacity at even stronger magnetic fields could show that the *C/T* will be further suppressed. This suppression of C/T may reduce the

enhancement factor down to the estimated enhancement from the measured effective quasiparticle masses and provide an explanation for the 'missing' mass.

4.4 Conclusions

The main objective of this experiment was to detect quantum oscillations in high quality single crystals of YFe_2Ge_2 for the first time using the field modulation technique. The reason for performing this measurement was to try to understand and explain the large discrepancy between the calculated band masses and the unusually large experimentally measured Sommerfeld coefficient of $\gamma \approx 100$ mJmol^{-1}K^{-2}. In this respect the measurement was quite successful as we have managed to account for a substantial part of the mass enhancement above the bare band masses from the DFT calculations.

A detailed rotation study of the dHvA quantum oscillations allowed us to track the dHvA frequencies as a function of applied magnetic field angle which were then compared to the calculated dHvA frequencies from the band structure calculations. A large effort was put into carefully correcting the magnitude of the applied magnetic field experienced by each sample due to the relative position and rotation of the two YFe_2Ge_2 samples measured. The predicted relatively 3D Fermi surface in YFe_2Ge_2, which is unusual for an iron-based unconventional superconductor, has been confirmed. Mass studies at a number of applied magnetic field angles relative to the c-axis have allowed estimates of the quasiparticle effective masses of the three hole-like Fermi surface sheets that have been observed and assigned to bands 32-34 from the DFT calculation. We have showed that for these sheets, a mass enhancement by a factor of around 2.5 - 5 is observed. While this accounts for around 40% of the enhancement observed in the Sommerfeld coefficient (of a factor of 6), more work is needed to understand the remaining missing contribution to the mass enhancement. The contribution from the electron pocket has been suggested as a source of this enhancement, however the preliminary data presented here is not of high enough quality to reliably discount this as the source. Further studies optimised to observe the low frequencies labelled δ are needed to draw a clear conclusion. A suggestion that, in strong applied magnetic fields, the electronic correlations could be reduced is a second possible explanation of the missing mass enhancement (as the normal-state Sommerfeld coefficient could be suppressed to a value closer to 4-5 times that of the bare band structure calculated value, which would then align well with the measured mass enhancements. Additional heat capacity measurements in strong magnetic fields at temperatures in the range ($0.1 \leq T \leq 2.5$) K are needed to support this theory.

CHAPTER 5

TOPOLOGICAL SEMIMETALS: NBXSB (X = GE/SI)

5.1 Introduction

The recent progress in our understanding of topological states of quantum matter has been realised via an intensive program of investigation in both materials science and in condensed matter physics. New characterisation techniques coupled with advances in materials processing and precise theoretical predictions have allowed the field to grow at an exceptionally fast pace. I will provide a brief overview of topology in condensed matter systems and then focus on a review of some of the work that has been done on topological semimetals, before introducing the experimental work.

5.1.1 Topology in condensed matter physics

The role of topology in the electronic structure of condensed matter systems has been firmly established since the discovery of topological insulators such as Bi_2Te_3 and SmB_6 [82, 83]. The topology of the ground state wave function was initially used to classify electronic phases with an energy gap, this was then extended to gapless systems and has led to the development of a major new theme in modern condensed matter research [84]. The first topologically nontrivial state of quantum matter was discovered in 1980, when a quantum Hall (QH) state was seen in a silicon metal oxide semiconducting field effect transistor (MOSFET) [85] after the invention of the MOSFET in 1959 allowed the study of electron behaviour in a 2D gas. In the QH state, under a strong externally applied magnetic field, Landau levels are formed in the bulk of a 2D system, the electric current travels along the edge of the sample only in a so-called skipping orbit. Figure 5.1a shows these edge states and also reveals that along each edge the current can travel in only one direction, which is opposite to that of the other edge, giving the edge states a chirality or handedness. This current flows without dissipation and gives rise to a quantised Hall conductance $\sigma_{xy} = C(e^2/h)$, where e is the charge on an electron, h is Planck's constant and C is an integer known as the first Chern number [86, 87]. Figure 5.2 shows an example

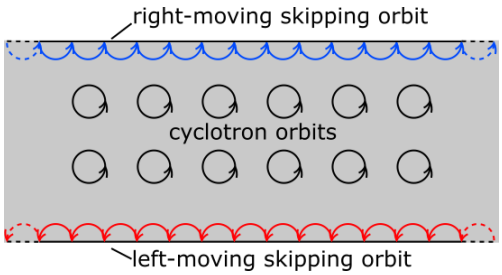

(a) Skipping orbits

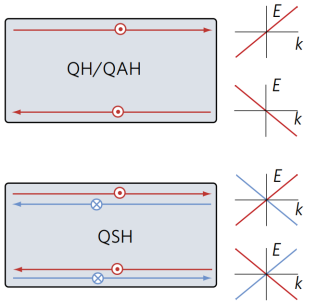

(b) QHE and QSH (Reprinted with permission from [84]).

Fig. 5.1 **(a)** Skipping orbits in a Hall bar: on the upper edge appear there are only left-moving states, and on the lower edge, right moving ones. Each edge contains states moving in one direction only, and the directions are opposite for opposite edges. These exotic states present at the edges are known as chiral edge states. **(b)** Top - QH/QAH states, TR symmetry is broken in both systems and the edge states carry a distinct chirality. Bottom - TR-invariant QSH insulator, TR symmetry is preserved and a helical pair of edge states exists with counterpropagating opposite spin states.

of a typical experimental data set showing the QH effect (the inverse of the Hall conductance, the Hall resistivity, is plotted in blue). At the plateau, the Landau levels are filled and there are no available states for electrons to scatter into, so they can only travel around the edge, resulting in dissipationless flow. At the jumps, Landau levels are not full and so there are additional final states available for electrons, allowing scattering in random directions which introduces dissipation and hence a jump is seen in the resistivity. As the degeneracy of the Landau levels grows as a function of applied magnetic field so does the number of available states in each level (as the cyclotron orbit shrinks). For large magnetic fields there are more available states as each Landau level is passed through, resulting in more dissipation and a growing Hall resistivity. The explanation for the quantisation seen in the Hall conductance/resistivity comes from the fact that it is a topological invariant and the electromagnetic response can be derived by direct consideration of the chiral edge states and is thus material independent. Time-reversal (TR) symmetry, the symmetry of laws of physics under a time reversal transformation, is explicitly broken in the topological class to which QH states belong. The QH state is topologically robust because of the spatial separation between the counter-propagating edge states, if an electron encounters a defect it will move around it and continue along the edge as it is not possible for it to turn around.

More recently, in 2006, a different class of topological states was both theoretically predicted [89] and observed experimentally [90]. These new states have been termed topological insulators [91, 92] or quantum spin Hall (QSH) states [89, 93, 94]. In these states the role of spin-orbit coupling (SOC) is very important. This relativistic effect in which the spin and orbital motion are coupled is strongest in heavier elements. Figure 5.1b (bottom) shows that in two dimensions the QSH state can be thought of as two versions of a QH state in which counter-propagating spin states are present along each edge.

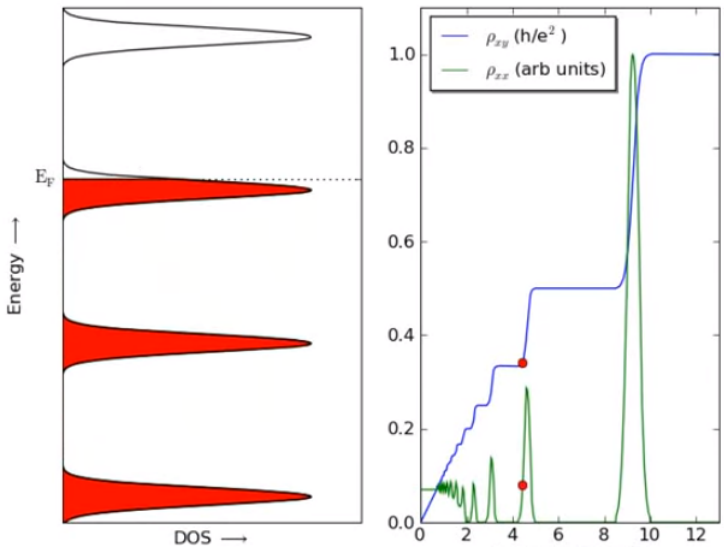

Fig. 5.2 **Left**: Filled (red) and empty (white) Landau levels. **Right**: Hall resistivity as a function of applied magnetic field, at strong enough magnetic fields, as each Landau level is passed trough there is a corresponding jump in the Hall resistivity, followed by a plateau, see main text for further explanation. Image obtained under a creative commons license from [88].

Time reversal-invariant topological insulators are characterised by a Z_2 topological number, where $Z_2 = 0$ is a trivial state and $Z_2 = 1$ is a topological insulator state [91, 95]. These materials have a full insulating gap in the bulk, however, the 1D edge states are gapless and contain an odd number of Dirac fermions. In general, a band inversion is required to find topological insulators: TR symmetry makes certain that at special points in the Brillouin zone (BZ) there are crossings of the energy levels of helical edge states. The QSH state can be generalised to a 3D topological insulator [96–98], where the surface state consists of a single 2D Dirac cone.

A closely related state of matter to the TR invariant QSH state is the quantum anomalous Hall (QAH) state, which breaks TR symmetry. This quantised version of the anomalous Hall effect exhibits a Hall conductance which is again quantised, however, this happens without the need for an orbital magnetic field. In 1988, Haldane proposed a model using a honeycomb lattice in which the QH effect could be realised without the need for an external field [99], and this was recently confirmed experimentally in TR-invariant topological insulators with magnetic doping [100, 101], emphasising the relationship between QSH and QAH states. Around the same time as the discovery of topological insulators, new gapless topological states called 3D topological semimetals were discovered, in which Dirac and Weyl fermions as well as the chiral anomaly can be observed in condensed matter systems [102].

5.1.2 Topological semimetals

The successful joining of special relativity and quantum mechanics was first suggested by Paul Dirac in 1928, in his now famous Dirac equation [103]. Dirac reconciled two key pieces of information to achieve this, first was the requirement from the special theory of relativity that spatial and time derivatives must appear to the same order in the equations of motion. The second was the probabilistic constraint of quantum mechanics that the equation of motion must depend only on the first derivative of time. This gave Dirac a clear conclusion and the resulting 4×4 complex matrices (the gamma matrices) and the four component wave function allowed for both up and down spin, as well as positive and negative energy solutions. These simple considerations led to the prediction of antimatter, and led to a deeper understanding of the concept of spin (as well as the birth of quantum field theory). The next year, in 1929, Hermann Weyl put forward a modified version of the Dirac equation that outlined massless fermions which possessed a chirality (or handedness) [104]. These two equations have proven to be invaluable in modern particle physics (along with another proposed by Ettore Majorana in 1937 which suggested a neutral particle that is it's own antiparticle [105]). In quantum field theories, the Dirac equation is the key to describing topological phenomena such as zero modes. Unfortunately in all high-energy physics experiments to date, no candidate Dirac/Weyl fermions have been observed as fundamental particles. When the energy scales are reduced to the scale of condensed matter physics (that is to scales much smaller than that of the rest mass of the electron), it would seem that relativistic corrections are unnecessary and Dirac physics would not be needed. Contrary to this it appears that even slow electrons propagating through a periodic potential of a crystal lattice results in a dressing of electronic states, which may result in an effective low-energy description which resembles the Dirac equation. This phenomena is most clearly demonstrated in two dimensional graphene, whose linear momentum dispersion relation is well described by the massless 2D Dirac equation. Since the isolation of single layer graphene sheets in 2004 by Geim and Novoselov [106] there has been a large amount of work on the synthesis and electronic properties of graphene [107]. For the remainder of this literature survey I will focus on the 3D Weyl equation [104], how it relates to Dirac fermions and condensed matter physics.

It is somewhat surprising that several of the physical properties that define a Weyl fermion (such as the chiral anomaly), are also present in the non-relativistic condensed matter regime. The chiral anomaly was first put forward by Adler [108], Bell and Jackiw [109] and is an example of an anomaly in a quantum field theory. Put simply the anomaly results in the non-conservation of electric field when a single Weyl fermion couples to an electromagnetic field. In order to get around this non-physical result, the net chirality of a set of Weyl fermions must vanish on a lattice. It was realised by Nielsen and Nimoniya that in this example the chiral anomaly can have a non-trivial effect which further demonstrated that there is a link between chiral fermions and band touchings in 3D crystals [110]. Wan *et al.* gave these band touchings the name 'Weyl nodes' [111]. These Weyl nodes lead to exotic surface states forming Fermi arcs which are a direct consequence of the topological nature of Weyl

fermions and the term 'Weyl semimetal' (WSM) was introduced to describe the phase in which the chemical potential is near to the Weyl node [111]. Several candidates have been proposed as experimental realisations of WSMs such as the spinel $HgCr_2Se_4$ [112], $Hg_{(1-x-y)}Cd_xMn_yTe$ films [113] and the search was successful in 2015 with the discovery of Fermi arc surface states attached to bulk Weyl points in TaAs [114] (as well as in other materials in this family [102, 115]). The possibility of stable four-fold degenerate Dirac points resulting from 3D materials as described by the Dirac equation was first established by Abrikosov and Beneslavskii [116] and much later by Wang *et al.* [117] and Young *et al.* [118]. However, the degeneracy is no longer topologically protected as is the case for Weyl points as the net Chern number is zero, this allows potential mixing of these terms by momentum conserving terms in the Hamiltonian resulting in a gap in the electronic spectrum. There are some cases in which the space group symmetries of a particular system can forbid this mixing allowing the nodes to remain as symmetry protected degeneracies. Again Wang *et al.* and Young *et al.* show that the formation of a stable electronic phase known as a Dirac semimetal (DSM) can be established over a wide range of Hamiltonian control parameters. As with WSMs there have been a number of experimental realisations of symmetry protected DMSs such as Cd_2As_3 [119, 120] and Na_3Bi [121].

The topological properties of WSMs can be stated simply in terms of their origin as monopoles of Berry curvature, Weyl nodes are sources and sinks of Berry flux (monopoles are allowed in the Berry field [122]. The physical properties associated with this topology manifest themselves in two ways: in non-trivial surface states, and in their response to applied electric and/or magnetic fields. The unusual surface states present in the form of Fermi arcs and have been seen most clearly in the WSM TaAs using ARPES and scanning tunnelling microscopy (STM) [123, 114, 115]. The response to applied fields can be attributed to the chiral anomaly discussed earlier, a simplified version of the response to **E** and **B** fields highlights the key features [124, 125]. The magnetoconductivity tensor has an anisotropic quadratic magnetic field dependence which is maximised for transport along the field direction. The modification to the zero field conductivity value along the magnetic field direction is [124]:

$$\sigma(B) = \sigma_0 + \frac{e^4 B^2 \tau_a}{4\pi^2 g(\varepsilon_F)}, \tag{5.1}$$

where $g(\varepsilon_F)$ is the density of states and $1/\tau_a$ is the inter-Weyl node scattering. Therefore the predicted behaviour of the magnetoresistance (inverse of magnetoconductivity) is negative. This negative magnetoresistance has been proposed as a signature of a WSM state, however, artefacts can arise during measurements which can dominate the experiment and can conceal such a dependence. Mixing between opposing Weyl nodes due to a large amount of disorder in a WSM will result in a strong effect on the transport phenomena associated with an isolated Weyl node due to the dependence on τ_a. In the limit of small τ_a there should be no signature of a Weyl node and the measured magnetoresistance will be small. The Weyl-like nature will increase, however, as τ_a increased and a large negative magnetoresistance will result from the chiral contribution.

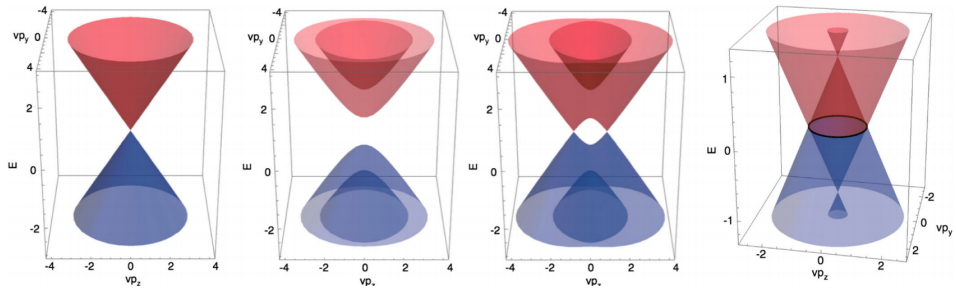

Fig. 5.3 (Left to right) Energy spectra of $\varepsilon_{s\mu}$ $(0, p_y, p_z)$ for a Dirac semimetal (m = b = b' = 0), magnetic semiconductor (m = 1, b = 0.5, b' = 0), Weyl semimetal (m = 0.5, b = 1, b' = 0), and line node semimetal (m = 0, b = 0, b' = 1) for the Hamiltonian equation 5.2. reproduced with permission from [127].

As well as any experimental difficulties, there is an additional potential intrinsic complication if the chiral current reaches the surface it can also be relaxed. Here, by sliding along the Fermi arc surface state, it can be converted into electrons at the opposite Weyl node. In the absence of direct internode scattering, this is the origin of chiral current relaxation [126]. However, since the Fermi arc relaxation mechanism is a surface effect, any bulk scattering mechanism between opposite Weyl nodes present will eventually dominate in the large volume limit.

In order to develop intuition and to visualise the band structures in the vicinity of DSMs/WSMs, Burkov, Hook, and Balents developed a model Hamiltonian with two orbitals plus spin [128]. This Hamiltonian can describe the cases of WSMs, line node semimetals and conventional gapped magnetic semiconductors and is reproduced in equation 5.2 below ([127]).

$$H = v\tau_x(\sigma \cdot \mathbf{k}) + m\tau_z + b\sigma_z + b'\tau_z\sigma_x, \tag{5.2}$$

where $\mathbf{k}$ = (k_x,k_y,k_z) is the momentum, m is a mass parameter and b and b' are Zeeman fields that correspond physically to magnetic field in the z- and x- directions respectively. The σ_n are the Pauli matrices for the spin degree of freedom, τ_n are Pauli matrices for pseudospin orbital degrees of freedom corresponding to sublattices or atomic orbitals. Several interesting cases can be obtained (as functions of m, b and b') by exploring m and b parameter space, setting b' = 0, the following eigenvalues are obtained [127]:

$$\varepsilon_{s\mu}(\mathbf{k}) = s\sqrt{m^2 + b^2 + v^2k^2 + 2\mu b\sqrt{v^2k_z^2 + m^2}}, \tag{5.3}$$

where k = $|\mathbf{k}|$ and s,μ = $\pm$1. The energy spectrum for $\varepsilon_{s\mu}$(0,k_y,k_z) is shown for several cases in Figure 5.3 which highlights the energy spectra of a Dirac semimetal, a magnetic semiconductor, a Weyl semimetal, and a line node semimetal (calculations have been performed using equation 5.2).

The case of $m = b = 0$ (far left) corresponds to a DSM which contains a pair of degenerate linear bands touching at the $\mathbf{k} = 0$ point. For $|m| > |b|$ (centre left) the energy bands are gapped over a range of E < $|m|$ - $|b|$ and this results in gapped magnetic semiconductor. A WSM is established for $|m| < |b|$ in which there are two touching points from the middle bands at a pair of isolated point nodes.

A new special class of metals, the topological semimetals (TSMs), have since been identified and have already seen much attention over the past decade [129]. TSMs have a characteristic Fermi surface which has its origins in the crossing of energy bands and is stabilised by topology. Several types of TSMs have been identified and can be distinguished by key features of the band crossing, such as local dispersion in the vicinity of the crossing, degeneracy, and the codimension, that is, whether the band degeneracy happens at either a point or at a line. Alternatively, the origin of the crossing, whether it is due to band inversion or is symmetry-protected can also be used to identify TSMs. From this, and in combination with topological characteristics, a number of TSM families have emerged, these include type-I and type-II semimetals [130], Dirac and Weyl semimetals [111, 117, 118, 131], and nodal-line semimetals [128, 132, 133] amongst others. Several Weyl points connect the conduction and valence bands of a Weyl semimetal, each point carries a topological monopole charge (from the first Chern number around it in momentum space). As a result of this, topological Fermi arcs connect the surface projections of oppositely charged Weyl points on the surface of WSMs. A breaking of TR or inversion symmetry is needed for a topological phase transition to occur in a 3D insulator, in which WSMs play an important role. This can be seen in the intermediate TR-invariant WSM phase which occurs during a TR-invariant transition between a noncentrosymmetric topological insulator and a regular insulator in 3D. The Weyl points, acting as Dirac monopoles of Berry curvature in the Brillouin zone, transfer the topological numbers of the insulators in the WSM phase. These topological effects have been demonstrated in several candidate materials including the impressive HgTe which can harbour a wide array of topological states [94]. A QSH insulator can be seen in HgTe quantum wells [94], doping the quantum well with manganese induces a QAH insulating state. Applying in-plane compressive strain to 3D HgTe produces an inversion-symmetry-breaking WSM state [134] while tensile strain will induce a 3D topological insulating state [135] and 3D $Hg_{(1-x-y)}Cd_xMn_yTe$ is a TR-symmetry-breaking WSM [113].

5.1.3 Motivation

The search for materials harbouring exotic quasiparticles, such as massless Dirac and Weyl fermions has received much attention in recent years, due in large part to their extraordinary physical properties such as ultra-high mobility and giant magnetoresistance. It has been suggested that these exceptional physical transport properties have potential in device applications [94, 111, 131]. There has been considerable recent interest in the material ZrSiS, a non-toxic and highly stable earth abundant material. First synthesised in 1964 [136], it wasn't until 2015 when Xu *et al.* predicted a 2D

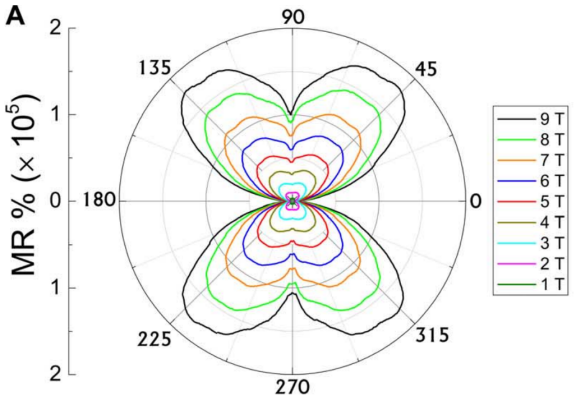

Fig. 5.4 Polar plot of the butterfly AMR effect in ZrSiS, the origins lie in a convolution of two- and four-fold symmetry dependencies. θ is the angle between the applied field and the current, which is applied along the a axis, From [139]. Reprinted with permission from AAAS.

topological insulating state ([137]) and then later in 2016 Schoop *et al.* found evidence for Dirac cones in the band structure using angle resolved photoemission spectroscopy (ARPES) that interest in this material started to grow. ZrSiS has an electronic band structure with several non-degenerate Dirac cones forming a diamond shaped line of Dirac-nodes on the Fermi surface; ARPES measurements show that the linear dispersion is unusually robust up to $\sim$2 eV [138]. Measurements of the angular magnetoresistance (AMR) along with angle dependent Shubnikov-de Haas measurements in ZrSiS reveal a so-called butterfly magnetoresistance and a quasi-2D Dirac Fermi surface, as demonstrated in Figure 5.4. The anisotropic magnetoresistance can have a significant impact in any potential technological applications or device fabrication.

The magnetoresistance in ZrSiS is large and positive, reaching as much as 1.8×10^5% at 2 K and a magnetic field of 9 T when the field is applied along $\phi = 45°$ (magnetic field angle relative to the applied current). Analysis of SdH oscillations show a sharp topological phase transition as ϕ approaches 90° [139]. Work by Wang *et al.* has shown that the unconventional MR does not saturate up to fields of 53 T, and they portray ZrSiS as a new type of quantum material with Dirac cones from both bulk and surface electronic states [140]. Singha *et al.* used magnetotransport measurements to show that ZrSiS has a large hole and small electron Fermi pockets. A non-trivial π Berry phase indicated the Dirac fermionic nature of both types of charge carrier [141]. In 2017, Pezzini *et al.* reported an unconventional mass enhancement around the Dirac nodal loop in ZrSiS which has been attributed to the correlation driven formation of a charge density wave phase [142, 143]. As much work had already been done on ZrSiS [138–147], we decided to concentrate our efforts on structurally similar, but previously unnoticed, compounds in the same PbFCl family. Initial DFT calculations performed by M. Dyer (University of Liverpool) suggested two candidate materials that may host Dirac or Weyl-like features: NbGeSb and NbSiSb. The goal was to synthesise these new materials and perform transport measurements searching for similar physics to that shown in ZrSiS (such as ultra-high

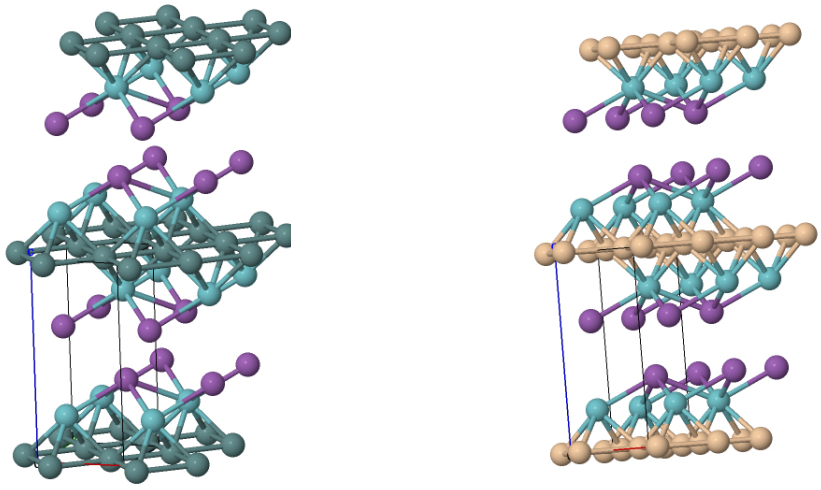

(a) NbGeSb: teal = Nb, green = Ge and purple = Sb (b) NbSiSb: teal = Nb, yellow = Si and purple = Sb

Fig. 5.5 Crystal structures of Nb*X*Sb, the Ge/Si square net can be seen in green/yellow respectively.

mobility, extremely large MR and evidence of topological phase transitions from SdH measurements). Initial attempts at crystal growth at the University of Liverpool (by the author) provided samples, which while single crystal, were not of high enough quality to show SdH oscillations at fields up to 14 T and at 2 K. A crystal growth facility was subsequently developed at the Cavendish laboratory in order to improve the quality of the single crystal samples and to measure their transport properties.

5.1.4 Nb*X*Sb (*X* = Ge/Si)

Nb*X*Sb crystallises in the PbFCl structure type in the tetragonal P4/nmm space group (no. 129) [148], the crystal structures of NbGeSb and NbSiSb are demonstrated in Figure 5.5 and can be described as a typical layered compound of quintuple layers of Sb-Nb-X-Nb-Sb, (see Tables 5.1 and 5.2 for crystallographic information). The centre of each quintuple layer contains Ge/Si which bonds to four Nb atoms in tetrahedral coordination, and the Sb atoms inhabit the sides of each quintuple layer, which form weak van der Waals-type bonds to neighbouring layers.

The structures are in the ZrSiS family of nonsymmorphic semimetals, with the aliovalent substitution of Nb for Zr and Sb for S. The total charge count in NbGeSb is the same as in ZrSiS, and so it should have a similar charge compensation between electron-like and hole-like carriers [114]. It should be noted that Nb has an additional valence electron relative to Zr and that Sb is missing one compared to S. The relative positions and occupations of the underlying electronic states should therefore be expected to have a significant change compared to that of ZrSiS. Nb*X*Sb is related to the stuffed version of the PbFCl structure type in the Weyl semimetal $YbMnBi_2$. Dirac electrons and exotic

transport phenomena have already been demonstrated in other Bi based, stuffed PbFCl structures, such as $EuMnBi_2$ and (Ca/Sr)$MnBi_2$, [149–151]. Square nets of Si and Bi atoms are present in both of these materials and are located on a glide plane. In NbXSb, the Si/Ge square net is located in the *ab*- plane and layers of Nb and Sb are sandwiched in between these square nets such that there are neighbouring Sb layers in between the Nb layers. Scanning electron microscopy (SEM) images of typical crystals of NbGeSb and NbSiSb are shown in Figures 5.9 and 5.11 respectively. The crystals are non-toxic and highly stable in water and in air.

5.2 Measurement setup, procedure and results

As discussed in Chapter Section 2.2.3 impurity scattering leads to lifetime broadening of Landau levels and the Dingle reduction of the amplitude. In order to observe quantum oscillations down to the lowest fields it is important to have the very highest purity single crystals possible. Samples of NbXSb grow as thin platelets and so it was decided to begin the search for quantum oscillations in the resistivity (SdH effect). Low temperature resistivity measurements have been performed on several samples of NbGeSb and NbSiSb using the Cambridge dilution refrigerator and a Quantum Design PPMS (detailed in Section 3.1.3). The PPMS has temperature control over a range (0.45 - 300) K and a sample magnetic field from (-9 to +9) T and was useful for relatively quick sample characterisation/screening and detailed resistivity sweeps. The dilution refrigerator has a temperature range from $\sim$30 mK to 10 K and a sample magnetic field from (0 to 18.4) T and so was used for much more detailed quantum oscillation studies to mK temperatures, it is also equipped with a rotator allowing the samples to be rotated relative to the applied magnetic field.

5.2.1 Materials growth and characterisation

High-quality NbXSb (X=Si,Ge) single crystals were synthesised using a chemical vapour transport (CVT) method. In general, a source material is transformed reversibly via a transport agent into gaseous products. The methods follow that of (amongst others) Lv *et al.* [114] and a more detailed outline of the CVT method is detailed in [152]; a summary of the methods used here are outlined below.

Chemical vapour transport

Heterogeneous Chemical vapour transport (CVT) reactions involve a condensed (typically solid) phase, which has an insufficient pressure for its own volatilisation (a process whereby a dissolved material is vaporised). In the presence of a gaseous reactant (known as the transport agent), however, the condensed phase can be volatilised and deposited elsewhere, most commonly in the form

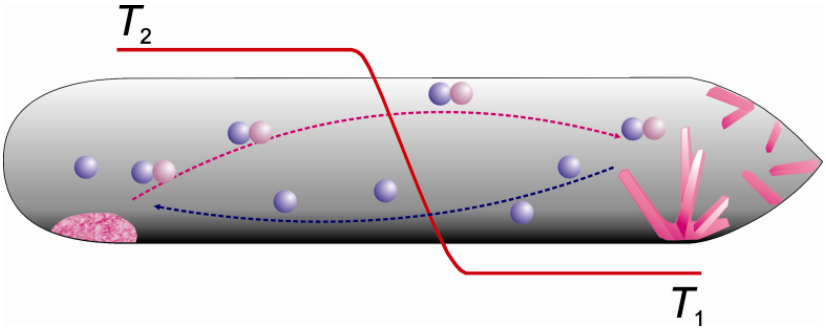

Fig. 5.6 A typical setup for the crystallisation of solids using a temperature gradient with the CVT technique. Reproduced with permission from [152].

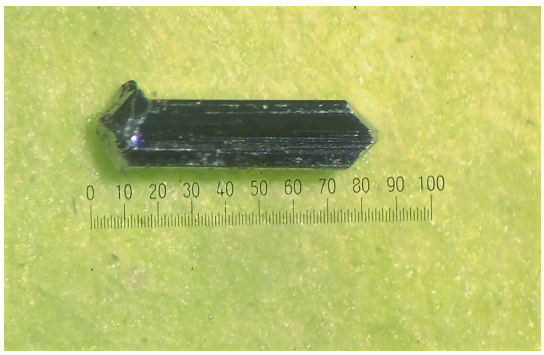

(a) NbGeSb, full scale is equal to 1.15 mm.

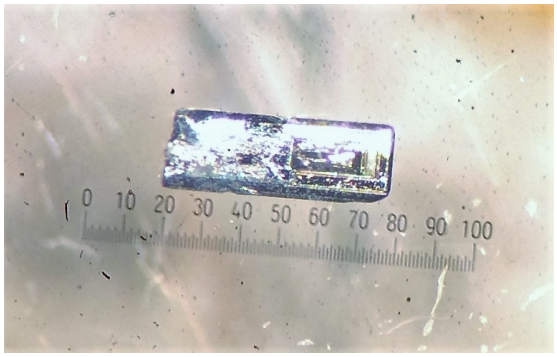

(b) NbSiSb. full scale is equal to 1.15 mm.

Fig. 5.7 Typical single crystals of NbGeSb and NbSiSb from the CVT growth, the NbGeSb tended to form either plate-like crystals or sword shape larger crystals, while NbSiSb formed much smaller needle-like crystals or small platelets.

of crystals. Deposition will occur if the external conditions for the chemical equilibrium differ between the position of crystallisation and of volatilisation. This is usually achieved via a temperature gradient between the volatilisation and crystallisation positions, demonstrated in Figure 5.6. A 1:1:1 stoichiometric mixture of Nb (Alfa Aesar -325 mesh, Puratronic, 4N metals basis excluding Ta, Ta $\leq$500ppm), Si (Alfa Aesar -325 mesh, 5N metals basis) or Ge (Alfa Aesar -100 mesh, 5N metals basis) and Sb (Alfa Aesar -200 mesh, 5N metals basis) powder was prepared in a glove box under an argon atmosphere (where the oxygen and humidity content was less than 0.5 ppm). The raw elements were ground to a fine powder using a pestle and mortar and then transferred into two quartz tubes (NbGeSb and NbSiSb) along with iodine used as a transport agent (Alfa Aesar iodine lump, ultra dry, 5N metals basis: 10 mg/cm^3) which was then sealed under a partial pressure of argon (150 mbar). The quartz tubes were then placed into a two-zone horizontal furnace and the temperature was increased for 166 minutes until a temperature gradient of T_{Hot} = 850 °C to T_{Cold} = 700 °C was applied, the tube was then left for 336 hours before being ramped down to room temperature over a period of 70 minutes.

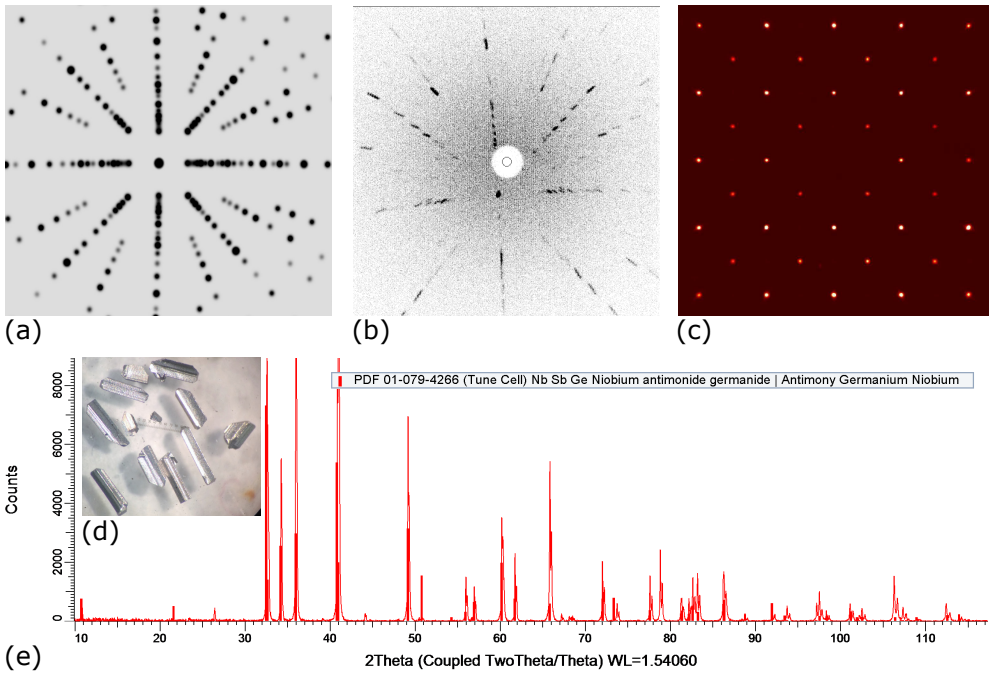

Fig. 5.8 **(a)** Laue Camera calculation of NbGeSb along [001]. **(b)** Laue camera image of the *ab*- plane of NbGeSb allowing the c-axis to be determined. **(c)** Single crystal NbGeSb XRD image. **(d)** Single crystals NbGeSb used to obtain powder XRD in: **(e)** Powder XRD analysis of NbGeSb to establish correct composition, data in thin red lines and structure calculation of NbGeSb in thick red bars.

Following this procedure, plate and needle-like single crystals of NbGeSb and NbSiSb with well-defined facets were obtained at the T_{Cold} end (typical crystals shown in Figure 5.7). The sizes of the crystals are typically (1.5 × 0.5 × 0.5) mm^3 (NbGeSb) and (0.8 × 0.2 × 0.4) mm^3 (NbSiSb). The crystals have mirror-like surfaces and are robust in the air and water. In order to improve the quality of the NbGeSb crystals, several samples were placed into alumina crucibles and resealed in a quartz tube with a titanium getter (to remove oxygen impurities) under a partial argon atmosphere of 150 mbar. The samples were then annealed at 400°C for two weeks in a box furnace.

5.2.2 Sample characterisation

The composition of the single crystal samples was determined by energy-dispersive X-ray (EDX) spectroscopy, which was equipped on a FEI Philips XL30 sFEG scanning electron microscope (SEM), the results of which are shown in Figures 5.9 and 5.11. For the as grown NbGeSb crystals the EDX analysis spectrum shows a slight excess of niobium and a slight deficiency of antimony (around 2%) suggesting that some niobium may be located at antimony sites. For the as grown NbSiSb crystals the EDX analysis spectrum shows a slight excess of antimony and a slight deficiency of niobium (around 1%) suggesting that a small amount of antimony may be located at niobium sites, however, this may be due to the error in the EDX measurement which is of order 1%. NbSiSb also shows a

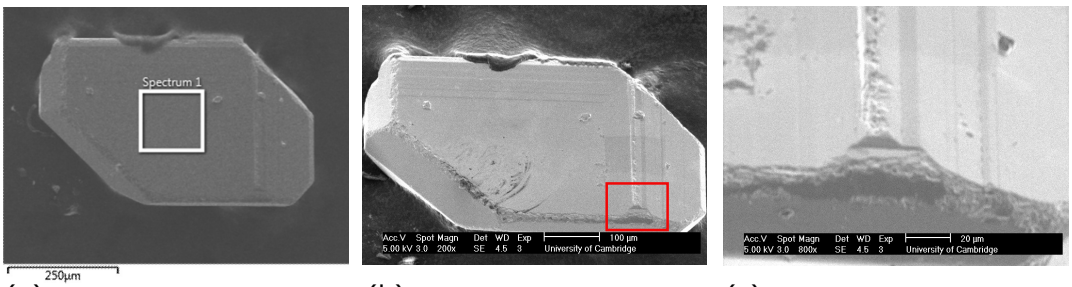

(a) (b) (c)

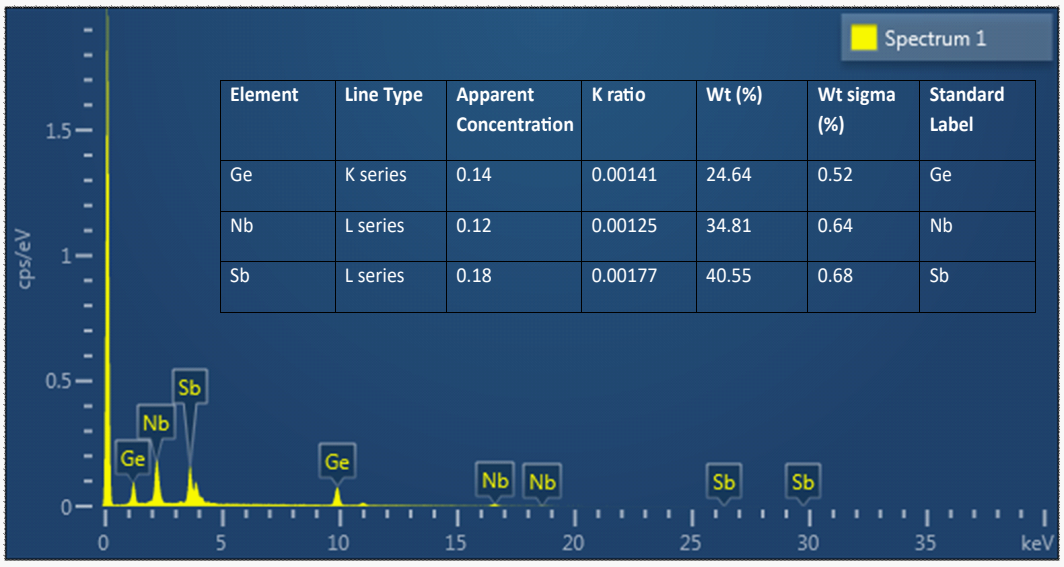

Element	Line Type	Apparent Concentration	K ratio	Wt (%)	Wt sigma (%)	Standard Label
Ge	K series	0.14	0.00141	24.64	0.52	Ge
Nb	L series	0.12	0.00125	34.81	0.64	Nb
Sb	L series	0.18	0.00177	40.55	0.68	Sb

(d)

Fig. 5.9 **(a)** SEM image of an as grown NbGeSb sample in the *ab*- plane, the square marks the region where the EDX analysis in **(d)** was performed. **(b)** SEM image of the same plate-like sample at higher resolution and at an angle of 15°. **(c)** Zoomed in region (red square) showing the steps at the edge of the platelet. **(d)** EDX elemental analysis confirming the composition of NbGeSb.

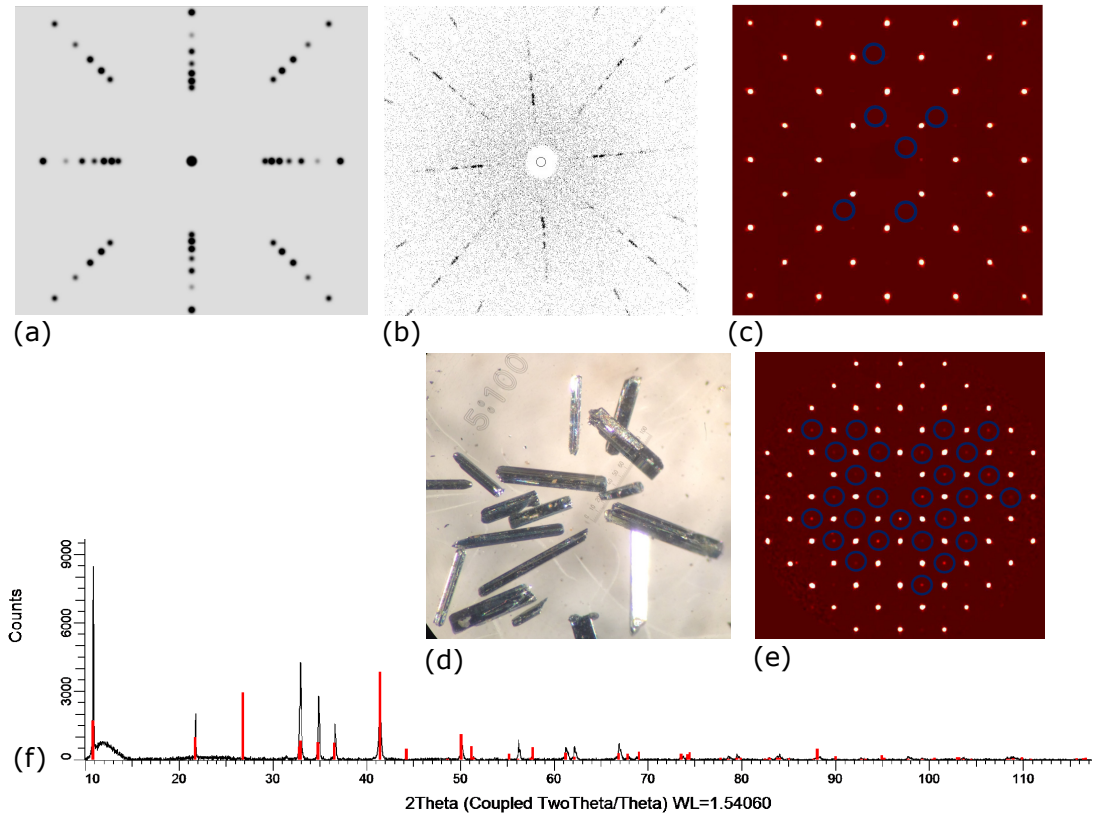

Fig. 5.10 **(a)** Laue Camera calculation of NbSiSb along [001]. **(b)** Laue camera image of the ab plane of NbSiSb allowing the c-axis to be determined. **(c)** Single crystal NbSiSb XRD image, blue circles indicate reflections from impurities and defects. **(d)** Single crystals of NbSiSb used to obtain powder XRD in (f). **(e)** Single crystal XRD of NbSiSb. **(f)** Powder XRD analysis of NbSiSb to determine correct composition, data in thin black lines and structure calculation of NbSiSb in thick red bars.

small amount of oxygen (as SiO_2) suggesting that there may be some oxygen inclusions. The crystal structure of the single crystals were checked using a powder x-ray diffraction (XRD) measurement, which was carried out on crushed single crystals using a Brüker x-ray diffractometer with Cu-Kα radiation (see Figures 5.8(e) and 5.10(f)). A quick analysis of the spectra shows a good match to the expected spectra for both NbGeSb and NbSiSb. A more detailed single crystal XRD analysis was also performed on several samples of both annealed and unannealed NbXSb at room temperature and at 100 K using an Agilent SuperNova system with Cu-Kα radiation (Figures 5.8(c) and 5.10(c)). The single crystal XRD experiments were carried out and analysed by Dr. M. Gamza (University of Central Lancashire) at the XRD user facility at Lancaster University, a summary of the findings are presented here.

An overnight scan at T = 100 K gave lattice parameters for as grown NbGeSb (space group number 129) of $a = 3.7011(10)$ Å and $c = 8.2045(20)$ Å. The same scan gave lattice parameters for the annealed NbGeSb of $a = 3.702\,60(1)$ Å and $c = 8.205\,69(4)$ Å (error bars for the lattice parameters

Table 5.1 Structural parameters from refinements of a complete data set collected at T = 100 K on as grown and annealed single crystals of NbGeSb. Two different codes (GSAS and Jana2006) gave consistent results (after excluding not matching peaks), well converged and with low statistical factors. B_{iso} is the isotropic atomic displacement parameter, GOF is the goodness of fit in a non-linear least squares algorithm.

(a) NbGeSb as grown

Refinement	**Jana2006**	**GSAS**
z for Nb	0.24657(2)	0.246513(8)
z for Sb	0.61264(2)	0.612579(6)
B_{iso} for Nb	0.189(4)	0.1747(11)
B_{iso} for Ge	0.157(5)	0.2074(10)
B_{iso} for Sb	0.187(5)	0.2254(9)
GOF	1.16	1.847

(b) NbGeSb annealed at 400°C

Refinement	**Jana2006**	**GSAS**
z for Nb	0.24652(2)	0.246452(7)
z for Sb	0.61273(1)	0.612647(5)
B_{iso} for Nb	0.235(2)	0.2084(9)
B_{iso} for Ge	0.277(3)	0.2431(8)
B_{iso} for Sb	0.268(2)	0.2499(7)
GOF	1.17	1.449

were taken directly from the fits, realistic error bars based on single crystal XRD data are certainly larger). Table 5.1(a) shows the structural parameters obtained from refinements of complete data sets for as grown NbGeSb, and Table 5.1(b) shows the same information but for the annealed samples.

From the refinements summarised in Tables 5.1(a,b), for all the good quality crystalline pieces atomic disorder effects are minimal. If there are any vacancies, it is not more than $\sim$1% of vacancies on Sb site and even less on Ge site. If there is some inter-site atomic exchange, not more than $\sim$2% of Ge atoms may be replaced by Sb, if any. For all the good quality pieces there are hardly any peaks on the (hk0) plane with h+k=2n (n=integer) that could be attributed to disorder effects resulting in incomplete systematic extinctions due to the n-type glide plane perpendicular to the [001] direction. For the annealed sample measured overnight there are no peaks on the (hk0) plane with h+k=2n (n=integer) that could be attributed to disorder effects resulting in incomplete systematic extinctions due to the n-type glide plane perpendicular to the [001] direction (as shown in Figure 5.8(C)), whereas for other high quality crystalline pieces only few extremely slight peaks were seen. The occupancies of all the lattice sites are very close to 100% for the best quality crystalline pieces, in agreement with the stoichiometry 1:1:1.

The lattice parameters for as grown NbSiSb from an overnight scan at T = 100 K are $a = 3.634\,19(2)$ Å and $c = 8.168\,47(6)$ Å (as with NbGeSb realistic error bars based on single crystal XRD data are most likely larger). The structural parameters obtained from refinements of complete data sets for as grown NbSiSb are detailed in Table 5.2. From these refinements, for the best quality crystalline pieces measured, if there are any vacancies then it is no more than $\sim$1% of vacancies on the Si site and not more than $\sim$0.5% of vacancies on the Sb site. Only very slight peaks due to atomic disorder are visible causing incomplete suppression of some of the (hk0) reflections with h+k=2n, where n=integer (systematic extinctions due to the n-type glide plane perpendicular to the [001] crystallographic direction - see Figure 5.10(c): blue circles). For crystalline pieces of slightly poorer quality, refinements revealed significant concentrations of vacancies on both Si and Sb sites ($\sim$2% on

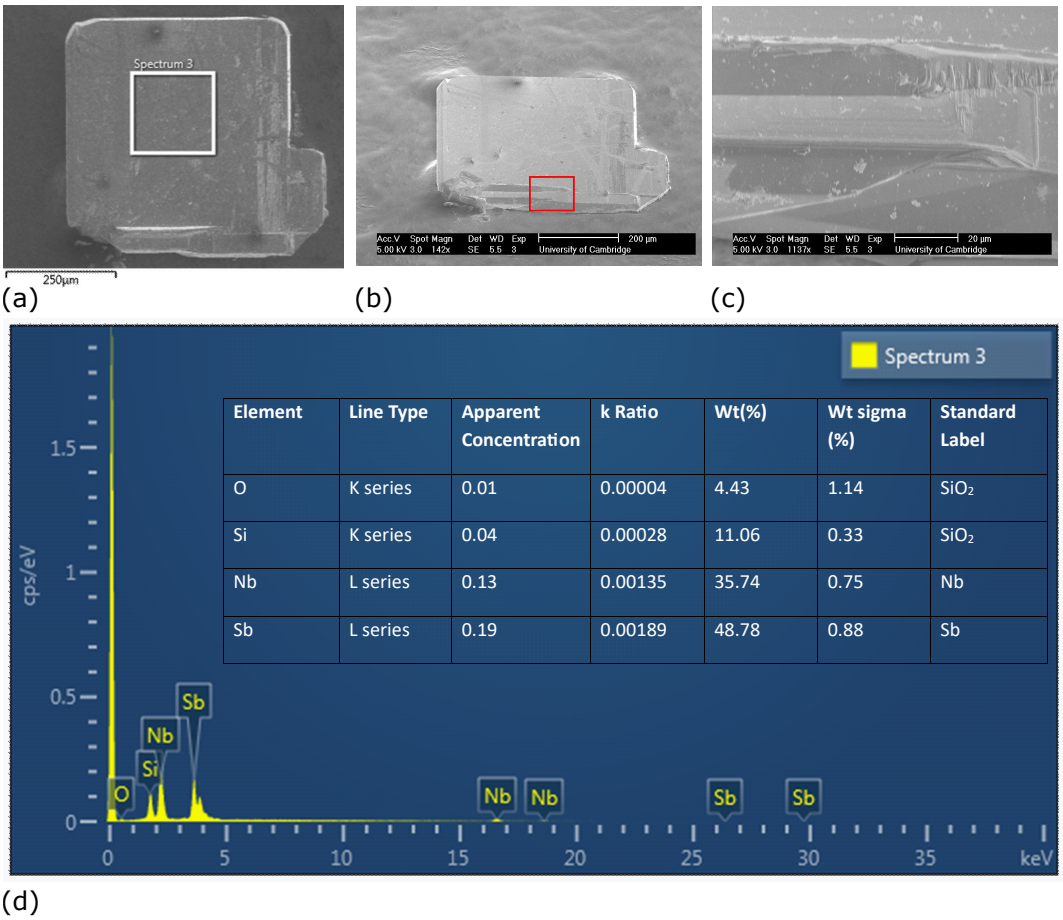

Fig. 5.11 **(a)** SEM image of an as grown NbSiSb sample in the ab-plane, the square marks the region where the EDX analysis in (d) was performed. **(b)** SEM image of the same plate-like sample at higher resolution and at an angle of 45°. **(c)** Zoomed in region (red square) showing the steps at the edge of the platelet. **(d)** EDX elemental analysis confirming the composition of NbSiSb, with some small amount of oxygen impurities.

the Si site and ∼3% on the Sb site). Their presence is also reflected in significant intensities of many (hk0) peaks with h+k=2n (n=integer) that should have been suppressed by the presence of the n-type glide plane perpendicular to the [001] crystallographic direction if there was no atomic disorder (see Figure 5.10(e) - blue circles). For the best quality single-crystalline pieces the occupancies of all the lattice sites are very close to 100%, implying a stoichiometry of 1:1:1.

Table 5.2 Structural parameters from refinements of a complete data set collected at T = 100 K on as grown single crystals of NbSiSb. Two different codes (GSAS and Jana2006) gave consistent results (after excluding not matching peaks), well converged and with low statistical factors. B_{iso} is the isotropic atomic displacement parameter, GOF is the goodness of fit in a non-linear least squares algorithm.

Refinement	**Jana2006**	**GSAS**
z for Nb	0.24063(2)	0.24059(1)
z for Sb	0.61523(1)	0.61527(1)
B_{iso} for Nb	0.209(3)	0.2084(12)
B_{iso} for Ge	0.320(7)	0.3232(25)
B_{iso} for Sb	0.228(3)	0.2321(10)
GOF	1.05	1.725

The single-crystal orientation was checked by a standard Laue diffraction technique (Figures 5.8(a,b) and 5.10(a,b)). In the calculated Laue diffraction pattern, the most intense points are the low Miller indices which were sufficient to determine the c-axis orientation.

5.2.3 Transport measurements

A summary of all of the samples of NbGeSb and NbSiSb measured in this chapter is given in Table's 5.3 and 5.4 respectively. It is important that contact resistances are kept low when using the low temperature transformers on the dilution fridge (see Section 3.1). A large effort was put into the contacting of samples which was done using a spot welder and 25 μm Au wires. Immediately before contacting, the surfaces of samples were cleaned via a cycle of acetone, followed by ethanol, and finally distilled water. Samples of both NbGeSb and NbSiSb are quite delicate and prone to breaking when too high a current is applied through the spot welder. A method of spot welding was developed first on poorer quality (quite visibly twinned) samples first to establish the correct voltage to apply using the spot welder. Starting with a low voltage (4.5 V), then without moving the spot welder, moving up in small increments to around 5.8 V worked well and resulted in a strong (low resistance) bond. Once a contact had been made using the spot welder, several 'welds' were applied to the same contact followed by DuPont 4929 Ag epoxy which cures at room temperature. Both of these additional measures help to increase the mechanical stability of the contact.

Low field characterisation measurements were performed on a QD PPMS equipped with a ^{3}He stage and a 9 Tesla magnet, several samples were contacted by spot welding 25 μm Au wires either onto as

Table 5.3 Summary of measurements performed on NbGeSb single crystal samples. QO = Quantum Oscillations, γ = exponent of temperature dependence of resistivity at low temperature (see Equation 2.3). ρ = resistivity, C = heat capacity, EDX = energy-dispersive x-ray, SC = single crystal, ASN = Agilent SuperNova (XRD), SEM = scanning electron microscopy.

Sample	**System**	**Measurements**	**RRR**	**Annealed?**	**Comments**
1908-101 (platelet)	PPMS	ρ (T,B)	10.1	800 °C.	$\gamma \sim 3.5$
1908-102 (platelet)	PPMS	ρ (T,B)	9.3	800 °C	$\gamma \sim 3.5$
1908-103 (needle)	PPMS	C (T)	-	As grown	mass = (0.6 $\pm$ 0.1) mg
1908-104 (platelet)	PPMS	ρ (T,B)	9.0	As grown	$\gamma \sim 3.5$
1908-105 (needle)	PPMS	ρ (T,B)	10.7	As grown	$\gamma \sim 3.5$
1908-106 (needle)	PPMS	C (T)	-	As grown	mass = (0.6 $\pm$ 0.1) mg
1908-107 (needle)	PPMS	C (T)	-	As grown	mass = (0.8 $\pm$ 0.1) mg
1908-108 (needle)	PPMS	C (T)	-	As grown	mass = (0.9 $\pm$ 0.1) mg
1908-109 (needle)	PPMS	C (T)	-	As grown	mass = (0.7 $\pm$ 0.1) mg
1908-112 (platelet)	PPMS	ρ (T,B)	8.9	800°C.	$\gamma \sim 3.5$
1908-113 (platelet)	ASN	SC XRD	-	As grown	
1908-114 (needle)	ASN	SC XRD	-	As grown	
1908-115 (needle)	PPMS	ρ (T,B)	9.0	Detwinned	$\gamma \sim 3.5$
1908-116-119 (platelet)	SEM	EDX	-	400°C (2 weeks)	
1908-120 (platelet)	Laue Camera	Laue Diffraction	-	As grown	
1908-121 (needle)	PPMS	ρ (T,B)	7.75	400°C (2 weeks)	$\gamma \sim 3.5$
1908-122 (platelet)	Dilution Fridge	ρ (T,B)	12.2	400°C (2 weeks)	$\gamma \sim 3$, QO observed
1908-123 (needle)	ASN	SC XRD	-	As grown	
1908-124 (platelet)	ASN	SC XRD	-	As grown	
1908-125 (needle)	ASN	SC XRD	-	As grown	
1908-126 (platelet)	ASN	SC XRD	-	As grown	
1908-129 (platelet)	PPMS	ρ (T,B)	10.02	400°C (2 weeks)	$\gamma \sim 3.5$
1908-131 (platelet)	PPMS	ρ (T,B) Hall	7.2	400°C (2 weeks)	$\gamma \sim 3.5$

Table 5.4 Summary of measurements performed on NbSiSb single crystal samples. QO = Quantum Oscillations, γ = exponent of temperature dependence of resistivity at low temperature (see Equation 2.3). ρ = resistivity, C = heat capacity, EDX = energy-dispersive x-ray, SC = single crystal, ASN = Agilent SuperNova (XRD), SEM = scanning electron microscopy.

Sample	**System**	**Measurements**	**Annealed?**	**Comments**
1908-201 (platelet)	PPMS and Dilution Fridge	ρ (*T,B*)	As grown	$\gamma \sim 2.5$, RRR = 218, QO observed
1908-202 (platelet)	PPMS	ρ (*T,B*)	800 °C	RRR = 198
1908-207 (platelet)	PPMS	ρ (*T,B*) Hall	400 °C	RRR = 216
1908-208 - 218 (platelet)	PPMS	C (T)	400 °C	mass = (1.2 $\pm$ 0.2) mg
1908-219 (platelet)	ASN	SC XRD	As grown	
1908-220 (platelet)	ASN	SC XRD	As grown	
1908-221 (needle)	ASN	SC XRD	As grown	
1908-222 (needle)	ASN	SC XRD	As grown	
1908-223 (needle)	ASN	SC XRD	As grown	
1908-224 (platelet)	ASN	SC XRD	As grown	
1908-227 (platelet)	Laue Camera	Laue Diffraction	As grown	

grown samples or samples that had Au pads evaporated onto them. Figure 5.12a shows the zero field temperature-dependent resistivity for a typical sample of NbGeSb. The RRR's of all 15 samples of as grown NbGeSb measured from this growth are in the range 8-13. Samples annealed in a partial pressure (200 mbar) argon at 400 °C for two weeks do not seem to have improved dramatically in quality when compared to the as grown samples, when RRR is used as the only measure. The room temperature resistivity of NbGeSb is around 100 $\mu\Omega$cm falling to around 10 $\mu\Omega$cm at 500 mK. Figure 5.12b shows the zero field temperature-dependent resistivity for a typical sample of NbSiSb, the RRR of several as grown NbSiSb measured from this growth fall in the range 210-250. NbSiSb has an extremely low resistivity at room temperature for a semimetal (sample 1908-201 is 13.9 $\mu\Omega$cm at T = 300 K, falling to 56.6 nΩcm at T = 500 mK). At room temperature the resistivity of NbSiSb is comparable to that of ZrSiS (15.5 $\mu\Omega$cm [139] and both are at least an order of magnitude smaller than that of other high-mobility Dirac and Weyl semimetals such as Cd_3As_2, LaBi and WTe_2 [153–155]. At low temperatures, only Cd_3As_2 has a lower resistivity (21 nΩcm) and NbSiSb is comparable to high-purity Bi [156] and $PdCoO_2$ [157]. NbGeSb shows metallic character in which ρ decreases monotonically with temperature down to below 100 K.

The low temperature behaviour of the resistivity can be compared to the expected metallic behaviour outlined in Section 2.1 where a T^2 dependence of the resistivity with temperature is predicted, equation 2.3 is repeated below.

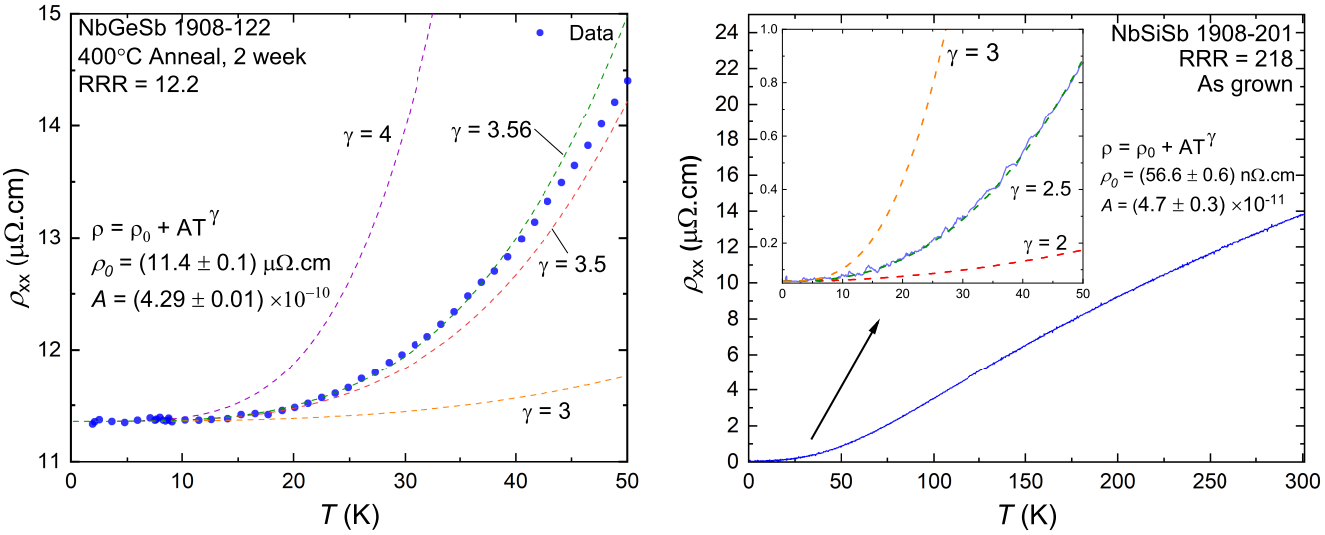

(a) NbGeSb

(b) NbSiSb

Fig. 5.12 Resistivity as a function of temperature of (a) NbGeSb annealed at 400°C for two weeks (1908-122), fitting of the low temperature region shows non-Fermi liquid behaviour. (b) As grown sample of NbSiSb: 1908-201, inset shows non-Fermi liquid behaviour at low temperatures. Both samples measured on a QD PPMS ^{3}He option from 300 - 0.4 K at a sweep rate of 0.5 K/min.

$$\rho(T) = \rho_0 + AT^{\gamma} \tag{5.4}$$

A is referred to as the A-coefficient and γ is the exponent of the temperature dependence of the resistivity (where $\gamma = 2$ for Fermi liquids). Figure 5.12a shows that for NbGeSb sample 1908-122 at low temperatures in the range 2 - 43 K a different T- dependence is shown, where the resistivity follows closer to a $T^{7/2}$ dependence ($\gamma = 3.56$) with a residual resistivity of $\rho_0 = (11.4 \pm 0.1)$ $\mu\Omega$.cm and an A-coefficient of $A = 4.29 \times 10^{-10}$ ΩcmK$^{-\gamma}$. Figure 5.12b shows that similarly for NbSiSb sample 1908-201 at low temperature in the range 2 - 51 K a different T- dependence is shown, where the resistivity follows closer to a $T^{5/2}$- dependence ($\gamma = 2.5$) with a residual resistivity of $\rho_0 = (56.6 \pm 0.6)$ nΩ.cm and an A-coefficient of $A = 4.7 \times 10^{-11}$ ΩcmK$^{-\gamma}$. This deviation from the expected Fermi liquid pure electronic correlation-dominated scattering mechanism ($\gamma = 2$) has been seen in other TSM candidate materials such as $TaSb_2$ ($\gamma = 2.56$ [158]) and ZrSiS ($\gamma = 3$ [141]) and in unconventional semimetals LaSb ($\gamma = 4$ [159]) and LaBi ($\gamma = 3$ [160]) and is attributed to interband electron-phonon scattering. The resistivity $\rho(T)$ is linear in the high temperature region above 85 K in NbGeSb, in NbSiSb however, above $\sim$150 K there appears to be a deviation from T-linear dependence of the resistivity.

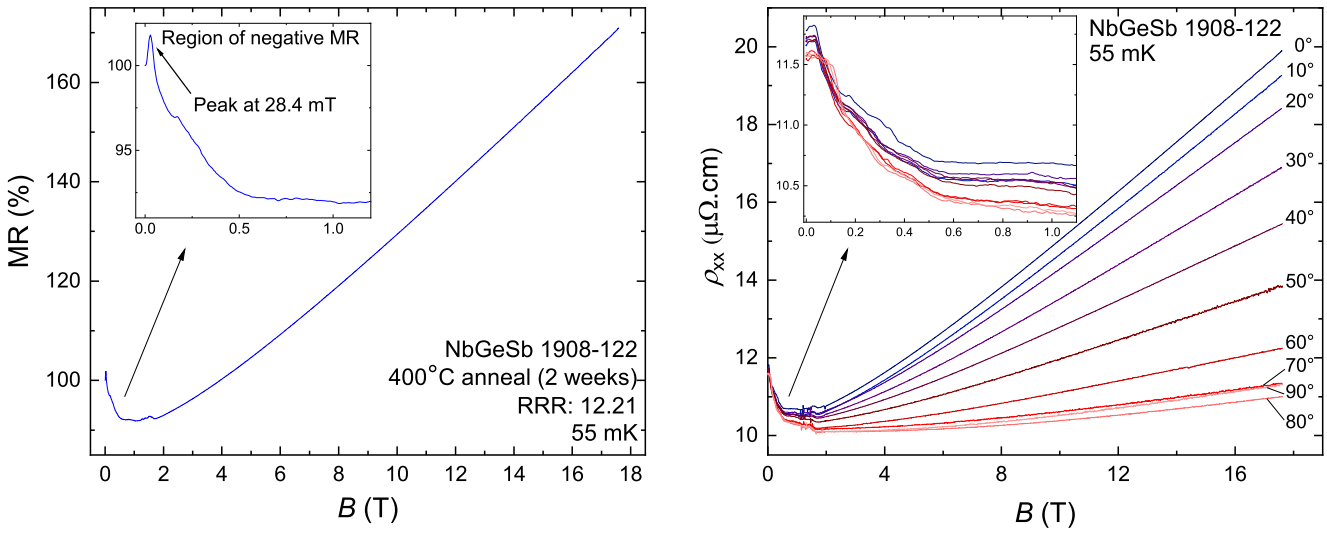

(a) NbGeSb

(b) NbGeSb

Fig. 5.13 Resistivity ρ(B) of annealed sample of NbGeSb (1908-122). Sample measured at 55 mK from 0 - 18 T at 0.23 T/min. **(a)** ρ_0 at 18 T is $\sim$ 170% of that at 0 T. Inset: low field region where negative MR is seen. **(b)** Applied magnetic field angle from H$\|$c to H$\|$a. The change in resistivity, $\Delta\rho = \rho/\rho_{(B=0)}$, reaches a minimum around $\phi = 80°$ from H$\|$c. Inset: negative MR region at low field.

At temperatures below 350 mK, the application of a magnetic field to NbGeSb (1908-122) results in a small (1.8% increase relative to the zero field value) but sharp increase in resistivity at very low fields (below 30 mT) which peaks at 28.4 mT. This is then followed by a slower decrease to around 1 T where the magnetoresistance (MR) dips to 92% of its zero field value. A second upturn in resistivity is then observed which does not saturate up to the highest applied fields (18 T) where it reaches 170% of its zero field MR. The inset of Figure 5.13a shows the field dependence of the unusual negative MR behaviour, and the main plot shows the non-saturating MR up to 18 T. The angular dependence of the MR is shown in Figure 5.13b.

The MR decreases from its maximum at H$\|$c, to a minimum at an angle of ($70° \leq \phi \leq 80°$) where H$\|$c corresponds to $\phi = 0°$. The inset shows the angular dependence of the negative MR region in which the overall trend remains but the initial rise in MR to a peak is suppressed at an applied magnetic field angle above ($50° \leq \phi \leq 60°$). There is also a reduction in the lowest value of ρ_{xx} which indicates that there are at least two competing mechanisms, a low field negative MR which is then overtaken by a positive contribution to the MR at fields above around 1 T (possibly due to magnetic impurities which dominate above 1T). The origin of the sharp initial peak was initially thought to be due to a field offset or a remnant field. This was confirmed by considering the effective-zero field point using the three TDO signals and the KM1 RuO_2 thermometer which all showed a peak

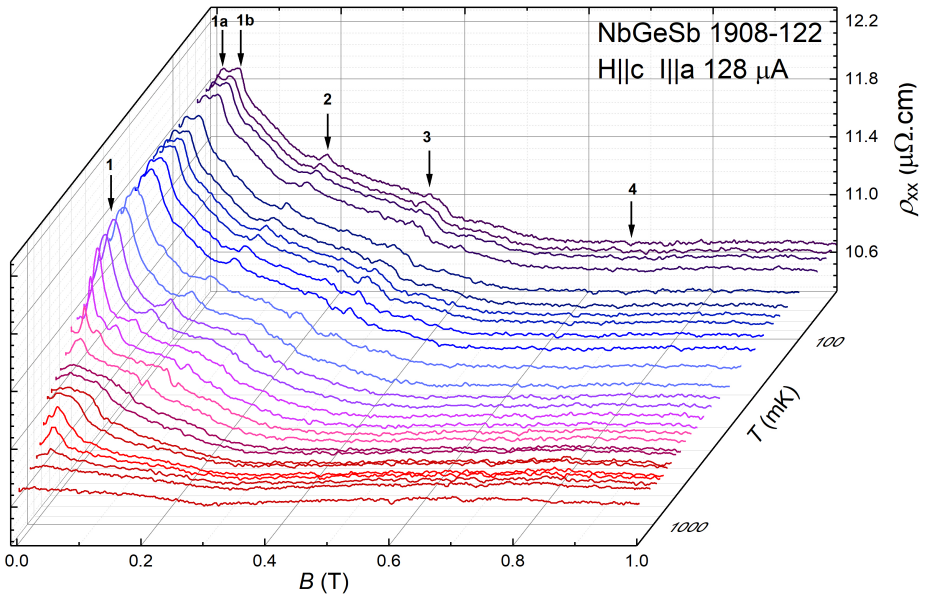

Fig. 5.14 (a) Resistivity $\rho(B)$ of NbGeSb 1908-122 at temperatures from 55 to 1050 mK. Sample measured in field from 0 - 1.2 T at a sweep rate of 0.046 T/min. Several features appear in the waterfall plot as a function of field and temperature and have been labelled from n = 1:4.

(KM1) or dip (TDO) symmetric about (26.0 $\pm$ 0.5) mT. The region of noise between 1.5 - 1.8 T is an intrinsic property of the Oxford Instruments superconducting magnet used and shows up in all measured samples, great care was taken to check that the negative MR signal seen below 1 T is real and comes from the NbGeSb sample.

A higher resolution data set of the negative MR region was obtained by sweeping in the magnetic field at a much slower rate of 0.046 T/min with ϕ = 0° (H||c). Figure 5.14 shows a waterfall plot of the negative MR signal, the features labelled n=1:4 were initially thought to be noise on a negatively sloping background, but each feature appeared over many sweeps. The temperature dependence of the negative MR region was investigated and these features can be tracked as a function of temperature. The features labelled n = 1, 1b, 3 and 4 all show a linear (almost constant) temperature dependence, while n = 1a and 2 have a more complicated temperature dependence. In order to check whether these features are down to some unusual contacting issue, the sample excitation was changed (from 3.2 μA to 320 μA) and all features could still be seen. At the higher excitation current (above 200 μA), however, the sample was being significantly heated (as seen in a nearby RuO_2 thermometer labelled KM1) and so some of the features were smeared out.

There are many topological semimetals such as $NbSb_2$, ZrSiS and $TaAs_2$ that demonstrate anisotropic MR with respect to the applied magnetic field direction, this is due to the anisotropy in their Fermi

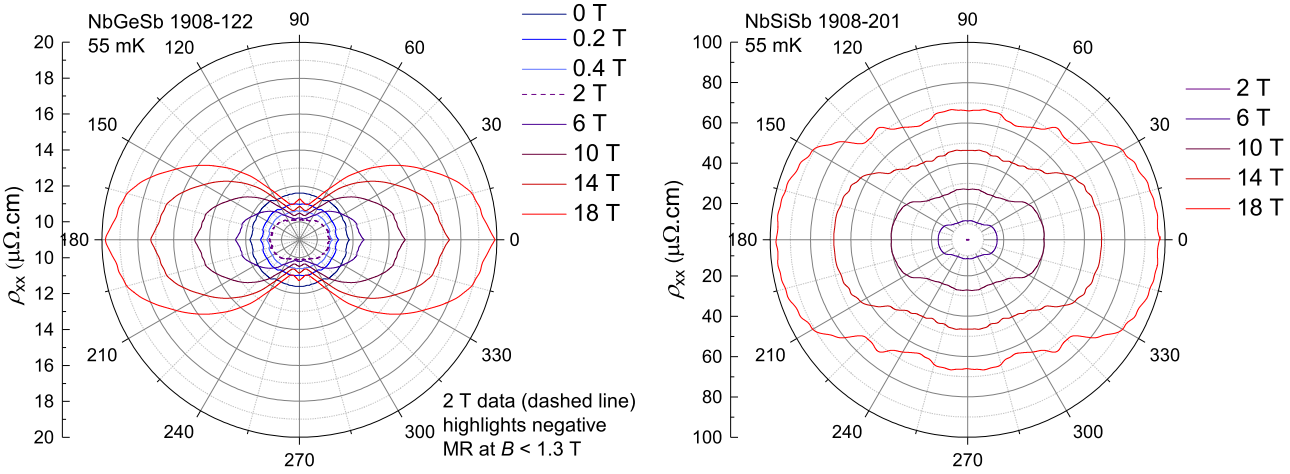

(a) NbGeSb

(b) NbSiSb

Fig. 5.15 Polar plot of AMR at 55 mK and in magnetic fields between 0 and 18 T of **(a)** NbGeSb sample 1908-122: the dashed line at 2 T highlights the negative MR at low fields. The AMR is relatively isotropic at low fields in the negative MR region and becomes quite 2D at higher fields with the largest magnitude of MR at H$\|$c, the minimum occurs at an angle of $\phi = 80°$. **(b)** NbSiSb sample 1908-201, the AMR is somewhat 2D but shows plateaus between $\phi = 30$ ° - 90°. The current is applied along the *a*-axis (I$\|$a).

surface [139, 141, 161–165]. Figure 5.15a shows a polar plot of the AMR of NbGeSb in which the sample was rotated from H$\|$c to H$\|$a with the current along the *a*- axis in the *ab*- plane. The resultant curve possesses a twofold rotational symmetry, indicating a considerable anisotropy in the magnetotransport properties in NbGeSb. The AMR is highly 2D and is maximised when the field is aligned parallel to the *c*- axis where at 18 T is ∼170% of that at 0 T. The minimum in AMR occurs at $\phi = 80°$ where the MR is only 95.1 % of the zero field value at 18 T, this is due to the negative MR region only varying slightly as a function of magnetic field angle. Above $\phi = 80°$ the positive MR region starts to increase again as it approaches H$\|$a. Figure 5.15b shows a polar plot of the AMR of NbSiSb in which the sample was rotated from H$\|$c to H$\|$a with the current along the *a*- axis in the *ab*- plane. The resultant curve possesses a twofold rotational symmetry, and like NbGeSb this indicates some anisotropy in the magnetotransport properties, however, this is not as prevalent in NbSiSb. The AMR is somewhat 2D but shows plateaus and steps in the MR between $\phi = 30°$ - 90°. The AMR is a maximimum when the field is aligned parallel to the *c*- axis (as in NbGeSb). At 18 T and 55 mK the AMR is 1.46×10^5% of that at 0 T. The minimum in AMR occurs at 65° on the second of three apparent plateaus where the MR is only 0.85×10^5% of the zero field value at 18 T and 55 mK. Several detectable kinks (NbGeSb) and steps/plateaus (NbSiSb) have been observed at certain angles (NbGeSb: between $\phi = 0°$ and 15°, NbSiSb: between $\phi = 30$ ° - 90°), which may be due to a possible

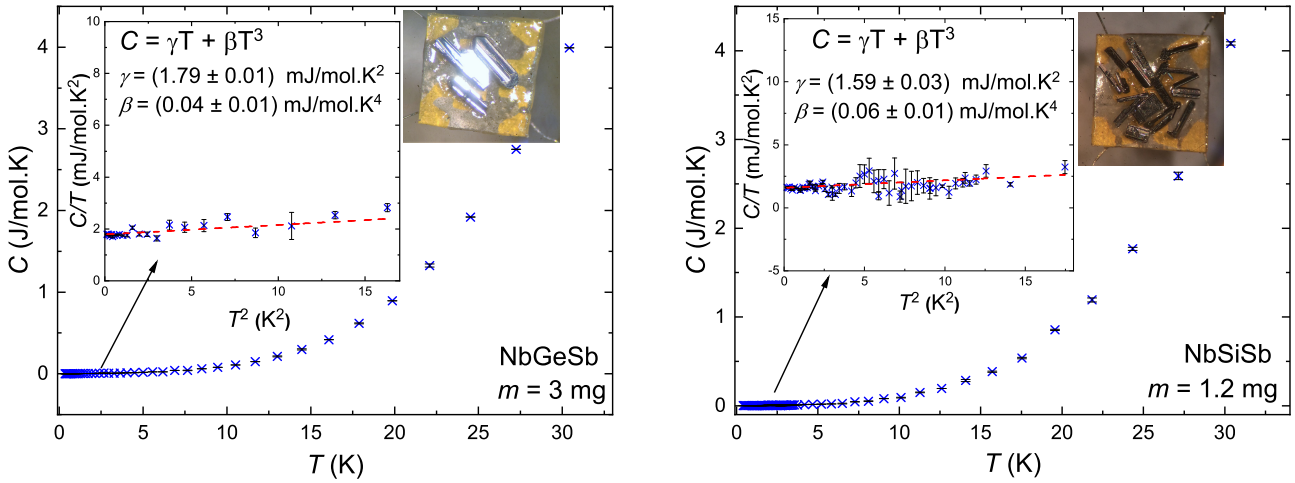

(a) NbGeSb

(b) NbSiSb

Fig. 5.16 $C(T)$ of **(a)** NbGeSb (1908-106 : 109) and **(b)** NbSiSb: (1908-203 : 218). A fit of the low temperature region gives the Sommerfeld coefficients. Measured on a QD PPMS ^{3}He option from 300 - 0.4 K. Both sets of samples were annealed at 400°C for two weeks.

higher-order texturing. This behaviour has also been reported in several isostructural compounds such as ZrSiS [139] and LaSbTe [164].

5.2.4 Heat capacity

Heat capacity (C) measurements have been performed on both materials on a calibrated PPMS ^{3}He heat capacity puck from 30 K to 0.4 K. Figure 5.16a shows the heat capacity of 3 mg of annealed NbGeSb, the inset of of Figure 5.16a shows C/T vs T^2) which gives a slope of β and a y-intercept of the Sommerfeld coefficient via $C(T) = \gamma T + \beta T^3$. The fit gives $\gamma = (1.787 \pm 0.006)$ mJmol^{-1}K^{-2} and a phonon component of $\beta = (0.04 \pm 0.01)$ mJmol^{-1}K^{-4}. Figure 5.16b shows the heat capacity of 1.2 mg of as grown NbSiSb from 30 K to 0.4 K. As the crystals are very small, many samples were needed to increase the signal/noise ratio by increasing the mass. Fitting of the low temperature region (inset of Figure 5.16b) gives $\gamma = (1.59 \pm 0.03)$ mJmol^{-1}K^{-2} and a phonon component of $\beta = (0.06 \pm 0.01)$ mJmol^{-1}K^{-4}.

5.2.5 Quantum oscillation rotation study

The transverse magnetoresistance (the change in resistance as a function of magnetic field applied perpendicular to the current direction) has been measured on a dilution refrigerator from 55 mK to 9 K in NbGeSb (1908-122) and NbSiSb (1908-201). The samples were mounted on a rotation stage

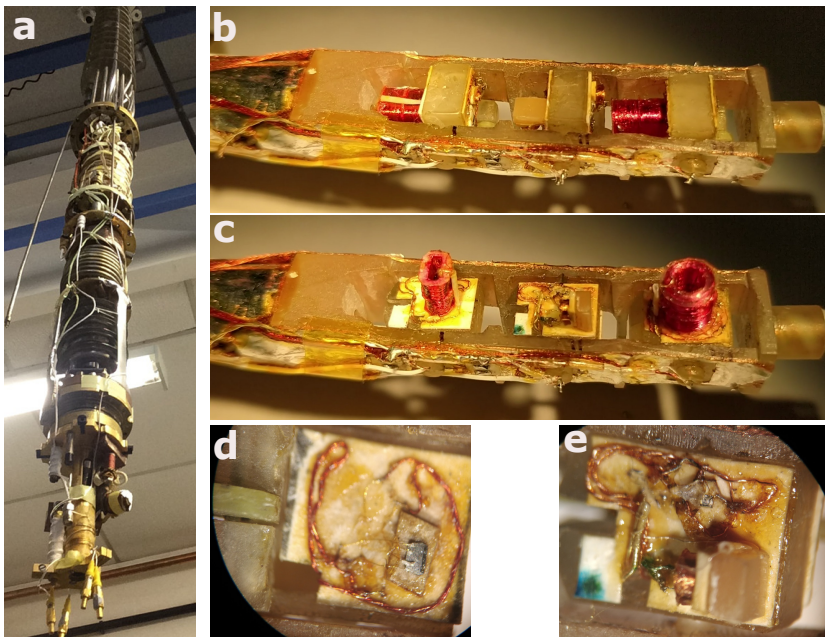

Fig. 5.17 **(a)** The dilution fridge insert used for the quantum oscillation study on Nb*X*Sb (rotation tail not attached). **(b)** A close up of the rotation tail set at $\phi = 0°$ (H||c, I||a for NbGeSb and I||b for NbSiSb). **(c)** A close up of the rotation tail set at $\phi = 90°$ (H||a, I||a for NbGeSb and I||b for NbSiSb). **(d)** A microscope image of platform six with the NbSiSb sample mounted. **(e)** A microscope image of platform two with the NbGeSb sample mounted.

which is attached to the mixing chamber via a quartz tube (to reduce eddy current heating during field sweeps) which allows the rotation stage to sit at the field centre. Rotation of samples through an angle of 90° allowed the angular response of the magnetoresistance to be mapped out. Thermal contact was made to the rotation stage via three high purity Ag wires (0.5 mm diameter) which attach to the mixing chamber at one end and break out into several bundles of mesh consisting of smaller 50 μm high purity Ag wires close to the rotation mechanism. Each bundle of fine Ag wire then attaches to each of the six rotation platforms (through a hole in the rotation axle) to allow thermal anchoring to the samples (while avoiding electrical contact). Further cooling of the samples is achieved by thorough thermal anchoring of the copper measurement wire loom which was custom made for this particular experiment and was well heat sunk at several points along the dilution fridge insert (along the Ag wires, at the mixing chamber and 1 K pot).

Figure 5.17 (a) shows the dilution fridge insert onto which the rotation tail was attached which is shown in (b) and (c) in H||c and H||a orientations respectively. Microscope images of the two samples, NbGeSb 1908-122 and NbSiSb 1908-201, are shown in (d) and (e) respectively, mounted on the tail. Lock-in amplifier detection was used to measure both samples simultaneously with NbGeSb being supplied 32 μA at a frequency of 118.46 Hz and NbSiSb supplied by 1.6 μA at a frequency of 161.02 Hz. These currents were used for measurements below 150 mK and were increased at

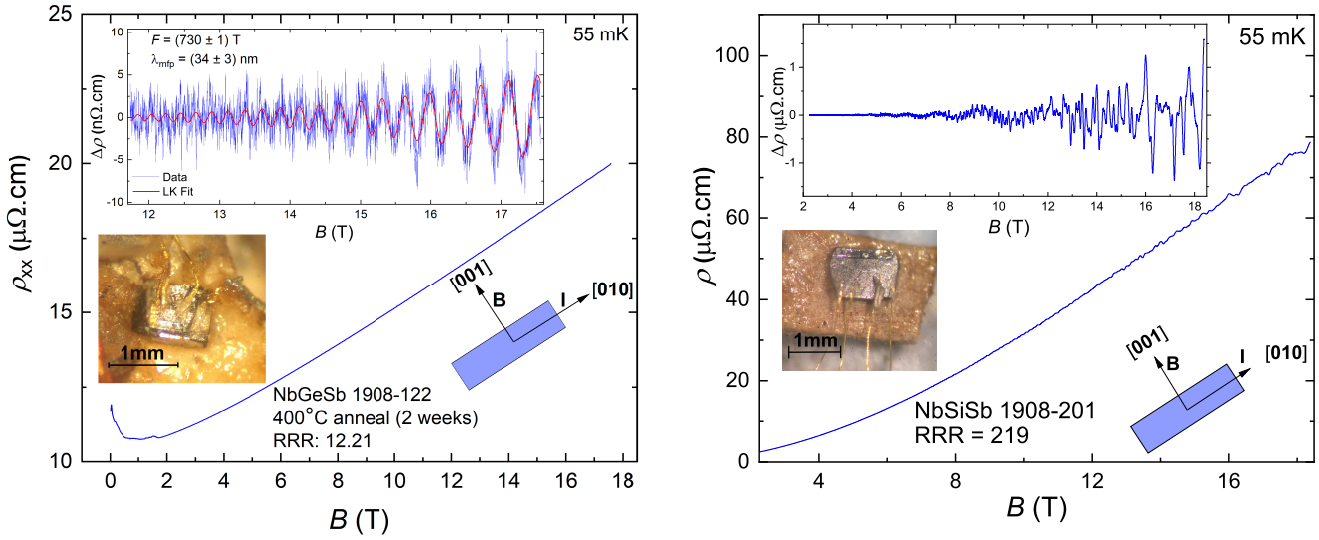

(a) NbGeSb (b) NbSiSb

Fig. 5.18 Resistivity as a function of applied magnetic field (H||c) of **(a)** NbGeSb sample 1908-122 and **(b)** NbSiSb sample 1908-201 measured at 55 mK. Inset's show the change in resistivity ($\Delta\rho$) after 3rd (a) and 5th (b) order polynomial background subtractions as a function of field from 11.8 - 17.8 T (a) and 2.2 - 18.4 T (b) in which quantum oscillations are visible. An LK fit (red) gives a frequency of (730 $\pm$ 1) T and a mean free path of (35 $\pm$ 3) nm for the NbGeSb sample.

temperatures above this, care was taken to ensure that no self heating of the samples occurred by monitoring nearby RuO_2 thermometers as well as other sample signals. Both samples were connected to CMR direct LTT-m low temperature transformers which sit at the 1 K pot on the insert, with turn ratios for each set at 1:1000, followed by room temperature amplification provided by EG&G 5004 ultra low noise preamplifier with gain set at $\times$100, the NbGeSb sample also had a Butterworth filter. The large winding ratio of the LTT was chosen in order to maximise signal to noise and was made possible by the relatively low contact resistances of the two samples (less than 400 mΩ for NbGeSb and better for NbSiSb). These settings and configuration were arrived at after several days of careful signal to noise optimisation on both samples and it was possible to achieve a noise level at the samples of $\sim$29 pV/$\sqrt{\text{Hz}}$ which is representative of the specification of the low temperature transformers used.

Figure 5.18a shows the resistivity of NbGeSb from 0 to 17.6 T at 55 mK, the magnetic field is applied parallel to the c-axis and the current along the a-axis. A large non-saturating MR is demonstrated (170% of zero field MR at 17.6 T). At low fields the MR shows a quadratic field dependence ($\propto B^2$) which becomes linear at higher fields where SdH oscillations start to emerge above $\sim$10 T. The inset shows the change in resistivity, $\Delta\rho(B)$, after a 3rd order polynomial background subtraction in order to extract the oscillatory component. To decide the appropriate polynomial order, we have subtracted higher as well as lower order polynomial background, however, no visible change has been noticed

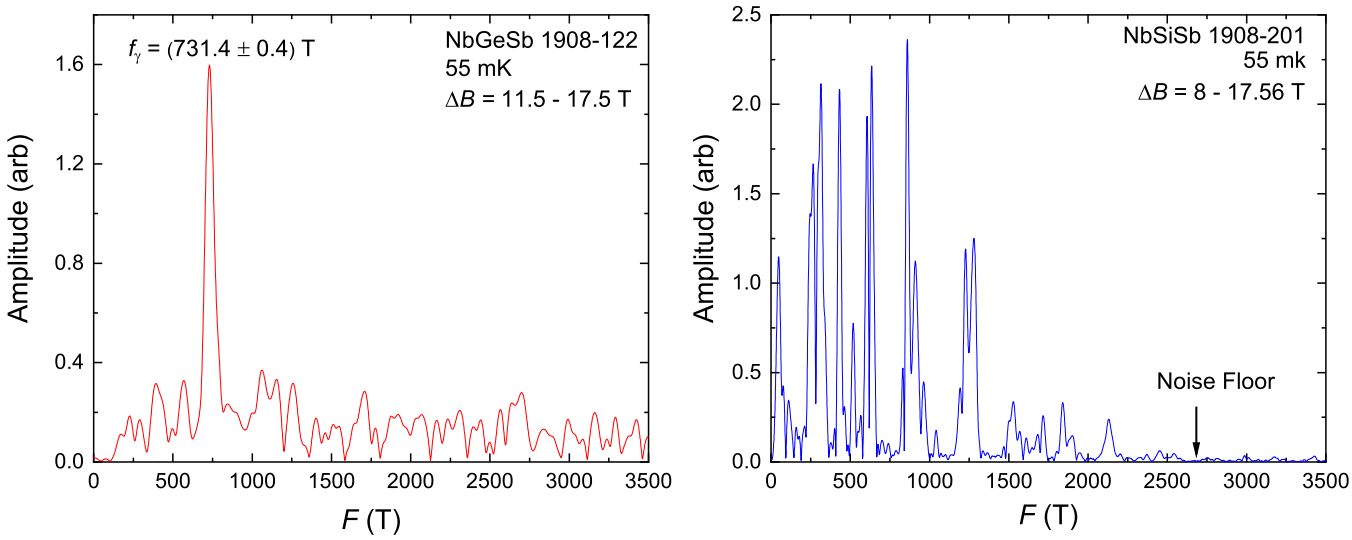

(a) NbGeSb

(b) NbSiSb

Fig. 5.19 FFT of the quantum oscillation signal seen in **(a)** NbGeSb sample 1908-122 in the field range 11.5-17.5 T, and **(b)** NbSiSb sample 1908-201, at 55 mK in the field range 8 - 17.5 T.

above 3rd order, which replicate the background most appropriately. An LK fit of the frequency visible in the fast Fourier transform (FFT) spectrum gives a frequency of F = (730 ± 1) T and a mean free path of λ = (35 ± 3) nm. Figure 5.18b shows the resistivity of NbSiSb from 0 to 17.6 T at 55 mK, the magnetic field is applied parallel to the c-axis and the current along the a-axis. A large non-saturating MR is demonstrated (1.46×10^5% of zero field MR at 17.6 T). At low fields the MR shows a quadratic field dependence ($\propto B^2$) which becomes linear at higher fields where SdH oscillations start to emerge as low as 2.5 T. The inset shows the change in resistivity, $\Delta\rho(B)$, after a 5th order polynomial background subtraction in order to extract the oscillatory component. Taking the FFT of the oscillatory component of the resistivity for NbGeSb gives the frequency spectrum shown in Figure 5.19a, a clear frequency at F = (731.4 ± 0.4) T is visible above the noise floor. The FFT for NbSiSb, shown in Figure 5.19b, shows a much richer array of frequencies, well distinguished from the noise floor. It is expected that many of these frequencies are harmonics of lower lying frequencies or are due to magnetic breakdown orbits which will be discussed later. The noise floor in the FFT spectrum in NbSiSb is significantly lower than in the FFT spectrum from the NbGeSb sample, indicating the higher quality of the NbSiSb sample.

The angular dependence of the oscillation frequencies were measured by rotating the samples over an angular range of 90° from H||c to H||a. The measurements were performed at a mixing chamber temperature of approximately T = 55 mK (unless otherwise stated). After each rotation it was necessary to allow ample time for the samples to reach equilibrium before starting field sweeps

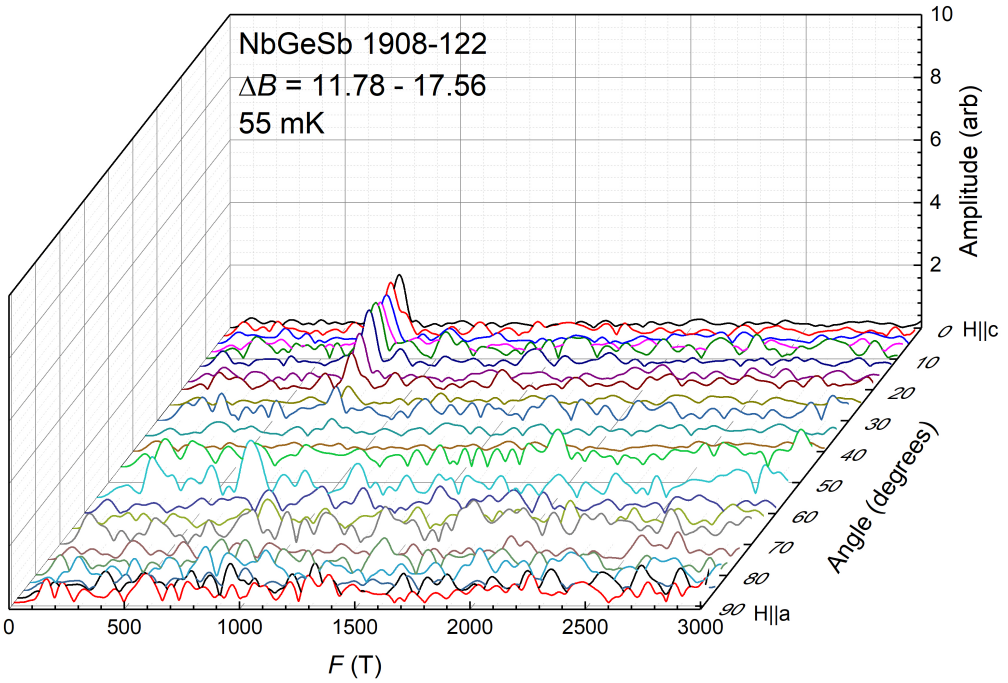

(a) NbGeSb

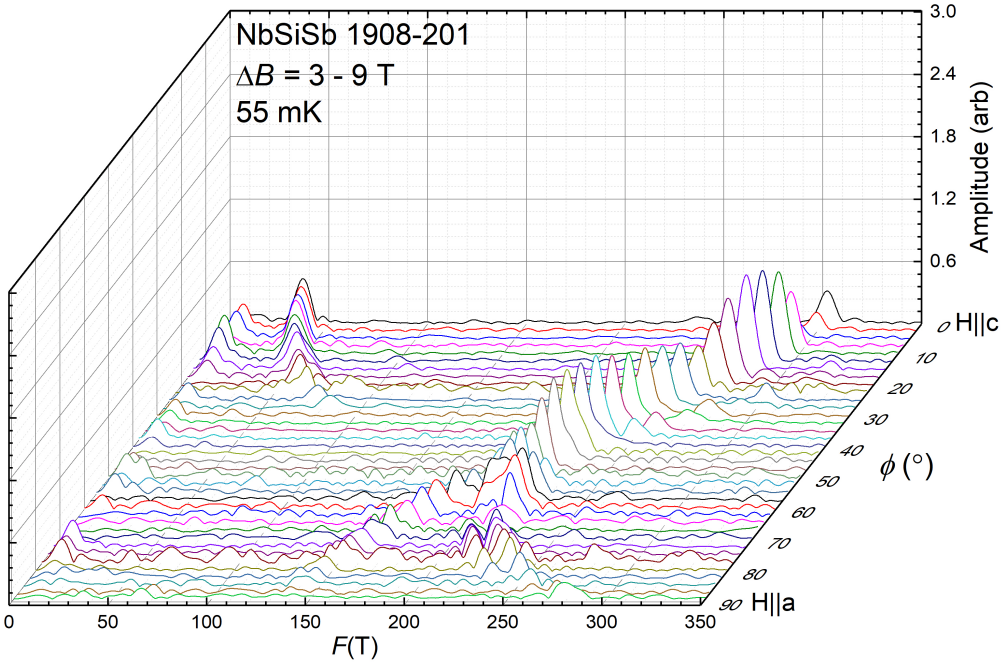

(b) NbSiSb

Fig. 5.20 FFT spectra at angles from H||c to H||a of the quantum oscillations at 55 mK seen in **(a)** NbGeSb sample 1908-122 over the magnetic field range 11.78 - 17.56 T and **(b)** NbSiSb sample 1908-201 over the magnetic field range 3 - 9 T.

as significant heating (to above 250 mK) occurs during rotations. A small amount of heating and cooling occurs during field sweeps, most likely due to some adiabatic demagnetisation heating and cooling effect from the measurement tail. Quantum oscillations were observed in NbGeSb in the field range ΔB = 10 - 18 T, while large oscillations in NbSiSb, visible without background removal, were observed down to fields as low as 2.5 T. As there were several samples being measured during this study, a compromise had to be made when deciding on sweep rates and ranges, as well as the resolution of the rotation study. The sweeps that were chosen are summarised in Table 5.5 (repeated

Table 5.5 Summary of magnetic field sweeps performed during this study.

Name	**ΔB (T)**	**Rate (T/min)**	**Optimised for**
Low Up	0-2	0.3	-
Fast Up	2 - 18	0.23	NbSiSb
Slow Down	18 - 12	0.06	NbGeSb and YFe_2Ge_2
Slow Up	12 - 18	0.06	NbGeSb and YFe_2Ge_2
Fast Down	18 - 2	0.23	NbSiSb
Low Down	2 - 0	0.3	-
Slow Low Up	0 - 1.2	0.023	NbGeSb
Slow Low Down	1.2 - 0	0.023	NbGeSb

from Section 4.2.2), the range is based on the field centre where the field strength is at a maximum. As there were several samples measured simultaneously on the rotation tail, the actual field experienced by each sample had to be corrected for using a previously measured magnetic field profile. The effective fields experienced by the two samples are: NbGeSb: 97.79% and NbSiSb: 97.26% of the maximal field strength at field centre (see Section 3.3.3 for more details of the field calibration). After an initial coarse study spanning 90° with data taken every 10 ° it was decided to take rotation data every 2.5°. This was a compromise between the rapidly changing nature of the NbSiSb FFT spectrum with rotation angle, and the time available to conduct the study (with each rotation angle taking a minimum of 15 hours to complete).

Figure 5.20a shows a waterfall plot displaying the angular dependence of the quantum oscillation frequencies observed in NbGeSb over the FFT frequency spectrum range 0 - 3 kT. The data are quite noisy but the frequency which starts at 730 T is visible in each FFT spectrum up to an angle of around ϕ = 40 °, and then returns at higher angles above ϕ = 55 °. A waterfall plot of for the NbSiSb sample is shown in Figure 5.20b over the FFT spectrum range 0 - 0.35 kT, the resolution is much better for this sample and several frequencies are observed. Over a larger FFT frequency window there are many additional frequencies observed and their evolution with magnetic field angle gets quite complicated. Figure 5.21a shows the FFT spectra over the frequency range 0 - 2.1 kT where several harmonics can be seen, over a larger range (1 - 6.5 kT) in Figure 5.21b harmonics can still be observed out as far as 6.5 kT.

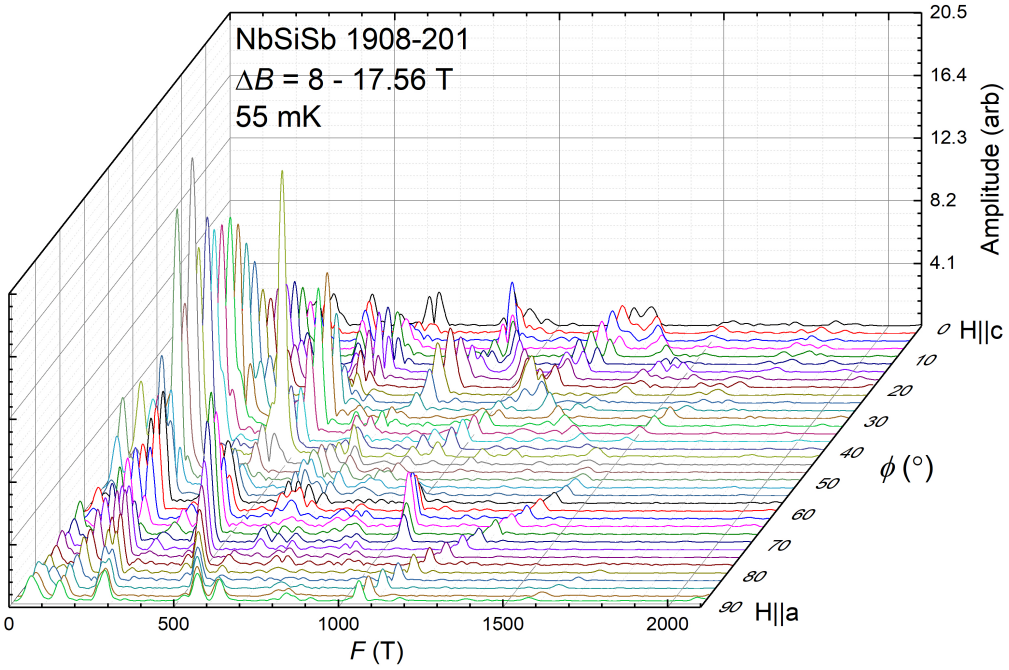

(a) Low frequency range

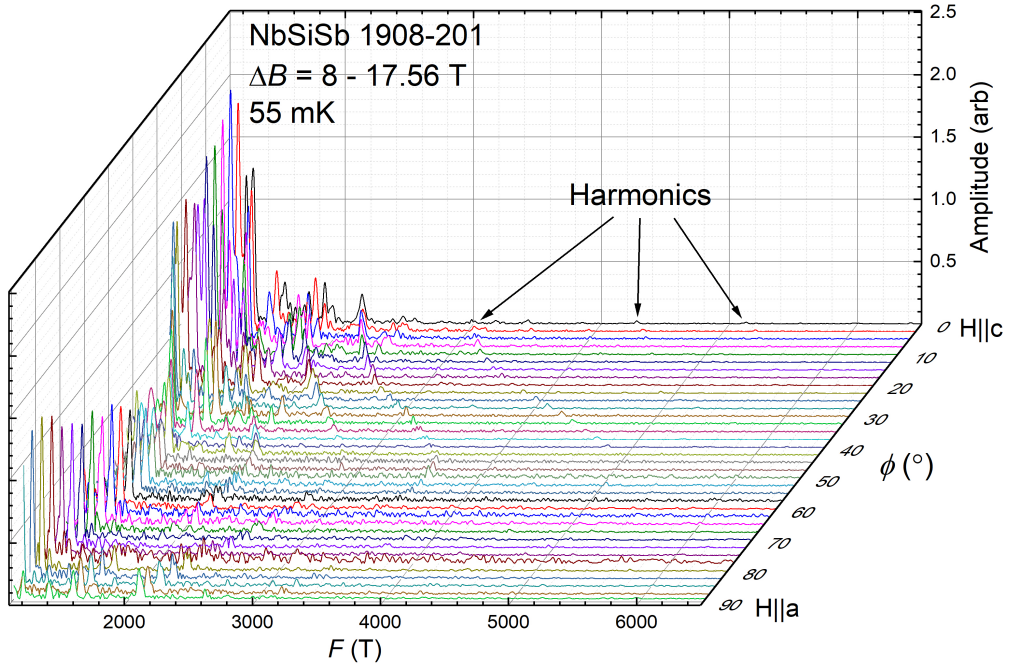

(b) High frequency range

Fig. 5.21 FFT spectra at angles from H||c to H||a of the quantum oscillations at 55 mK seen in NbSiSb sample 1908-201 over the magnetic field range 8 - 17.57 T. **(a)** Low frequency range **(b)** Zoomed in region of the high frequency range showing the many visible harmonics.

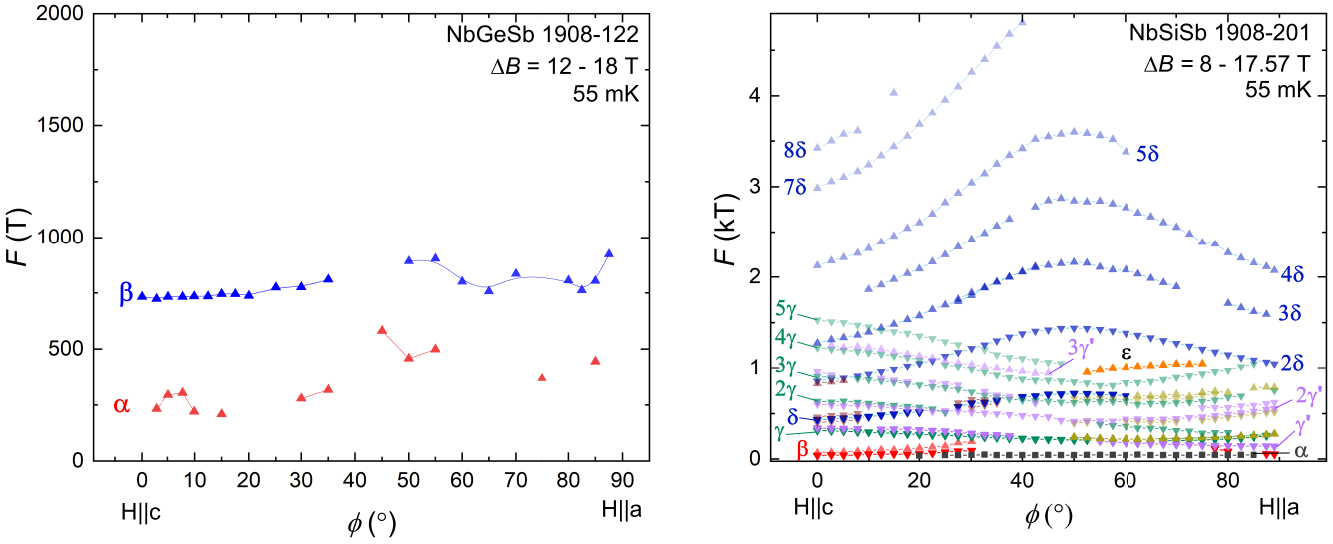

(a) NbGeSb (b) NbSiSb

Fig. 5.22 Rotation study of the FFT frequencies from **(a)** NbGeSb sample 1908-122 and **(b)** NbSiSb sample 1908-201, in the field range 11.5-17.5 T from H||c to H||a.

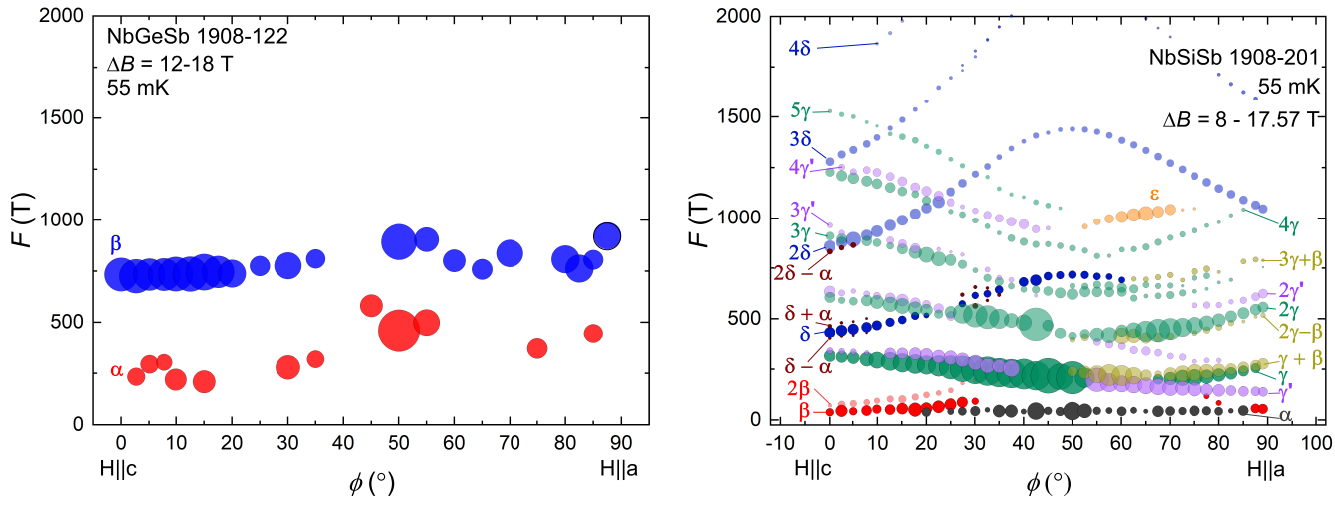

(a) NbGeSb (b) NbSiSb

Fig. 5.23 Rotation study of the FFT frequencies from **(a)** NbGeSb sample 1908-122 and **(b)** NbSiSb sample 1908-201, in the field range 11.5-17.5 T from H||c to H||a. The area of each data point now represents the normalised amplitude of the observed peaks in the FFT.

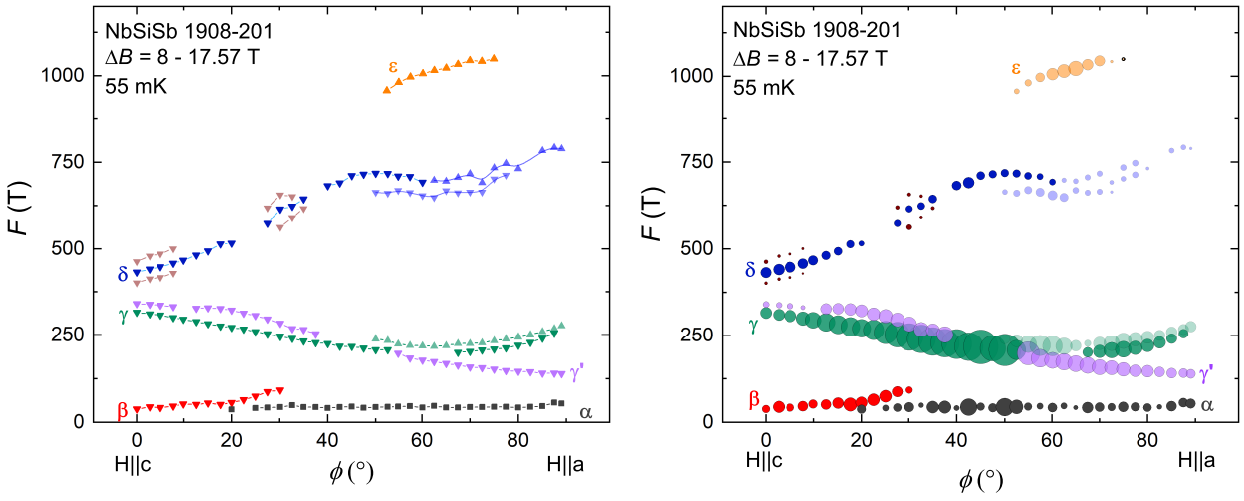

(a) NbSiSb

(b) NbSiSb

Fig. 5.24 Rotation study of the FFT frequencies from NbSiSb sample 1908-201, in the field range 11.5-17.5 T from H||c to H||a. Focussing on the fundamental frequencies.

An arbitrary naming scheme has been introduced to help keep track of the observed frequencies for both materials, this will prove useful when discussing DFT calculations in section 5.3.1 - see Tables 5.6 and 5.7 for details. The angular dependence of the observed frequencies in NbGeSb are shown in Figure 5.22a. Some lower frequency oscillations (at $\alpha = 250$ T) start to become visible as the field is rotated away from $\phi = 0°$. The clearest frequency, β at around 730 T is fairly constant as the field is rotated from H||c to H||a. All peaks that appear in the FFT spectra have been fitted using a standard Gaussian fit, and where there are two or more closely located peaks (as is the case with NbSiSb), the second derivative of the FFT spectrum was used to locate 'hidden' peaks before a multiple Gaussian fit was performed, for more details on this fitting procedure see Appendix B.1.1.

The relative amplitudes of the frequencies in the FFT spectra are shown in the bubble plot of Figure 5.23a. Figure 5.22b shows the angular dependence of the observed frequencies in NbSiSb, several frequencies can be identified (at $\phi = 0°$, field range 8 - 17.5 T): $\beta = 38$ T, $\gamma = 315$ T and $\delta = 431$ T, and at a low field range (3 - 9 T) an additional frequency $\alpha = 12$ T can be identified. Several harmonics (possibly as much as the 8^{th} for δ) of these frequencies can also be seen in the high field region and are labelled in the figure. There are many splitting and closely spaced frequencies which are most likely due to magnetic breakdown orbits, Zeeman splitting and possibly from the magnetic interaction effect. Figure 5.24 shows the same spectra but with all off the harmonics removed for clarity of the fundamental frequencies. A frequency labelled ε appears between rotation angles of $52.5° \leq \phi \leq 75°$ and does not appear to be related to the other fundamental frequencies identified so far. It is curious that the harmonics of δ can be identified out to as much as the 14^{th} harmonic but

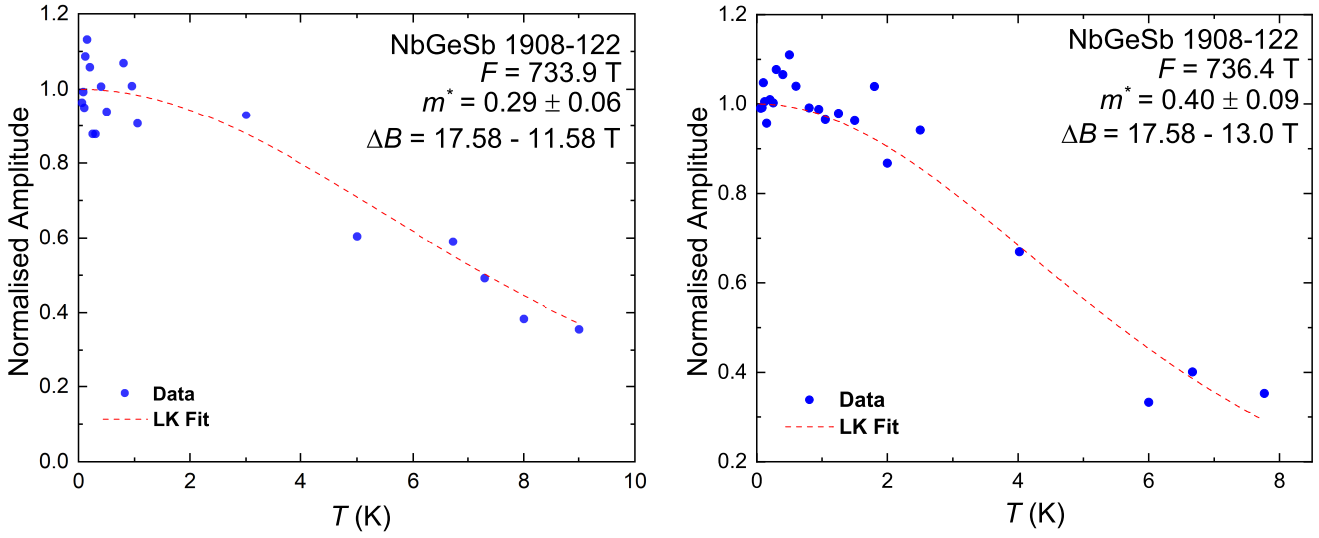

(a) Fast sweep rate

(b) Slow sweep rate

Fig. 5.25 Fitting of the LK form of the temperature smearing factor in NbGeSb sample 1908-122 over two field ranges and at different field sweep rates. **(a)** 11.58 - 17.58 T at 0.231 T/min. **(b)** 13 - 17.58 T 0.069 T/min. Quantum oscillations were measured from 55 mK to 9 K. The data are quite noisy from this sample at higher temperatures and field sweeps in which no oscillations are observed have been removed.

the 6th harmonic appears to be absent, as seen in Figure 5.22b. A bubble plot, shown in Figure 5.23b allows the FFT amplitudes to be seen easily thus making it slightly easier to track the many peaks.

Temperature studies of the quantum oscillation amplitudes have been performed so that, where possible, quasiparticle masses can be extracted using the Liftshitz-Kosevich (LK) formula. The effective quasiparticle mass m* can be obtained through the fit of the temperature dependence of the oscillation amplitude to the thermal damping factor R_T (equation 2.14). Data were taken at angles of $\phi = 0°$, 12.5° and 30° for NbSiSb and at $\phi = 0°$ for NbGeSb. Figure 5.25 shows the fitting of the LK(T) relation for the NbGeSb β frequency at $\phi = 0°$ over two field ranges and sweep rates. The spread of data are quite large and so the estimates for the effective quasiparticle mass of the β frequency, of 0.3 m_e and 0.4 m_e for the fast and slow sweep rates respectively, should be taken as an upper bound. Estimates were limited by both the working range of the low temperature transformers before they became overloaded at higher temperatures (> 9 K) as well as the overall quality of the data.

Table 5.6 summarises the extracted quasiparticle masses for the low field range (3 - 9 T) in NbSiSb and Table 5.7 for the high field range (8 - 17.5 T). It should be noted that the absolute frequency field values quoted are likely not known well enough to give such absolute precision as stated, but the relative positions of the frequencies (with an overall common scale factor) are. This what has been used to

Table 5.6 Effective masses of as grown NbSiSb sample 1908-201, H||c, magnetic field range 3 - 9 T.

Label	***F* (T)**	**Mass (m_e)**
α	11.12 ± 0.06	0.6 ± 0.1
β	37.0 ± 0.2	0.54 ± 0.03
γ	302.1 ± 0.3	1.1 ± 0.1
γ'	319.2 ± 0.3	0.7 ± 0.2
δ'	417.4 ± 0.2	0.5 ± 0.1
δ	427.4 ± 0.5	0.7 ± 0.1
2γ	610.3 ± 0.5	1.9 ± 0.1
$2\gamma'$	627.9 ± 0.4	1.3 ± 0.4
$2\delta'$	841.7 ± 0.5	1.0 ± 0.3
2δ	857.1 ± 0.6	0.83 ± 0.09
3γ	915.7 ± 0.8	3.0 ± 0.7
4γ	1220 ± 2	3.9 ± 0.3
3δ	1273 ± 4	1.4 ± 0.4

determine possible magnetic breakdown orbits. In the low field range, six fundamental frequencies are observed: α, β, γ, γ', δ and δ' (the labelling is arbitrary and is used to keep track of harmonics and to compare to DFT calculations later). Even over this low field range, several harmonics of the fundamental frequencies can be observed (up to the third harmonic of γ). Magnetic breakdown orbits start to become visible as the field range is increased to higher fields, then at the highest fields (in the range 8 - 17.56 T), the FFT spectra contains a large variety of magnetic breakdown orbits and many harmonics are visible up to the 14^{th} harmonic of the δ. Several of the harmonics and breakdown orbits are 'missing', such as the third harmonic of γ' and the seventh harmonic of γ, this is likely because they are hidden behind other nearby peaks that have a larger amplitude. The effective mass estimates become more unreliable at higher frequency as the amplitude of the signal is so small to begin with, this made obtaining effective masses above the seventh harmonic of δ very unreliable and so they have not been included.

Figure 5.26 shows a representative fitting of the LK(T) relation for NbSiSb at $\phi = 0°$ of two frequencies (γ and 2γ) over a low field range. The observed frequencies are $\gamma = 301.7$ T and $2\gamma = 609.9$ T with effective quasiparticle masses of $m^* = (1.11 \pm 0.07)\ m_e$ and $m^* = (1.9 \pm 0.1)\ m_e$ respectively. This suggests that the second peak is indeed the 1^{st} harmonic of γ as suspected. Figure 5.27 shows a representative fitting of the LK(T) relation for NbSiSb at $\phi = 30°$ of two frequencies (γ and 2γ) at a high field range. The observed frequencies at $\phi = 0.0°$ are $\gamma = 311.3$ T and $2\gamma = 637.9$ T with effective quasiparticle masses of $m^* = (1.4 \pm 0.1)\ m_e$ and $m^* = (2.5 \pm 0.1)\ m_e$ respectively. This suggests that the second peak is indeed the 1^{st} harmonic of γ, however, the effective masses and

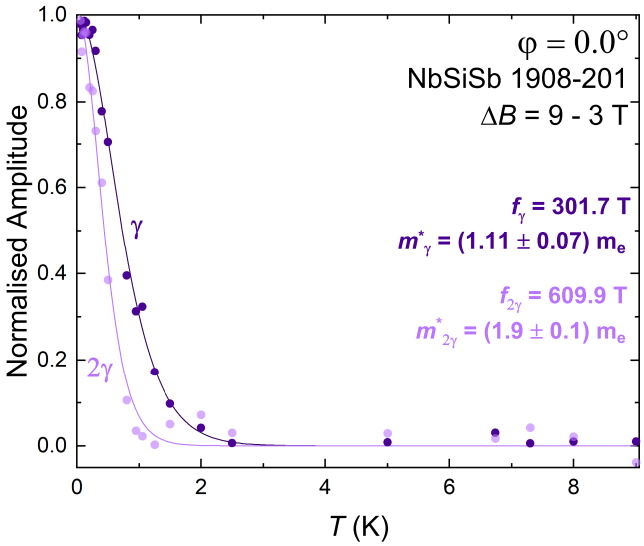

Fig. 5.26 Fitting of the LK form of the temperature smearing factor in NbSiSb sample 1908-201 at $\phi = 0.0°$. Field range 3 - 9 T at a sweep rate of 0.231 T/min. Quantum oscillations were measured over a temperature range from 55 mK to 9 K.

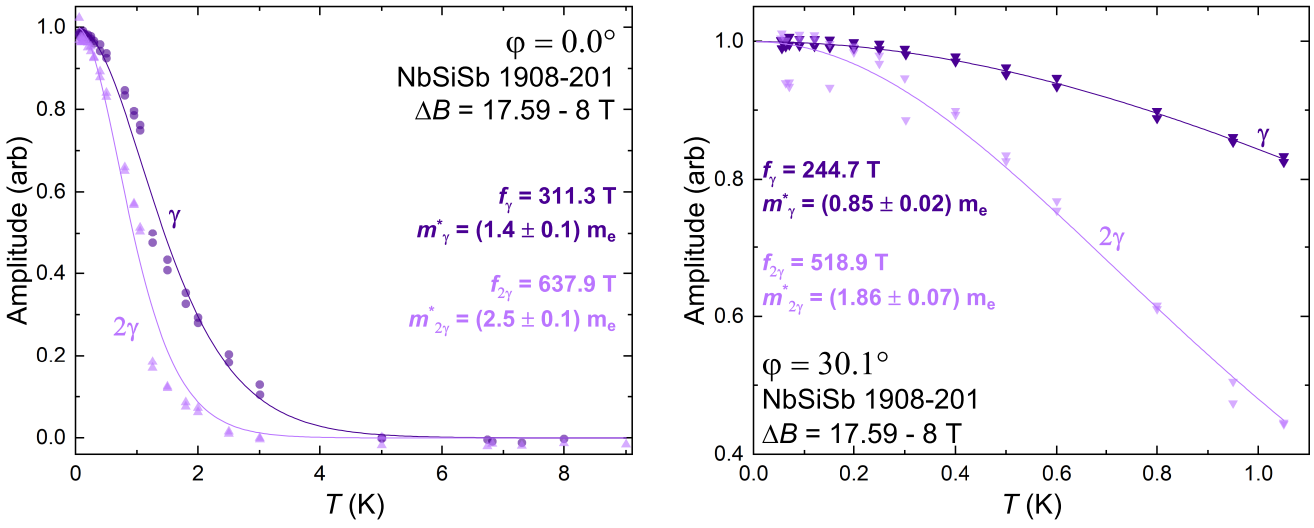

(a) Low Field

(b) High Field

Fig. 5.27 Fitting of the LK form of the temperature smearing factor in NbSiSb sample 1908-201 at angles of **(a)** $\phi = 0.0°$ and **(b)** $\phi = 30.1°$. Field range 8 - 17.59 T at a sweep rate of 0.069 T/min. Quantum oscillations were measured over a temperature range from 55 mK to 9 K.

Table 5.7 Frequencies and quasiparticle effective masses of as grown NbSiSb sample 1908-201, H‖c, magnetic field range 8 - 17.5 T.

Label	F **(T)**	**Mass** (m_e)	**Label**	F **(T)**	**Mass** (m_e)
α	Frequency hidden behind β	-	2δ	860.06 ± 0.02	1.5 ± 0.2
β	37.30 ± 0.06	0.76 ± 0.08	3γ	910.713 ± 0.008	2.6 ± 0.1
2β	73.9 ± 0.9	1.1 ± 0.4	$3\gamma'$	962.55 ± 0.04	3.9 ± 0.4
3β - α	99.2 ± 0.3	1.9 ± 0.3	4γ - 3β	1041.068 ± 0.002	2.1 ± 0.3
$3\beta + \alpha$	123.2 ± 0.3	1.6 ± 0.2	4γ	1188.8 ± 0.4	3.0 ± 0.1
4β - α	140.8 ± 0.2	1.4 ± 0.2	$4\gamma + \beta$	1227.7 ± 0.2	3.6 ± 0.1
γ' - 2β	245.7 ± 0.2	1.23 ± 0.06	3δ	1277.0 ± 0.2	1.8 ± 0.2
γ - β	269.7 ± 0.2	1.30 ± 0.06	$5\gamma'$ - β	1497.3 ± 0.2	3.9 ± 0.3
γ	294.48 ± 0.08	1.4 ± 0.1	5γ	1528.7 ± 0.1	4.6 ± 0.4
γ'	315.13 ± 0.08	1.00 ± 0.03	$5\gamma + \beta$	1571.0 ± 0.1	4.2 ± 0.3
$\gamma + \beta$	342.1 ± 0.1	1.32 ± 0.03	$5\gamma + 2\beta$	1609.0 ± 0.2	3.7 ± 0.5
$\gamma + 2\beta$	375.9 ± 0.1	1.29 ± 0.1	$5\gamma + 3\beta$	1645.1 ± 0.2	3.0 ± 0.5
$\gamma + 3\beta$	401.7 ± 0.1	1.3 ± 0.3	$5\gamma + 4\beta$	1681.8 ± 0.2	1.6 ± 0.6
δ	431.74 ± 0.07	0.9 ± 0.07	4δ	1716.5 ± 0.1	1.8 ± 0.2
$\delta + \beta$	467.8 ± 0.3	1.22 ± 0.1	$6\gamma + 2\beta$	1840.1 ± 0.2	5.2 ± 0.5
$\gamma + 5\beta$	484.61 ± 0.05	1.4 ± 0.4	$6\gamma + 3\beta$	1894.0 ± 0.4	6.2 ± 0.6
$\gamma + 6\beta$	518.23 ± 0.05	2.1 ± 0.2	5δ	2130.5 ± 0.3	2.1 ± 0.2
$\delta + 3\beta$	549.1 ± 0.3	1.1 ± 0.1	8γ	2368.7 ± 0.5	2.0 ± 0.4
2γ - β	566.3 ± 0.2	2.0 ± 0.4	$8\gamma + 2\beta$	2450.1 ± 0.5	7 ± 1
2γ	605.3 ± 0.1	1.9 ± 0.1	6δ - β	2545.8 ± 0.7	5.8 ± 0.9
$2\gamma'$	635.5 ± 0.1	2.5 ± 0.1	7δ - β	2985.7 ± 0.2	4 ± 1
$2\gamma + 2\beta$	674.7 ± 0.1	1.0 ± 0.3	$7\delta + 4\beta$	3176.6 ± 0.3	3 ± 1
$2\gamma + 3\beta$	691 ± 8	1.7 ± 0.3	8δ	3426.8 ± 0.3	-
$2\gamma' + 2\beta$	707 ± 3	1.7 ± 0.3	9δ	3853.1 ± 0.2	-
$2\gamma + 4\beta$	738 ± 4	1.1 ± 0.2	10δ	4274.4 ± 0.2	-
$2\gamma' + 3\beta$	749 ± 6	1.1 ± 0.2	12δ	5133.13 ± 0.08	-
$2\gamma + 5\beta$	766 ± 4	-	13δ	5551.29 ± 0.07	-
$2\gamma' + 4\beta$	793.1 ± 0.1	-	$\sim 14\delta$	5984 ± 5	-
$3\gamma'$ - β	831.40 ± 0.07	1.6 ± 0.2	$\sim 15\delta$	6417.2 ± 4	-

frequencies of 2γ do not match up with two times that of γ as well as in the low field range. Mass estimates of the higher harmonics of γ and δ do not seem to match up with the expected behaviour, for

example the measured mass of the 4th harmonic of δ is 2.1 m_e, with the fundamental having a mass of 0.9 m_e. The 6th harmonic of γ is 2.0 m_e, with the fundamental having a mass of 1.4 m_e. The low field analysis, however, gave much smaller values for the mass of δ (0.7 ± 0.1 m_e) and γ (1.1 ± 0.1 m_e) which the harmonics of δ and γ seem to match more reliably to in the high field study. The reason for this discrepancy may be due to a combination of the influences of magnetic breakdown and the magnetic interaction, discussed in Section 5.3.2.

From the observed frequencies the extremal cross-sectional areas of the Fermi surface (A_F) can be extracted using the Onsager relation (equation 2.8). From this the Fermi velocities can be calculated using the estimates of the effective quasiparticle mass. A summary of the observed frequencies can be seen in Table 5.8, the Fermi wavevector (k_F) and Fermi velocity (v_F) are also been shown.

Table 5.8 Calculation of the Fermi surface extremal cross-sectional area using the observed frequencies at $\phi = 0°$. The Fermi wavevector (k_F) and Fermi velocity (v_F) have also been calculated using the estimates for the effective quasiparticle masses from Figure 5.25 and Table 5.7.

	F (T)	A_F (nm^{-2})	k_F (nm^{-1})	$v_F/\times 10^4$ (m/s)
NbGeSb	$\beta = 756$	7.41	1.49	5.0 ± 0.4
NbSiSb	$\beta = 39$	0.38	0.34	0.74 ± 0.04
	$\gamma = 309$	3.03	0.97	1.02 ± 0.09
	$\gamma' = 318$	3.12	0.98	1.6 ± 0.5
	$\delta = 442$	4.34	1.16	2.7 ± 0.5
	$\delta' = 434$	4.25	1.15	1.9 ± 0.3

5.2.6 Berry phase

The Berry phase acquired by the charge carriers can provide more information about the nature of the electronic band structure in NbXSb. A Berry phase of π accumulated along cyclotron orbits, as well as a light effective mass and high carrier mobility, is another key feature of Dirac fermions. The Berry phase appears as an additional phase shift in quantum oscillations, which can be determined via two methods: directly from a fit of the full LK formula (equation 2.21), or via a Landau level index fan diagram. The quantisation of a closed orbit in a magnetic field according to Lifshitz-Onsager rule is [166]:

$$A_F \frac{\hbar}{eB} = 2\pi \left(n + \frac{1}{2} - \beta - \Delta \right) = 2\pi \left(n + \lambda - \Delta \right) \ , \tag{5.5}$$

where the Berry phase is equal to $2\pi\beta$, Δ is a phase shift, which has a value 0 for 2D and $\pm 1/8$ for 3D band structures. Conventional metals with a parabolic band dispersion have a Berry phase of zero but for Dirac/Weyl type electronic systems with linear band dispersions the Berry Phase is equal to π.

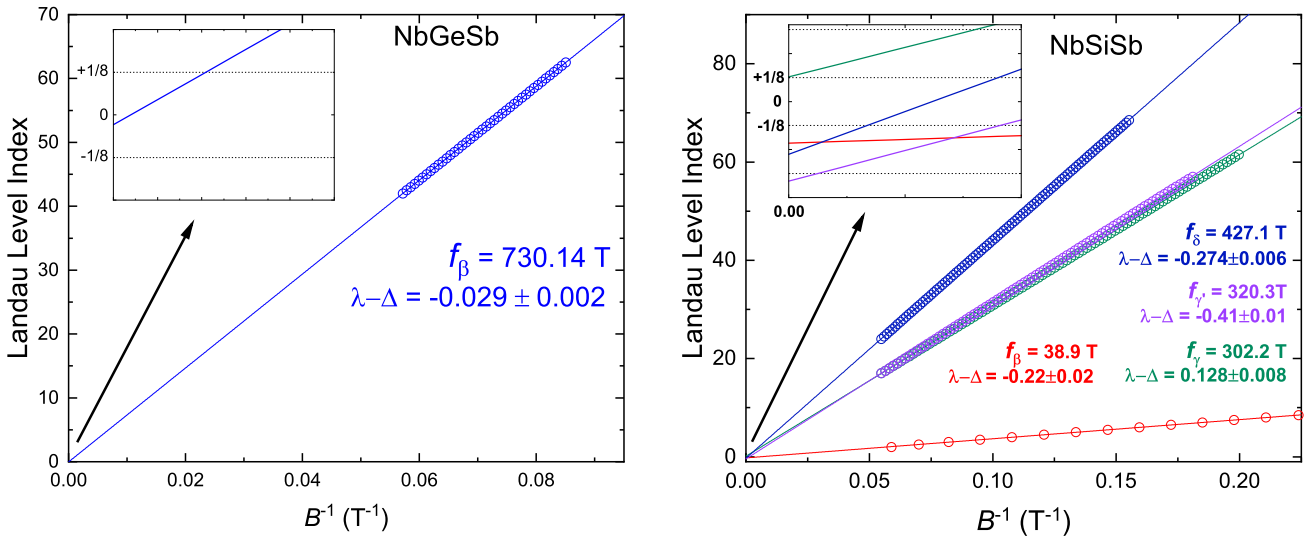

(a) NbGeSb (b) NbSiSb

Fig. 5.28 Landau level fan diagrams for **(a)** NbGeSb sample 1908-122 and **(b)** NbSiSb sample 1908-201. The integer index n is assigned such that a linear extrapolation of the index plots yields an intercept closest to zero index (n = 0).

For quantum oscillation with single frequency, the parameter $\lambda - \Delta = 1/2 - \beta - \Delta$, can be extracted from the y-axis intercept in the Landau level index plot and will remain within the range -1/8 to +1/8 for 3D Dirac fermions [166]. A Landau level fan diagram has been constructed for the β frequency in NbGeSb from the SdH oscillations, shown in Figure 5.28a. Assigning maxima as integers and minima positions as half-integers, the level index n is assigned such that a linear extrapolation of the index plots yields an intercept closest to zero index (n = 0). The obtained intercept of -0.029 ± 0.002 is within the theoretical range for 3D Dirac fermions but far from the expected intercept for a regular parabolic dispersion ($\sim$0.5), which suggests the presence of 3D Dirac fermions in NbGeSb. Figure 5.28b shows the same construction for the four main fundamental frequencies observed in NbSiSb. The intercepts obtained are -0.22 ± 0.02 for the β frequency, 0.128± 0.008 and -0.41± 0.01 for the γ and γ' frequencies respectively and -0.274± 0.006 for the δ frequency. None Of the four lie close to the expected value of $\sim$0.5 which would suggest a regular parabolic dispersion. The β, γ' and δ intercepts are somewhere in between -1/8 and -1/2 suggesting a that the band dispersions lie somewhere in the region between parabolic and linear but with a non-trivial Berry phase. The value of λ - Δ = 0.128 for the γ frequency suggests a linear dispersion and the presence of 3D Dirac fermions in NbSiSb. As there are several frequencies that are quite closely spaced in the FFT spectrum of NbSiSb, the Landau level analyses presented in Figure 5.28b can be somewhat unreliable.

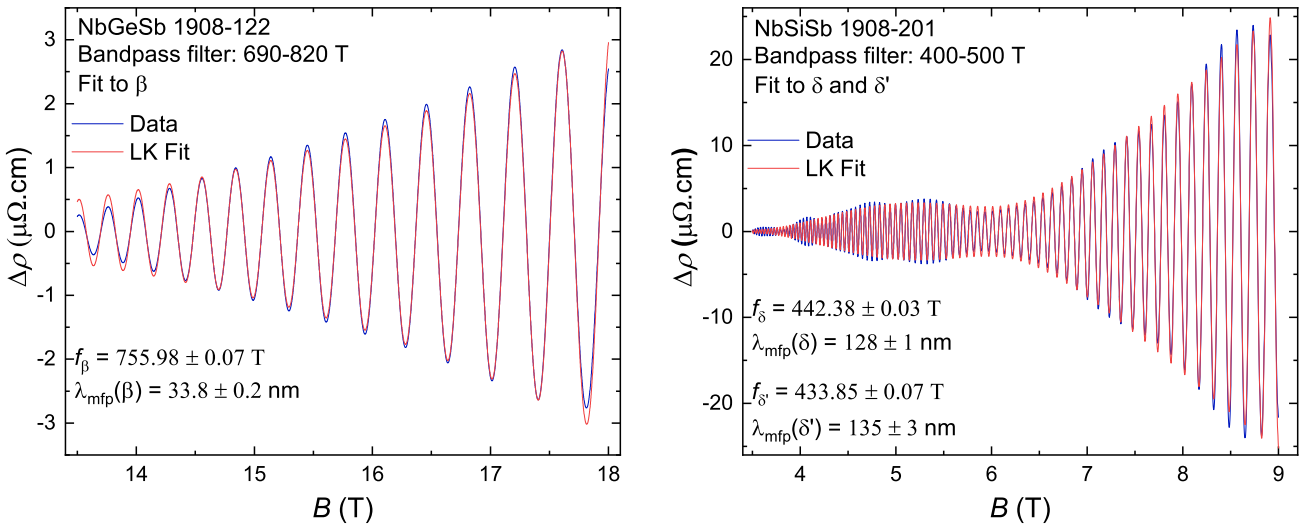

(a) NbGeSb

(b) NbSiSb

Fig. 5.29 Fits to the LK formula (red solid line) and band-pass filtered quantum oscillation data (blue solid line) for **(a)** β frequency oscillation component in NbGeSb and **(b)** δ and δ' frequency oscillation components in NbSiSb.

As a further check the Berry phase can be extracted from the full LK fit of the frequencies after they have been separated by employing a band-pass filter. Figure 5.29a show a fit of the full LK formula to the γ frequency in NbGeSb, a band-pass filter between 690 - 820 T has been used to remove noise around the γ frequency. Previously calculated values of m* (0.29) and frequency (756 T) have been set as fixed parameters in the fit, which is quite reasonable and the Dingle temperature has been extracted. From the Dingle temperatures, the quantum relaxation time $\tau_q = (\hbar/2\pi k_B T_D)$ as well as the quantum mobility μ_q $e\tau_q/m^*$ has been calculated and the results are shown in Table 5.9. The Berry phase has also been estimated based on the phase (λ - Δ) that has been extracted from the fits. This Berry phase can be compared with the previously estimated Berry phase from the Landau level index plots. For NbGeSb, a phase factor (λ - Δ) of -0.03 from the LK fit method corresponds to a Berry phase of $\Phi_B = 1.12\pi$ for $\Delta = 0$ (2D Fermi surface), $\Phi_B = 0.87\pi$ for Δ = -1/8 (3D Fermi surface), and $\Phi_B = 1.37\pi$ for Δ = +1/8 (3D Fermi surface). This matches well with the Berry phase estimates from the Landau level index plot in Figure 5.28a where a phase factor of -0.06 corresponding to a Berry phase of $1.06\pi \pm 0.25$ for the three cases of Δ was found. This further indicates the topological nature of the fermions present NbGeSb. As already suggested the mobility of Dirac fermions should be very high, the estimated value from the LK fit, while not insignificant at 850 cm^2/Vs, is an order of magnitude smaller than the previously reported value in ZrSiS [114] and several orders of magnitude smaller than in Cd_2As_3 [153]. However, the value of the effective mass estimated from the fitting of the thermal dampening factor of the LK formula may well be an overestimate as we have already

stated that measurements at higher temperatures were limited by the Cambridge dilution refrigerator. To match the mobilities seen in ZrSis and Cd_2As_3, the effective quasiparticle mass in NbGeSb would need to be of order 0.003 - 0.03 m_e, similar to the effective mass estimates in ZrSiS and Cd_2As_3. The low value of μ_q from the SdH analyses may be caused by the Zeeman effect (spin splitting) not being taken into consideration and the possible breakdown of the LK formula for the SdH oscillations which has been seen in other layered materials [167]. An analysis of the Hall effect in NbGeSb would help to confirm this, preliminary analysis of a recent Hall effect measurement are presented in Appendix B.1.2 which suggest much higher mobilities, approaching the values of ZrSiS.

For NbSiSb, the same technique has been used to extract the Dingle temperatures of the five fundamental frequencies identified at $\phi = 0°$ (β, γ, γ', δ and δ'). A representative example of the fit for the δ frequency is shown in Figure 5.29b. The estimated Berry phases, shown in Table 5.9, can be compared with those from the Landau level index plots.

Table 5.9 Parameters derived from the analyses of SdH oscillations for NbXSb T_D = Dingle temperature; m^* = effective mass (extracted from the low field fits in Table 5.6); τ_q = quantum relaxation time; μ_q = quantum mobility and Φ_B is the Berry phase.

	F (T)	T_D (K)	m^* (m_e)	τ_q (ps)	μ_q (cm^2/Vs)	Φ_B
NbGeSb	β = 755.98 ± 0.01	8.7 ± 0.1	0.29 ± 0.06	0.14 ± 0.02	850 ± 160	(1.12 ± 0.25)π
NbSiSb	β = 38.89 ± 0.03	14.2 ± 0.5	0.54 ± 0.03	0.09 ± 0.02	280 ± 20	(0.54 ± 0.25)π
	γ = 308.83 ± 0.04	7.4 ± 0.3	1.1 ± 0.1	0.16 ± 0.04	260 ± 20	(1.76 ± 0.25)π
	γ' = 318.0 ± 0.1	50 ± 2	07 ± 0.2	0.024 ± 0.02	60 ± 20	(1.22 ± 0.25)π
	δ = 442.38 ± 0.03	18.8 ± 0.4	0.5 ± 0.1	0.065 ± 0.03	230 ± 50	(1.78 ± 0.25)π
	δ' = 433.85 ± 0.07	17.8 ± 0.4	0.7 ± 0.1	0.068 ± 0.03	170 ± 30	(-0.46 ± 0.25)π

The Berry phases from the Landau level index plots agree qualitatively but the values are somewhat different from those presented in Table 5.9 from the LK fits. For the β frequency, the value from the Landau level index plot is Φ_B = 1.4(4) ± 0.25 which is around three times that estimated from the LK fit. The other three frequencies show a similar discrepancy with factors of 0.4 (γ), 1.5 (γ') and 0.9 (δ) between the LK fit value and the Landau level index estimate. The fact that the Berry phase found from the single frequency in NbGeSb agree for both methods suggests that the LK fit method is robust and as predicted the Landau level index plots for closely spaced frequencies may be unreliable for NbSiSb. The Berry phases found for the various frequencies in NbSiSb are, however, non-trivial in both cases.

5.3 Discussion

NbGeSb has shown an unusual negative magnetoresistance at low fields, the origins of which will now be considered and the possibility of whether it is linked to the topological chiral anomaly is discussed. In a DSM each Dirac node can be resolved into two Weyl nodes that possess a chirality (or handedness) which do not mix. The key experimental signature of the chiral anomaly is a negative longitudinal magnetoresistance at moderately low fields when the electric current is parallel to the applied magnetic field as charge is predicted to flow between the nodes due to charge pumping, the effect should be heavily suppressed as the field is rotated away towards perpendicular **E** and **B** fields. It should be noted, however, that a negative MR has also been seen in semimetals that do not have a Dirac-like dispersion, such as $Cd_xHg_{1-x}Te$[168] and $PdCoO_2$ [169]. Figure 5.30(a) shows a sketch of a Dirac cone centered on **K** which is split into two Weyl nodes of opposite chirality. Figure 5.30(b) shows the Landau levels of Weyl states subject to a strong magnetic field. As well as the Landau levels there is an additional shift of the Weyl nodes away from **K** due to the Zeeman spin energy of:

$$\delta k_N = \frac{\chi g \mu_B B}{\hbar v}, \tag{5.6}$$

where $\hbar$ is the reduced Planck's constant, μ_B is the Bohr magneton, g is the g-factor and v is the frequency [117]. The shifts are exaggerated in the figure for clarity. The linear dispersion at the zeroth Landau level is depends on the chirality χ: left(right) for χ = -1(+1). Upon the application of $\mathbf{E}\|\mathbf{B}$, charge pumping begins to occur between the two nodes at a rate of:

$$W = \chi \frac{e^3}{4\pi^2 h^2} E \cdot B. \tag{5.7}$$

This represents the chiral anomaly [111, 110, 124, 128]. The longitudinal or axial current relaxes at a rate of:

$$\frac{1}{\tau_a} \sim |M|^2 \left(\frac{eB}{\hbar v}\right), \tag{5.8}$$

$$\sigma_\chi = \frac{e^2}{4\pi^2 hc} \frac{v}{c} \frac{(eBv)^2}{E_F^2} \tau_a \tag{5.9}$$

and $1/\tau_a$ is now independent of magnetic field B. The axial conductivity increases as B^2 with increasing B but in the quantum limit it saturates to a B-independent value [125].

Figure 5.30**(c)** shows the axial current ($\Delta\sigma_{xx}$) as a function of magnetic field angle as **E** is rotated away from $\mathbf{E}\|\mathbf{B}$ at several fixed magnetic fields in the range 0 - 2 T in the DSM Na_3Bi (from [170]).

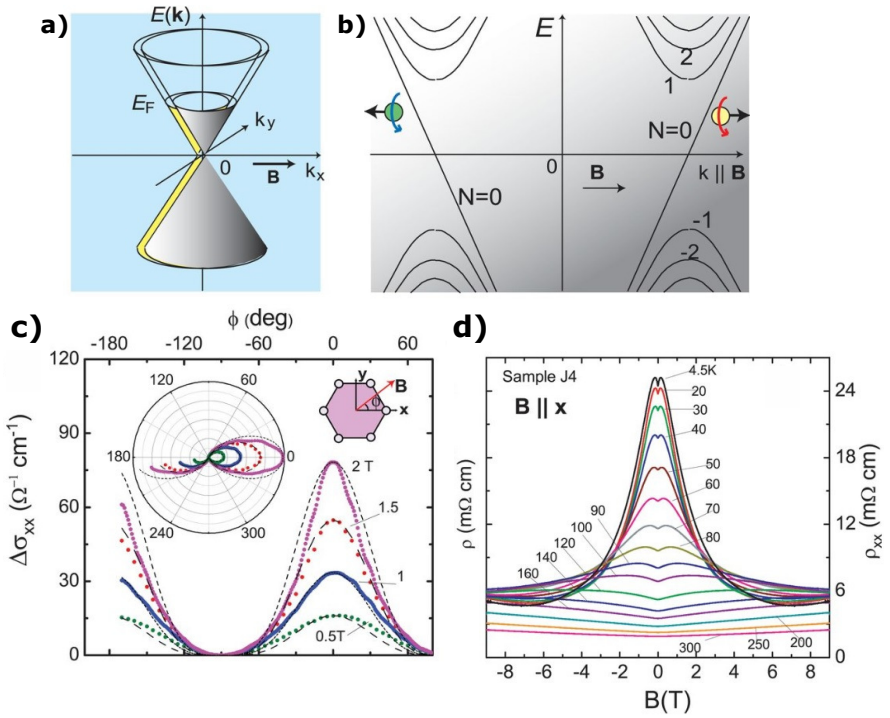

Fig. 5.30 **a)** Dirac cone centered on **K**, represented by two displaced Weyl nodes with a distinct chirality: grey cone has χ = +1, yellow cone χ = -1. **b)** A strong magnetic field increases the separation of the Weyl nodes due to spin Zeeman energy: Weyl states are quantised into Landau levels (LL). Linear dispersion of the zeroth LL has a slope given by χ (yellow and green circles). **c)** Angular dependence of the axial current in Nb_3Bi, plotted is the conductance enhancement vs ϕ at fixed **B** between 0 and 2 T. Fits to $\cos^4\phi$ show reasonable agreement in this range. **d)** Longitudinal MR at T = 4.5 - 300 K measured with **E**||**B**. From [170]. Reprinted with permission from AAAS.

The inset shows a polar plot of how the axial current is suppressed as **E** is rotated away from **B**. Figure 5.30**(d)** shows the negative MR region at low fields at several temperatures in the range 4.5 K to 300 K. At 4.5 K and at very low fields there is an initial small rise in the resistivity which peaks at around 100 mT before sharply turning around into the negative magnetoresistance region which persists to around 6 T where it begins to plateau. With increasing temperature, the size of the negative MR feature decreases, reducing to around 50% of its magnitude at 60 K, and it is still visible up to 120 K. Comparing the data on Nb_3Bi to the negative MR data shown in NbGeSb in Figure 5.14, there are several similarities, however the temperature and magnetic field scales over which they occur are much smaller. The field region of the negative MR feature is around and order of magnitude smaller than that shown in Nb_3Bi (0 - 0.6 T in NbGeSb), the field at which the initial peak occurs is around 20 - 30 % of the value in Nb_3Bi. The temperature at which the negative MR feature is reduced by 50% occurs at around 350 mK in NbGeSb, approximately 20× smaller than in Nb_3Bi. Crucially, the angular dependence of the axial current in Nb_3Bi is maximised for **E**||**B** and is suppressed for angles moving away from this. In NbGeSb, as shown in Figure 5.31, the same behaviour is not seen and in

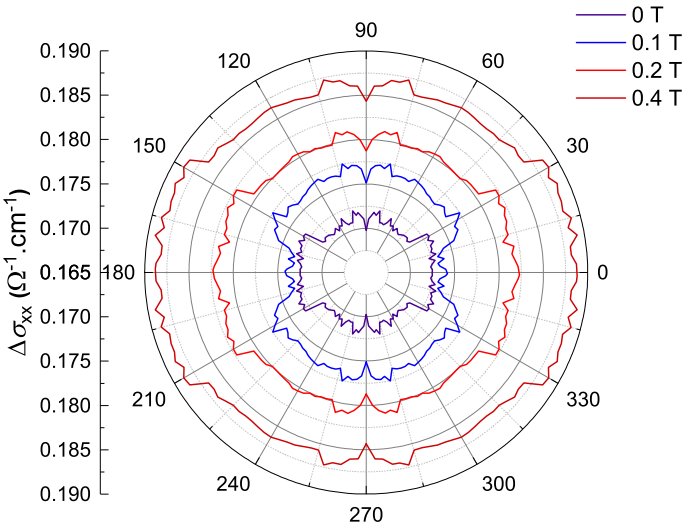

Fig. 5.31 Conductivity of the negative MR region in NbGeSb, $\theta = 0°$ corresponds to $\mathbf{E}\|\mathbf{B}$.

fact the negative MR signal persists over the entire measured range of $0° \leq \phi \leq 90°$. Over the same magnetic field region as Nb_3Bi in Figure 5.30**(c)** (adjusted assuming an order of magnitude difference) the polar plot of the conductivity of NbGeSb shows some 2D character but does not reduce to zero as θ approaches 90°. There is a small reduction in the conductivity as θ approaches 90° that may be due to a chiral current, however, this sits on top of a much larger negative MR signal which does not possess the same angular dependence and in fact remains independent of the applied magnetic field angle. It has been shown by Schumann *et al.* that the chiral anomaly is not needed to explain negative MR in Cd_3As_2 thin films and in fact it can be explained by conductivity fluctuations [171]. It should be noted that the negative MR feature has only been seen in one annealed sample of NbGeSb measured on the dilution refrigerator, further work is needed in order to ascertain the physical origin of this phenomenon.

5.3.1 Comparison to Density Functional Theory calculations

The *k*-space area of a Fermi surface orbit is related to the corresponding quantum oscillation frequency via the Onsager relation, from which the number of electrons within the Fermi surface per unit cell can be calculated using Luttinger's theorem. For 2D materials which possess a constant Fermi area along a given axis with no dispersion, it is then easy to calculate the electron density using areas perpendicular to the same axis. The Fermi surface of 3D materials often is more complicated with multiple connections resulting in some extremal cross-sectional areas producing only weak oscillations. Additionally, neither the position within the Brillouin zone nor the in plane contour are given by the cross-sectional area.

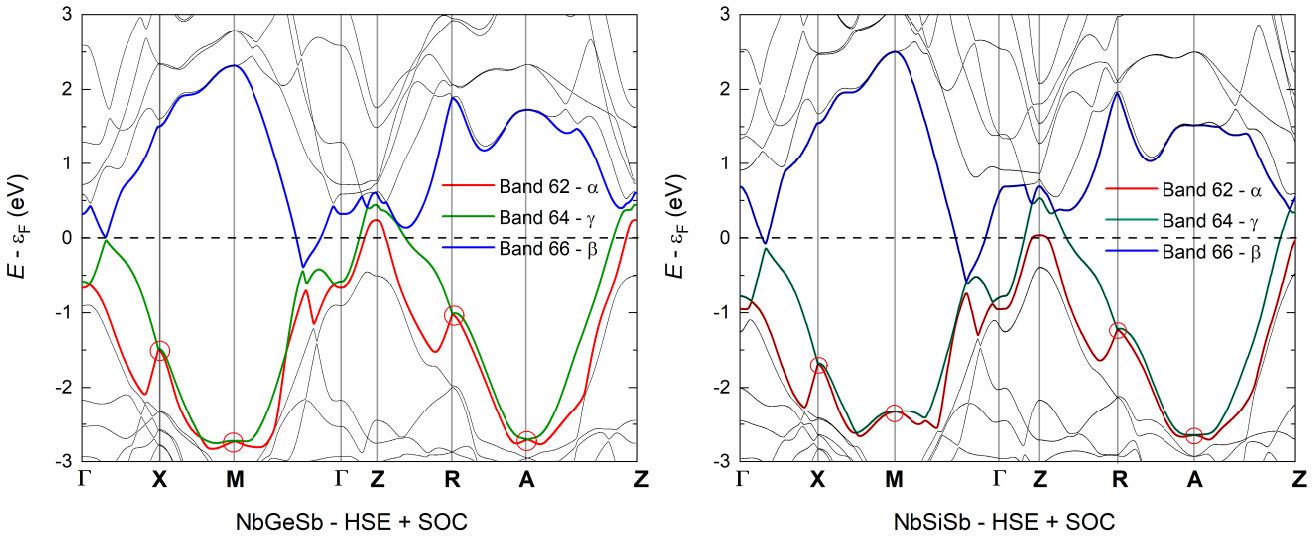

(a) NbGeSb (b) NbSiSb

Fig. 5.32 Calculated bandstructures of both NbGeSb (left) and NbSiSb (right) using HSE06 with spin orbit coupling (SOC). The symmetry enforced Dirac nodal lines at **X**, **M** **R** and **A** are circled in green. Calculations performed by fellow PhD student Bo Peng.

A determination of the Fermi surface and the bandstructure of NbXSb requires a calculation of the electronic structure, which can be achieved using density functional theory (DFT) calculations. The calculations presented here were performed by fellow PhD student Bo Peng with help from Dr. Bartomeu Monserrat (of the Theory of Condensed Matter Group, Cavendish Laboratory), details of these calculations are beyond the scope of this thesis but the key points are briefly described in order to help distinguish experimental scenarios. DFT calculations were carried out using HSE06 (after Heyd–Scuseria–Ernzerhof: an exchange-correlation functional which uses an error function screened Coulomb potential to calculate the exchange portion of the energy in order to improve computational efficiency, especially for metallic systems [172]) including spin-orbit coupling (HSE+SOC). The calculated bandstructures using HSE are shown in Figure 5.32 for NbGeSb (left) and NbSiSb (right). NbGeSb shows two bands with linear dispersion (which continues up to 300 meV) that touch at the Fermi energy along Γ-X without SOC, when SOC is included in the calculation a small gap ($\sim$25 meV) opens up at the Fermi level. NbSiSb shows a similar bandstructure with two bands having a linear dispersion that touch just below the Fermi level along Γ-X without SOC, again when SOC is included in the calculation a small gap (around 50 meV) opens up around 100 meV below the Fermi level. Enforced Dirac nodes are circled, one at **X** and another at **M**. The enforced Dirac points are present at all plotted values of k_z, which results in nodal lines along the **M**–**A** and **X**–**R** lines in the three-dimensional Brillouin zone, as in ZrSiS.

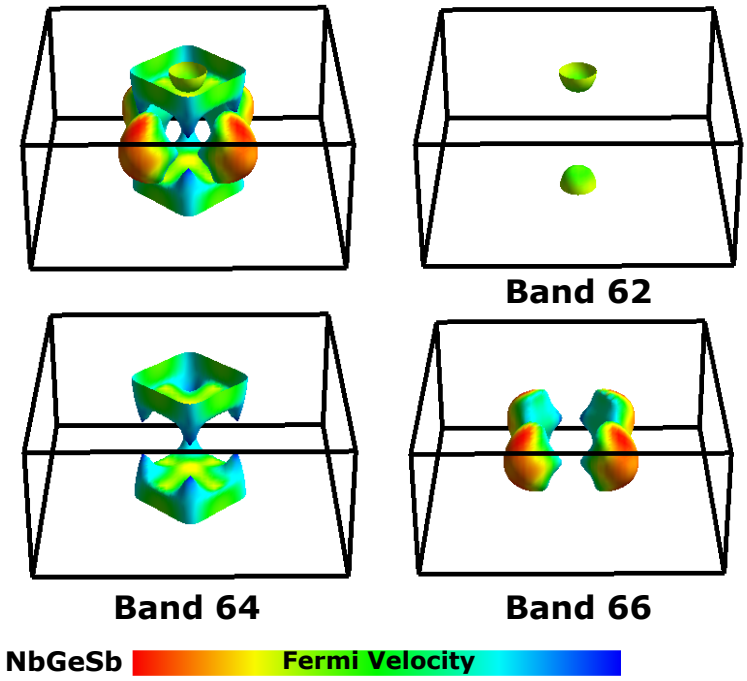

Fig. 5.33 Calculated Fermi surface of NbGeSb using HSE06 with spin orbit coupling (SOC). Bands 62 and 66 are hole-like and band 64 is electron-like.

Figure 5.33 shows the calculated Fermi surface of NbGeSb using HSE06 + SOC with a colour scale indicating the Fermi velocity. Three bands contribute to the Fermi surface two of which are hole-like (bands 62 and 66) and one electron-like (band 64). The electron-like Fermi surface harbours the suspected Dirac-like cones along Γ-X. There is also a cone-like feature on the four lobes of the hole-like band 66 situated along Γ-M, this like much further away from the Fermi energy as seen in the left panel of Figure 5.32. The other hole-like pocket is from band 62 and lies along Γ-Z.

Figure 5.34 shows the calculated Fermi surface of NbSiSb using HSE06 + SOC with a colour scale indicating the Fermi velocity. As with NbGeSb, three bands contribute to the Fermi surface two of which are hole-like (bands 62 and 66) and one electron like (band 64). The two Fermi surfaces appear quite similar, the main difference between the two is that in NbSiSb the four lobes of band 66 (along Γ-M) have joined to make a single surface. The Dirac-like points of band 64 seen in NbGeSb along Γ-X are now much more rounded and further apart. The small hole pocket along Γ-Z is reduced in size relative to NbGeSb.

In order to calculate the expected quantum oscillation spectra from the calculated Fermi surfaces, the cross-sectional area perpendicular to the applied field needs to be calculated and then summed over the Brillouin zone parallel to the field. This will allow the discovery of regions of the Fermi surface that will produce quantum oscillations (extremal orbits) and was performed using SKEAF (Supercell

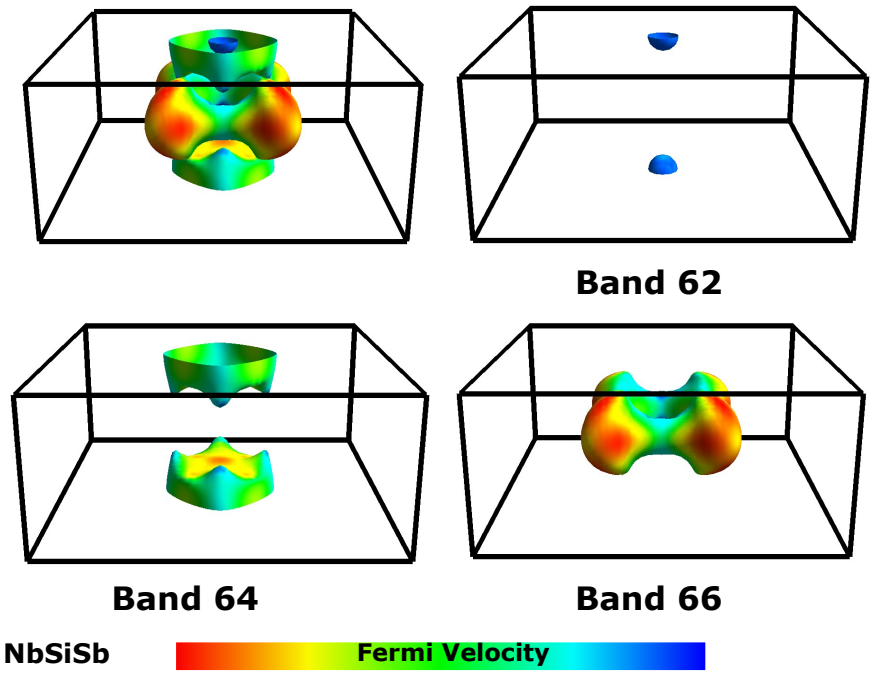

Fig. 5.34 Calculated Fermi surface of NbSiSb using HSE06 with spin orbit coupling (SOC). Bands 62 and 66 are hole-like and band 64 is electron-like.

K-space Extremal Area Finder [81]). The resulting frequencies along with the experimental data for NbGeSb and NbSiSb are displayed in Figures 5.35a and 5.35b respectively.

For the case of NbGeSb, a relatively good agreement between DFT calculations and experiment is seen for the low frequency band (β = band 66) which follows the calculated band to $\phi = 35°$, however, above this magnetic field angle the data are too noisy to reliably track the frequency and match to the calculation. The higher frequency band (γ = band 64) was not observed at all, and the low frequency band attributed to α (= band 62) was barely visible and not over the whole range of applied magnetic field angles. The missing high frequency band (γ) is likely not seen due to the poor quality of the quantum oscillation data and (if real) is hidden in the noise and would require higher quality single crystal samples, higher magnetic fields, or using a different technique (such as dHvA) in order to be observed. The effective mass of the β frequency (band 66 - blue) is calculated to be 0.38 m_e, this matches well with the effective mass from the LK fit at $\phi = 0°$ of 0.4 m_e. The calculated effective mass of the α frequency (band 62 - red) is calculated to be 0.185 m_e at $\phi = 0°$. It was not possible to compare this to the experiment at $\phi = 0°$, or indeed at any of the angles for which a mass study was performed as the noise was too great. At $\phi = 0°$ the effective mass of band 64 (green) is calculated to be 0.8 m_e, it was not possible to compare this to the experiment as over all ϕ this frequency was not observed.

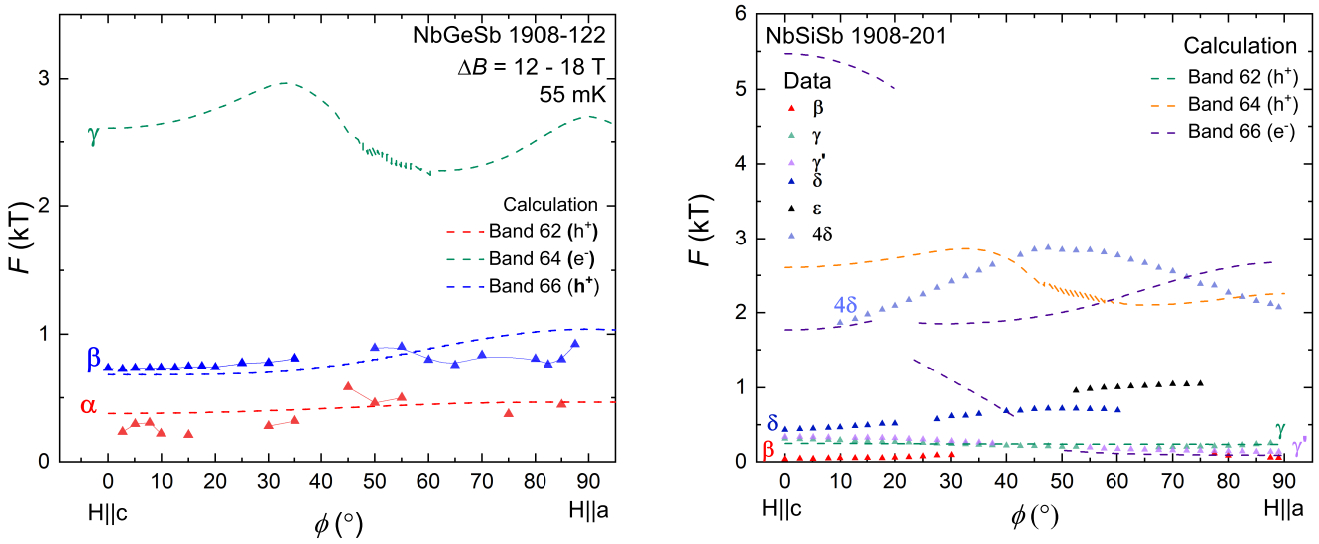

(a) NbGeSb

(b) NbSiSb

Fig. 5.35 Rotation study of the FFT frequencies from **(a)** NbGeSb sample 1908-122 and **(b)** NbSiSb sample 1908-201, in the field range 11.5-17.5 T from H||c to H||a. Calculated quantum oscillation frequencies from DFT calculations performed by Bo Peng have been included.

For the case of NbSiSb, the low lying frequency γ (green) appears to match reasonably well to the calculated frequency from the hole-like band 62, both in frequency and in angular dependence. Band 66 appears to match relatively closely with the γ' frequency (purple) above $\phi = 50°$, however, below this the behaviour of the measured frequency and the calculation differs significantly. The higher frequencies of band 64 (orange) and band 66 (purple) have not been observed, suggesting that the model needs altering to match up with experiment. This could be due to some small oxygen doping in NbSiSb which the EDX measurement seems to suggest, this can alter the level of the Fermi energy and shift the bands, further DFT calculations can be performed to reflect this and matched to the observed frequencies. The calculated effective mass of the γ frequency (band 62 - green) is 0.46 m_e, this is around half of the measured effective mass from the LK fit at $\phi = 0°$ of 1.1 $\pm$ 0.1 m_e. The effective mass of the β frequency (band 62) is calculated to be 0.511 m_e at $\phi = 0°$, it was not possible to compare this to the experiment as at at $\phi = 0°$ this frequency was not observed. At $\phi = 0°$ the effective mass of band 64 is calculated to be 0.68 m_e, however, this frequency has not been observed in experiment.

5.3.2 Magnetic breakdown in NbSiSb

There are many frequencies observed in NbSiSb which have been identified as either harmonics or sums and differences of five or six fundamental frequencies. The origin of these frequencies will

now be discussed. As mentioned in Section 2.2.6 there are two effects which can lead to multiples of frequencies as well as combinations of frequencies, these are magnetic breakdown and the magnetic interaction effect. The amplitude of MB orbits should be reduced by a factor:

$$R_{MB} = exp\left(\frac{-B}{B_c}\right), \tag{5.10}$$

where B_c is the MB field and is proportional to Δk^2, where Δk is the energy gap between adjacent pockets of the Fermi surface [25]. The existence of a MB field implies that below a certain field range MB orbits should not occur. A comparison of the observed frequencies in Tables 5.6 and 5.7 suggest that MB orbits do occur in this material, with several breakdown orbits possibly visible even at comparatively low fields (below 9 T). A full understanding of the origin of these peaks will require revised DFT calculations as well as additional measurements and analysis going beyond the scope of this initial investigation. To help distinguish between MB orbits and the MI effect, data from dHvA measurements is needed. To model the expected amplitudes of combinations of frequencies due to the MI, a combination of dHvA and SdH data can be used as in Section 2.2.6. The model can then be used to confirm or rule out the MI effect, aided in refinements to DFT calculations. The estimated quasiparticle effective masses of combinations of frequencies at high fields (such as $\gamma + \beta$, $\delta + \beta$, etc) can also help to disentangle the complicated FFT spectra.

5.3.3 Surface states in NbGeSb

Recent ARPES measurements performed on samples of as grown NbGeSb (the crystals were grown by the author but do not form part of this work) have demonstrated topological surface states that show Weyl-like character. The work of Markovic, *K. Murphy et al.* shows that two pairs of surface states, which had been previously seen in ZrSiS [173], intersect each other near the Fermi level in NbGeSb resulting in pronounced spin splittings [174]. The authors argue that mirror symmetry leads to protected crossing points in the surface band structure, which stabilise surface state analogues of three-dimensional Weyl points. This evidence of the topological nature of surface states in NbGeSb is encouraging for further work on improving the quality of the quantum oscillation data.

5.4 Summary

The main objective of this experiment was to detect quantum oscillations in high quality single crystals of NbGeSb and NbSiSb for the first time using the Shubnikov - de Haas effect. In this respect the measurement has been a great success. The reason for performing this measurement was to look for evidence of any topological nature in these materials. The development of the procedure for producing the high quality crystals of NbXSb presented in this chapter has been an on-going process

which has taken many years of trial and improvement. The first hints of quantum oscillations in the magnetoresistance came in late 2018 after many, slowly improving, growth attempts which were initially started in early 2016.

A detailed rotation study of the SdH quantum oscillations allowed us to track the SdH frequencies as a function of applied magnetic field angle which were then compared to the SdH frequencies from the band structure calculations. Much effort was put into carefully correcting the magnitude of the applied magnetic field experienced by each sample due to the relative position and rotation of the two samples measured. Estimates of the Berry phase have been extracted, both from Landau level index fan diagrams and from full LK fits, both of which suggest a topological nature in NbGeSb and possibly also in NbSiSb. The DFT calculation for NbGeSb match fairly well with the observed SdH data, however, the higher predicted frequency from the electron-like band was not observed. It is essential that effort is put into observing this frequency as this is thought to be the origin of the Dirac-like linear dispersion predicted from band structure calculations. The DFT calculations for NbSiSb do not resemble the observed SdH frequencies for the most part. Further work on these calculations is needed, which will need to be guided by additional experiments discussed below.

5.4.1 Future work

NbGeSb: There are many interesting features of the data presented here on NbGeSb, most notably the negative MR at low fields, the origins of which are as yet unaccounted for. In order to investigate this phenomenon further, it would be useful to screen many more NbGeSb samples which have undergone more annealing to improve the crystal quality. This was not possible due to the time constraints of running the dilution refrigerator which can only measure so many samples at a time and usually runs for months at a time. Further crystal growths of NbGeSb are planned with the aim of improving the sample purity to allow a better quality of quantum oscillation data to be collected allowing a better comparison to DFT calculations. Measuring the dHvA effect in NbGeSb at low field could also help to rule out the nature of this feature, this much more sensitive technique would also allow us to detect the missing high frequency predicted from band structure calculations.

NbSiSb: Work by Pezzini *et al.* on ZrSiS using a high magnetic field facility have shown an unusual mass enhancement of quasiparticles in strong magnetic fields [142]. As NbSiSb has shown similar features (such as a large non-saturating positive MR) high field measurements would prove useful for further elucidating the nature of the quasiparticles. Measurements are planned at the High Magnetic Field Lab (HMFL) in Nijmegen in early 2020 where the dHvA and the SdH effects will be probed in fields up to 35 T. These measurements will also aid in the understanding of the large number of frequencies observed in the initial SdH FFT spectra, allowing MB orbits to be identified and the MI to be modelled.

A careful Hall effect study for both materials would enable a better comparison of the measured effective masses from quantum oscillation studies to the calculated effective masses from DFT calculations. The results from a recent preliminary Hall study are presented in Appendix B.1.2.

CHAPTER 6

CONCLUSIONS

6.1 YFe_2Ge_2

Quantum oscillations have been measured using the de Haas - van Alphen effect in magnetic fields up to 18 T. Comparing the rotational dependence of the observed frequencies to recent DFT calculations, using an updated experimental Z-parameter for Ge, we have established that the Fermi surface is consistent with the predicted 3D surface with four Fermi surface sheets. Measurements of the quasiparticle masses were used to determine the mass enhancement between the band structure calculated quasiparticle effective masses and those observed. We find that a mass enhancement of a factor of $\sim$ 3-4 in the three hole sheets, which is inconsistent with the mass enhancement extracted from heat capacity data which predicts an enhancement of a factor of six. We conclude that the missing mass enhancement could come from the electron pocket of the Fermi surface, however preliminary measurements that have been presented seem to suggest this is not the case. Alternatively, a field induced suppression of the electron correlations lowers the mass enhancement in strong magnetic fields, as evidenced by recent heat capacity measurements at 10 T.

6.1.1 Future work

We hope that with ongoing improvements in sample quality further quantum oscillation measurements can be performed at higher fields at national facility such as the High Magnetic Field Laboratory in Nijmegen, Netherlands. A proposal to perform these measurements has already been approved. The access to higher fields will allow us to search for the missing/partially observed electron pocket and pin down its mass enhancement with more confidence, it will also allow us to rule out any additional Fermi surface sheets not predicted in the latest calculations, but which had been previously predicted. Further specific heat measurements on the latest batch of samples in fields greater than 10 T would allow the nature of the possible suppression of electronic correlations to be understood and provide

further evidence that this is the source of the observed missing mass enhancement. Measurements of quantum oscillations under applied pressure on the latest single crystal samples would allow the predicted QCP to be probed experimentally as the effect of pressure moves YFe_2Ge_2 closer towards the quantum critical region.

6.2 NbXSb

6.2.1 NbGeSb

Quantum oscillations have been measured using the Shubnikov - de Haas effect in magnetic fields up to 18 T. Comparing the rotational dependence of the observed frequencies to recent DFT calculations, using the experimental Z-parameters from recent single crystal XRD measurements, we have established that the Fermi surface is consistent with the predicted 3D surface with three Fermi surface sheets. Of the three predicted Fermi surface sheets, only one of the observed frequencies has been matched well with the calculated frequency, the hole sheet from band 66. Measurements of the quasiparticle masses were used to determine any possible mass enhancement between the band structure calculated quasiparticle effective masses and those observed.

6.2.2 NbSiSb

Quantum oscillations have been measured using the Shubnikov - de Haas effect in magnetic fields up to 18 T. Comparing the rotational dependence of the observed frequencies to recent DFT calculations, using the experimental Z-parameters from recent single crystal XRD measurements, we have established that the Fermi surface is not consistent with the predicted 3D surface with three Fermi surface sheets. Of the three predicted Fermi surface sheets, only one of the observed frequencies has resembles the calculated frequency, the hole sheet from band 62. Measurements of the quasiparticle masses were used to determine the mass enhancement between the band structure calculated quasiparticle effective masses and those observed.

6.2.3 Future work

The latest batch of high quality single crystals are due to be measured at the High Magnetic Field Laboratory in Nijmegen, Netherlands where further quantum oscillation measurements can be performed at higher fields. We will use this opportunity to measure the de Haas - van Alphen effect in these samples and we hope that the increased sensitivity of this techniques, along with the access to stronger magnetic fields (up to 35 T) will allow us to search for the missing Fermi surface sheets that have been predicted in NbGeSb, and to help understand the complex FFT frequency spectrum in

NbSiSb. It will also be interesting to see if the unusual negative magnetoresistance feature that has been observed at low fields in NbGeSb has any signatures that show up in the magnetic susceptibility.

REFERENCES

[1] Yoshinori Tokura, Masashi Kawasaki, and Naoto Nagaosa. Emergent functions of quantum materials. *Nature Physics*, 13(11):1056–1068, November 2017.

[2] Lev Landau. The Theory of a Fermi Liquid. *Journal of Experimental and Theoretical Physics*, 3(6):920, 1956.

[3] A. J. Schofield. Non-Fermi liquids. *Contemporary Physics*, 40(2):95–115, March 1999.

[4] Jing-Rong Wang, Guo-Zhu Liu, and Chang-Jin Zhang. Topological quantum critical point in a triple-Weyl semimetal: Non-Fermi-liquid behavior and instabilities. *Physical Review B*, 99(19):195119, May 2019.

[5] Alessandro Principi, Giovanni Vignale, and E. Rossi. Kondo effect and non-Fermi-liquid behavior in Dirac and Weyl semimetals. *Physical Review B*, 92(4):041107, July 2015.

[6] H. v. Löhneysen, T. Pietrus, G. Portisch, H. G. Schlager, A. Schröder, M. Sieck, and T. Trappmann. Non-Fermi-liquid behavior in a heavy-fermion alloy at a magnetic instability. *Physical Review Letters*, 72(20):3262–3265, May 1994.

[7] J. Custers, P. Gegenwart, H. Wilhelm, K. Neumaier, Y. Tokiwa, O. Trovarelli, C. Geibel, F. Steglich, C. Pépin, and P. Coleman. The break-up of heavy electrons at a quantum critical point. *Nature*, 424(6948):524–527, July 2003.

[8] Hiroaki Shishido, Rikio Settai, Hisatomo Harima, and Yoshichika Ōnuki. A Drastic Change of the Fermi Surface at a Critical Pressure in $CeRhIn_5$: dHvA Study under Pressure. *Journal of the Physical Society of Japan*, 74(4):1103–1106, April 2005.

[9] R. P. Smith, M. Sutherland, G. G. Lonzarich, S. S. Saxena, N. Kimura, S. Takashima, M. Nohara, and H. Takagi. Marginal breakdown of the Fermi-liquid state on the border of metallic ferromagnetism. *Nature*, 455(7217):1220–1223, October 2008.

[10] Mike Sutherland, R. P. Smith, N. Marcano, Y. Zou, S. E. Rowley, F. M. Grosche, N. Kimura, S. M. Hayden, S. Takashima, M. Nohara, and H. Takagi. Transport and thermodynamic evidence for a marginal Fermi-liquid state in $ZrZn_2$. *Physical Review B*, 85(3):035118, January 2012.

[11] P. B. Littlewood and C. M. Varma. Phenomenology of the superconductive state of a marginal Fermi liquid. *Physical Review B*, 46(1):405–420, July 1992.

[12] Jing-Rong Wang, Guo-Zhu Liu, and Chang-Jin Zhang. Breakdown of Fermi liquid theory in topological multi-Weyl semimetals. *Physical Review B*, 98(20):205113, November 2018.

[13] Y. Zou, Z. Feng, P. W. Logg, J. Chen, G. Lampronti, and F. M. Grosche. Fermi liquid breakdown and evidence for superconductivity in YFe_2Ge_2. *physica status solidi (RRL) – Rapid Research Letters*, 8(11):928–930, November 2014.

[14] Tetsuya Fujiwara, Naofumi Aso, Hideaki Yamamoto, Masato Hedo, Yuta Saiga, Masakazu Nishi, Yoshiya Uwatoko, and Kazuma Hirota. Pressure Effect on Magnetic Short Range Ordering of $LuFe_2Ge_2$. *Journal of the Physical Society of Japan*, 76(Suppl.A):60–61, January 2007.

[15] W. Pauli. Über Gasentartung und Paramagnetismus. *Zeitschrift für Physik A Hadrons and nuclei*, 41(2):81–102, June 1927.

[16] H. R. Ott, H. Rudigier, Z. Fisk, and J. L. Smith. UBe_{13}: An Unconventional Actinide Superconductor. *Physical Review Letters*, 50(20):1595–1598, May 1983.

[17] Patrick A. Lee and T. V. Ramakrishnan. Disordered electronic systems. *Reviews of Modern Physics*, 57(2):287–337, April 1985.

[18] John A. Hertz. Quantum critical phenomena. *Physical Review B*, 14(3):1165–1184, August 1976.

[19] Hilbert v. Löhneysen, Achim Rosch, Matthias Vojta, and Peter Wölfle. Fermi-liquid instabilities at magnetic quantum phase transitions. *Reviews of Modern Physics*, 79(3):1015–1075, August 2007.

[20] J. M. Luttinger. Fermi Surface and Some Simple Equilibrium Properties of a System of Interacting Fermions. *Physical Review*, 119(4):1153–1163, August 1960.

[21] Masaki Oshikawa. Topological Approach to Luttinger's Theorem and the Fermi Surface of a Kondo Lattice. *Physical Review Letters*, 84(15):3370–3373, April 2000.

[22] Lev Landau. Diamagnetism of Metals. *Zeitschrift für Physik A Hadrons and Nuclei*, 64(9):629–637, 1930.

[23] L Schubnikow and W J de Haas. Magnetische Widerstandsvergrösserung in Einkristallen von Wismut bei tiefen Temperaturen. *Proceedings of the royal netherlands academy of arts and science,*, 33(2):130–133, 1930.

[24] W. J. de Haas and P. M. van Alphen. The dependence of the susceptibility of diamagnetic metals upon the field. *Proceedings of the royal netherlands academy of arts and science,*, 30(10):1106–1118, 1930.

[25] D. Shoenberg. *Magnetic Oscillations in Metals*. Cambridge University Press, 1984.

[26] L Onsager. Interpretation of the de Haas-van Alphen effect. *The London, Edinburgh, and Dublin Philosophical Magazine and Journal of Science*, 43(344):1006–1008, 1952.

[27] R. B. Dingle. Some Magnetic Properties of Metals. II. The Influence of Collisions on the Magnetic Behaviour of Large Systems. *Proceedings of the Royal Society of London Series A*, 211:517–525, 1952.

[28] I. M. Lifshitz and A. M. Kosevic. Theory of magnetic susceptibility in metals at low temperatures. *Sov. Phys. JETP*, 2(4):636–645,, 1956.

[29] M. G. Priestley and David Shoenberg. An experimental study of the Fermi surface of magnesium. *Proceedings of the Royal Society of London. Series A. Mathematical and Physical Sciences*, 276(1365):258–277, November 1963.

[30] E. I. Blount. Bloch Electrons in a Magnetic Field. *Physical Review*, 126(5):1636–1653, June 1962.

[31] Mets501. Helium phase diagram.Data from Matter and methods at low temperatures, F Pobell, 2007., March 2013.

[32] H. London, G. R. Clarke, and Eric Mendoza. Osmotic pressure of He^3 in liquid He^4, with proposals for a refrigerator to work below 1K. *Physical Review*, 128(5):1992–2005, December 1962.

[33] Frank Pobell. *Matter and Methods at Low Temperatures*. Springer, 3rd edition, 2007.

[34] Steffen Schlör. English: Sketch of a wet helium dilution refrigerator, February 2019.

[35] R. G Goodrich, Donavan Hall, Eric Palm, and Tim Murphy. Magnetoresistance below 1K and temperature cycling of ruthenium oxide–bismuth ruthenate cryogenic thermometers. *Cryogenics*, 38(2):221–225, February 1998.

[36] E. N. Adams and T. D. Holstein. Quantum theory of transverse galvano-magnetic phenomena. *Journal of Physics and Chemistry of Solids*, 10(4):254–276, August 1959.

[37] Yoichi Kamihara, Hidenori Hiramatsu, Masahiro Hirano, Ryuto Kawamura, Hiroshi Yanagi, Toshio Kamiya, and Hideo Hosono. Iron-Based Layered Superconductor: LaOFeP. *Journal of the American Chemical Society*, 128(31):10012–10013, August 2006.

[38] A. P. Drozdov, M. I. Eremets, I. A. Troyan, V. Ksenofontov, and S. I. Shylin. Conventional superconductivity at 203 Kelvin at high pressures in the sulfur hydride system. *Nature*, 525(7567):73–76, September 2015.

[39] A. P. Drozdov, P. P. Kong, V. S. Minkov, S. P. Besedin, M. A. Kuzovnikov, S. Mozaffari, L. Balicas, F. F. Balakirev, D. E. Graf, V. B. Prakapenka, E. Greenberg, D. A. Knyazev, M. Tkacz, and M. I. Eremets. Superconductivity at 250 K in lanthanum hydride under high pressures. *Nature*, 569(7757):528–531, May 2019.

[40] J. Bardeen, L. N. Cooper, and J. R. Schrieffer. Theory of Superconductivity. *Physical Review*, 108(5):1175–1204, December 1957.

[41] B. T. Matthias, V. B. Compton, and E. Corenzwit. Some new superconducting compounds. *Journal of Physics and Chemistry of Solids*, 19(1):130–133, April 1961.

[42] B. S. Chandrasekhar and J. K. Hulm. The electrical resistivity and super-conductivity of some uranium alloys and compounds. *Journal of Physics and Chemistry of Solids*, 7(2):259–267, November 1958.

[43] Hans F. Braun. Superconductivity of rare earth-iron silicides. *Physics Letters A*, 75(5):386–388, February 1980.

[44] Katsuya Shimizu, Tomohiro Kimura, Shigeyuki Furomoto, Keiki Takeda, Kazuyoshi Kontani, Yoshichika Onuki, and Kiichi Amaya. Superconductivity in the non-magnetic state of iron under pressure. *Nature*, 412(6844):316–318, July 2001.

[45] Fong-Chi Hsu, Jiu-Yong Luo, Kuo-Wei Yeh, Ta-Kun Chen, Tzu-Wen Huang, Phillip M. Wu, Yong-Chi Lee, Yi-Lin Huang, Yan-Yi Chu, Der-Chung Yan, and Maw-Kuen Wu. Superconductivity in the PbO-type structure α-FeSe. *Proceedings of the National Academy of Sciences*, 105(38):14262–14264, September 2008.

[46] X. C. Wang, Q. Q. Liu, Y. X. Lv, W. B. Gao, L. X. Yang, R. C. Yu, F. Y. Li, and C. Q. Jin. The superconductivity at 18 K in LiFeAs system. *Solid State Communications*, 148(11):538–540, December 2008.

[47] Yoichi Kamihara, Takumi Watanabe, Masahiro Hirano, and Hideo Hosono. Iron-Based Layered Superconductor La[$O_{1-x}F_x$]FeAs (x = 0.05-0.12) with T_c = 26 K. *Journal of the American Chemical Society*, 130(11):3296–3297, March 2008.

[48] Marianne Rotter, Marcus Tegel, and Dirk Johrendt. Superconductivity at 38 K in the Iron Arsenide $Ba_{1-x}K_xFe_2A_2$. *Physical Review Letters*, 101(10):107006, September 2008.

[49] Hiraku Ogino, Yutaka Matsumura, Yukari Katsura, Koichi Ushiyama, Shigeru Horii, Kohji Kishio, and Jun-ichi Shimoyama. Superconductivity at 17 K in (Fe_2P_2)($Sr_4Sc_2O_6$): a new superconducting layered pnictide oxide with a thick perovskite oxide layer. *Superconductor Science and Technology*, 22(7):075008, June 2009.

[50] Patricia L. Alireza, Y. T. Chris Ko, Jack Gillett, Chiara M. Petrone, Jacqueline M. Cole, Gilbert G. Lonzarich, and Suchitra E. Sebastian. Superconductivity up to 29 K in $SrFe_2As_2$ and $BaFe_2As_2$ at high pressures. *Journal of Physics: Condensed Matter*, 21(1):012208, December 2008.

[51] N. Ni, A. Thaler, A. Kracher, J. Q. Yan, S. L. Bud'ko, and P. C. Canfield. Phase diagrams of $Ba(Fe_{1-x}M_x)_2As_2$ single crystals (M=Rh and Pd). *Physical Review B*, 80(2):024511, July 2009.

[52] H. Chen, Y. Ren, Y. Qiu, Wei Bao, R. H. Liu, G. Wu, T. Wu, Y. L. Xie, X. F. Wang, Q. Huang, and X. H. Chen. Coexistence of the spin-density wave and superconductivity in $Ba_{1-x}K_xFe_2As_2$. *EPL (Europhysics Letters)*, 85(1):17006, January 2009.

[53] Johnpierre Paglione and Richard L. Greene. High-temperature superconductivity in iron-based materials. *Nature Physics*, 6(9):645–658, September 2010.

[54] F. Steglich, J. Aarts, C. D. Bredl, W. Lieke, D. Meschede, W. Franz, and H. Schäfer. Superconductivity in the Presence of Strong Pauli Paramagnetism: $CeCu_2Si_2$. *Physical Review Letters*, 43(25):1892–1896, December 1979.

[55] Hideo Hosono and Kazuhiko Kuroki. Iron-based superconductors: Current status of materials and pairing mechanism. *Physica C: Superconductivity and its Applications*, 514:399–422, July 2015.

[56] Steffen Backes, Daniel Guterding, Harald O. Jeschke, and Roser Valentí. Electronic structure and de Haas–van Alphen frequencies in KFe_2As_2 within LDA+DMFT. *New Journal of Physics*, 16(8):083025, August 2014.

[57] I. I. Mazin and J. Schmalian. Pairing symmetry and pairing state in ferropnictides: Theoretical overview. *Physica C: Superconductivity*, 469(9):614–627, May 2009.

[58] Matthew D. Watson, Pavel Dudin, Luke C. Rhodes, Daniil V. Evtushinsky, Hideaki Iwasawa, Saicharan Aswartham, Sabine Wurmehl, Bernd Büchner, Moritz Hoesch, and Timur K. Kim. Probing the reconstructed Fermi surface of antiferromagnetic $BaFe_2As_2$ in one domain. *npj Quantum Materials*, 4(1):1–9, July 2019.

[59] Jiasheng Chen, Konstantin Semeniuk, Zhuo Feng, Pascal Reiss, Yang Zou, Peter W. Logg, Giulio I. Lampronti, and F. Malte Grosche. Unconventional superconductivity in the layered iron germanide YFe_2Ge_2. *Physical Review Letters*, 116(12), March 2016.

[60] H. Shishido, A. F. Bangura, A. I. Coldea, S. Tonegawa, K. Hashimoto, S. Kasahara, P. M. C. Rourke, H. Ikeda, T. Terashima, R. Settai, Y. Ōnuki, D. Vignolles, C. Proust, B. Vignolle, A. McCollam, Y. Matsuda, T. Shibauchi, and A. Carrington. Evolution of the Fermi Surface of $BaFe_2(As_{1-x}P_x)_2$ on Entering the Superconducting Dome. *Physical Review Letters*, 104(5):057008, February 2010.

[61] Taichi Terashima, Nobuyuki Kurita, Motoi Kimata, Megumi Tomita, Satoshi Tsuchiya, Hidetaka Satsukawa, Atsushi Harada, Kaori Hazama, Motoharu Imai, Akira Sato, Shinya Uji, Kunihiro Kihou, Chul-Ho Lee, Hijiri Kito, Yasuhide Tomioka, Toshimitsu Ito, Akira Iyo, Hiroshi Eisaki, Tian Liang, Masamichi Nakajima, Shigeyuki Ishida, Shin-ichi Uchida, Taku Saito, Hideto Fukazawa, Yoh Kohori, and Hisatomo Harima. Quantum oscillations in iron-based superconductors: $BaFe_2As_2$ vs. KFe_2As_2. *Journal of Physics: Conference Series*, 449:012022, July 2013.

[62] Teppei Yoshida, Shin-ichiro Ideta, Ichiro Nishi, Atsushi Fujimori, Ming Yi, Rob Moore, Sung-Kwan Mo, Donghui Lu, Zhi-Xun Shen, Zahid Hussain, Kunihiro Kihou, C. H. Lee, Akira Iyo, Hiroshi Eisaki, and Hisatomo Harima. Orbital character and electron correlation effects on two- and three-dimensional Fermi surfaces in KFe_2As_2 revealed by angle-resolved photoemission spectroscopy. *Frontiers in Physics*, 2, 2014.

[63] H. Fukazawa, T. Saito, Y. Yamada, K. Kondo, M. Hirano, Y. Kohori, K. Kuga, A. Sakai, Y. Matsumoto, S. Nakatsuji, K. Kihou, A. Iyo, C. H. Lee, and H. Eisaki. NMR/NQR and Specific Heat Studies of Iron Pnictide Superconductor KFe_2As_2. *Journal of the Physical Society of Japan*, 80(Suppl.A):SA118, January 2011.

[64] G. Venturini and B. Malaman. X-ray single crystal refinements on some RT_2Ge_2 compounds (R = Ca, Y, La, Nd, U; T = Mn-Cu, Ru-Pd): evolution of the chemical bonds. *Journal of Alloys and Compounds*, 235(2):201–209, March 1996.

[65] Sándor Rózsa and Hans-Uwe Schuster. Zur Struktur von KFe_2As_2, KCo_2As_2, KRh_2As_2 / Crystal Structure of KFe_2As_2, KCo_2As_2, KRh_2As_2 and KRh_2P_2. *Zeitschrift für Naturforschung B*, 36(12):1668–1670, 2014.

[66] Yasuyuki Nakajima, Renxiong Wang, Tristin Metz, Xiangfeng Wang, Limin Wang, Hyunchae Cynn, Samuel T. Weir, Jason R. Jeffries, and Johnpierre Paglione. High-temperature superconductivity stabilized by electron-hole interband coupling in collapsed tetragonal phase of KFe_2As_2 under high pressure. *Physical Review B*, 91(6):060508, February 2015.

[67] Jiasheng Chen, Monika B. Gamża, Konstantin Semeniuk, and F. Malte Grosche. Composition dependence of bulk superconductivity in YFe_2Ge_2. *Physical Review B*, 99(2):020501, January 2019.

[68] K Semeniuk. *Correlated low temperature states of YFe_2Ge_2 and pressure metallised NiS_2*. PhD Thesis, University of Cambridge, 2018.

[69] Sheng Ran, Sergey L. Bud'ko, and Paul C. Canfield. Effects of substitution on low-temperature physical properties of $LuFe_2Ge_2$. *Philosophical Magazine*, 91(34):4388–4400, December 2011.

[70] M. A. Avila, S. L. Bud'ko, and P. C. Canfield. Anisotropic magnetization, specific heat and resistivity of RFe_2Ge_2 single crystals. *Journal of Magnetism and Magnetic Materials*, 270(1):51–76, March 2004.

[71] David J. Singh. Superconductivity and magnetism in YFe_2Ge_2. *Physical Review B*, 89(2):024505, January 2014.

[72] J. K. Dong, S. Y. Zhou, T. Y. Guan, H. Zhang, Y. F. Dai, X. Qiu, X. F. Wang, Y. He, X. H. Chen, and S. Y. Li. Quantum Criticality and Nodal Superconductivity in the FeAs-Based Superconductor KFe_2As_2. *Physical Review Letters*, 104(8):087005, February 2010.

[73] Yong Liu, M. A. Tanatar, V. G. Kogan, Hyunsoo Kim, T. A. Lograsso, and R. Prozorov. Upper critical field of high-quality single crystals of KFe_2As_2. *Physical Review B*, 87(13):134513, April 2013.

[74] N. Sirica, F. Bondino, S. Nappini, I. Píš, L. Poudel, A. D. Christianson, D. Mandrus, D. J. Singh, and N. Mannella. Spectroscopic evidence for strong quantum spin fluctuations with itinerant character in YFe_2Ge_2. *Physical Review B*, 91(12):121102, March 2015.

[75] Hongliang Wo, Qisi Wang, Yao Shen, Xiaowen Zhang, Yiqing Hao, Yu Feng, Shoudong Shen, Zheng He, Bingying Pan, Wenbin Wang, K. Nakajima, S. Ohira-Kawamura, P. Steffens, M. Boehm, K. Schmalzl, T.R. Forrest, M. Matsuda, Yang Zhao, J.W. Lynn, Zhiping Yin, and Jun Zhao. Coexistence of Ferromagnetic and Stripe-Type Antiferromagnetic Spin Fluctuations in YFe_2Ge_2. *Physical Review Letters*, 122(21):217003, May 2019.

[76] Alaska Subedi. Unconventional sign-changing superconductivity near quantum criticality in YFe_2Ge_2. *Physical Review B*, 89(2):024504, January 2014.

[77] Kazuhiko Kuroki, Seiichiro Onari, Ryotaro Arita, Hidetomo Usui, Yukio Tanaka, Hiroshi Kontani, and Hideo Aoki. Unconventional Pairing Originating from the Disconnected Fermi Surfaces of Superconducting $LaFeAsO_{1-x}F_x$. *Physical Review Letters*, 101(8):087004, August 2008.

[78] J. Chen. *Unconventional Superconductivity in the Layered Iron Germanide YFe_2Ge_2*. PhD Thesis, University of Cambridge, 2019.

[79] Hui Chang. *High Pressure Quantum Oscillation Study of the Mott Insulator NiS_2*. PhD Thesis, University of Cambridge, 2016.

[80] S. Hornfeldt, J. B. Ketterson, and L. R. Windmiller. Influence of field inhomogeneity on the de Haas-van Alphen effect. *Journal of Physics E: Scientific Instruments*, 6(3):265–268, March 1973.

[81] P. M. C. Rourke and S. R. Julian. Numerical extraction of de Haas–van Alphen frequencies from calculated band energies. *Computer Physics Communications*, 183(2):324–332, February 2012.

[82] Dong-Xia Qu, Y. S. Hor, Jun Xiong, R. J. Cava, and N. P. Ong. Quantum Oscillations and Hall Anomaly of Surface States in the Topological Insulator Bi_2Te_3. *Science*, 329(5993):821–824, August 2010.

[83] B. S. Tan, Y.-T. Hsu, B. Zeng, M. Ciomaga Hatnean, N. Harrison, Z. Zhu, M. Hartstein, M. Kiourlappou, A. Srivastava, M. D. Johannes, T. P. Murphy, J.-H. Park, L. Balicas, G. G. Lonzarich, G. Balakrishnan, and Suchitra E. Sebastian. Unconventional Fermi surface in an insulating state. *Science*, 349(6245):287–290, July 2015.

[84] Jing Wang and Shou-Cheng Zhang. Topological states of condensed matter. *Nature Materials*, 16(11):1062–1067, November 2017.

[85] K. v. Klitzing, G. Dorda, and M. Pepper. New Method for High-Accuracy Determination of the Fine-Structure Constant Based on Quantized Hall Resistance. *Physical Review Letters*, 45(6):494–497, August 1980.

[86] R. B. Laughlin. Quantized Hall conductivity in two dimensions. *Physical Review B*, 23(10):5632–5633, May 1981.

[87] D. J. Thouless, M. Kohmoto, M. P. Nightingale, and M. den Nijs. Quantized Hall Conductance in a Two-Dimensional Periodic Potential. *Physical Review Letters*, 49(6):405–408, August 1982.

[88] Numpy Matplotlib Mencoder and a template by Josh Grj23 Glenton Jelbert Lifton 2004, using Python. Quantum Hall Effect, September 2009.

[89] B. Andrei Bernevig, Taylor L. Hughes, and Shou-Cheng Zhang. Quantum Spin Hall Effect and Topological Phase Transition in HgTe Quantum Wells. *Science*, 314(5806):1757–1761, December 2006.

[90] Markus König, Steffen Wiedmann, Christoph Brüne, Andreas Roth, Hartmut Buhmann, Laurens W. Molenkamp, Xiao-Liang Qi, and Shou-Cheng Zhang. Quantum Spin Hall Insulator State in HgTe Quantum Wells. *Science*, 318(5851):766–770, November 2007.

[91] Xiao-Liang Qi and Shou-Cheng Zhang. Topological insulators and superconductors. *Reviews of Modern Physics*, 83(4):1057–1110, October 2011.

[92] M. Z. Hasan and C. L. Kane. Colloquium: Topological insulators. *Reviews of Modern Physics*, 82(4):3045–3067, November 2010.

[93] C. L. Kane and E. J. Mele. Quantum Spin Hall Effect in Graphene. *Physical Review Letters*, 95(22):226801, November 2005.

[94] B. Andrei Bernevig and Shou-Cheng Zhang. Quantum Spin Hall Effect. *Physical Review Letters*, 96(10):106802, March 2006.

[95] C. L. Kane and E. J. Mele. Z_2 Topological Order and the Quantum Spin Hall Effect. *Physical Review Letters*, 95(14):146802, September 2005.

[96] J. E. Moore and L. Balents. Topological invariants of time-reversal-invariant band structures. *Physical Review B*, 75(12):121306, March 2007.

[97] Liang Fu and C. L. Kane. Topological insulators with inversion symmetry. *Physical Review B*, 76(4):045302, July 2007.

[98] Rahul Roy. Topological phases and the quantum spin Hall effect in three dimensions. *Physical Review B*, 79(19):195322, May 2009.

[99] F. D. M. Haldane. Model for a Quantum Hall Effect without Landau Levels: Condensed-Matter Realization of the "Parity Anomaly". *Physical Review Letters*, 61(18):2015–2018, October 1988.

[100] Xiao-Liang Qi, Yong-Shi Wu, and Shou-Cheng Zhang. Topological quantization of the spin Hall effect in two-dimensional paramagnetic semiconductors. *Physical Review B*, 74(8):085308, August 2006.

[101] Chao-Xing Liu, Xiao-Liang Qi, Xi Dai, Zhong Fang, and Shou-Cheng Zhang. Quantum Anomalous Hall Effect in $Hg_{1-y}Mn_yTe$ Quantum Wells. *Physical Review Letters*, 101(14):146802, October 2008.

[102] Su-Yang Xu, Nasser Alidoust, Ilya Belopolski, Zhujun Yuan, Guang Bian, Tay-Rong Chang, Hao Zheng, Vladimir N. Strocov, Daniel S. Sanchez, Guoqing Chang, Chenglong Zhang, Daixiang Mou, Yun Wu, Lunan Huang, Chi-Cheng Lee, Shin-Ming Huang, BaoKai Wang, Arun Bansil, Horng-Tay Jeng, Titus Neupert, Adam Kaminski, Hsin Lin, Shuang Jia, and M. Zahid Hasan. Discovery of a Weyl fermion state with Fermi arcs in niobium arsenide. *Nature Physics*, 11(9):748–754, September 2015.

[103] Paul Adrien Maurice Dirac and Ralph Howard Fowler. The quantum theory of the electron. *Proceedings of the Royal Society of London. Series A, Containing Papers of a Mathematical and Physical Character*, 117(778):610–624, February 1928.

[104] Hermann Weyl. Gravitation and the Electron. *Proceedings of the National Academy of Sciences*, 15(4):323–334, April 1929.

[105] Ettore Majorana. Teoria simmetrica dell'elettrone e del positrone. *Il Nuovo Cimento (1924-1942)*, 14(4):171, September 2008.

[106] K. S. Novoselov, A. K. Geim, S. V. Morozov, D. Jiang, Y. Zhang, S. V. Dubonos, I. V. Grigorieva, and A. A. Firsov. Electric Field Effect in Atomically Thin Carbon Films. *Science*, 306(5696):666–669, October 2004.

[107] H. Cheun Lee, Wei-Wen Liu, Siang-Piao Chai, Abdul Rahman Mohamed, Azizan Aziz, Cheng-Seong Khe, N. M. S. Hidayah, and U. Hashim. Review of the synthesis, transfer, characterization and growth mechanisms of single and multilayer graphene. *RSC Advances*, 7(26):15644–15693, March 2017.

[108] Stephen L. Adler. Axial-Vector Vertex in Spinor Electrodynamics. *Physical Review*, 177(5):2426–2438, January 1969.

[109] J. S. Bell and R. Jackiw. A PCAC puzzle: $\pi_0 \longrightarrow \gamma\gamma$ in the σ-model. *Il Nuovo Cimento A (1965-1970)*, 60(1):47–61, March 1969.

[110] H. B. Nielsen and Masao Ninomiya. The Adler-Bell-Jackiw anomaly and Weyl fermions in a crystal. *Physics Letters B*, 130(6):389–396, November 1983.

[111] Xiangang Wan, Ari M. Turner, Ashvin Vishwanath, and Sergey Y. Savrasov. Topological semimetal and Fermi-arc surface states in the electronic structure of pyrochlore iridates. *Physical Review B*, 83(20):205101, May 2011.

[112] Gang Xu, Hongming Weng, Zhijun Wang, Xi Dai, and Zhong Fang. Chern Semimetal and the Quantized Anomalous Hall Effect in $HgCr_2Se_4$. *Physical Review Letters*, 107(18):186806, October 2011.

[113] Daniel Bulmash, Chao-Xing Liu, and Xiao-Liang Qi. Prediction of a Weyl semimetal in $Hg_{(1-x-y)}Cd_xMn_yTe$. *Physical Review B*, 89(8):081106, February 2014.

[114] B.Q. Lv, H.M. Weng, B.B. Fu, X.P. Wang, H. Miao, J. Ma, P. Richard, X.C. Huang, L.X. Zhao, G.F. Chen, Z. Fang, X. Dai, T. Qian, and H. Ding. Experimental Discovery of Weyl Semimetal TaAs. *Physical Review X*, 5(3):031013, July 2015.

[115] Su-Yang Xu, Ilya Belopolski, Daniel S. Sanchez, Chenglong Zhang, Guoqing Chang, Cheng Guo, Guang Bian, Zhujun Yuan, Hong Lu, Tay-Rong Chang, Pavel P. Shibayev, Mykhailo L. Prokopovych, Nasser Alidoust, Hao Zheng, Chi-Cheng Lee, Shin-Ming Huang, Raman Sankar, Fangcheng Chou, Chuang-Han Hsu, Horng-Tay Jeng, Arun Bansil, Titus Neupert, Vladimir N. Strocov, Hsin Lin, Shuang Jia, and M. Zahid Hasan. Experimental discovery of a topological Weyl semimetal state in TaP. *Science Advances*, 1(10):e1501092, November 2015.

[116] A.A Abrikosov and S.D Beneslavskii. Possible Existence of Substances Intermediate Between Metals and Dielectrics. *Journal of Experimental and Theoretical Physics*, 32(4):699, 1971.

[117] Zhijun Wang, Yan Sun, Xing-Qiu Chen, Cesare Franchini, Gang Xu, Hongming Weng, Xi Dai, and Zhong Fang. Dirac semimetal and topological phase transitions in A_3Bi (A= Na, K, Rb). *Physical Review B*, 85(19):195320, May 2012.

[118] S. M. Young, S. Zaheer, J. C. Y. Teo, C. L. Kane, E. J. Mele, and A. M. Rappe. Dirac Semimetal in Three Dimensions. *Physical Review Letters*, 108(14):140405, April 2012.

[119] Sergey Borisenko, Quinn Gibson, Danil Evtushinsky, Volodymyr Zabolotnyy, Bernd Büchner, and Robert J. Cava. Experimental Realization of a Three-Dimensional Dirac Semimetal. *Physical Review Letters*, 113(2):027603, July 2014.

[120] Madhab Neupane, Su-Yang Xu, Raman Sankar, Nasser Alidoust, Guang Bian, Chang Liu, Ilya Belopolski, Tay-Rong Chang, Horng-Tay Jeng, Hsin Lin, Arun Bansil, Fangcheng Chou, and M. Zahid Hasan. Observation of a three-dimensional topological Dirac semimetal phase in high-mobility Cd_3As_2. *Nature Communications*, 5(1):1–8, May 2014.

[121] Z. K. Liu, B. Zhou, Y. Zhang, Z. J. Wang, H. M. Weng, D. Prabhakaran, S.-K. Mo, Z. X. Shen, Z. Fang, X. Dai, Z. Hussain, and Y. L. Chen. Discovery of a Three-Dimensional Topological Dirac Semimetal, Na_3Bi. *Science*, 343(6173):864–867, February 2014.

[122] M. V. Berry. Aspects of Degeneracy. In Giulio Casati, editor, *Chaotic Behavior in Quantum Systems: Theory and Applications*, NATO ASI Series, pages 123–140. Springer US, Boston, MA, 1985.

[123] Su-Yang Xu, Ilya Belopolski, Nasser Alidoust, Madhab Neupane, Guang Bian, Chenglong Zhang, Raman Sankar, Guoqing Chang, Zhujun Yuan, Chi-Cheng Lee, Shin-Ming Huang, Hao Zheng, Jie Ma, Daniel S. Sanchez, BaoKai Wang, Arun Bansil, Fangcheng Chou, Pavel P. Shibayev, Hsin Lin, Shuang Jia, and M. Zahid Hasan. Discovery of a Weyl fermion semimetal and topological Fermi arcs. *Science*, 349(6248):613–617, August 2015.

[124] D. T. Son and B. Z. Spivak. Chiral anomaly and classical negative magnetoresistance of Weyl metals. *Physical Review B*, 88(10):104412, September 2013.

[125] A. A. Burkov. Chiral anomaly and transport in Weyl metals. *Journal of Physics: Condensed Matter*, 27(11):113201, February 2015.

[126] Yuya Ominato and Mikito Koshino. Magnetotransport in Weyl semimetals in the quantum limit: Role of topological surface states. *Physical Review B*, 93(24):245304, June 2016.

[127] Mikito Koshino and Intan Fatimah Hizbullah. Magnetic susceptibility in three-dimensional nodal semimetals. *Physical Review B*, 93(4):045201, January 2016.

[128] A. A. Burkov, M. D. Hook, and Leon Balents. Topological nodal semimetals. *Physical Review B*, 84(23):235126, December 2011.

[129] N.P. Armitage, E.J. Mele, and Ashvin Vishwanath. Weyl and Dirac semimetals in three-dimensional solids. *Reviews of Modern Physics*, 90(1):015001, January 2018.

[130] Alexey A. Soluyanov, Dominik Gresch, Zhijun Wang, QuanSheng Wu, Matthias Troyer, Xi Dai, and B. Andrei Bernevig. Type-II Weyl semimetals. *Nature*, 527(7579):495, November 2015.

[131] Hongming Weng, Chen Fang, Zhong Fang, B. Andrei Bernevig, and Xi Dai. Weyl Semimetal Phase in Noncentrosymmetric Transition-Metal Monophosphides. *Physical Review X*, 5(1):011029, March 2015.

[132] Petr Hořava. Stability of Fermi Surfaces and K Theory. *Physical Review Letters*, 95(1):016405, June 2005.

[133] T. T. Heikkilä and G. E. Volovik. Dimensional crossover in topological matter: Evolution of the multiple Dirac point in the layered system to the flat band on the surface. *JETP Letters*, 93(2):59–65, March 2011.

[134] Jiawei Ruan, Shao-Kai Jian, Hong Yao, Haijun Zhang, Shou-Cheng Zhang, and Dingyu Xing. Symmetry-protected ideal Weyl semimetal in HgTe-class materials. *Nature Communications*, 7(1):1–6, April 2016.

[135] Liang Fu, C. L. Kane, and E. J. Mele. Topological Insulators in Three Dimensions. *Physical Review Letters*, 98(10):106803, March 2007.

[136] A. J. Klein Haneveld and F. Jellinek. Zirconium silicide and germanide chalcogenides preparation and crystal structures. *Recueil des Travaux Chimiques des Pays-Bas*, 83(8):776–783, 1964.

[137] Qiunan Xu, Zhida Song, Simin Nie, Hongming Weng, Zhong Fang, and Xi Dai. Two-dimensional oxide topological insulator with iron-pnictide superconductor LiFeAs structure. *Physical Review B*, 92(20):205310, November 2015.

[138] Leslie M. Schoop, Mazhar N. Ali, Carola Straßer, Andreas Topp, Andrei Varykhalov, Dmitry Marchenko, Viola Duppel, Stuart S. P. Parkin, Bettina V. Lotsch, and Christian R. Ast. Dirac cone protected by non-symmorphic symmetry and three-dimensional Dirac line node in ZrSiS. *Nature Communications*, 7(1):1–7, May 2016.

[139] Mazhar N. Ali, Leslie M. Schoop, Chirag Garg, Judith M. Lippmann, Erik Lara, Bettina Lotsch, and Stuart S. P. Parkin. Butterfly magnetoresistance, quasi-2d Dirac Fermi surface and topological phase transition in ZrSiS. *Science Advances*, 2(12):e1601742, December 2016.

[140] Xuefeng Wang, Xingchen Pan, Ming Gao, Jihai Yu, Juan Jiang, Junran Zhang, Huakun Zuo, Minhao Zhang, Zhongxia Wei, Wei Niu, Zhengcai Xia, Xiangang Wan, Yulin Chen, Fengqi Song, Yongbing Xu, Baigeng Wang, Guanghou Wang, and Rong Zhang. Evidence of Both Surface and Bulk Dirac Bands and Anisotropic Nonsaturating Magnetoresistance in ZrSiS. *Advanced Electronic Materials*, 2(10):1600228, 2016.

[141] Ratnadwip Singha, Arnab Kumar Pariari, Biswarup Satpati, and Prabhat Mandal. Large nonsaturating magnetoresistance and signature of nondegenerate Dirac nodes in ZrSiS. *Proceedings of the National Academy of Sciences*, 114(10):2468–2473, March 2017.

[142] S. Pezzini, M. R. van Delft, L. M. Schoop, B. V. Lotsch, A. Carrington, M. I. Katsnelson, N. E. Hussey, and S. Wiedmann. Unconventional mass enhancement around the Dirac nodal loop in ZrSiS. *Nature Physics*, 14(2):178–183, February 2018.

[143] Maximilian Trescher, Emil J. Bergholtz, and Johannes Knolle. Quantum oscillations and magnetoresistance in type-II Weyl semimetals: Effect of a field-induced charge density wave. *Physical Review B*, 98(12):125304, September 2018.

[144] B.-B. Fu, C.-J. Yi, T.-T. Zhang, M. Caputo, J.-Z. Ma, X. Gao, B. Q. Lv, L.-Y. Kong, Y.-B. Huang, P. Richard, M. Shi, V. N. Strocov, C. Fang, H.-M. Weng, Y.-G. Shi, T. Qian, and H. Ding. Dirac nodal surfaces and nodal lines in ZrSiS. *Science Advances*, 5(5):645–9, May 2019.

[145] M. Novak, S. N. Zhang, F. Orbanić, N. Biliškov, G. Eguchi, S. Paschen, A. Kimura, X. X. Wang, T. Osada, K. Uchida, M. Sato, Q. S. Wu, O. V. Yazyev, and I. Kokanović. Highly anisotropic interlayer magnetoresitance in ZrSiS nodal-line Dirac semimetal. *Physical Review B*, 100(8):085137, August 2019.

[146] Chris P. Weber, Leslie M. Schoop, Stuart S. P. Parkin, Robert C. Newby, Alex Nateprov, Bettina Lotsch, Bala Murali Krishna Mariserla, J. Matthew Kim, Keshav M. Dani, Hans A. Bechtel, Ernest Arushanov, and Mazhar Ali. Directly photoexcited Dirac and Weyl fermions in ZrSiS and NbAs. *Applied Physics Letters*, 113(22):221906, November 2018.

[147] Chih-Chuan Su, Chi-Sheng Li, Tzu-Cheng Wang, Syu-You Guan, Raman Sankar, Fangcheng Chou, Chia-Seng Chang, Wei-Li Lee, Guang-Yu Guo, and Tien-Ming Chuang. Surface termination dependent quasiparticle scattering interference and magneto-transport study on ZrSiS. *New Journal of Physics*, 20(10):103025, October 2018.

[148] Vancliff Johnson and Wolfgang Jeitschko. PbFCl-type pnictides of niobium with silicon or germanium. *Journal of Solid State Chemistry*, 6(2):306–309, February 1973.

[149] Joonbum Park, G. Lee, F. Wolff-Fabris, Y. Y. Koh, M. J. Eom, Y. K. Kim, M. A. Farhan, Y. J. Jo, C. Kim, J. H. Shim, and J. S. Kim. Anisotropic Dirac Fermions in a Bi Square Net of $SrMnBi_2$. *Physical Review Letters*, 107(12):126402, September 2011.

[150] Andrew F. May, Michael A. McGuire, and Brian C. Sales. Effect of Eu magnetism on the electronic properties of the candidate Dirac material $EuMnBi_2$. *Physical Review B*, 90(7):075109, August 2014.

[151] Geunsik Lee, Muhammad A. Farhan, Jun Sung Kim, and Ji Hoon Shim. Anisotropic Dirac electronic structures of $AMnBi_2$ (A= Sr, Ca). *Physical Review B*, 87(24):245104, June 2013.

[152] Peer Schmidt, Michael Binnewies, Robert Glaum, and Marcus Schmidt. Chemical Vapor Transport Reactions–Methods, Materials, Modeling. *Advanced Topics on Crystal Growth*, February 2013.

[153] Tian Liang, Quinn Gibson, Mazhar N. Ali, Minhao Liu, R. J. Cava, and N. P. Ong. Ultrahigh mobility and giant magnetoresistance in the Dirac semimetal Cd_3As_2. *Nature Materials*, 14(3):280–284, March 2015.

[154] Chandra Shekhar, Ajaya K. Nayak, Yan Sun, Marcus Schmidt, Michael Nicklas, Inge Leermakers, Uli Zeitler, Yurii Skourski, Jochen Wosnitza, Zhongkai Liu, Yulin Chen, Walter Schnelle, Horst Borrmann, Yuri Grin, Claudia Felser, and Binghai Yan. Extremely large magnetoresistance and ultrahigh mobility in the topological Weyl semimetal candidate NbP. *Nature Physics*, 11(8):645–649, August 2015.

[155] Mazhar N. Ali, Leslie Schoop, Jun Xiong, Steven Flynn, Quinn Gibson, Max Hirschberger, N. P. Ong, and R. J. Cava. Correlation of crystal quality and extreme magnetoresistance of WTe_2. *EPL (Europhysics Letters)*, 110(6):67002, June 2015.

[156] P. B. Alers and R. T. Webber. The Magnetoresistance of Bismuth Crystals at Low Temperatures. *Physical Review*, 91(5):1060–1065, September 1953.

[157] Clifford W. Hicks, Alexandra S. Gibbs, Andrew P. Mackenzie, Hiroshi Takatsu, Yoshiteru Maeno, and Edward A. Yelland. Quantum Oscillations and High Carrier Mobility in the Delafossite $PdCoO_2$. *Physical Review Letters*, 109(11):116401, September 2012.

[158] P. Kumar Sudesh and S. Patnaik. Origin of exceptional magneto-resistance in Weyl semimetal $TaSb_2$. *Journal of Physics Communications*, 3(11):115007, November 2019.

[159] F. F. Tafti, Q. D. Gibson, S. K. Kushwaha, N. Haldolaarachchige, and R. J. Cava. Resistivity plateau and extreme magnetoresistance in LaSb. *Nature Physics*, 12(3):272–277, March 2016.

[160] Shanshan Sun, Qi Wang, Peng-Jie Guo, Kai Liu, and Hechang Lei. Large magnetoresistance in LaBi: origin of field-induced resistivity upturn and plateau in compensated semimetals. *New Journal of Physics*, 18(8):082002, August 2016.

[161] Kefeng Wang, D. Graf, Lijun Li, Limin Wang, and C. Petrovic. Anisotropic giant magnetoresistance in $NbSb_2$. *Scientific Reports*, 4(1):1–6, December 2014.

[162] Zhujun Yuan, Hong Lu, Yongjie Liu, Junfeng Wang, and Shuang Jia. Large magnetoresistance in compensated semimetals $TaAs_2$ and $NbAs_2$. *Physical Review B*, 93(18):184405, May 2016.

[163] Jin Hu, Zhijie Tang, Jinyu Liu, Xue Liu, Yanglin Zhu, David Graf, Kevin Myhro, Son Tran, Chun Ning Lau, Jiang Wei, and Zhiqiang Mao. Evidence of Topological Nodal-Line Fermions in ZrSiSe and ZrSiTe. *Physical Review Letters*, 117(1):016602, June 2016.

[164] Ratnadwip Singha, Arnab Pariari, Biswarup Satpati, and Prabhat Mandal. Magnetotransport properties and evidence of a topological insulating state in LaSbTe. *Physical Review B*, 96(24):245138, December 2017.

[165] Yongkang Luo, R. D. McDonald, P. F. S. Rosa, B. Scott, N. Wakeham, N. J. Ghimire, E. D. Bauer, J. D. Thompson, and F. Ronning. Anomalous electronic structure and magnetoresistance in $TaAs_2$. *Scientific Reports*, 6(1):1–7, June 2016.

[166] H. Murakawa, M. S. Bahramy, M. Tokunaga, Y. Kohama, C. Bell, Y. Kaneko, N. Nagaosa, H. Y. Hwang, and Y. Tokura. Detection of Berry's Phase in a Bulk Rashba Semiconductor. *Science*, 342(6165):1490–1493, December 2013.

[167] Mark V. Kartsovnik. High Magnetic Fields: A Tool for Studying Electronic Properties of Layered Organic Metals. *Chemical Reviews*, 104(11):5737–5782, November 2004.

[168] I. M. Tsidilkovskii, W. Giriat, G. I. Kharus, and E. A. Neifeld. Longitudinal Magnetoresistance and Hall Effect of $Cd_xHg_{1-x}Te$ in Strong Magnetic Fields. *physica status solidi (b)*, 64(2):717–727, 1974.

[169] N. Kikugawa, P. Goswami, A. Kiswandhi, E. S. Choi, D. Graf, R. E. Baumbach, J. S. Brooks, K. Sugii, Y. Iida, M. Nishio, S. Uji, T. Terashima, P. M. C. Rourke, N. E. Hussey, H. Takatsu, S. Yonezawa, Y. Maeno, and L. Balicas. Interplanar coupling-dependent magnetoresistivity in high-purity layered metals. *Nature Communications*, 7(1):1–8, March 2016.

[170] Jun Xiong, Satya K. Kushwaha, Tian Liang, Jason W. Krizan, Max Hirschberger, Wudi Wang, R. J. Cava, and N. P. Ong. Evidence for the chiral anomaly in the Dirac semimetal Na_3Bi. *Science*, 350(6259):413–416, October 2015.

[171] Timo Schumann, Manik Goyal, David A. Kealhofer, and Susanne Stemmer. Negative magnetoresistance due to conductivity fluctuations in films of the topological semimetal Cd_3As_2. *Physical Review B*, 95(24):241113, June 2017.

[172] Jochen Heyd, Gustavo E. Scuseria, and Matthias Ernzerhof. Hybrid functionals based on a screened Coulomb potential. *The Journal of Chemical Physics*, 118(18):8207–8215, April 2003.

[173] Andreas Topp, Raquel Queiroz, Andreas Grüneis, Lukas Müchler, Andreas W. Rost, Andrei Varykhalov, Dmitry Marchenko, Maxim Krivenkov, Fanny Rodolakis, Jessica L. McChesney, Bettina V. Lotsch, Leslie M. Schoop, and Christian R. Ast. Surface Floating 2d Bands in Layered Nonsymmorphic Semimetals: ZrSiS and Related Compounds. *Physical Review X*, 7(4):041073, December 2017.

[174] I. Marković, C. A. Hooley, O. J. Clark, F. Mazzola, M. D. Watson, J. M. Riley, K. Volckaert, K. Underwood, M. S. Dyer, P. a. E. Murgatroyd, K. J. Murphy, P. Le Fèvre, F. Bertran, J. Fujii, I. Vobornik, S. Wu, T. Okuda, J. Alaria, and P. D. C. King. Weyl-like points from band inversions of spin-polarised surface states in NbGeSb. *Nature Communications*, 10(1):1–8, December 2019.

APPENDIX A

APPENDIX

A.1 YFe_2Ge_2

A.1.1 Preliminary quantum oscillation measurements: TDO

Figure A.1 shows the first measured quantum oscillation signal in YFe_2Ge_2 using the tunnel diode oscillator (TDO) technique at 150 mK using the Cambridge dilution refrigerator. The TDO setup and signal optimisation were performed by Dr. Jordan Baglo. The data are quite noisy but the frequency at 1.22 kT can clearly be observed.

This then motivated us to improve the quality of the data. Figure A.2 shows the same sample and TDO coil after a large effort to improve the signal to noise, while the data is of better quality than the initial measurement of Figure A.1, only the single frequency is observed. The TDO technique will always dump heat into the sample as the tunnel diode is powered on, the lowest temperatures we were able to reach were of the order of 150 mK with the tunnel diode powered on. This severely limited the frequencies that we could observe in YFe_2Ge_2 as several heavy masses had been predicted which would have been smeared out by the thermal damping factor. This prompted us to try the dHvA technique and to focus our efforts on this, now that we had observed quantum oscillations in this new batch of high quality single crystals.

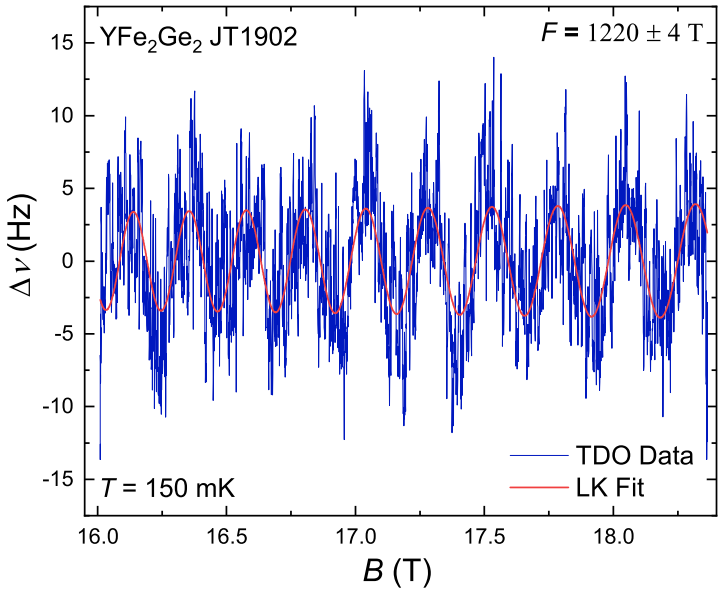

Fig. A.1 Preliminary TDO measurement of quantum oscillations in YFe_2Ge_2, at 150 mK - before signal optimisation.

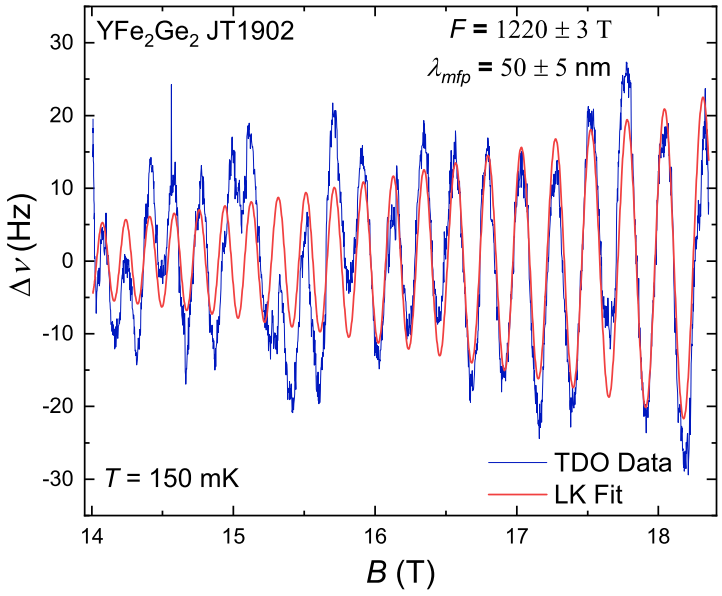

Fig. A.2 Preliminary TDO measurement of quantum oscillations in YFe_2Ge_2, at 150 mK - after signal optimisation.

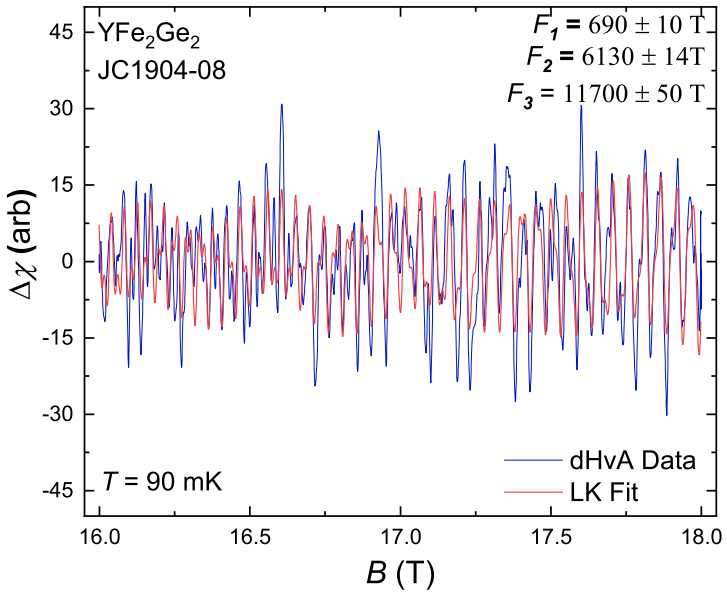

Fig. A.3 Preliminary dHvA measurement of quantum oscillations in YFe_2Ge_2, at 90 mK - after some signal optimisation.

A.1.2 Preliminary quantum oscillation measurements: dHvA

Figure A.3 shows the first attempt at setting up a dHvA coil to measure quantum oscillations in YFe_2Ge_2, the data are of a much higher quality than seen with the TDO technique and we were able to obtain a lower temperature of 90 mK. From this initial measurement which was done at a fixed angle of H||c we were able to observe at least three frequencies, which later turned out to be the peaks labelled δ, β and 2β. After this initial measurement, which was tagged onto a dilution fridge run as an additional measurement, a dedicated full rotation experiment was set up which forms the majority of this thesis. A lot more time was invested into the set up of the dHvA coils and their optimisation.

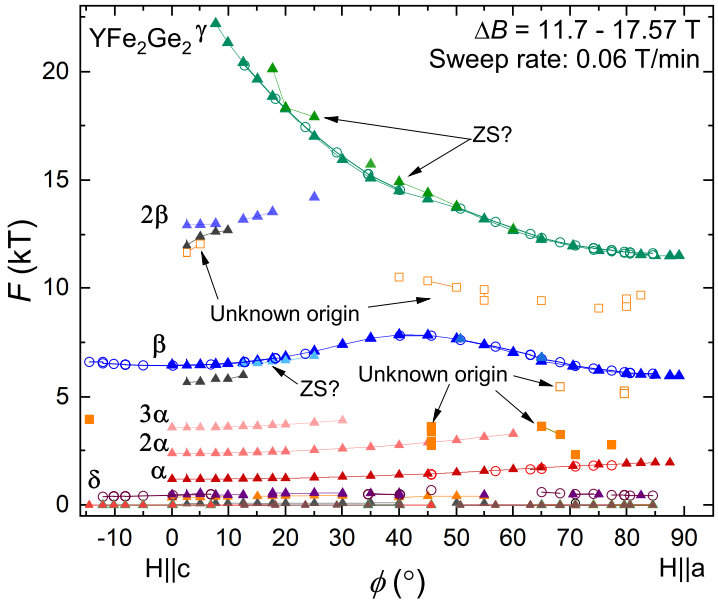

Fig. A.4 Full dHvA rotation measurement from both samples JC1904-08 and JT1902-06. ZS = Zeeman splitting, suspected peaks resulting from spin splitting have been coloured to match the peak it is thought they originate from. Peaks of unknown origin have been coloured orange and are from sample JT1902-06 (solid squares) and sample JC1904-08 (open squares).

A.1.3 Full rotation study

Figure A.4 shows the full rotation study from both measured dHvA samples in which spurious peaks have not been removed.

APPENDIX B

APPENDIX

B.1 NbXSb

B.1.1 Fitting of Gaussian peaks to quantum oscillation FFT spectra

In order to separate the many closely spaced peaks present in the quantum oscillation data, specifically in NbSiSb, a multi-peak Gaussian analysis techniques was employed. Figure B.1 shows a representative example of four closely spaced peaks present in NbSiSb at 55 mK at an angle of $\phi = 30.1°$. The measured FFT spectra (solid black line) is reproduced from a combination of two fits (dashed dark/light blue lines). This first fit of two peaks is achieved via the addition of the amplitudes from f_1 (dashed red line) and f_2 (dashed green line) resulting in the dashed dark blue line. The second fit of three peaks is achieved via the addition of the amplitudes from f_3 (dashed red line), f_4 (dashed green line) and f_5 (dashed dark blue line) resulting in the dashed light blue line. This method was particularly necessary when estimating the effective quasiparticle masses using the quantum oscillation amplitudes.

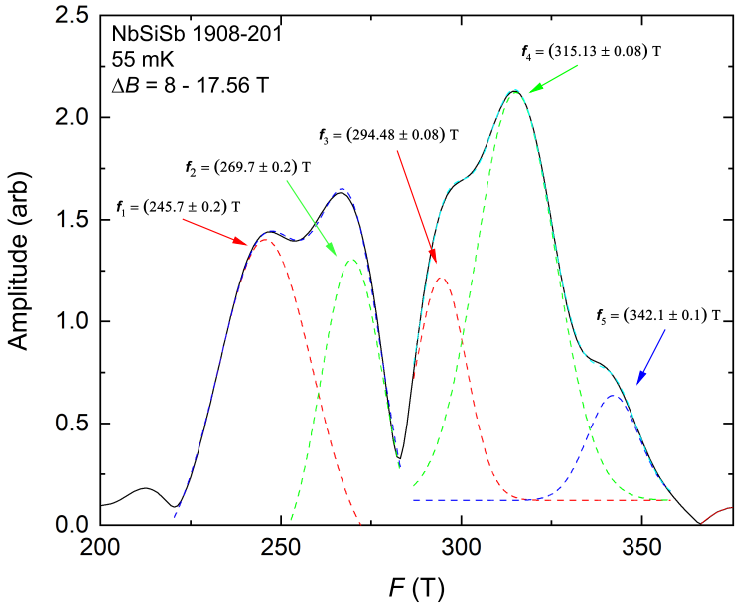

Fig. B.1 Resolving several closely space frequencies in the SdH spectra of NbSiSb using Gaussian fits.

B.1.2 Preliminary Hall data

To determine the nature of the charge carriers in NbXSb, a preliminary Hall effect measurement has very recently been performed on both NbGeSb and NbSiSb. Due to time constraints only a limited analysis has been performed. In NbGeSb at 300 K the Hall resistivity is found to be almost linear with field and positive, this behaviour persists down to the lowest measured temperature of 2.8 K, as shown in Figure B.2a. This behaviour indicates holes as the majority carrier. For NbSiSb at 300 K the Hall resistivity is found to be almost linear with field and also positive, this behaviour persists down to 200 K as shown in Figure B.2b. With decreasing temperature, the Hall resistivity starts to develop a sublinear character and at around 80 K the slope becomes negative at the highest fields. At even lower temperatures, this trend becomes more pronounced and at the lowest temperature (0.62 K) the Hall resistivity becomes negative for fields above 8 T. This suggests that there is more than one type of charge carrier present in NbSiSb.

The mobility can be extracted from the measured Hall resistivity and is shown in Figure B.3 for NbGeSb and NbSiSb. The mobility increases with decreasing temperature for both NbGeSb and NbSiSb reaching values similar to those seen in ZrSiS at low temperatures. Below 2.5 K there is a turnaround in the mobility of NbSiSb which is likely due to the nature of the fit used, a 2-band model

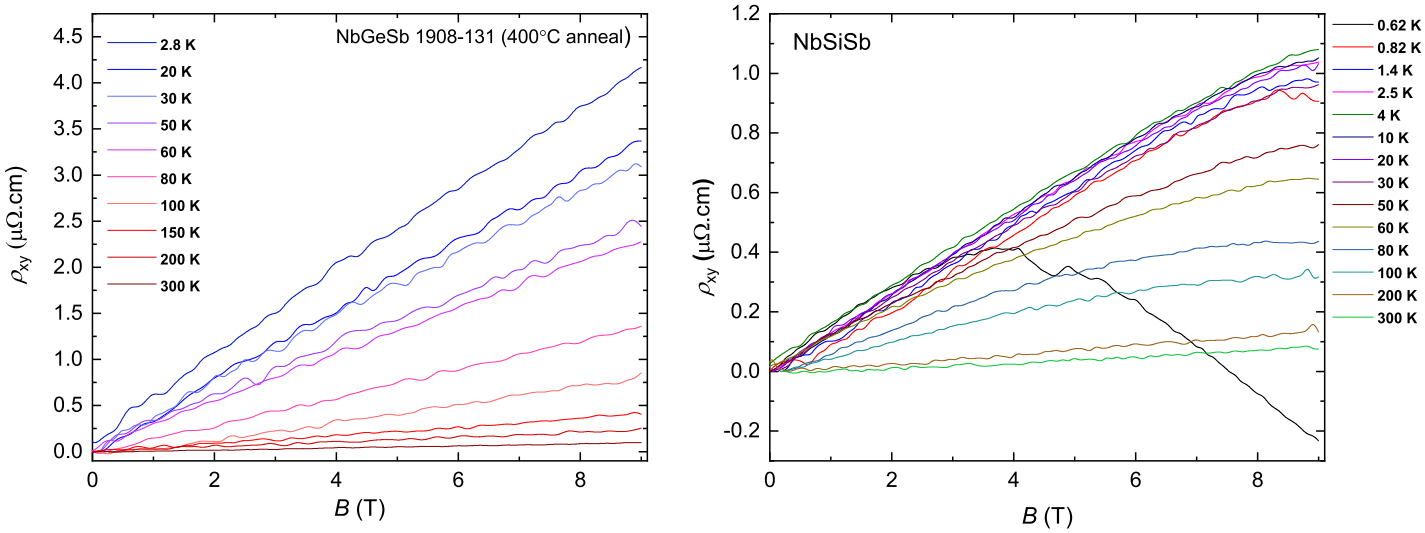

(a) NbGeSb (b) NbSiSb

Fig. B.2 Hall resistivity of **(a)** NbGeSb sample 1908-131 (400°C anneal, 2 weeks), and **(b)** NbSiSb sample 1908-207 (400°C anneal, 2 weeks). Field sweeps were performed at several temperatures in the range 0.7 - 300 K using a QD PPMS ^{3}He option from at a sweep rate of 0.24 T/min.

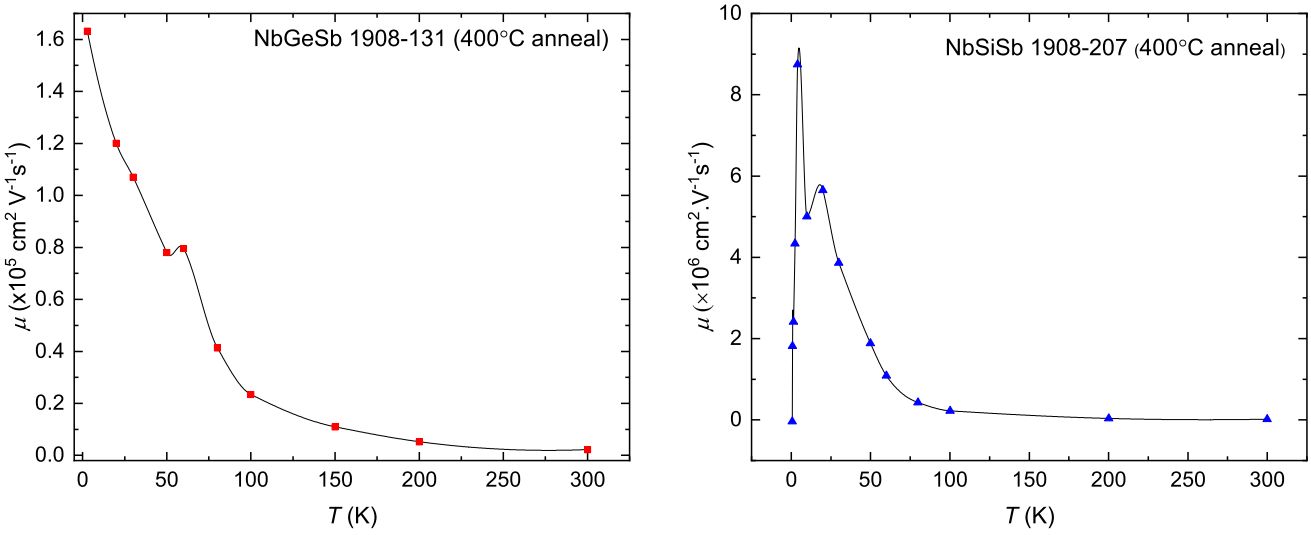

(a) NbGeSb (b) NbSiSb

Fig. B.3 Carrier mobility, μ, as a function of temperature of **(a)** NbGeSb sample 1908-131 (400°C anneal, 2 weeks), and **(b)** NbSiSb sample 1908-207 (400°C anneal, 2 weeks).

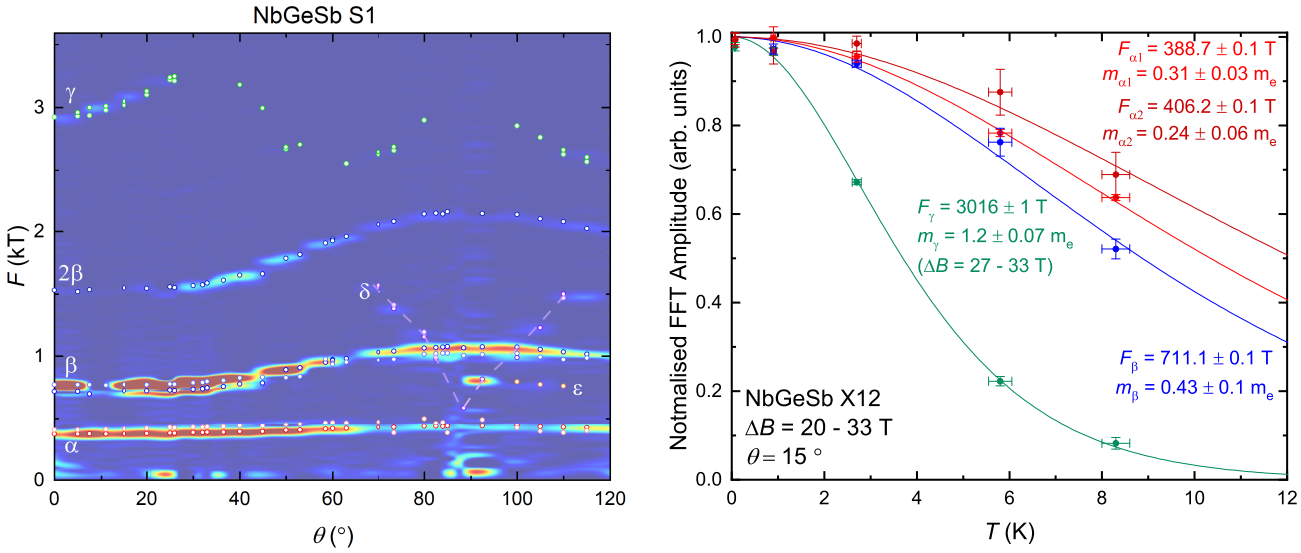

(a) NbGeSb (b) NbSiSb

Fig. B.4 Data from HFML: **(a)** NbGeSb sample 1908-142 (as grown), colourmap showing the quantum oscillation spectra as a function of applied magnetic field angle **(b)** Mass study from HFML.

fit is needed to get a better estimate of the carrier mobilities as it is thought there is more than one type of carrier.

B.1.3 HFML data, March 2020

In early March 2020 samples of NbGeSb were taken to the high magnetic field lab (HFML) in Nijmegen and measured using the piezoresistive torque cantilever method in magnetic fields up to 33 T. A summary of the results are presented in Figure B.4. The data matches very well with the predicted frequency dependence from DFT calculations. We were now able to observe all three predicted frequencies and map their frequency response as a function of applied magnetic field angle. The predicted effective masses also agree well with the DFT predictions. There are, however, two addition frequencies observed which we assume to be due to magnetic breakdown orbits in NbGeSb, labelled δ and ε.